Inauguraldissertation zur Erlangung der Doktorwürde

Visually-evoked dynamics in turtle dorsal cortex examined using large-scale, chronic electrocorticogram recordings

vorgelegt
von
Ingmar Schneider
Gießen, im Mai 2015

Institut für Tierphysiologie
Justus-Liebig-Universität
Gießen

Abteilung Neuronale Systeme
Max-Planck-Institut für Hirnforschung
Frankfurt am Main

Erstgutachter:	Prof. Dr. Reinhard Lakes-Harlan
Zweitgutachter:	Prof. Dr. Dr. Gilles Laurent
Betreuer:	Prof. Dr. Dr. Gilles Laurent

Contents

Zusammenfassung

Frühe anatomische, elektrophysiologische und bildgebende Untersuchungen des zerebralen Kortex von Sumpfschildkröten zeigten, dass die dorsalen Regionen des dreischichtigen Kortex an der Verarbeitung visueller Informationen beteiligt sind. Einige der Studien beschrieben außerdem, dass relativ unspezifische visuelle Stimulation Oszillationen mit komplexen räumlichen und zeitlichen Gradienten in den lokalen Feldpotenzialen evoziert. Anatomische und physiologische Studien deuten weiterhin darauf hin, dass kortikale Neurone ausgedehnte rezeptive Felder aufweisen, ohne dass es eine klare retinotope Abbildung des Gesichtsfeldes im Kortex gäbe. Daher ist noch immer unklar, ob und wie räumliche und zeitliche Aktivitätsmuster mit spezifischen Eigenschaften der visuellen Stimulation korrelieren.

In der vorliegenden Studie wurden mittels großflächiger, chronisch implantierter Oberflächenelektrodengitter visuell evozierte Potenziale vom Dorsalkortex wacher Rotwangen-Schmuckschildkröten (*Trachemys scripta elegans*) abgeleitet. Die visuelle Stimulation erfolgte über ein Projektionssystem mit einer halbkugelförmigen Leinwand, die die Stimulation großer Teile des Gesichtsfeldes erlaubte. Das Stimulusrepertoire umfasste komplexe, natürliche Reize (Bilder und Videos), die sich in globalen Charakteristiken wie Frequenzzusammensetzung sowie räumlicher und zeitlicher Struktur unterschieden.

Die evozierte Aktivität war konsistent in derselben Region des Dorsalkortex lokalisiert und beinhaltete evozierte, kohärente Oszillationen zwischen 15 und 35Hz, die einen rostrokaudalen Phasengradienten formten. Diese Beobachtungen bestätigten und erweiterten die Ergebnisse früherer Untersuchungen. Zusätzlich evozierten natürliche Stimuli (Bilder und Videos) signifikant stärkere und kohärentere Oszillationen als Stimuli mit reduzierter räumlicher und zeitlicher Struktur. Aktivität, die durch natürliche Videos evoziert wurde, enthielt weiterhin Oszillationen höherer Frequenzen (bis 45Hz). Die kortikale Dynamik scheint folglich durch räumliche und zeitliche Charakteristika visueller Stimuli beeinflusst zu werden. Mittels multilinearer Regression war es möglich 32% der Varianz in der aufgezeichneten oszillatorischen Leistung durch globale Stimuluscharakteristika, basierend auf dem Intensitätshistogramm, der Verteilung lokaler Kontrastelemente und der räumlichern Frequenzzusammensetzung zu erklären. Daher ist anzunehmen, dass diese Charakteristika für die Verarbeitung natürlicher visueller

Reize im Dorsalkortex der Schildkröte relevant sind.
Die erhöhte kortikale Aktivität nach natürlicher Stimulation gegenüber Kontrollstimuli sowie die Abwesenheit von Retinotopie legen eine Ähnlichkeit des Dorsalkortex der Schildkröte mit nicht-retinotopen, extrastriären Arealen des Objekterkennungssystems der Säugetiere nahe.

Summary

Early anatomical, electrophysiological and voltage-sensitive dye imaging studies of the cerebral cortex of slider turtles indicate that the dorsal regions of the three-layered cortex are involved in the processing of visual information. Some of these studies revealed that relatively unspecific visual stimulation evokes oscillations in the local field potential with complex spatio-temporal gradients. Anatomical and physiological studies further suggest that cortical neurons possess extensive receptive fields in the absence of a clear retinotopic map of visual space in dorsal cortex. Therefore, it is still not clear whether and if so, how, spatio-temporal activity patterns correlate with specific features of visual stimulus space.

Here, visually-evoked responses were recorded from awake red-eared sliders (*Trachemys scripta elegans*) using chronically implanted, high-density surface electrode grids covering large areas of dorsal cortex. Stimuli were delivered using a projection system and a semi-spherical screen, enabling the stimulation of extensive parts of visual space. The stimulus set consisted of complex natural visual stimuli (scenes and videos) that differed in global features such as frequency content, spatial and/or temporal structure.

Evoked activity was consistently located in the same region of dorsal cortex and contained evoked, coherent oscillations in the 15-35Hz range forming a rostrocaudal phase gradient, confirming and extending earlier results. Furthermore, natural stimuli (static and dynamic) evoked significantly stronger and more coherent oscillations than stimuli with reduced spatial or temporal integrity. Responses to stimulation with natural movies contained additional high-frequency components (up to 45Hz). These results indicate that cortical dynamics are influenced by spatio-temporal features of visual stimuli. Using multilinear regression it was possible to explain approximately 32% of the variance in the recorded oscillatory power using a set of global stimulus features based on the intensity histogram, the distribution of local contrast elements and spatial frequency composition. These features may therefore be considered to be relevant for the processing of natural scenes in turtle dorsal cortex.

The increased cortical responses to natural vs. matched control stimulation and the absence of retinotopy suggest a similarity of turtle dorsal cortex to non-retinotopic extrastriate cortex in the mammalian object recognition pathway.

1. Introduction

1.1. The turtle as a model system in neuroscience

1.1.1. The phylogenetic position of turtles among amniotes

Turtles are often simply classified as reptiles or Reptilia in a classical systematic context. However, in modern phylogenetic systematics the Reptilia are no longer considered as an appropriate taxonomic unit, but as a complex paraphyletic group which represents a subset of the monophyletic Sauropsida (see Fig. 1.1). The Sauropsida are an ancient group which includes the taxa Lepidosauria (Rhynchocephalia and Squamata), Archosauria (Crocodylia and Aves), and Testudines (Pleurodira and Cryptodira). Together, they form a sister branch to the Synapsida which include the extant mammals.

From genomic data, the divergence of sauropsids and therapsids (a synapsid branch

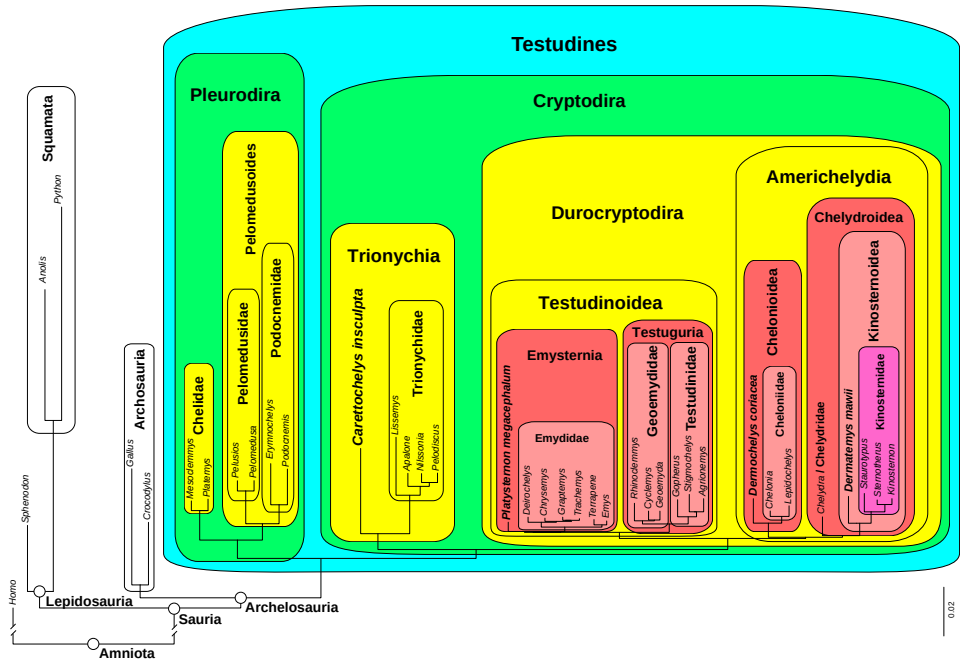

Figure 1.1.: Phylogenetic hypothesis based on the phylogenomic analysis of 2381 ultraconserved elements sampled from 32 turtle taxa and six outgroup species (Gallus, Crododylus, Anolis, Python, Sphenodon, Homo). Note that Sauria is used equivalently to Sauropsida in this figure. From Crawford et al., 2014.

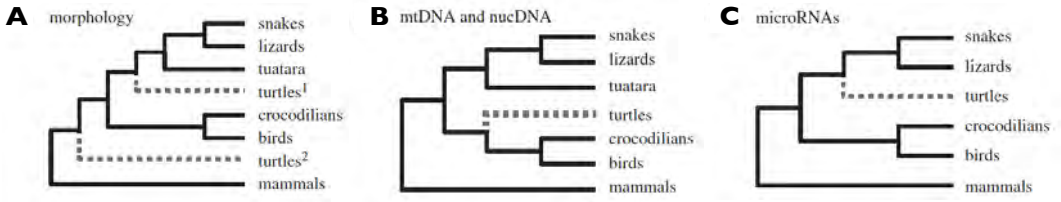

Figure 1.2.: Proposed phylogenetic positions of Testudines among the Sauropsida. **A|** Hypothetical positions based on morphological data (Anapsida hypothesis: turtles^2 vs. Diapsida hypothesis: turtles^1). **B+C|** Hypothetical positions of the Testudines among the Diapsida based on molecular data. **B|** Testudines as sister group to the Archosauria. **C|** Testudines as sister group to the Lepidosauria. Modified from Crawford et al., 2012.

including mammals) is estimated to have happened approximately 315 million years ago in the Karbon age. The sauropsid lines eventually giving rise to extant birds and turtles are estimated to have diverged around 275 million years ago (Wang et al., 2011). The sauropsid crown group Testudines (see Fig. 1.1), which includes fossil and extant turtles, is believed to have developed approximately 212 million years ago. Within the Testudines, the swamp turtle species used in this lab (*Trachemys scripta* and *Chrysemys picta*) belong to the taxon Emydidae which is estimated to be approximately 44 million years old (Joyce et al., 2013).

The phylogenetic position of the Testudines among sauropsids is a heavily discussed and yet unresolved issue. Three major hypotheses (see Fig. 1.2) based on different approaches to and interpretations of the available fossil, morphological and molecular data place turtles in different positions of the amniote phylogenetic tree (Lee, 1997, Hedges, 2012).

(A) **Anapsida hypothesis|** The 'Anapsida hypothesis' is largely based on the absence of temporal fenestrae in the skulls of extant and fossil turtle species. According to this differentiation, the Testudines should be considered a basal sister group (Anapsida) to both the Lepidosauria (squamata, rhynchocephalia) and Archosauria (crocodylia, aves) groups which both feature temporal fenestrae in their skulls (Diapsida; see Fig. 1.2 A).

(B+C) **Diapsida hypothesis|** Alternatively, Olivier Rieppel and colleagues (Rieppel and deBraga, 1996, Rieppel, 1999) suggested that the anapsid state of turtles, especially the lack of temporal fenestration, is a secondary feature and that the Testudines should thus be placed among the diapsid (Lepidosauria, Archosauria) sauropsids (Fig. 1.2 B, C). However, supporters of this alternative 'Diapsid hypothesis' are debating the exact position of the Testudines among the diapsid

Sauropsida. Based on a novel approach focused on microRNA data, Lyson et al. 2012 (Fig. 1.2 C) suggested that turtles should be considered a sister group to the Lepidosauria clade (Lyson et al., 2012). Other studies however (Fig. 1.2 B) place the Testudines in a closer relation to the Archosauria using molecular evidence from mitochondrial DNA, nuclear DNA and microRNA (Zardoya and Meyer, 1998, Hedges, 1999, Crawford et al., 2012).

Although recent innovations in phylogenetic analysis techniques have raised hopes to finally solve certain long-standing phylogenetic problems, the question of the phylogenetic position of turtles among reptiles does not appear to be unequivocally answered. Two recent studies provide strong evidence for a phylogenetic Archelosauria taxon (Archosauria and Testudines) based on several thousand genomic ultraconserved elements from 32 turtle species and 6 outgroups (Crawford et al., 2012, Crawford et al., 2014). The authors were able to construct a single robust phylogeny by applying three distinct phylogenetic analysis methods (maximum likelihood, Bayesian, species tree; see Fig. 1.1). Because of its consistency with stratigraphic and biogeographic fossil distributions, the authors suggest this phylogeny to be more plausible than purely morphological approaches.

1.1.2. The simplicity of the turtle brain

The forebrains of turtles and other non-avian sauropsid groups feature cytoarchitectonically simple, sheet-like, layered cerebral cortices which exhibit an intriguing similarity to presumably old cortex structures in modern mammals. Fig. 1.3 displays exemplary cross sections of the forebrains of five extant amniote species as well as a cladogram illustrating the basic phylogenetic relationships of the exemplified species. All of the displayed examples, except for the chick, feature a sheetlike layered cortical structure in their dorsal pallium. However, certain pallial structures in birds do exhibit a tendency to layering. It is therefore assumed that a stem cortex had already evolved before Sauropsida and Synapsida diverged and that this layered structure was secondarily lost or modified in the avian branch.
Data from developmental and evolutionary biology indicate that the pallium of all amniotes can be subdivided into four developmentally distinct divisions (ventral, dorsal, lateral and medial pallium) which are considered homologous across amniote groups (Medina and Abellan, 2009). Of these subdivisions the dorsal pallium gives rise to the nuclear avian hyperpallium, the three-layered reptilian dorsal cortex and most likely also to the

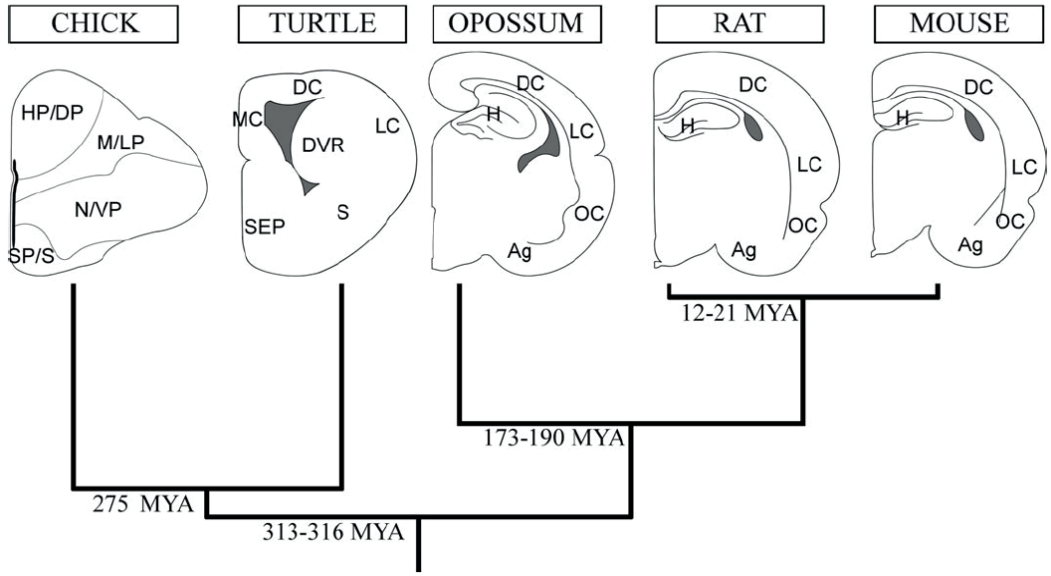

Figure 1.3.: Top| Schematic cross sections through the forebrains of five modern amniote species. **Bottom|** Cladogram displaying the phylogenetic relation of turtles with respect to other recent amniote species. Layered structure of presumed stem-cortex lost in avian sauropsid branch. Abbreviations: hyperpallium/dorsal pallium(HP/DP), mesopallium/lateral pallium(M/LP), nidopallium/ventral pallium(N/VP), subplate/striatum(SP/S), medial cortex(MC), dorsal cortex(DC), lateral cortex(LC), dorsoventricular ridge(DVR), striatum(S), septum(SEP), hippocampus(H), olfactory cortex(OC), amygdala(Ag). From Wang et al., 2011.

six-layered mammalian isocortex (Aboitiz et al., 2002a). Within the isocortex, the deep cortical layers (5, 6) are generally considered to be evolutionarily older than the superficial layers. The superficial layers are believed to be later additions which triggered the inverted neurogenic gradient together with the tangential expansion of isocortex (Aboitiz et al., 2002b). The particularly primitive mammalian paleo- and archicortices (pyrifom cortex and hippocampal formation) show a high degree of similarity to the reptilian dorsal cortex in their cellular composition and may represent the remnants of the common ancestral cortex of early amniote evolution.
Due to these structural and developmental similarities, it is assumed that the dorsal pallia of reptiles and mammals are homologous and that reptilian cortex may represent a simpler, archetypical and ancient prototype (Medina and Abellan, 2009).

While it is ultimately important to establish the exact phylogenetic position of turtles, it is sufficient for the purpose of this study to point out that (1) turtles are non-avian sauropsids, (2) that all non-avian sauropsids have a sheetlike layered cortex (lateral, dorsal and medial regions), that turtle cortex cytology appears to be simpler than that of lacertians (Smeets et al., 1986), (4) that turtles are easily accessible, and (5) turtles are highly resistant to anoxia (Belkin, 1963,Bickler and Buck, 2007), making this system

attractive for *in-vitro* studies. The work presented here was thus carried out in turtles, because this lab has made a choice of animal model system based on arguments of evolution, simplicity and robustness.

1.2. Oscillatory activity in neuronal networks

Periodic signals are frequently observed when examining the dynamics of recurrent neuronal networks. Since the first description of the alpha rhythm (8-12Hz) in the human electroencephalogram by Hans Berger (Berger, 1929), rhythmic brain activity has been recorded from intact and reduced brain preparations in insects (Laurent and Naraghi, 1994), mollusks (Gelperin and Tank, 1990), and all vertebrate classes (Berger, 1929, Vanderwolf, 1969, Eckhorn et al., 1987, Kreiter and Singer, 1992, Neuenschwander et al., 1992, Prechtl, 1994). Synchronized oscillations have been observed as brief oscillatory bouts and as sustained, stable oscillations.
Originally, synchronized 'inactive' brain states (i.e. sleep and anesthesia) were opposed to desynchronized 'active' (waking) states, but with the development of sophisticated stimulation and recording techniques oscillations have been shown to correlate with a broad spectrum of brain functions and states (Laurent, 2002, Buzsáki and Draguhn, 2004, Singer, 2013).
Neuronal oscillations occur over a wide range of frequencies (0.05Hz to 500Hz) and classes of oscillations have been described based on their mean oscillation frequencies [See table 1.1 and review (Buzsáki and Draguhn, 2004)]. The mean frequencies of the typically observed classes form a line along a natural logarithmic frequency scale and, in mammalian cortex, the power density of extracellular recordings is inversely proportional to the frequency (Freeman et al., 2000). Different classes have been associated with competing brain states, but different oscillations can also co-exist and interact.
Neuronal populations have been shown to synchronize very locally, but also over large distances across different brain regions. The period of oscillations is limited by the network size such that high frequency oscillations are spatially very confined while low-frequency oscillations can be generated and maintained over longer distances. Mathematically, neuronal oscillators belong to limit-cycle and weakly chaotic oscillators uniting characteristics of both harmonic and relaxation oscillators. In combination these characteristics result in oscillatory behavior with a predictable time-course and simple phase reset.

Because of their abundance and correlation with behavioral and perceptual phenomena, it is important to understand oscillations in the extracellular field potential at a

Table 1.1.: Typical oscillation frequencies in mammalian brains and their labels (Singer, 2013).

DELTA	δ	<2	Hz
THETA	θ	4-7	Hz
ALPHA	α	8-12	Hz
BETA	β	15-30	Hz
LOW-GAMMA	γ	30-60	Hz
HIGH-GAMMA	γ	60-$\sim$90	Hz
RIPPLES	-	$\sim$200	Hz

mechanistic level. Oscillations in various frequency ranges are commonly observed across different animal species (invertebrates and vertebrates; see below) and over a broad spectrum of brain sizes. This has been considered to suggest common mechanisms of generation.

As described in section 2.1, the extracellular potential reflects a weighted average of the ionic processes (esp. synaptic processes) in an observed specimen. Oscillations in the extracellular field are thus indicative of periodically co-active neurons with outputs in the vicinity of the recording electrode. However, multiple scenarios of cellular activity can result in identical oscillatory patterns in the extracellular field and it is impossible to determine from the extracellular field alone whether all neurons in a network fire in phase or if smaller subgroups fire in more complex alternating patterns.

It is well established that oscillations arise through a dynamic interplay of the cellular properties of the constituent neurons and the circuit properties in the oscillating network. While the activity of single cortical pyramidal neurons shows Poisson statistics, these neurons often show oscillatory behavior in assemblies. In many neuronal systems, the grouping of principal neurons into such synchronous assemblies is achieved through inhibitory interneuron "clocking" networks. Chemical synaptic coupling in these "clocking" networks is frequently enhanced through additional electrical coupling via gap junctions. Particular types of inhibitory GABAergic interneurons have been shown to be involved in the generation of coherent oscillations in mammalian cortex and hippocampus (Klausberger and Somogyi, 2008, Lasztóczi and Klausberger, 2014, Hu et al., 2014) as well as the insect olfactory system (MacLeod and Laurent, 1996).

The topology of many neuronal networks with a high density of local connections and a low density of long range connections may represent a cost-efficient wiring scheme similar to mathematically described 'small-world networks' (Watts and Strogatz, 1998,Strogatz, 2001, Buzsáki et al., 2004).

Neuronal oscillations have been recorded in both sensory and motor systems and could be shown to correlate with various brain functions and states. The following list provides an overview over a set of (hypothetical) functional principles attributed to cortical oscillations [Modified from (Buzsáki and Draguhn, 2004)]. Whenever possible suitable examples are provided.

(A+B) For individual neurons in a synchronized network, oscillations in the extracellular potential could serve as rhythmic pacemakers defining a temporal framework for the summation of synaptic signals (A) or the precise timing of action potentials (B).

(A) Input selection| Oscillations are energy efficient means to synchronize neuronal assemblies, enabling them to integrate information from convergent inputs. Neurons exhibit distinct temporal filtering properties such that afferent input signals are selected based on their frequency. The filtering properties of neurons arise from an interplay of high-pass (voltage-gated currents) and low-pass (leak conductance and capacitance) filter characteristics. Through different combinations of these characteristics neurons can exhibit resonator (band-pass), notch (band-stop) or sub-threshold oscillator properties. Cortical interneuron classes show various filtering properties and may be considered as implementations of different filter types. Active hippocampal pyramidal neurons, for example, recruit surrounding basket cells via their high frequency outputs and thereby inhibit other pyramids in their vicinity (Marshall et al., 2002). On a larger scale, thalamocortical feedback loops show resonance properties observed in the form of thalamocortical spindle oscillations during slow-wave sleep. Through neuromodulatory inputs from the brainstem to the thalamus, reticular and thalamocortical neurons are shifted from a tonic to a rhythmic firing mode and successively entrain cortical neurons thereby effectively reducing their responsiveness to external inputs. This leads to a progressive decoupling of cortex from the sensory input and shifting sleep into deeper stages (Steriade et al., 1993).

The above described principle can be further refined by phase biasing inputs with respect to ongoing network oscillations, enabling the network to gate information. Neuronal responses within oscillating networks are determined by both the timing of external inputs and the intrinsic network dynamics (i.e. rhythms). In a network of pyramidal neurons which receive phase-coupled somatic inhibition and transient dendritic excitation, the rhythmic inhibition generates discrete temporal windows in which the pyramidal cells are susceptible to dendritic inputs. Only inputs arriving during phases of low interneuronal inhibition can sufficiently excite principal neu-

rons in the network to fire action potentials. Additionally, synchronous oscillations represent a reference framework for Hebbian synaptic plasticity mechanisms modifying the synaptic connection weights of co-active neurons within the oscillating population (Markram et al., 1997). For example, the timing of principal cells firing in hippocampus with respect to the phase of ongoing theta oscillations determines directly whether connections undergo long-term potentiation or depression (Huerta and Lisman, 1995).

(B) Representation by phase information| Ongoing network oscillations can not only gate information processing, but the interplay of the strength of dendritic inputs and the phase of an ongoing network oscillation can also determine when a pyramidal neuron fires within a window of opportunity. Strong dendritic drive will cause neurons to fire earlier during these temporal windows, generating a short-term representation of input strength by the phase of spikes with respect to the underlying network oscillation. An example for this representation of information by phase is phase-precession in hippocampus. Hippocampal place cells in freely moving animals fire successively earlier in each theta cycle when the animal moves through their place fields (O'Keefe and Recce, 1993). Such repetitive temporal patterns can subsequently exploit spike-timing-dependent plasticity mechanisms for memory consolidation. The phase of single action potentials with respect to an oscillation cycle can thus serve as a general temporal coding scheme across different classes of oscillations (O'Keefe and Recce, 1993, Fries et al., 2007).

(C) Binding cell assemblies| Neuronal oscillations enable the transient synchronization of neuronal assemblies. This is cost effective and even possible with weak synaptic links as long as the frequencies of the coupled oscillators are similar. Transient synchronization of neuronal assemblies has been proposed as a possible solution to the so-called 'binding problem' in visual perception (Milner, 1974, von der Malsburg, 1981, Treisman, 1996). Specifically, synchronization in the gamma (γ) band has been suggested to bind distributed neuronal assemblies processing different aspects of a coherent visual object (Singer, 1999). Stimulus-evoked γ-oscillations have been described in the visual cortices of mice (Nase et al., 2003), cats (Gray and Singer, 1989,Gray et al., 1989), and macaque monkeys (Kreiter and Singer, 1992). Precise phase-synchronization of distributed networks has been demonstrated to be required for a meaningful interaction between the connected assemblies (Womelsdorf et al., 2007) and synchronous oscillations across different brain regions have been described as a potential means for the flexible

routing of information flow in the brain supporting population codes (Akam and Kullmann, 2010, Akam and Kullmann, 2014). Since its discovery, gamma-band synchronization has been proposed to be associated with a wide spectrum of sensory and cognitive processing and proposed as a fundamental process involved in the segmentation and selection of converging neuronal inputs (Fries, 2009).
However, the hypothesis of a precise temporal code in neuronal discharges is heavily debated. A central argument against the existence of temporal codes is the high amount of variability and the irregular interspike intervals frequently observed in neuronal discharges (Shadlen and Newsome, 1994). It has thus been proposed that information in the brain is more likely to be encoded in a noisy rate code which is less susceptible to temporal inaccuracies and thus more robust (Shadlen and Movshon, 1999).
It should be noted that the existence of one coding scheme in a particular brain region does not exclude the implementation of alternative codes in other brain regions. Thus both temporal and rate codes may co-exist in different parts of the nervous system.

(D) Consolidation and combination of learned information| Global oscillations are an inherent property of unperturbed, balanced systems and may represent their default state. The sleeping brain exhibits a variety of oscillatory rhythms through which it progresses in an orderly fashion. During sleep in mammals and birds, four stages of slow-wave and paradoxical rapid-eye-movement (REM) sleep alternate in the extracellular field potential. In a repetitive pattern, the brain successively progresses through the four stages of slow-wave sleep and then enters a REM phase (see thalamocortical resonance in (A)). While the slow-wave sleep stages are characterized by large amplitude, low-frequency oscillations, the REM sleep phases are very similar to the 'desynchronized' awake state. Similarly, several other physiological markers (i.e. breathing, heart rate, muscle tone etc) are reduced during slow-wave sleep and almost at awake levels during REM sleep.
Place cell assemblies as well as theta rhythms in the hippocampal formation of rats were shown to be re-activated in slow-wave and REM sleep phases following behavioral tasks during which these cell assemblies had been active (Wilson and McNaughton, 1994, Louie and Wilson, 2001). These replay discharges occur predominantly during episodes of 200Hz ripple oscillations in hippocampus (Buzsáki et al., 1992) and neocortical sleep spindles (Siapas and Wilson, 1997). The rhythmic activity during sleep has thus been considered to be involved in the consol-

idation and combination of replayed waking experiences and their transfer from hippocampus to neocortex (Wilson, 2002). Similarly, it has been suggested that episodes of high firing rates during 'decoupling' of neocortex represent cortical processing of internally generated activity patterns (Steriade et al., 2001) and periods of increased plasticity which serve to consolidate memory traces (Steriade, 2001).

While the previous paragraphs described synchronous neuronal oscillations and their proposed functions mainly in mammalian species, oscillatory activity has also been shown to occur in non-mammalian vertebrates as well as invertebrate species.
The brains of locusts exhibit pronounced odor-evoked oscillations in the range of 20Hz which have been demonstrated to reflect the coherent activation of cell assemblies in the olfactory system. These oscillations have been demonstrated to be functionally relevant for odor perception (Stopfer et al., 1997) and for the transformation of olfactory information from the antennal lobe to the mushroom body (Perez-Orive et al., 2002). Additionally, a spike-timing-dependent plasticity mechanism has been shown to stabilize sparse odor representations in the mushroom body within the framework of these oscillations (Cassenaer and Laurent, 2007, Cassenaer and Laurent, 2012).
As will be described in more detail in section 1.3, spontaneous and stimulus-evoked $\sim$20Hz oscillations have also been observed in the cerebral cortex of turtles (Prechtl, 1994). Oscillations in the local field potential in turtle cortex were demonstrated to be generated by local current sources exhibiting systematic phase gradients across cortex (Prechtl et al., 2000). However, the exact mechanisms underlying the generation of these oscillations as well as their functional role for perception or cognition are still unknown.

While it is tempting to label and lump oscillatory activity observed in different brain regions or even species according to their frequency, this should only be done after careful consideration. Oscillations in similar frequency bands could be generated by entirely different network structures and also serve very different purposes. Conversely, oscillations in different frequency bands might fulfill similar functions in different animals or brain regions. The labeling framework displayed in Tab. 1.1 should thus be taken as purely descriptive, because apparently similar rhythms may not be equal in function.

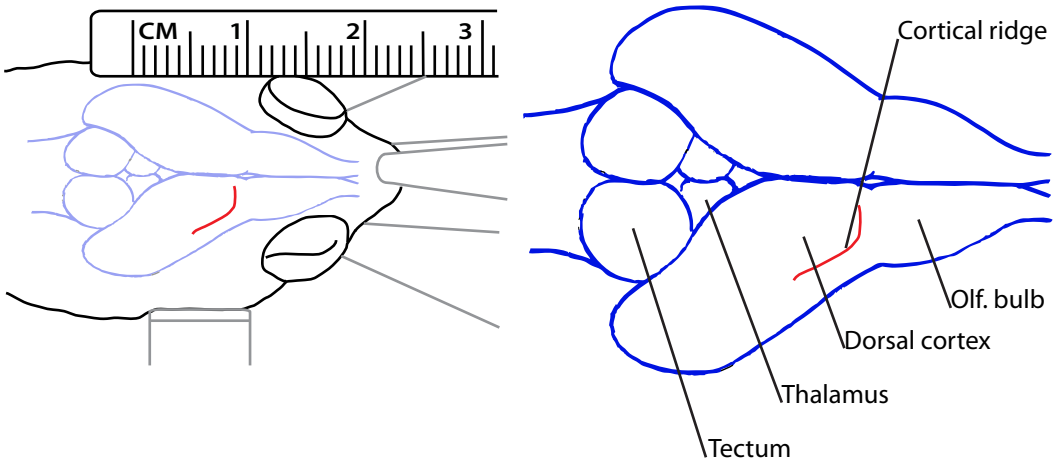

Figure 1.4.: Schematic illustration of the position of the turtle brain (blue elements) within the skull (left) as well as location of macroscopically visible brain structures (right). Note that skull bones and muscles are not shown to improve visibility. Gray lines correspond to elements of the stereotactic apparatus. The red line indicates the approximate location of the cortical ridge which represents a reliable landmark on the otherwise smooth cerebral hemisphere.

1.3. The visual system of turtles

The main focus of this study is the examination of dynamics in the visually responsive areas in the dorsal cortex of turtles using electrocorticogram (ECoG) recording techniques. Therefore, this overview over the neuroanatomy of reptiles will be focused on the basic characteristics of the visual system. An overview of the approximate position of the turtle brain within the skull as well as the locations of a set of major brain structures are provided in Fig. 1.4. For a more detailed description of the anatomy and connectivity of the turtle brain, please refer to the PhD thesis of Paul Desan (Desan, 1984) and the anatomical atlas of Powers and Reiner (Powers and Reiner, 1980).

1.3.1. Processing of visual information in the turtle retina

As in other vertebrates, processing of visual information in reptiles begins in the retina where light is absorbed by photoreceptors. In the photoreceptors the absorbed light is translated into electrical signals and transmitted via several intermediate neurons (bipolar cells, amacrine cells, horizontal cells) to a layer of ganglion cells.
The retina of turtles has been intensively studied in the past and extensive reviews of the literature on the functional architecture of the turtle retina have been compiled by Granda & Dvorak and Ammermüller & Kolb (Granda and Dvorak, 1977, Ammermüller and Kolb, 1996). Its general inverted architecture and layering are very similar to those of mammals, with inner and outer nuclear and plexiform layers.

However, in contrast to the trichromatic primate retina, the turtle photoreceptor layer features, in addition to one type of rod photoreceptors, a larger set of cones (Baylor and Hodgkin, 1974, Ammermüller and Kolb, 1996). The turtle cone system consists of three types of long wavelength (L) cones, and one type of each medium (M), short (S) and ultraviolet (UV) cones. The cones themselves appear as single or double cones and are combined with oil droplets of various additional filtering properties which further diversify their wavelength specificities. Ammermüller reviewed data from several original studies and reported relative cone abundances of 26-50% for single red-sensitive cones with red oil droplets, 17-27% for green sensitive cones with yellow oil droplets, 15-20% for red-sensitive double cones, 6-18% for blue sensitive cones with fluorescent oil droplets, and 1-6% for UV-sensitive cones with non-fluorescent oil droplets. Rod density was reported to range from 2.5% to 15% (Ammermüller and Kolb, 1996).
The nuclear layers show the vertebrate-typical complement of constituent cell types. Horizontal, bipolar, and amacrine cells populate the inner nuclear layer while the outer nuclear layer mainly contains ganglion cells. The morphological (and functional) subtypes of these cells form complex connection patterns in the well-developed neuropils of the inner and outer plexiform layers. Based on morphological and physiological criteria, the turtle retina features four distinct types of horizontal cells, 12 types of bipolar cells, 37 types of amacrine cells as well as 24 types of retinal ganglion cells (Ammermüller and Kolb, 1996). This cell diversity is accompanied by complex connectivity patterns, especially in the multistratified inner plexiform layer. Functional characterization of the individual cell types in the retinal circuit showed that neurons in the outer retina have 'simple', concentric receptive fields while neurons in the inner retina exhibit a high level of selectivity (color, orientation, motion, direction), indicating a high degree of pre-processing of visual information in the retina (Granda and Dvorak, 1977, Ammermüller and Kolb, 1996).

The density distribution of retinal ganglion cells (RGCs) corresponds largely to that of photoreceptors. The location of highest ganglion cell density in the turtle retina ($18.000 \frac{\text{cells}}{\text{mm}^2}$; PD in Fig. 1.5 A) is embedded in an extensive area of high ganglion cell density ($>6000 \frac{\text{cells}}{\text{mm}^2}$; thin line in Fig. 1.5 A). From the region of peak density to the periphery, the density of RGCs decreases anisotropically, resulting in an elongated strip of high ganglion cell density that is oriented along the nasotemporal axis and that is called the visual streak (Peterson and Ulinski, 1979). The streak runs slightly above the meridian separating the dorsal and ventral halves of the retina and the optic disc is situated approximately two millimeters ventral to the location of highest density (black

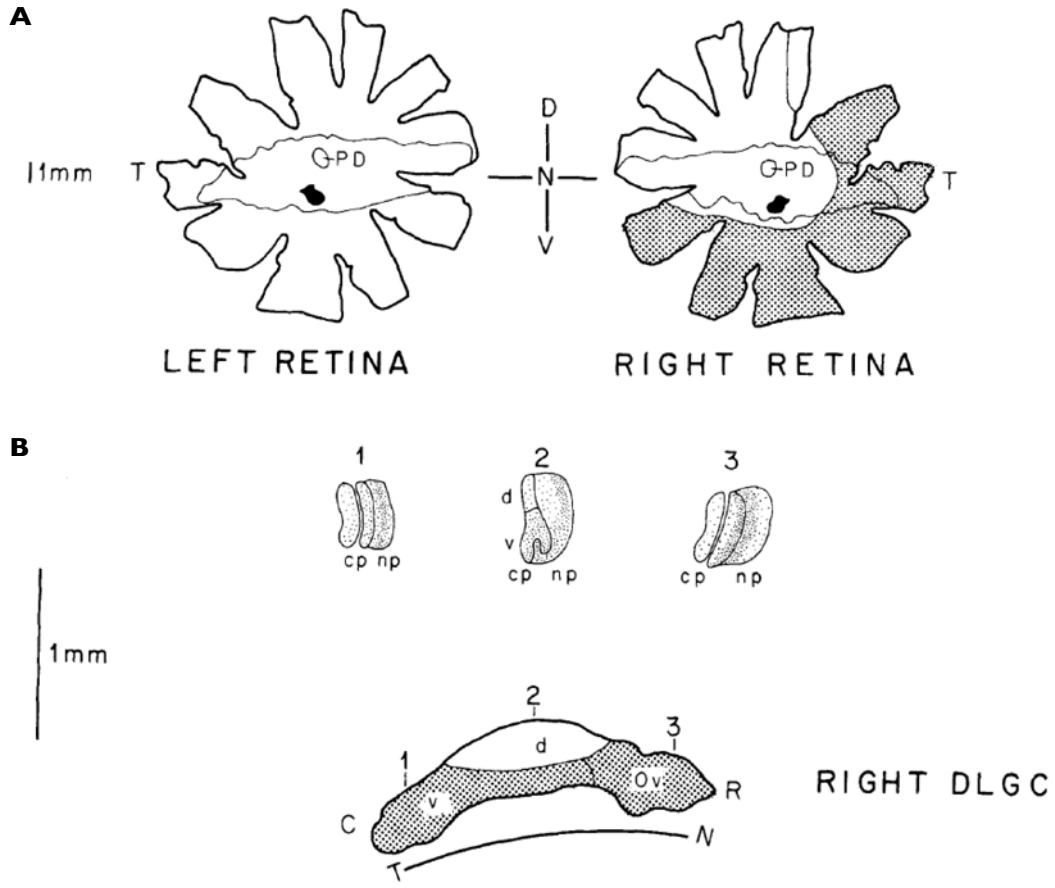

Figure 1.5.: A| Schematic display of two whole-mounted retinae with a contour indicating the visual streak, area of peak RGC density (PD) and optic disk (black spots). Note that while the entire left retina projects to the right dLGC, only the patterned part of the right retina sends axons to the ipsilateral thalamus. **B|** Retinal projections to the dLGC. Subnucleus ventralis (v), sn. ovalis (Ov) and sn. dorsalis (d); cell plate (cp), neuropile (np). Additional abbreviations: Caudal (C), Rostral (R), Temporal (T), Nasal (N), Dorsal (D), Ventral (V). From Ulinski and Nautiyal 1988.

spot in Fig. 1.5 A). Anatomical studies of soma sizes with respect to cell density showed that retinal ganglion cells in densely packed central regions tend to be smaller than in the periphery. Along the nasotemporal axis, nasal retinal ganglion cells are significantly smaller than temporal ganglions cells (Peterson and Ulinski, 1982). The close correspondence of ganglion cell and photoreceptor densities suggests that regions of high cell density represent areas of high visual acuity, but to my knowledge there are no studies which systematically characterized the receptive fields of RGCs as a function of their eccentricity.

The axons of the RGCs project into the forebrain via the optic nerve. At the point of the optic chiasm the majority of fibers originating in one eye cross over to the contralateral side with only a small portion of the fibers remaining on the ipsilateral side (Kosareva,

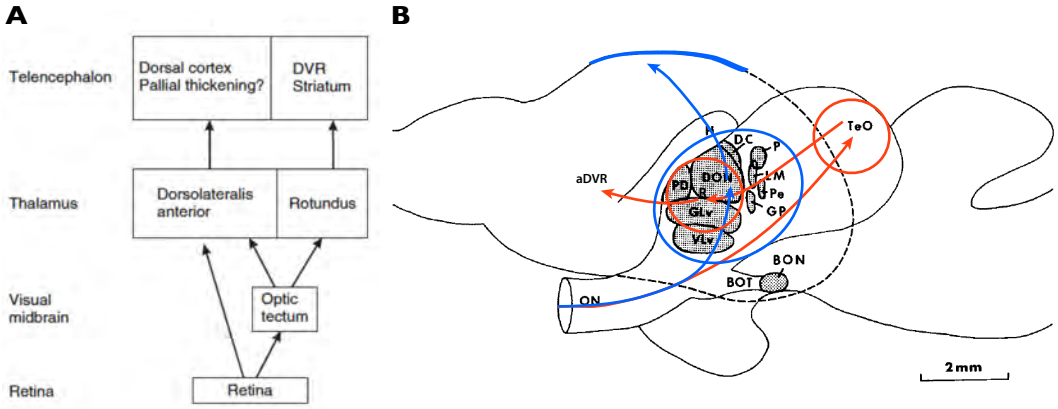

Figure 1.6.: A| Flow-chart display of the main stations of central visual projections in non-avian reptiles. Modified from Kaas, 2009. **B|** Schematic display of the main retinorecipient nuclei in the diencephalon and mesencephalon of the turtle. Modified from Bass and Northcutt, 1981. Blue = retinogeniculocortical pathway; Red = retinotectofugal pathway. Abbreviation: anterior dorsoventricular ridge (aDVR), basal optic nucleus (BON), basal optic tract (BOT), dorsal central neucleus (DC), dorsal optic nucleus (DON), pars ventralis of the lateral geniculate nucleus (GLv), nucleus geniculatis pretectalis (GP), habenula (H), nucleus lentiformis mesencephali (LM), optic nerve (ON), nucleus posterodorsalis (P), pars dorsalis of the lateral geniculate nucleus (PD), external pretectal nucleus (Pe), nucleus rotundus (R), optic tectum (TeO), pars ventralis of the nucleus ventrolateralis (VLv).

1967, Bass and Northcutt, 1981, Ulinski and Nautiyal, 1988). The exact proportions of decussating to non-decussating fibres have not been quantified, but comparative studies across turtle species revealed considerable interspecific variability in the extent of ipsilateral projections and indicate that ipsilateral projections are unrelated to stereoscopic vision (Hergueta et al., 1991, Hergueta et al., 1994).
From the optic chiasm, the fibers project onward in the optic tract and form two distinct major projection pathways [cf. Fig. 1.6; (Kaas, 2009)]:

(I) The retinogeniculocortical pathway (see 1.3.2)

(II) The retinotectofugal pathway (see 1.3.3)

The first pathway leads to the dorsal lateral geniculate complex of the thalamus from where projections are relayed to the dorsal cortex via the lateral forebrain bundle. In the second pathway, the projections travel on to the optic tectum in the midbrain from where they are relayed to the nucleus rotundus of the thalamus. From the nucleus rotundus, visual information is sent to the anterior parts of a subcortical structure called the dorsoventricular ridge which sends projections to the dorsal cortex. Both pathways will be described in more detail below.

1.3.2. The retinogeniculocortical pathway

The dorsal lateral geniculate complex (dLGC) is one of the first projection sites of RGC axons in the turtle visual system (Kosareva, 1967, Bass and Northcutt, 1981, Ulinski and Nautiyal, 1988). It extends rostrocaudally and consists of the nucleus ovalis and the dorsal lateral geniculate nucleus of Papez. Cytoarchitectonically, it is subdivided into three distinct subnuclei: (a) subnucleus ovalis, (b) dorsal and (c) ventral subnuclei; each featuring a lateral neuropil region and a medial cell plate region (compare Fig. 1.5 B and PD+GLv in Fig. 1.6 B). Neurons in the cell plate separate into medial and lateral sublaminae based on soma sizes (Rainey and Ulinski, 1986).
Anatomical tracing studies show that the dLGC receives retinal inputs from the entire contralateral retina as well as a ventrotemporal region of the ipsilateral retina (shaded area in Fig. 1.5 A). Note that projections from the ipsilateral retina only include a small temporal part of the visual streak and do not contain the region of peak ganglion cell density. Anterograde tracing experiments (see Fig. 1.5) revealed that ganglion cell fibers from the frontal visual field (temporal retina) terminate in the caudal parts of dLGC; fibers from the caudal visual field (nasal retina) terminate in rostral regions of dLGC (Ulinski and Nautiyal, 1988). In addition to the representation of the nasotemporal axis of the retina along the rostrocaudal axis of the dLGC, a representation of the dorsoventral axis of the retina has been suggested along the dorsoventral axis of the dLGC through a layering of inputs (Ulinski and Nautiyal, 1988).

Unfortunately, there is very little known about the physiology of neurons within the dLGC. Mazurskaya characterized the receptive fields of presumed dLGC neurons indirectly by recording from afferent visual fibers in the dorsal cortex of the bog turtle *Emys orbicularis*. The author described simple and composite receptive fields with sizes ranging from 2-6° visual angle (Mazurskaya, 1973a).
Another study examined the receptive fields of visually responsive neurons in the thalamus of the same species (Boiko, 1980). The author classified visually responsive neurons into two distinct types based on their responses to differently sized stimuli. Type I neurons (85% of the recorded neurons) responded to visual stimuli of all tested sizes (1-2° vis. angle; 20-26° vis. angle; 4x26° vis. angle) and had small ($\leq$11° vis. angle), medium (11-30° vis. angle) or large ($>$30° vis. angle) receptive fields. Type II neurons responded only to large visual objects (20-26° vis. angle), predominantly had large receptive fields and showed stronger adaptation. Both groups of neurons further contained cells exhibiting a selectivity for motion direction (9% and 20%, respectively).

In contrast to the small receptive fields described by Mazurskaya, Boiko found a predominance of large receptive fields (88.7% of all neurons), considerably less medium receptive fields (10.0%) and only very few small receptive fields (1.3%). Data obtained for retinal ganglion cells in the same study showed that most ganglion cells had small (57%) or medium (43%) receptive fields. No large receptive fields were observed in RGCs. This indicates a high level of convergence of visual information in the thalamus of turtles.

Geniculocortical projections arising in the dLGC travel through the ipsilateral lateral forebrain bundle and terminate in the dorsal cortex (Mulligan and Ulinski, 1990). Anterograde tracing showed an orderly lateromedial projection through cortex in what the authors called iso-azimuth lamellae along the rostrocaudal axis. According to this study, rostral parts of the dLGC send axons to caudal parts of cortex and caudal parts of dLGCs project to rostral cortex. Projections were shown to terminate in the outer 100µm of dorsal cortex; mainly on spiny dendrites of principal neurons, but also on smooth dendrites of subpial interneurons. An electron-microscopical quantification showed that stellate cells receive approximately six times more thalamic inputs than pyramidal cells (Smith et al., 1980).
In combination with retinogeniculate tracing data, this pattern would imply that in turtle dorsal cortex visual space is represented in a strip-wise manner resolving azimuth, but discarding elevation. In the proposed scheme, nasal segments of visual space would be represented in rostral regions of dorsal cortex while temporal visual space would be represented caudally. Currently, tract tracing experiments are conducted in this lab to verify the described projection patterns.

Turtle cortex| The cerebral cortex of turtles is quite similar to mammalian archi- and paleocortices (i.e. pyriform cortex and hippocampal formation). It comprises three layers (Fig. 1.7 B) of neurons and features only one layer containing spiny principal neurons (Fig. 1.7 C). The superficial or 'molecular layer' of the turtle cortex consists mainly of incoming thalamic axons, superficially interspersed with interneurons (Fig. 1.7 D) and the apical dendrites of the pyramidal-like principal neurons of the second layer called 'cell layer'. The third, 'subcellular' layer again contains mostly local interneurons and the axons and basal dendrites of the principal neurons. In an early study of the turtle forebrain, Mazurskaya et al. stained neurons in the turtle cortex with the Golgi method and classified four types of neurons (two spiny, two aspiny) based on their morphology (Mazurskaya et al., 1966).
Based on morphological characteristics, the cerebral cortex of turtles is usually subdivided

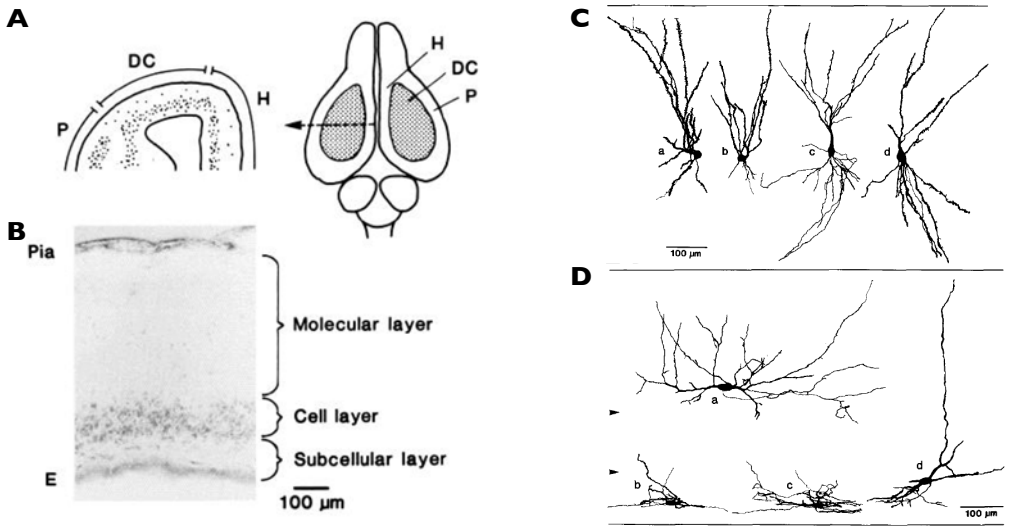

Figure 1.7.: A| Schematic of the dorsal part of a frontal section (left) through a turtle brain (right). The position of the section is indicated by the arrow. Dorsal cortex (DC), pyriform cortex (P), hippocampus (H). **B|** Cresyl violet stain of a dorsal cortex section indicating the position of the three layers. Ependymal layer (E). Camera lucida drawings of Golgi-stained **C|** pyramidal neurons and **D|** stellate cells. Modified from Connors and Kriegstein 1986.

into lateral (olfactory), dorsal (visual), dorsomedial, and medial cortex areas (Desan, 1984). Unfortunately, this nomenclature was not consistently applied throughout the turtle literature and some authors used alternative labels to imply functional similarities to mammalian brain areas. An example is provided in Fig. 1.7 A where the lateral cortex is labeled as pyriform cortex (P) and the medial cortex is labeled as hippocampus (H). The dorsal (visual) cortex is further compartmentalized into a lateral subarea D2 and a medial subarea D1. The border between D2 and D1 is commonly defined by a shift in the density and depth of the cell layer (Desan, 1984) which is further considered to represent the medial limit of afferent projections from dLGC (Mulligan and Ulinski, 1990). Stained thalamic axons bearing fusiform varicosities along their entire length were observed to enter cortex ventrolaterally and traverse medially through the pallial thickening into Desan's cortical area D2 (Desan, 1984, Mulligan and Ulinski, 1990).
However, it should be noted that the definition of the D2/D1 border in the existing literature is often unclear. Recent experiments in this lab indicate that the thalamic afferents extend beyond the shift in the cell layer.

The morphological and physiological properties of neurons within the cytoarchitectonic layers of turtle dorsal cortex have been intensively studied using sharp electrode intracellular recordings (Connors and Kriegstein, 1986, Kriegstein and Connors, 1986). The authors described two morphological and physiological classes of neurons in isolated

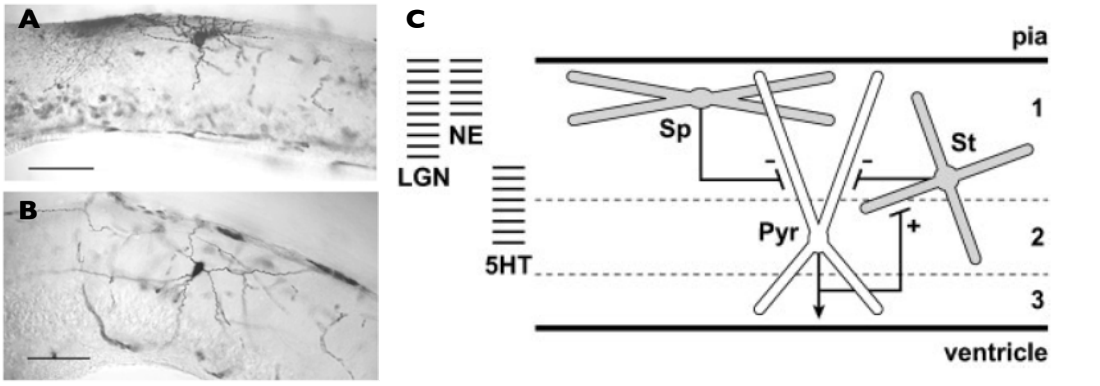

Figure 1.8.: A| Light micrograph of a Neurobiotin filled subpial cell. **B|** Light micrograph of a Neurobiotin filled stellate cell. **C|** Proposed microcircuit diagram marking inputs to cortex as well as intracortical feedforward and feedback connections. Subpial cells (Sp), stellate cells (St), pyramidal neuron (Pyr), thalamic inputs (LGN), noradrenergic afferents (NE), serotonergic inputs (5HT). Modified from Colombe et al., 2004.

turtle dorsal cortex (cf. Fig. 1.7 C,D): (1) Pyramidal cells in the cell layer with spiny apical and basal dendrites showing frequency adaptation and two distinct action potential amplitudes; (2) Stellate cells in the molecular and subcellular layers with horizontal aspiny dendrites showing one action potential size and no frequency adaptation. From the morphological and physiological data, the authors concluded that pyramidal cells are projection neurons and stellate cells are local interneurons releasing the inhibitory neurotransmitter γ-aminobutyric acid (GABA) (Connors and Kriegstein, 1986).

Electrical stimulation of afferents to isolated dorsal cortex revealed distinct response patterns for pyramidal and stellate neurons. Stellate cells showed long-lasting barrages of excitatory postsynaptic potentials (EPSPs) accompanied by bursts of action potentials in response to brief stimulation. Pyramidal cells showed brief periods of short-latency excitation followed by prolonged inhibition. Excitation of the distal dendrites of pyramidal cells evoked dendritic spikes detectable at the soma. In addition, the authors demonstrated two distinct inhibitory mechanisms acting on pyramidal neurons: (1) a short-latency, fast, bicuculline-sensitive, chloride-dependent component ($GABA_A$); (2) a slower, bicuculline-insensitive, chloride-independent component with a negative reversal potential (presumably $GABA_B$).

From their results, the authors proposed a microcircuit in which both pyramidal neurons and stellate cells receive excitatory afferent inputs, pyramidal cells mutually excite each other and in which stellate neurons mediate feedforward and feedback inhibition (Kriegstein and Connors, 1986).

Subsequent single-cell studies showed that interneurons in the turtle cortex fall into at least two distinct populations: (a) subpial cells which are situated in the molecular layer (Fig. 1.8 A) and (b) stellate cells in the inner two thirds of the molecular and more rarely the cellular and subcellular layers (Fig. 1.8 B) of dorsal cortex (Colombe et al., 2004). The varicose dendrites of subpial interneurons run parallel to the pial surface and co-localize with fascicles of the geniculate afferents while the smooth or sparsely spiny dendrites of stellate neurons run obliquely across all layers of turtle cortex. Upon direct stimulation, subpial cells showed spike-rate adaptation on electrical stimulation, stellate cells showed little to no spike-rate adaptation.

Summed up, this results in the microcircuit proposed in figure 1.8 C where subpial cells and principal neurons receive direct geniculate inputs. The subpial cells contact the principal neurons forming a putative feed forward inhibitory loop. Stellate cells receive inputs from the principal neurons and project back onto them forming a putative feed back inhibitory loop. Principal neurons, the presumed only type of projection neurons, send their axons towards the ventricular surface and from there on to long range targets. There is no consensus on the exact number of subtypes of excitatory and inhibitory cells and subtyping efforts are currently ongoing in this lab.

To identify the core physiological traits of primitive cortical neurons, Larkum et al. examined the dendritic properties of turtle pyramidal neurons and found a set of properties similar to those of mammalian pyramidal neurons. These comprised active, decremental, sodium-channel-dependent spike backpropagation accompanied with calcium influx, somatic and dendritic spike initiation following weak or strong stimulation respectively, and most forms of calcium signaling like voltage-gated calcium entry following action potential propagation and delayed calcium release waves from intracellular calcium stores following synaptic stimulation (Larkum et al., 2008).

1.3.3. The retinotectofugal pathway

The optic tectum of turtles has been shown to receive direct retinotopic inputs from crossed retinal projections (Bass and Northcutt, 1981). Its constituent neurons were shown to respond to local stimuli of various sizes (5-110° of visual angle) with a large fraction also exhibiting direction selectivity (cited in Northmore and Granda 1991; unfortunately the original literature was not available). Electric stimulation of the optic nerve as well as photic stimulation were demonstrated to evoke strong, short-latency potentials in the optic tectum of turtles (Karamian et al., 1966). Amplitude and latency of

the tectal evoked responses were later shown to vary with the applied stimulus intensity and wavelength. The higher the stimulus intensity, the stronger and faster the evoked responses. Of the tested wavelengths (blue = 468nm, green = 523nm, yellow = 589nm, red = 646nm; neutral/white), red and neutral stimuli evoked the strongest and fastest tectal responses (Zagorul'ko, 1968).
Stein et al. characterized the receptive fields of neurons in the optic tectum of the green Iguana (*Iguana iguana*). Receptive fields were circular or elliptical and varied between 0.5 and 40° of visual angle in diameter. Neurons responding to stimuli in the center of the visual field exhibited smaller receptive fields and preferred stationary stimuli while neurons responding to stimuli in more peripheral regions showed increasingly larger receptive fields and preferred moving stimuli. The authors demonstrated on, off, as well as on/off receptive fields, and both spatial summation and inhibition. Neurons with peripheral receptive fields exhibiting direction selectivity were modulated by the stimulus velocity. In addition to purely visual neurons, bi- and trimodal neurons were shown to respond to visual, somatosensory and auditory stimulation. The authors concluded that the receptive field properties of neurons in the reptilian optic tectum show a certain degree of similarity to the response properties of neurons in the mammalian superior colliculus in combination with species specific specializations. It should be noted that it is unclear to what extend these results apply to the turtle optic tectum, because comparable literature is very sparse (Stein and Gaither, 1983).
Northmore and Granda used the properties of potentials evoked in the optic tectum by square wave gratings to estimate the visual acuity of freshwater turtles (Northmore and Granda, 1991). The authors estimated contrast thresholds as low as 1% and high spatial frequency cutoffs ranging from 4.4 to 9.9 cycles per degree of visual angle.

From the optic tectum projections carrying visual information are sent to the thalamic nucleus rotundus where they are relayed to the anterior dorsoventricular ridge. A combination of tracing and degeneration techniques showed that tectothalamic projections are non-retinotopic and projecting axons exhibit extensive arborizations in nucleus rotundus (Rainey and Ulinski, 1982). When combined with the extensive dendritic arbors in nucleus rotundus these data suggest a high degree of convergence of visual information onto rotundus neurons (Rainey, 1979). Projections from nucleus rotundus terminate in an anterior subregion of the dorsoventricular ridge (Balaban and Ulinski, 1981).

The anterior dorsoventricular ridge (aDVR) is a subcortical structure involved in the processing of multiple sensory modalities. Several subareas and cytoarchitectonic zones

have been described in the DVR (Balaban, 1978). Especially its anterior portion receives sensory inputs from various sensory thalamic nuclei (Desan, 1984, Balaban and Ulinski, 1981). The dorsal part of the aDVR receives visual inputs from the thalamic nucleus rotundus, the ventral part of aDVR receives inputs from the auditory nucleus reuniens in the thalamus and the medial aDVR receives inputs from the somatosensory nucleus caudalis of the thalamus (Balaban and Ulinski, 1981). In return, the DVR projects to the dorsal cortex (Desan, 1984, Balaban, 1978).
Neurons in aDVR respond to a broad variety of visual stimuli (Dünser et al., 1981). According to this study, neurons in aDVR have non-homogeneous receptive fields of at least 140° visual angle, wide spectral tuning and respond most strongly to moving bar or spot stimuli. In addition, a small population of neurons exhibited a remarkable selectivity for novel stimuli suggesting fast adaptation. At the population level, extracellular wire electrodes were used to record oscillatory ($\sim$20Hz), evoked potentials in aDVR in response to moving bar (3.5x19.5cm^2) stimuli (Prechtl, 1994).

1.3.4. Literature-review on evoked activity in turtle dorsal cortex

Because turtle neuronal tissue (esp. in aquatic and semi-aquatic species) is very resistant to anoxic conditions (Belkin, 1963, Bickler and Buck, 2007), the turtle visual system can be studied in various degrees of reduction. The spectrum of possible preparations ranges from recordings in intact animals (anesthetized or awake), over isolated and perfused heads, to fully isolated brains with attached eyes, and to cortical slabs and slices. Responses to direct electrical stimulation, electrical stimulation of the visual pathways as well as visual stimulation have been examined and described in both *in-vivo* and *in-vitro* turtle preparations.
In the following section, I will review the most significant literature on the physiology of the turtle forebrain and its involvement in sensory processing. It should be noted that the existing literature is relatively limited and that some of the presented studies used somewhat outdated recording and stimulation techniques. Given these limitations, the available evidence suggests that the visually responsive areas of turtle dorsal cortex differ from what is known from mammalian studies.

In one of the oldest available studies responses of single neurons in the turtle forebrain, especially in the pallial thickening (PT), were tested after unspecific electrical stimulation of three sensory pathways: (a) visual, (b) somatosensory, and (c) auditory. The authors found neurons in PT which responded to the stimulation of single as well as multiple

sensory modalities and suggested PT as a site of convergence of afferent exteroreceptive paths (Mazurskaya and Smirnov, 1966).
Superficially recorded field potential data from the same lab showed that evoked responses to different sensory modalities were spatially segregated in cortex. Visual, auditory and somatosensory responses were strongest in anterior regions of cortex while olfactory responses were strongest in more posterior, lateral regions. Field potentials in PT evoked by visual, somatosensory and auditory stimulation showed an inversion of field polarity at the depth of the cell layer while such an inversion was absent in potentials evoked by olfactory stimulation. The authors interpreted this as indicative of the local generation of visually, somatosensory and auditory evoked potentials in PT and concluded that the superficially recorded field potentials originated from postsynaptic potentials in the apical dendrites of radially oriented neurons (Mazurskaya et al., 1966).
Zagorul'ko tested the influence of the intensity and wavelentgh of light stimuli on the amplitude and latency of the cortical evoked responses and described a set of basic characteristics. Raising the intensity of a white light flash increased the amplitude and decreased the latency of cortical responses. Similar to the results obtained for population responses in the optic tectum, red (646nm) and white stimuli evoked the strongest and fastest cortical responses. However, cortical responses to identical stimuli were generally stronger and slower than in the optic tectum (Zagorul'ko, 1968).

While mammalian primary visual cortex is characterized by a precise retinotopic representation of visual space and a high degree of spatial selectivity of its constituent neurons (Hubel and Wiesel, 1959), the visually responsive regions of turtle dorsal cortex exhibit striking differences.
Coarse, physiological studies of the representation of visual space in immobilized, awake turtles showed that retinal quadrants are predominantly represented in specific yet extensive regions of the turtle forebrain (Mazurskaya, 1973b, Mazurskaya, 1973a). According to the spatial distribution of response magnitudes, the author concluded that the nasotemporal axis of the visual field is represented along the anterioposterior axis of the cortex, while the dorsoventral axis of the visual field is represented along the lateromedial axis of the cortex (Mazurskaya, 1973b). The full visual field was estimated to span approximately 140° of visual angle along the horizontal and vertical meridians and many neurons had wide receptive fields spanning it entirely. The author further stated that neurons responded strongly to motion and novelty and that superficial neurons were spatially less selective than neurons in deeper layers of cortex (Mazurskaya, 1973b). Interestingly, different regions in the receptive fields of single neurons were demonstrated

to show complex interactions. Depending on the depth of the recorded neurons, the temporal order of focal stimuli had different effects on the responses. Superficial neurons (200-300µm depth) responded strongest when stimuli where presented simultaneously while deep neurons (800-1000µm depth) showed strongest responses to the sequential presentation of focal stimuli (Mazurskaya, 1973a).
These results only partially agree with the tracing data obtained later (Mulligan and Ulinski, 1990). Mulligan and Ulinski found an anatomical substrate for the orderly representation of the nasotemporal axis in the retina along the rostrocaudal axis of cortex, but could not reproduce the dorsoventral representation observed in the evoked responses.

In an *ex-vivo* preparation, light-evoked responses of identified pyramidal neurons were described as biphasic with a transient (50-100ms) phase of parallel excitation and inhibition and a prolonged (250-600ms) GABAergic inhibitory response phase. Responses to direct electrical stimulation of the afferent pathways and light-evoked responses were shown to be similar. The author suggested that the response profile is shaped by an initial co-activiation of pyramidal and GABAergic non-pyramidal neurons followed by feedforward and feedback inhibition via non-pyramidal interneurons (Kriegstein, 1987). The results were supported by previously described anatomical connectivity patterns (Connors and Kriegstein, 1986, Kriegstein and Connors, 1986), but did not add much to the understanding of visual processing in turtle cortex.

More recently, the attention of several labs shifted to population activity in the dorsal cortex in response to visual stimulation. Moving visual stimuli shown to awake turtles were demonstrated to evoke sustained, synchronous activity in the form of coherent, spindle-like 20Hz field potential oscillations in the dorsal cortex and anterior DVR (Prechtl, 1994, Prechtl, 1995). Responses consisted of a slow (1-5Hz) surface potential and superimposed oscillatory spindles in the range of 15 to 25Hz (cf. Fig. 1.9 A). In addition, the author described complex, frequency-dependent changes in coherence (Fig. 1.9 B). Stimulus-evoked activity in the 1Hz, 2Hz and 20Hz bands showed increased coherence while activity in the 10Hz, 30Hz and 45Hz bands showed decreased coherence (Prechtl, 1994).
Using optical imaging and electrophysiological recordings, close correspondences between voltage sensitive dye (VSD) signals and intracellular microelectrode recordings (Senseman, 1996) as well as extracellular field potential recordings (Prechtl et al., 1997) in dorsal cortex were demonstrated. In reduced eye-brain preparations as well as intact, anesthetized turtles, the VSD recordings of visually evoked responses exhibited com-

plex spatiotemporal wave patterns (Prechtl et al., 1997, Senseman, 1999, Senseman and Robbins, 1999, Senseman and Robbins, 2002). Analyses and descriptions of the observed wave patterns were either based on spectral analysis techniques using variations of Fourier transformations (Prechtl et al., 1997) or modifications of principal component analysis methods (Senseman and Robbins, 1999, Senseman and Robbins, 2002) and will be described in more detail below.

Prechtl et al. showed that responses evoked by looming visual stimuli were consistently localized in dorsal cortex and contained multiple frequency components. The different frequency components exhibited different spatiotemporal gradients. The authors described phase gradients corresponding to plane, spiral-like, and more complex wave propagation. Phase gradients of activity $<$5Hz (Fig. 1.9 D) were aligned to the afferent thalamocortical axons while oscillatory activity of $\sim$18Hz (Fig. 1.9 D) showed phase gradients perpendicular to the afferents. The authors concluded that the phase gradients at frequencies $>$5Hz are emergent phenomena of the dynamics of the neuronal oscillators in turtle cortex and their interconnectivity (Prechtl et al., 1997).
Subsequently, Prechtl et al. used simultaneous local field potential recordings and current source density (Mitzdorf, 1985) analysis techniques to demonstrate that the observed oscillations are generated by local, intracortical current sources and suggested that the phase gradients might be a result of a cortical network of coupled oscillators (Prechtl et al., 2000).

Senseman and colleagues consistently observed a (mainly) rostrocaudal spread (Fig. 1.10 C,D) of flash-evoked activity in their VSD recordings (Senseman, 1999) and focused their data analysis on a Karhunen-Loéve decomposition. They decomposed video recordings of single evoked VSD responses into spatially coherent modes (or basis images) with little trial to trial variability and interpreted these modes as representing intrinsic network properties (Senseman and Robbins, 1999). Different combinations of the first and second or first and third basis images or modes could be used to reconstruct the observed intra- and intercortical wave patterns respectively. The extracted modes were similar for VSD recordings of the intact and unfolded dorsal cortex preparation (Fig. 1.10 E,F). Subsequently, the same group published a series of studies modeling the dynamics in turtle dorsal cortex. Unfortunately, the models were only weakly supported by actual experimental data.
The authors concluded that the waves represent the coordinated output of the cortical sheet with the identified basis images reflecting the anatomical shape and location of

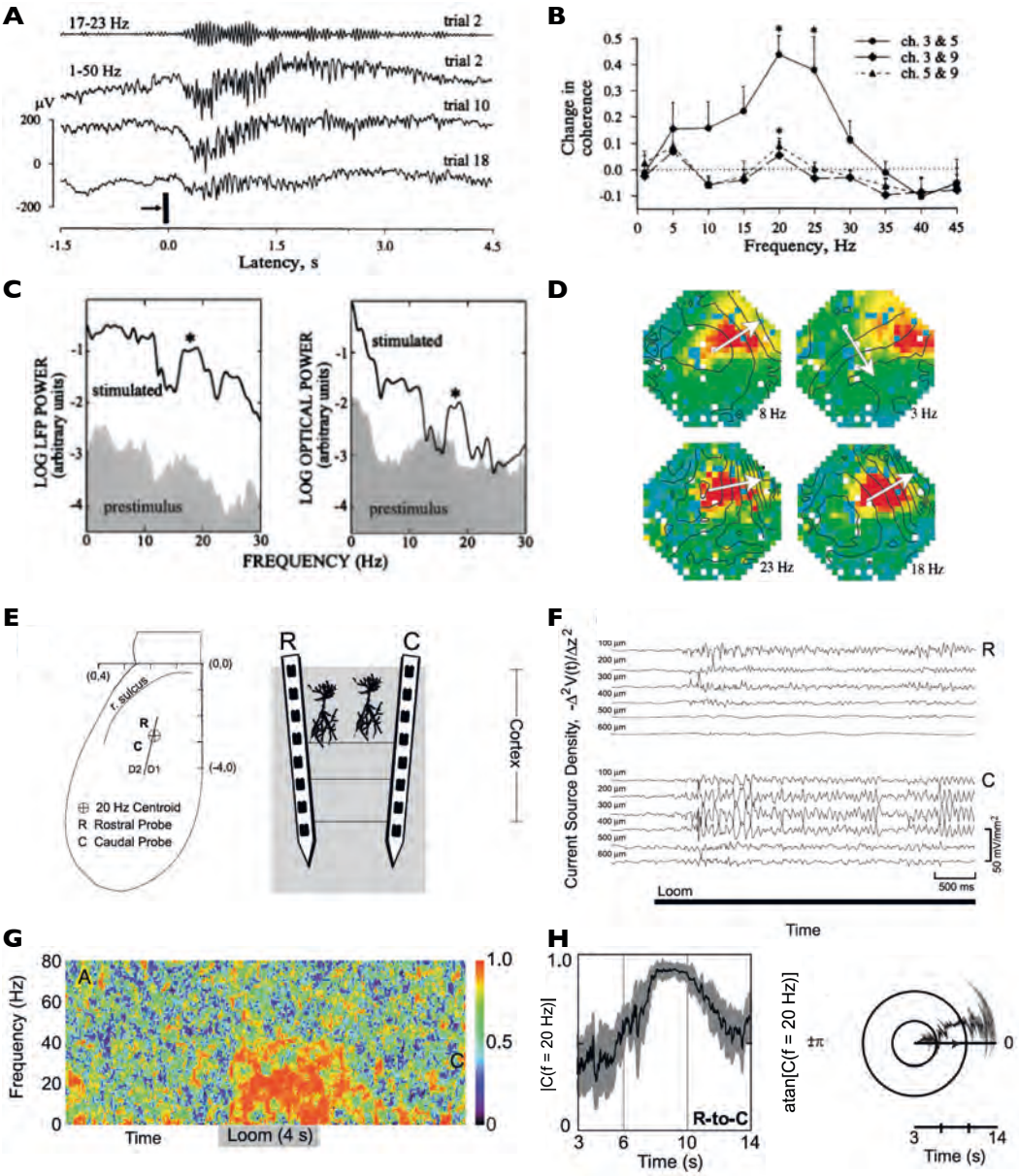

Figure 1.9.: A| Single-trial field potential responses to visual stimulation recorded in dorsal cortex. **B|** Average changes in coherence between three different recording electrodes. **C|** Logarithmic power spectra of the LFP (left) and VSD (right) signals showed peaks at ∼18Hz. **D|** Maps of average coherence phase (contour lines) and magnitude (false colors) at four different frequencies (bottom right of each plot). Red corresponds to high, blue/green to low coherence magnitude. Arrows indicate the dominant direction of the phase gradient. **E|** Schematic display of the recording situation with two silicone depth probes. Crosshair marks the centroid location of 20Hz oscillatory activity. **F|** Current source density data for one exemplary response on both electrodes (R and C) across the cortical depth. **G|** Time frequency representation of coherence magnitude between current sources identified on both electrodes. **H|** Average coherence magnitude (left) and phase (right) between current sources on R and C. Modified from various Prechtl papers.

turtle primary (Desan's D/D2) and secondary (Desan's DM/D1) visual areas (Desan, 1984, Senseman and Robbins, 2002).

It is difficult to directly compare the results obtained by Senseman et al. and Prechtl et al., because the applied analysis approaches use different sets of basis functions for the decomposition of neuronal responses. Both groups report a stimulus-evoked rostrocaudal and to a lesser extent lateromedial propagation of activity, but the observed propagation velocities differ significantly. Prechtl et al. described velocities ranging between 200 and $400\frac{\mu m}{ms}$, while Senseman et al. observed velocities between 10 and $40\frac{\mu m}{ms}$, depending on the direction of propagation. Differences in the experimental preparation are unlikely to cause the differing results, because Senseman et al. were able to confirm their observations on data obtained by Prechtl et al. Both groups suggest that the observed wave patterns arise from intrinsic properties of the cortical network, but did not conduct systematic studies to examine the underlying mechanisms. Furthermore, both groups did not attempt to correlate the observed wave patterns with properties of the applied visual stimulation. Thus, the functional significance of the observed propagating waves for visual processing is still unknown.

More recently, some attempts were made to record activity in the isolated visual system of turtles using magnetic resonance imaging. Using bloodless eye-brain preparations it was shown that although robust local field potential responses were observed in the preparation, no MRI signal could be detected (Luo et al., 2009). Because BOLD MRI responses are related to changes in blood flow and oxygenation level, the absence of BOLD signal in the *ex-vivo* preparation is, in retrospect, not surprising.
In a follow-up experiment the same group compared tectal and cortical LFP responses to blank and structured stimuli in the isolated eye-brain preparation (Luo et al., 2010). They demonstrated strong adaptation of cortical field potential responses if stimuli were displayed with interstimulus intervals shorter than 16 seconds. They could not demonstrate differences in the amplitudes of responses to uniform and simple structured (checkerboard) stimuli. Unfortunately, the authors do not mention if they observed differences in the oscillatory response components.

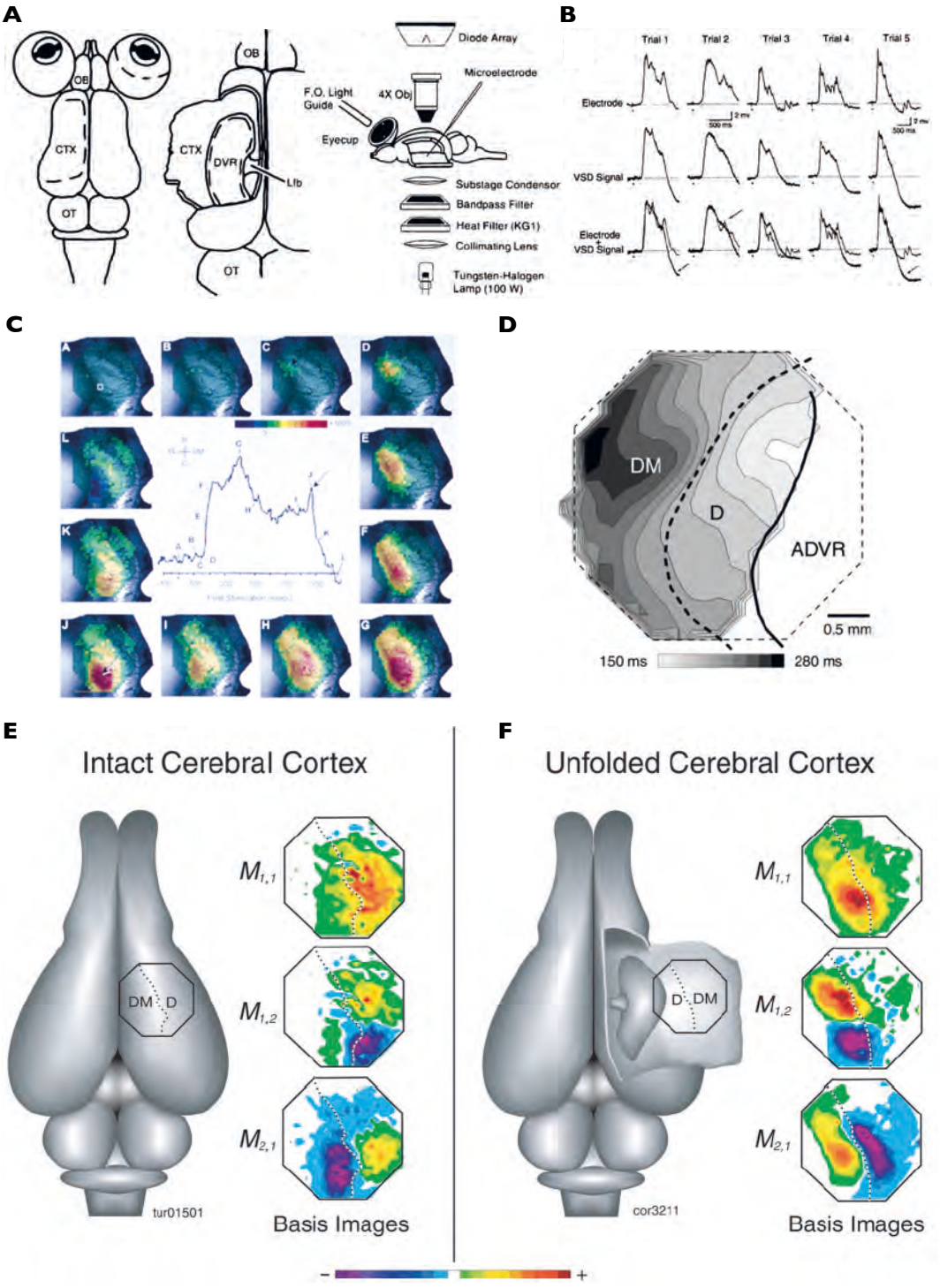

Figure 1.10.: A| Overview of the isolated turtle eye-brain preparation. Dashed lines indicate surgical cuts. Dorsal views of the isolated brain before (left) and after (center) unfolding dorsal cortex and removing DVR. Schematic of the components of the experimental setup (right). **B|** Comparison of individual pyramidal cell responses and the corresponding VSD signal. **C|** Illustration of a flash-evoked VSD response (center) surrounded by spatial representations of the VSD signal at time points indicated by letters in the center. **D|** Interpolated spatial display of the response latency to half maximum. DM = dorsomedial cortex; D = dorsal cortex. **E+F|** Karhunen-Loéve basis modes extracted from responses recorded in **E|** intact and **F|** unfolded cortex. Modified from various Senseman papers.

1.3.5. Concluding remarks

Taken together, the reviewed anatomical and physiological literature provides an incomplete overview over the visual system of the turtle and allows only speculations on the computational roles of the described structures. This is mainly due to the relatively limited amount of recent literature on the subject and methodological issues with a considerable portion of the available literature. Many authors applied outdated techniques which restrict the informative value of their conclusions.
The high degree of processing in the retina, the absence of retinotopy, and extensive receptive fields in the thalamorecipient dorsal cortex suggest that these structures are not functionally equivalent to their presumed mammalian counterparts.
To identify the computations performed by the substructures of the turtle visual system and to characterize them functionally will require parallel efforts in the fields of anatomy, physiology, behavior, and computational modeling.

I Anatomy| Long-range and local connectivity patterns need to be established to determine the afferent and efferent connections of the visual centers of the turtle brain as well as the local circuitry of their constituent neurons.

II Physiology| In-depth characterizations of the single-cell and population dynamics in response to well-controlled visual stimulation are required to identify which stimulus features are relevant for the activity in a particular structure and how they are represented.

III Behavior| Experimental paradigms need to be developed in which the behavioral relevance of particular brain structures can be explored by means of reversible inactivation methods.

IV Computation| The experimentally gathered data have to be used to biologically constrain computational models of the visual system of the turtle. Only such constrained models allow reasonable conclusions on the computations performed in neuronal circuits.

The presented project represents an exploratory effort in complex II and aims to provide a better understanding of the location and extent of visually responsive regions in the dorsal cortex of awake turtles; their large-scale stimulus-evoked population dynamics; and the dependence of these dynamics on global stimulus features.

1.4. Motivation and Objectives

1.4.1. Summary and Motivation

Based on anatomical and functional evidence, the three-layered cortex of turtles is usually subdivided into medial, dorsal and lateral regions (Desan, 1984, Medina and Abellan, 2009). Earlier anatomical, electrophysiological and voltage-sensitive dye imaging studies in various swamp turtles (Emydidae) indicate that the dorsal regions of turtle cortex are involved in the processing of visual information (Mazurskaya and Smirnov, 1966, Zagorul'ko, 1968, Kriegstein, 1987, Prechtl, 1994, Senseman, 1996). Several studies on both *in-vitro* and *in-vivo* turtle preparations revealed that relatively unspecific visual stimulation (i.e. flashes) evokes propagating waves of oscillatory activity with complex spatiotemporal gradients (Prechtl, 1994, Senseman, 1996, Prechtl et al., 1997, Senseman, 1999, Senseman and Robbins, 1999, Prechtl et al., 2000, Senseman and Robbins, 2002, Robbins et al., 2004). Anatomical and physiological studies further suggest the absence of a clear-cut retinotopy in dorsal cortex despite the existence of retinotopic mapping in the lateral geniculate nucleus and in tectum (Mazurskaya, 1973b, Mulligan and Ulinski, 1990).

Taking all anatomical and functional characteristics into account, it seems interesting to ask whether turtle dorsal cortex is a low-level (primary) visual cortex similar to mammalian V1, or whether it might be involved in more complex ("higher-order") visual information processing.
The absence of retinotopy and the extensive receptive fields in dorsal cortex stand in stark contrast to the precise retinotopic representation of visual space and the strict selectivity of neurons in mammalian primary visual cortex (Hubel and Wiesel, 1959).
Synchronized oscillatory neural activity in distinct frequency bands has been observed in recurrent neuronal networks of a variety of species including turtles and was shown to correlate with various perceptual and cognitive processes. However, it is still unclear whether (and how) the stimulus-evoked spatiotemporal activity patterns in turtle cortex correlate with specific features of the visual stimuli and thus, if stimulus-driven patterns of activity represent features of visual stimulus space.
Moreover, it is remarkable that in turtles both visual (dorsal) and olfactory (lateral) cortical areas share the same primitive three-layered architecture (Desan, 1984). This structural similarity suggests that basic cortical computations might be shared across sensory modalities, although the stimuli which they process are very different.
The turtle cortex may thus be considered as a model system of simple sensory or even

associative cortical areas predating mammalian evolution and specialization.

1.4.2. Objectives

Based on these observations and considerations, the following set of important objectives for an exploratory research project focused on visually-evoked dynamics in turtle dorsal cortex were defined:

(1) The visually responsive cortical regions need to be localized and circumscribed.

(2) The hypothesis of the absence of retinotopy needs to be tested on a large physical scale.

(3) The existence of putative stimulus-selective subregions corresponding to Desan's D2/D1 needs to be tested.

(4) Stimulus-evoked dynamics need to be identified and described on a large scale.

(5) The dependence of the response dynamics on stimulus features (i.e. nature of stimulus, image statistics, movies, movie statistics, etc) needs to be tested.

(6) All experiments should optimally be conducted *in-vivo*, in awake turtles.

To pursue these objectives, electrocorticogram (ECoG; see section 2.1) recordings seemed to be an optimal approach. ECoG electrodes can be chronically implanted and allow to systematically probe the visual stimulus space while recording neuronal activity in awake animals.
Thus, the goal of the presented research project was to explore stimulus space in a finer fashion, to identify visual stimuli that drive visually responsive regions of dorsal cortex and to record and analyze the associated evoked activity using high density, surface electrode grids covering large areas of dorsal cortex in *Trachemys scripta elegans*.

2. Material and Methods

2.1. High-density electrocorticography

The focus of the presented research project was the recording and characterization of electrocorticogram (ECoG) data. Therefore, the following section will provide a brief overview of the biophysical basics of macroscopically recordable extracellular signals. An in-depth description of these processes is provided in the detailed review by Buzsáki, Anastassiou and Koch on 'The origin of extracellular fields and currents' (Buzsáki et al., 2012) which served as basis for this section. After presenting the theoretical framework, the custom ECoG array will be described.

2.1.1. The extracellular potential

In isolation, the ionic currents generated by individual neurons are very small and local, but if populations of neurons are co-active, the resulting electric fields reach levels that are sufficient to be recorded from the extracellular space.
The extracellular potential V_e recorded in a sample of neuronal tissue represents a superposition of all ionic processes at any location in the tissue and is measured in Volts. Differences in the extracellular potential between two spatial locations give rise to an extracellular electric field (measured in voltage per distance) that represents the negative spatial gradient of the extracellular potential.
In principle, there are three types of processes (Fig. 2.1 A) contributing to the extracellular potential: (1) synaptic sources, (2) extrasynaptic sources, (3) noise sources. The contribution of an individual source to the recorded extracellular potential is mainly influenced by its distance (d) to the recording site, because the voltage signal scales with $\frac{1}{d}$. Signals from co-active sources interact linearly and influence the recorded V_e based on their individual magnitude and sign as well as their spatial density and temporal relations.

(1) Synaptic processes are generally considered to have the strongest influence on the extracellular potential, because they are relatively slow and thus tend to show considerable temporal overlap. Additionally, they commonly overlap in space as well.
The synaptic activation of a neuron causes two distinct ionic currents: (a) the transmitter-

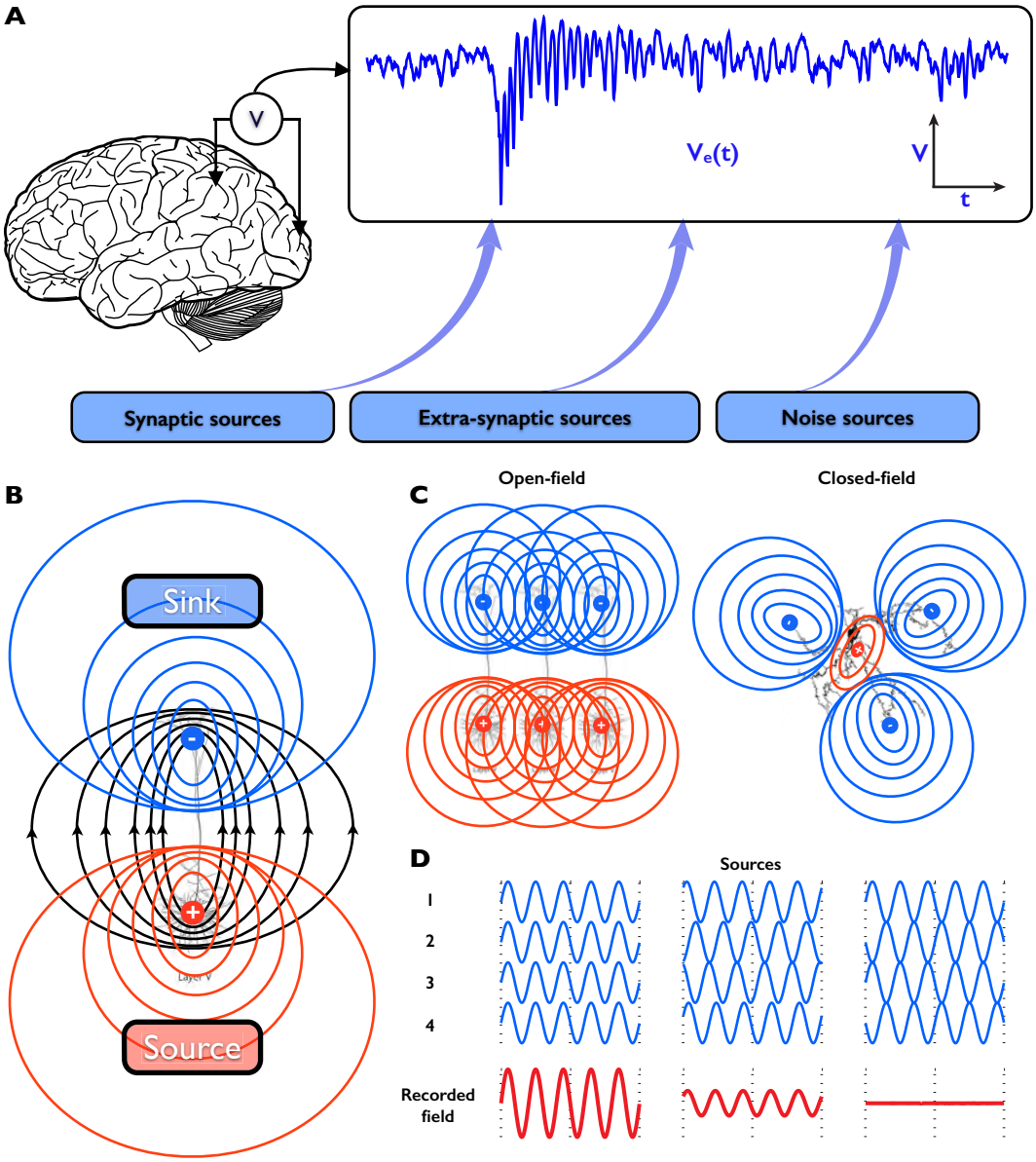

Figure 2.1.: A| Illustrative local field potential trace recorded from live brain tissue and main sources contributing to the signal. **B|** Current source/sink configuration of an active cortical pyramidal neuron. **C|** Examples of neuronal geometries leading to open- and closed-field configurations. **D|** Three exemplary temporal interactions of four hypothetical co-active field potential sources and the resulting extracellular fields.

induced transmembrane currents at the neuron's dendrites and (b) passive 'balancing' currents of the opposite direction maintaining the neuron's electroneutrality. Therefore, transmitter-induced cation influx (Fig. 2.1 B; sink) into a pyramidal neuron's dendrites is accompanied by cation efflux (Fig. 2.1 B; source) and passive return currents along the neuron. In general, the contributions of AMPA and NMDA related cation (Na^+ and Ca^{2+}) currents are considered to be greater than $GABA_A$ related anion (Cl^-) currents,

because the equilibrium potential for chloride is closer to the neuron's resting membrane potential. However, this relation can change considerably if an activated neuron is not at its resting membrane potential.

Because of the co-occurrence of active and passive currents, neurons form electrical dipoles or higher order n-poles of current sources and sinks with open- or closed-field configurations depending on their geometry (Fig. 2.1 C). The field configuration directly influences the spatial reach of a source, because extracellular fields of n-polar sources scale with $\frac{1}{d^n}$. Depending on the spatial relations and orientations of multiple n-polar sources as well as their temporal relations, the individual extracellular signals can positively or negatively interfere. Large extracellular signals are usually recorded from regular neuronal structures with well-aligned, open-field sources like cortical structures (Fig. 2.1 C left) with densely packed elongated pyramidal neurons. However, cortical folding can influence the density and regularity of these structures. Similarly, synchronous activity (cf. section 1.2) in cell populations leads to positive interference of the signals from individual sources and strengthens their contribution to the extracellular signal (Fig. 2.1 D).

As already mentioned in section 1.2, the power spectra of spontaneous extracellular potentials often exhibit a power-law relation ($p \propto \frac{1}{f^a}$; with $a = 1$ to 2) of field potential power (p) and frequency (f). This power-law relation is generally considered to originate from the filtering properties of neuronal dendrites, the extracellular medium as well as properties of the neuronal networks. Purely passive dendrites exhibit low-pass filtering characteristics which are mostly determined by the distance between soma and input source and the membrane time constant. However, these can be altered by active, synaptically induced conductance changes. The electrical properties of the extracellular medium are still being debated, but capacitive characteristics may be considered to contribute to the high-frequency attenuation. On the network level, the integration mechanisms (slow: $GABA_B$ and NMDA; fast: $GABA_A$ and AMPA) for different rhythms limit the recruited number of neurons in each oscillatory cycle and thus limit the amplitude of extracellular signals. It should be noted however, that the strict $p \propto \frac{1}{f^n}$ characteristic does not apply to the short time-windows of transient neuronal activity generally associated with neuronal computations.

(2) Extra-synaptic current sources comprise a wide spectrum of processes, but their influence on the extracellular potential is considered rather small.

Fast action potentials are associated with strong transmembrane Na^+ currents, but due to their short duration and spatially restricted quadrupolar fields, their contribution to

the extracellular field is small. However, if large populations of neurons fire synchronously, they generate high-frequency contributions to V_e. In addition, non-synaptic *afterhyperpolarizations* associated with action potential bursts can reach magnitudes and lengths of synaptic events and therefore generate low-frequency contributions to V_e. The spike contributions to the field potential are spatially restricted, related to the types of active neurons as well as their spiking synchrony and frequency, co-vary with synaptic events, and can be phase-locked to low frequency oscillations (see section 1.2). High-frequency power in the field potential may be considered as a proxy metric for spiking activity in an observed population.

Calcium-mediated spikes are long lasting (10-100ms) non-synaptic events that reach considerable magnitudes (10-50mV) and therefore can contribute to the extracellular potential.

Intrinsic currents refer to intrinsic voltage-dependent conductance changes (i.e. the hyperpolarization-activated I_h and I_T currents), which are directly associated with *intrinsic resonance* phenomena observed in many neuronal cell types. While they are synaptically induced, the actual currents are non-synaptic and contribute to the extracellular potential in a complex way due to their frequency- and voltage-dependence. Especially synchronous resonant fluctuations in local networks can strongly contribute to the extracellular signal.

Cortical down states represent complex disfacilitatory, non-synaptic events, which are at least partially caused by bursting activity and the associated spike afterhyperpolarizations. A cascade of conductance changes and network effects are considered to lead to a positive extracellular potential in infragranular cortical layers and a negative extracellular potential in supragranular cortical layers.

Ionic currents via gap junctions contribute indirectly to the extracellular potential, because they influence the synchrony and excitability of connected neurons without being associated with extracellular return currents themselves. In this context, fluctuations of the gap junction-coupled glial syncytium might contribute to slow and infraslow components of the extracellular potential.

Furthermore, the extracellular electric field is discussed to exert a feedback effect on the neurons generating it. Via these so-called *ephaptic effects*, fluctuations of the extracellular field, generated by synchronously active networks, are considered to influence the discharge properties of the neurons within the spatiotemporal field gradients.

Depending on their strength and spatial as well as temporal configurations, these processes contribute more or less strongly to the recorded signals, but usually to a weaker extent than synaptic sources.

(3) Finally, recording environments are rarely free of noise sources contaminating electrophysiological recordings. Therefore, it is mandatory to keep the full spectrum of potential noise sources for each specific recording configuration in mind. In the *in-vivo* configuration, these sources are cephalic noise, extra-cephalic cranial noise, extra-cranial physiological noise (e.g. heartbeat), thermal noise, movement artifacts, electronic noise, environmental noise and quantization noise. While some of these sources (esp. those associated with the recording equipment) can be minimized, others (esp. physiological noise sources within the specimen) can hardly be avoided and therefore need to be taken into account when analyzing and interpreting extracellular recordings.

Based on the observed preparation and the stimulation/recording configuration, there can be large numbers of co-active current sources within a given preparation. The bioelectromagnetic fields created by the extracellular return currents are instantaneously transmitted from their sources towards measurement sensors in a process called volume conduction. The resulting volume-conducted extracellular signal is determined by the complex interplay of the location and magnitude of co-active current sources (see above) and the conductive properties of the extracellular medium. Conductivity in the brain is often assumed to be purely ohmic within the relevant frequency range (1-10kHz), but experimental data showed conflicting results regarding the isotropy and homogeneity and even capacitive nature of the extracellular medium.
A set of spatially distributed recording electrodes will thus record different contributions from all individual sources at all times. Each sensor records a mixed signal from an unknown number of co-active sources making it almost impossible to exactly reconstruct the configurations of microscopic current sources from the recorded macroscopic fields although advanced experimental and computational methods make solving this so-called 'inverse problem' tractable today. Usually, such approaches require to solve the 'forward problem'; that is to experimentally or computationally establish the correlations of microscopic and macroscopic signals. Subsequently, the obtained relations can be applied to interpret recorded macroscopic extracellular field potential data.

2.1.2. Micro-electrocorticogram (μECoG) recordings

The fact that all ionic processes within a sample of neuronal tissue superimpose and create a mixed 'macroscopic' extracellular field, allows neuroscientists to implant electrodes into living neuronal tissue and record the activity of significant amounts of neurons in parallel at various spatial and temporal scales. Micro-electrocorticgrams (μECoGs) are

recorded using flat, round metal (platinum-iridium or stainless steel) microelectrodes of variable diameters and spatial arrangements which are embedded in a thin flexible carrier material. Micro-ECoG probes are subduraly implanted on the pial surface of the cortex, circumventing signal distortions introduced by the meninges, skull and scalp. Depending on electrode size and arrangement on the array, spatiotemporal resolutions in the range of square millimeters are possible with signal strengths of several hundred microvolts.

2.1.3. The customized high-density ECoG probe

Prior to the first chronic implantations, pilot recordings were carried out using commercial NeuroNexus (Ann Arbor, Michigan, USA) MEMS-based (microelectromechanical systems-based) probes for surface recordings. These were later replaced by customized versions developed together with engineers at NeuroNexus. NeuroNexus E-probes are thin surface probes on which the recording sites are flat round platinum pads on a flexible Polyamide carrier material.
The initial tests were mainly done using small 32 channel electrodes and served to explore the suitability of this kind of surface electrodes for the chronic use in turtles. After a set of successful tests, the custom surface electrode (shown in Fig. 2.2) was developed to achieve optimal implantability and maximal coverage of cortical surface in the experimental animals.
The custom 'E64-500-20-60-H64' electrode (http://neuronexus.com/custom-design/mr-ingmar-schneider) features 64 flat recording sites with a diameter of 60µm each. The recording sites are aligned on a flexible polyamide carrier material in a rectangular 6x11 pattern with an inter-electrode pitch of 500µm. In addition to the general hydrophobic character of the carrier material, 200µm wide holes between recording sites improve the electrode adhesion to the cortical surface. In total the probe covers an area of 2.75mmx5.25mm corresponding to 14.44mm^2. The connection to the recording system is achieved through an equally flat and flexible band-cable comprised of the carrier material with embedded wires which is attached to one of the short sides of the recording grid and terminates in a printed circuit board. This board features two 32 channel Nano Strip connectors (Omnetics) which serve as the interface between the electrode and the recording system. A set of fine wires attached to the printed circuit board allows the connection of external references and grounds.

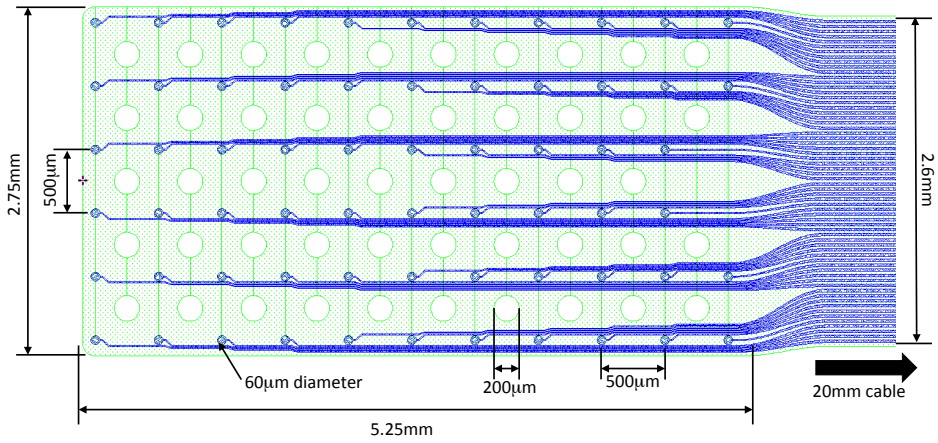

Figure 2.2.: Schematic of the customized NeuroNexus ECoG probe. Blue portions of the schematic indicate conducting material deposited on/in the flexible carrier material shown in green. At the recording position, the probe covers a 2.75mmx5.25mm area and features 200µm wide wholes for improved tissue adhesion. 64 recording pads (diameter 60µm) are distributed on this area with 500µm inter-electrode spacing.

2.2. Implantation and recording procedures

2.2.1. Chronic implantation of ECoG grids

The ECoG-electrodes were surgically implanted under deep Isoflurane anesthesia. Animals were initially anesthetized using Ketamine hydrochloride (100mg/ml) and Dexmedethomidine hydrochloride (0.5mg/ml). Approximately 20 minutes after the injection, head retraction was sufficiently suppressed by the anesthetic and the animals were intubated and artificially ventilated with a mixture of vaporized Isoflurane (2-4%) and air. Artificial ventilation was absolutely mandatory, since reptiles lack the capability of reflexive breathing under anesthesia.

Once the animals had reached a sufficiently deep Isoflurane anesthesia (indicated by extremely reduced reflexes), they were transferred into a modified stereotactic apparatus (David Kopf Instruments). After removing all skin and connective tissue, a craniotomy (appr. 4-5mmx3mm) was prepared using a dental drill equipped with a medium sized rose-head burr. Through a lateral slit in the dura mater, which was prepared with a pair of fine iris scissors, the electrodes were implanted subdurally. Special care was taken not to injure any blood vessel descending into cortex to avoid uncontrollable bleeding.

In the following, the craniotomy and electrode were covered with a light-flowing two-component dental silicone (FlexiTime, Heraeus Kulzer). The silicone flowed into small crevices and sealed the craniotomy, fixing the electrode tightly in place. Once the craniotomy was sealed, the 2cm flatband cable attached to the electrode was folded in place

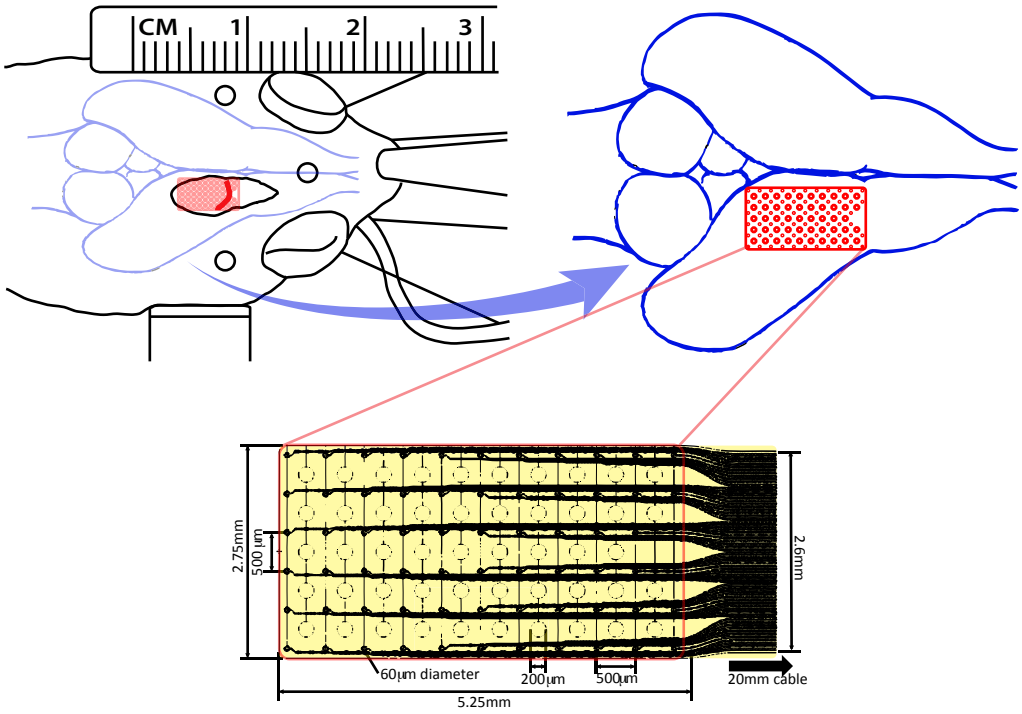

Figure 2.3.: The implantation procedure **Top left|** Schematic display of the turtle head in the stereotactic apparatus. The superposition of the blue brain structures illustrate the limited part of the brain that is visible through the craniotomy. **Top right|** Magnified view of the turtle brain in blue superimposed with the final position of the subdural recording grid in red. **Bottom|** Relation of the ECoG grid dimensions and the superimposed illustration above.

on top of the silicone plug and the electrode connectors were placed on top of the skull. The entire implant was cast in a light-curing dental acrylic and cured under a UV light source. Maximum adhesion was achieved through the usage of a bonding agent (Optibond, Kerr dental), which was applied to the skull before the craniotomy was opened as well as through the placement of three gold-coated skull screws. In addition to their anchoring function, the skull screws served as reference and grounding points for the ECoG electrode. While placing the connectors and shaping the plastic implant cap, special care was taken to construct a flat, smooth cap. Post-surgically, this allowed the chronically implanted animals to fully retract their heads into their shells with their skin folding smoothly over the implant.

After the animals had recovered from the deep anesthesia, they were treated with Baytril (2.5% Enrofloxacine, Bayer) and Rimadyl (50mg/ml Caprofen, Pfizer) for one week to allow for a good healing and to avoid inflammatory responses. During this week no recording sessions took place and the animals remained in their regular home tanks.

2.2.2. Recording procedure

After the recovery period, animals were taken from the husbandry in the morning and placed in the recording setup for the duration of a recording session. During the sessions, animals were fixed in position using commercial hook-and-loop tape. They were free to move their head and limbs, but could not move away from the recording position. Because space constraints did not allow the direct connection of the headstage preamplifiers to the implant, customized cable adapters had to be used to bridge the required distance. Through these adapters the animals were able to move their heads freely without risks of injury or risk of damage to the recording equipment. After each recording session, the animals were returned to their home tanks in the husbandry.

2.2.3. Marking recording locations and tissue processing

Marking the locations of ECoG implantation| Prior to the implantation, the ECoG arrays were coated with a lipophilic fluorescent dye (DiI) to mark the covered surface area. This was intended to determine which cortex areas were recorded from and to extrapolate how activity patterns map onto the anatomy. The dye was supposed to stain the brain tissue underneath the recording electrode without diffusing in the cerebrospinal fluid. Post-mortem, the heads were perfused with phosphate buffered saline and fixed with 4% paraformaldehyde solution.
In one acute preparation (animal ID P50, anesthetized turtle), a large craniotomy was prepared. The ECoG grid was not coated with DiI, but placed on the cortex without prior dye application. After placement, local dye markings were made through the regular perforations in the ECoG grid.
After post-fixation, the brains were extracted from the skull and imaged under a Zeiss V12 Stereo microscope (Carl Zeiss AG, Jena, Germany). The brains of four animals (IDs H5, K12, K11 and K8) were thoroughly cleaned prior to imaging. Meninges and blood vessels were carefully removed after perfusion and post-fixation. To avoid inadvertently removing dye deposits, the brains of two additional animals (IDs P44 and P50) were not cleaned prior to the image acquisition. The V12 featured sufficiently low-magnification objectives to image entire turtle brains without the need to tile and refocus in both brightfield as well as fluorescent mode. Thus, it was possible to obtain images of intact brains with the DiI deposits in place.

Tissue processing| A selection of brains was sliced and histologically processed to be imaged at higher magnification with the goal of a more detailed analysis of the fine-

anatomy of cortical tissue underlying regions showing strong visually evoked activity. The brain of P50 was perfused and fixed in 4% PFA as usual. After post-fixation the brain was embedded in an egg albumin based embedding medium containing 1.6% glutaraldehyde, sliced and treated with antibodies against NeuN and VGlut2. Special care was taken to avoid using detergents like TritonX during the staining procedure, because this would wash out deposits of the lipophilic DiI. Secondary antibodies coupled to Alexa 488 and Alexa 647 were selected such that they allowed parallel imaging in the presence of DiI. After staining, the slices were imaged under a Zeiss LSM microscope using a 10x objective.

2.3. The chronic recording setup

The following section will provide an overview of the major components of the recording setup that was developed as part of the presented research project. As depicted in Fig. 2.4, the recording and stimulating hardware was constructed around a large hemispherical backprojection screen that allowed to present immersive stimuli covering a large part of the visual field of the experimental animals. From the components and connections it can be appreciated that the system was set up in a closed-loop configuration. Stimulating and recording components of the system were interfaced through a computer capable of controlling both sides of the recording setup while performing online analyses of the acquired data.

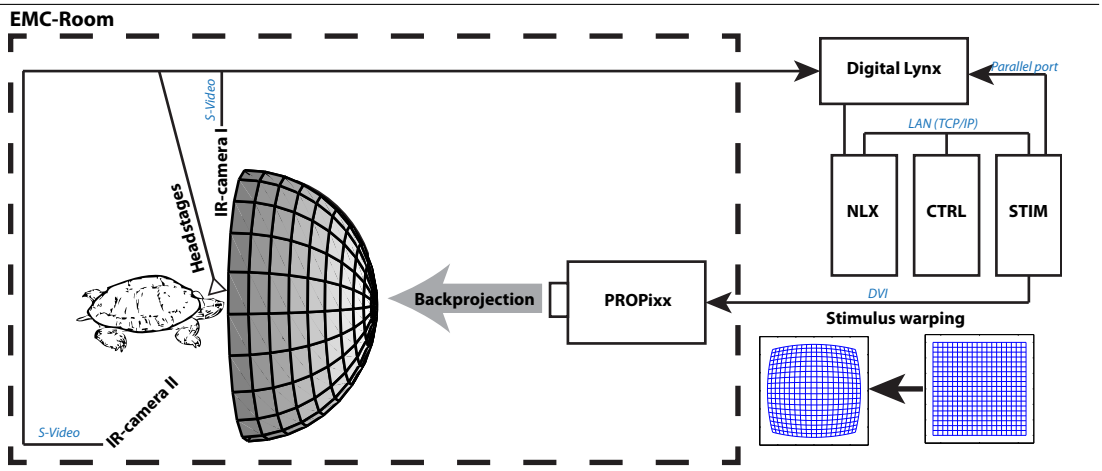

Figure 2.4.: The chronic recording setup| Schematic display of the entire recording/stimulation system. The control PC (CTRL) works as a hub connecting the recording side of the setup (Digital Lynx, NLX) to the stimulation side (STIM, PROPixx). The communication protocols used are indicated by the blue labels adjacent to connecting lines. Components within the dashed rectangle are place within an electromagnetically shielded room.

2.3.1. The stimulation hardware

A central feature of the experimental setup was a hemispherical perspex dome with a diameter of 80cm. The originally transparent dome was lightly sandblasted from the outside in order to condition the surface of the perspex as a backprojection screen. It covered the entire front of the bench on which the experimental animals were placed. The screen was mounted on a custom rail system to allow movement of the large dome and easy access to the experimental animal placed inside of the setup. The rail system itself was mounted on a vibration isolation table (Technical Manufacturing Corporation, Peadbody MA, USA). A height adjustable pedestal was used to position the experimental animals such that their head was in the center of the hemispherical backprojection screen. Fixation was achieved through the use of small pieces of hook-and-loop tape which was placed on the plastron (ventral portion of the shell) of the animals. Animals were thus free to move their head and limbs when placed in the recording setup. The chronically implanted electrodes were connected to the recording system via a set of customized cable adapters which were necessary to allow free head movements and to accommodate for the restricted space when the turtle head was retracted into the shell. The connectors interfacing with the implant furthermore featured infrared light emitting diodes used to determine the animal's head position. During the experiment the head position was monitored through a system of two perpendicularly mounted infrared cameras which were attached to the frame holding the dome.

Initially, a commercially available Canon (Ota, Tokio, Japan) liquid crystal on silicone (LCoS) projector was used as stimulation device. Because this was a consumer display solution, it was suboptimal for scientific usage (see section 2.3.1.1). Therefore, it was replaced with a VPixx (St. Bruno, Quebec, Canada) PROPixx digital light processing (DLP) projector which had several advantages over the LCoS projector. While the former features one lamp as light source from which colors are generated by chromatic splitting of the original white beam, the latter features three independent (R,G,B) LED light sources. These do not suffer from short lifetimes like regular projector lamps and are more stable regarding the constancy of their light output. In addition, the color channels can be independently adjusted and controlled. Furthermore, the VPixx projector generates images via digital micro mirror devices (DMDs) which are superior to the LCoS technology as they are faster and do not require the projection of light through a liquid crystal layer. Finally, the VPixx projector was designed specifically for vision research and thus image optimization routines commonly implemented into commercial consumer devices

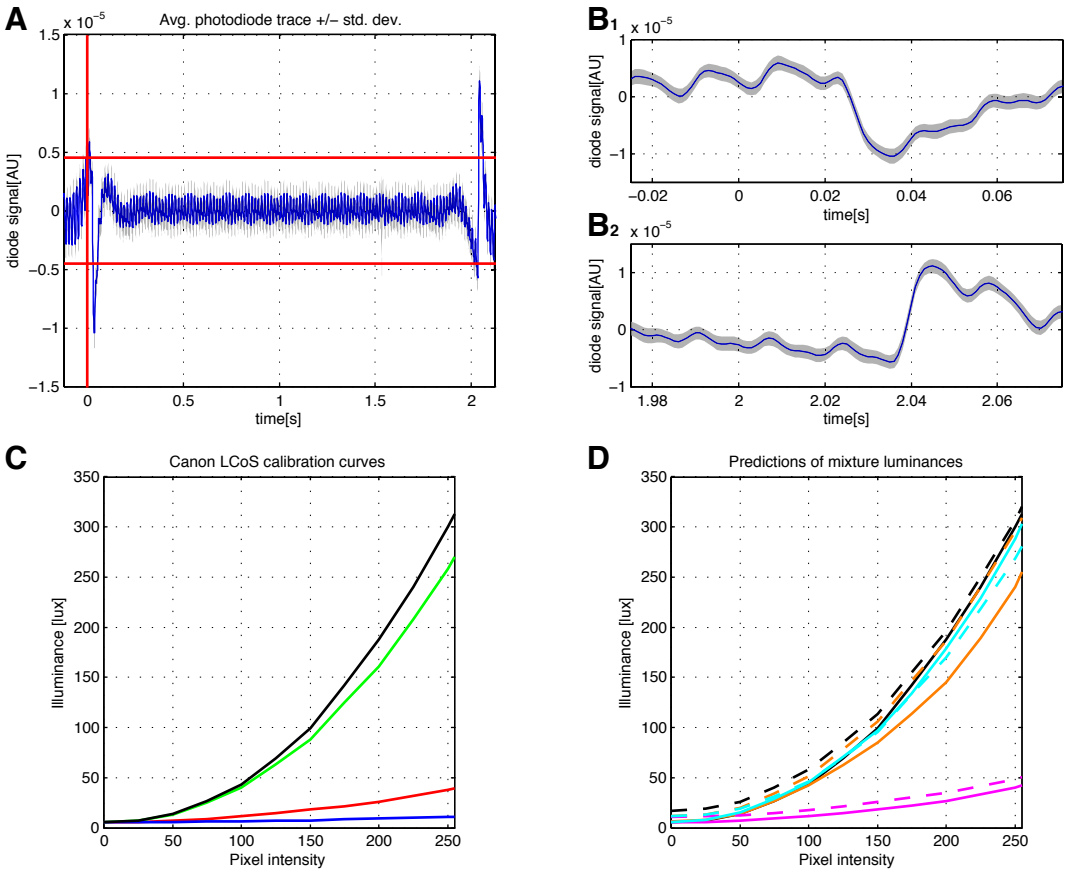

Figure 2.5.: Characteristics of the Canon LCoS projector. **A|** Avg. photodiode signal ± standard deviation for multiple presentations of the same stimulus. The red vertical line indicates the TTL trigger sent by the stimulation software. **B|** Magnified displays of the diode signals around the stimulus onset (0s) in $\mathbf{B}_1$ and offset (2s) in $\mathbf{B}_2$. **C|** Measured illuminances of uniform pure color (red, green, blue, white) stimuli. **D|** Measured (solid) and predicted (dashed) illuminances of uniform stimuli composed of color mixtures (red+green+blue, red+green, red+blue, green+blue).

for viewing pleasure are absent allowing a much tighter control of the presented stimuli.

2.3.1.1. Properties of the display devices

To be able to properly relate the presented stimuli to the recorded neuronal responses, it was mandatory to characterize the stimulation devices used with respect to luminance and timing. Because signal averaging techniques rely on a precise temporal relation between stimulus and response, a jitter in the presentation of stimuli can have detrimental effects on the average responses.

For this reason, the timing of the system was characterized using a photodiode to measure when and how reliable stimuli were actually displayed (See top panels of Figs. 2.5 and 2.6 A+B). The graphs clearly show that the actual change in the display state was offset from the trigger signal (red line at time point $t = 0$) sent by the STIM-PC. This offset,

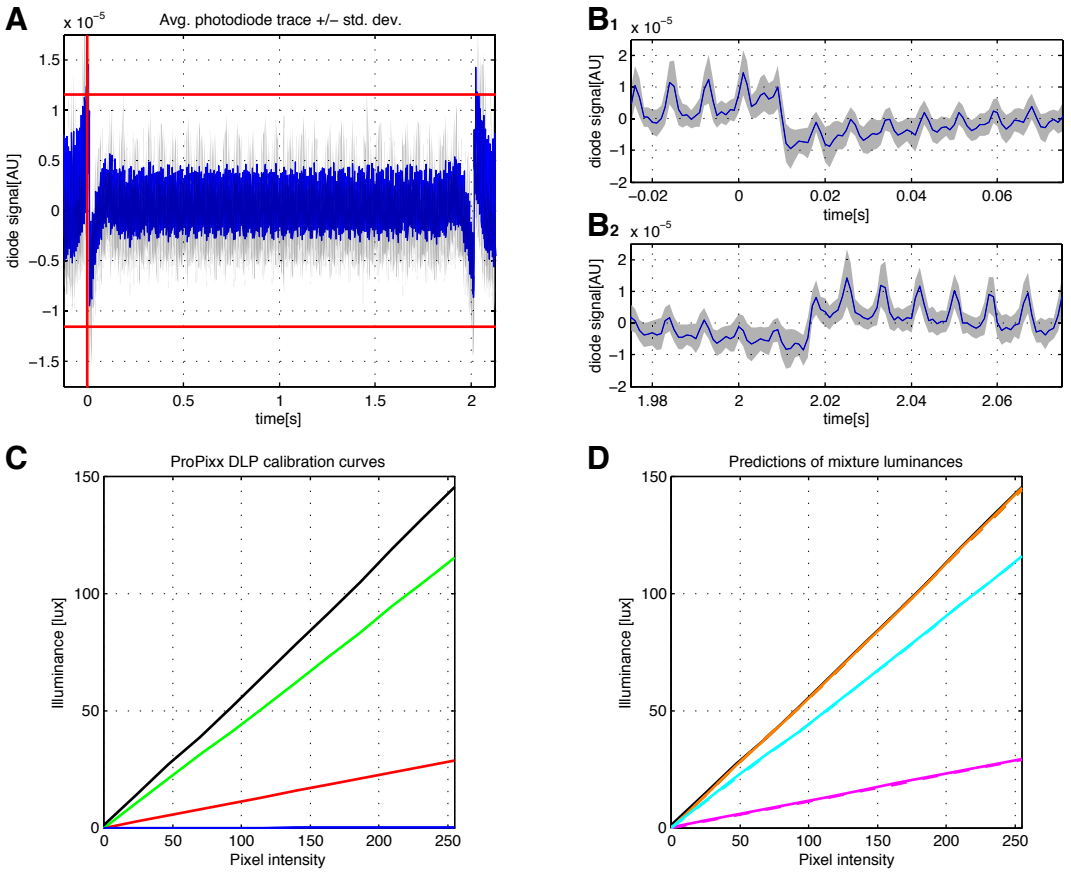

Figure 2.6.: Characteristics of the VPixx DLP projector. **A|** Avg. photodiode signal ± standard deviation for multiple presentations of the same stimulus. The red vertical line indicates the TTL trigger sent by the stimulation software. **B|** Magnified displays of the diode signals around the stimulus onset (0s) in $\mathbf{B}_1$ and offset (2s) in $\mathbf{B}_2$. **C|** Measured illuminances of uniform pure color (red, green, blue, white) stimuli. **D|** Measured (solid lines) and predicted (dashed lines) illuminances of uniform stimuli composed of color mixtures (red+green+blue, red+green, red+blue, green+blue).

however, was highly reliable in both devices as can be seen in the average photodiode traces. The difference in the general appearance of the recorded photo-diode signals between the VPixx DMD and the Canon LCoS projector can be attributed to the different technologies used for the image generation. With the DMD technology intermediate pixel intensities are created through pulse-width modulation of the individual micro-mirrors, which are either in an On or Off state. The noisy appearance of the photo diode traces obtained for the PROPixx can thus be explained by the fast switching of the DMD and is not a sign of unreliability.

The white points (6000K for Canon LCoS, 6500K for VPixx ProPixx) of both projectors were verified by means of display colorimeters (Spyder2Pro, Datacolor, Lawrenceville, NJ, USA; or ColorMunki Photo, X-Rite, Grand Rapids, MI, USA) and the input/output relations of the devices were characterized using a lux-meter (Voltcraft LX-1108). For

this characterization pure-color stimuli with defined red/green/blue (RGB) composition were projected onto the screen while the luxmeter was positioned at the position of the animal's head within the setup. The recorded illuminances for various RGB combinations were recorded and analyzed. As can be appreciated from the bottom panels in figures 2.5 and 2.6, both projectors had significantly different input/ouput relations.
The Canon projector behaved non-linearly and it was not trivial to predict the illuminance of a color mixture from its components without considerable deviations (cf. Fig. 2.5 C+D). The PROPixx on the other hand behaved linearly and it was straightforward to predict the illuminances of mixtures from the pure-color calibration data (see Fig. 2.6 C+D).
These differences can be attributed to the fact that in the Canon projector a single white lamp is used as light source and the three color channels are generated using prisms or dichroic mirrors. Depending on how clean this separation is, the color-channels can exhibit spectral side-peaks which need to be compensated on the software side by introducing inter-dependencies. The PROPixx uses three individual LED modules to generate the red, green and blue channels which, thus, behave independently.

2.3.1.2. Stimulus pre-warping

To counteract the image distortions introduced when using a non-flat projection screen, the presented stimulation had to be pre-warped (cf. Fig. 2.4, bottom left). Because the dome was hemispherical with an even curvature, it was possible to devise a mathematical description of the introduced distortions $T(x, y)$ and to formulate the required inverse operation $S(x, y)$ (see Eqns. 2.1 and 2.2).

$$S(x, y) = \left(\frac{Rx}{\sqrt{R^2 + x^2 + y^2}}, \frac{Ry}{\sqrt{R^2 + x^2 + y^2}} \right) \tag{2.1}$$

$$(x, y) = T(S(x, y)) \tag{2.2}$$

The implementation of this inverse operation was achieved by translating it into OpenGL shading language and writing a pixel fragment shader which is executed directly in the shading units of the STIM-PC's graphics processor. Through this general implementation it was not necessary to manually pre-warp all potential visual stimuli, but to outsource this modification to the graphics hardware. A special preparation of the stimuli for the use on the curved screen was not necessary, adding to the flexibility and versatility of the stimulation setup. Furthermore, the pixel shader has been included into

the repositories of the PsychToolbox (http://www.psychtoolbox.org/) and equipped with a configuration function which allows the user to customize the pre-warping to curved screens different from the one used in this study.

2.3.2. The recording hardware

All presented data were recorded with a Neuralynx (Bozeman, MT, USA) Digital Lynx SX system. The system featured a total of 96 individually referenceable analog recording channels as well as a digital interface for the precise co-registration of trigger signals with respect to its central sampling clock. Data were recorded in a pass band between 0.1Hz and 9kHz at a sampling rate of 32kHz.
The measurement chain consisted of two separate amplification steps. Initially, the neurophysiological signal was pre-amplified in the headstage pre-amplifier, which served as an impedance converter to minimize the influence of the recording system on the sample. From the pre-amplifier, the signal was transferred to the main recording system where it was digitized at 16Bit and sent to the NLX-PC via a high throughput fiber glass network interface for storage.
In addition, the system was equipped with two phase alternating line (PAL) tracking cameras acquiring 24 video frames per second and which were synchronized to the recording clock. This allowed a co-registration of tracking videos and electrophysiological data.
During data acquisition, processing of the electrophysiological data was minimized to achieve the highest possible temporal precision and record data as raw and unaltered as possible. The acquired video frames were subject to an online tracking algorithm which extracted the locations of the IR tracking LEDs and computed an approximate head position in both azimuth and elevation.

2.3.3. The computer infrastructure

In its final configuration, the experimental system consisted of three computers (NLX, STIM, CTRL; see Fig. 2.4 on the right) which served dedicated functions during the recording sessions. All PCs had only restricted access to the internet and the institute's local area network in general, because both kinds of connections can have detrimental effects on the recording performance as well as the temporal accuracy of the stimulus presentation. For local and secure interactions, the PCs were connected to a protected so-called demilitarized zone (DMZ) in the institute's network.

The NLX-PC was directly connected to the Neuralynx Digital Lynx SX recording system via a high throughput Gigabit fiberglass Ethernet connection. It ran the proprietary Neuralynx Cheetah software package which was used to configure and directly control the Digital Lynx SX data acquisition system. In addition to controlling the recording system, the NLX-PC received the recorded electrophysiological and video data via the Ethernet link and stored them before they were transferred to the definite data storage system where they were archived for later analysis.

The STIM-PC ran the stimulation software and drove the stimulation display. Initially, this was a commercial Canon LCoS projector, which was eventually replaced by a special VPixx PROPixx DLP projector (see section 2.3.1). Visual stimulation was carried out using the PsychToolBox (http://www.psychtoolbox.org/) for MATLAB (The Mathworks). The toolbox provides a widely used and well-tested set of MATLAB functions for the design of precisely controlled and temporally accurate visual stimulation paradigms. The STIM-PC was furthermore interfaced with the Digital Lynx SX via a parallel port cable sending digital trigger signals whenever stimuli were presented or when a new stimulation session began. For further details refer to section 2.4 on the stimulation paradigm.

The CTRL-PC served as a control center and interface for the experiments. Through a custom MATLAB program called StimOMatic, developed in the Laurent lab (Rutishauser et al., 2013), it served as a hub between the actual recording and stimulation systems. Based on the Neuralynx NetCom library, StimOMatic is capable of streaming electrophysiology and video tracking data from the recording system and analyzing them on the fly. In addition, it can interact with the STIM-PC through a set of data variables shared over the network. Through this closed-loop interaction it was possible to control the stimulation system dependent on the recorded activity

2.4. Naturalistic visual stimulation

2.4.1. The stimulation paradigms

Visual stimuli were presented in blocks consisting of either static images or video clips. Within each block, all stimuli were presented in a pseudo-randomized fashion with a variable interstimulus interval which consisted of a base ten second duration with a random jitter of 30% (10s$\pm$30%; see Fig. 2.7). The random component was incorporated to prevent entrainment of the stimulated animals as well as to avoid artifacts

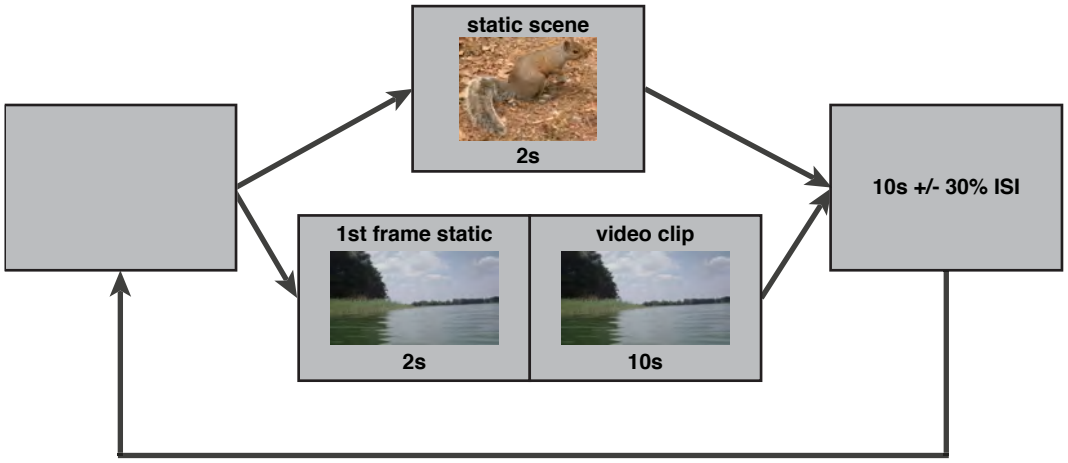

Figure 2.7.: The stimulation paradigms: Schematic display of the stimulation paradigms used. **Top|** Static natural scenes were displayed on a gray background for two seconds followed by a variable interstimulus interval. **Bottom|** Video stimuli are displayed for a total of 12 seconds where the first image is flashed to the screen for two seconds followed by ten seconds of video playback.

introduced by rhythmic physiological events like breathing or heartbeat. The parameters were determined in pilot experiments with anesthetized animals to avoid habituation and avoid the entrainment of the animal to a fixed stimulation rate [see also (Luo et al., 2010)].
The following sections will introduce the composition of the stimulus sets used during this project as well as the applied preprocessing steps.

2.4.1.1. Presentation of static natural-scene stimuli

Static natural-scene stimuli were flashed onto a uniform gray background for two seconds and then removed from the stimulus screen (compare Fig 2.7 top). The set of static images comprised 320 different stimuli of which 120 were actual natural-scene stimuli and 200 were control or localizer stimuli.

The natural-scene set| To prepare the natural-image stimuli, 60 images were selected from the McGill image database (http://tabby.vision.mcgill.ca/html/browsedownload.html). The images were to equal parts selected from three arbitrary categories: Images containing (1) animals, (2) landscapes (land or water) or (3) man-made scenes. As demonstrated by Torralba and Oliva, these coarse categories differ in their global spatial frequency composition and were therefore considered as a promising sample of natural scenes (Torralba and Oliva, 2003). The selection was re-formatted from their original tagged image file (TIF) format into uncompressed portable network graphics

(PNG) files (768x576 pixels). Copies of the RGB images were converted to gray scale using the MATLAB function rgb2gray.m which scales and sums the RGB color channels.

For each of the 120 (RGB + gray scale) natural images, a phase-scrambled counterpart was generated. The original images were subjected to a discrete Fourier transformation and uniform, random phase noise ($\pm$180 degrees) was added to the complex phase component of the transform. Subsequently, the transformation was inverted with the manipulated phase spectra. This procedure created phase-scrambled images with frequency contents matching those of the original images. However, the addition of the random phase noise resulted in a massive reduction of local contrast, thereby strongly reducing sharp contours and spatially coherent image structures (Wichmann et al., 2006).
Further, the average pixel intensities for the natural images were calculated and two-dimensional white noise patterns with the same average pixel intensities were generated. These served as additional control stimuli with flat power spectra and no intrinsic spatial correlations.
Lastly, two sets of unstructured uniform stimuli with the same x/y dimension as the natural images were generated. In these control stimuli, the entire 768x576 rectangle was uniformly colored in either red or gray to generate one highly efficient localizer stimulus and one near-threshold mock stimulus (Zagorul'ko, 1968).

Localizer| Red full-field flashes were used as localizer and benchmark stimuli to locate the visually responsive regions of turtle dorsal cortex and to assess a set of general response properties. Red was chosen as color for the localizer stimulus, because the turtle retina has a high density of red cones and pilot experiments in anesthetized animals showed very strong responses to red flash stimulation [see section 1.3 and (Zagorul'ko, 1968, Ammermüller and Kolb, 1996)].

Luminance adjustment| All natural and control stimuli were luminance adjusted according to the calibration data obtained for the display devices based on their average red, green and blue content. This means that the stimuli were adjusted to have an illuminance within $\pm$5% of the illuminance of the gray background at the position of the turtle head in the setup. Examples of the resulting images in the set of static stimuli are given in Fig. 2.8.

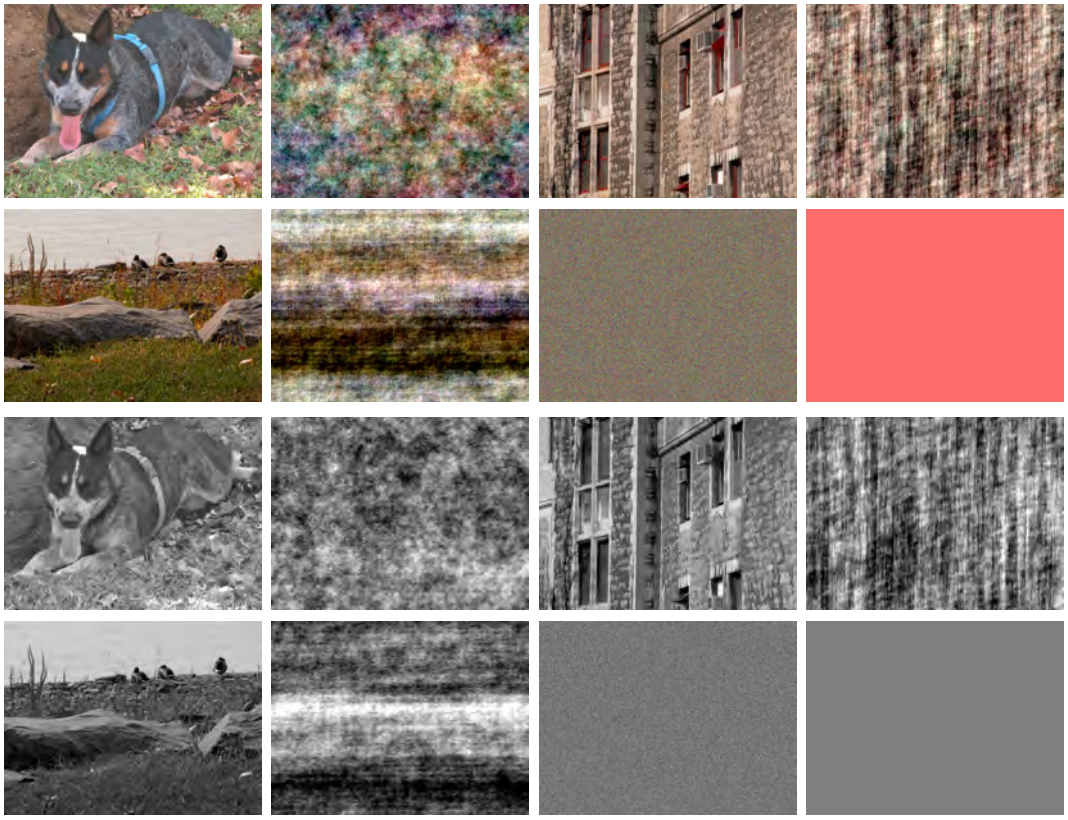

Figure 2.8.: Image categories: Example images illustrating the different stimulus categories used for the static-scene stimulation paradigm. **Top|** Example images in color. Corresponding natural and scrambled scenes are displayed side by side. **Bottom|** Same images as above after the transformation into grayscale.

Stimulus features| To characterize the stimuli and quantify relations between stimuli and evoked responses, a set of global stimulus features was extracted from each individual stimulus. The images were subject to a set of feature extraction routines and the extracted features were used to assess correlations between the recorded neurophysiological responses and the corresponding stimuli used to evoke them.
For each image, an estimated luminance based on the calibration of the projector used was calculated. In addition, the set of image features comprised mainly parameters (moments) describing the distributions of particular quantities within the images.
The distribution of local contrast elements in the stimuli was computed through the convolution of the original stimulus (I) with a Scharr edge detection filter (Scharr, 2000). Through a comparison of the gradients along the x (G_x in Eq. 2.3) and y (G_y in Eq. 2.3) dimension for each local contrast element, the predominant direction of the gradients was computed.

$$G_x = \begin{bmatrix} 3 & 0 & -3 \\ 10 & 0 & -10 \\ 3 & 0 & -3 \end{bmatrix} * I; G_y = \begin{bmatrix} 3 & 10 & 3 \\ 0 & 0 & 0 \\ -3 & -10 & -3 \end{bmatrix} * I; \tag{2.3}$$

Both the pixel intensity histogram and the distribution of local contrast were characterized by their: (1) mean, (2) median, (3) variance, (4) skewness and (5) kurtosis. In addition, a weighted distribution of the local contrast orientations was computed for each image. Subsequently, the average strength of oriented local contrast objects was calculated in 15 degree bins for orientations from 0 to 180 degrees. Furthermore, continuous line objects stronger than $\frac{1}{6}$ of the maximum contrast and exceeding a size of 15 pixels were identified and their distribution was described by the total number of objects as well as the mean, median, variance, skewness, kurtosis and 99th quantile of their size distribution.
For the RGB stimuli, all image features were calculated for the color channels (red, green, blue) individually. To collapse the three individual sets of features into one, weighted sums were computed according to the cone type density (R:0.6, G:0.25, B:0.15) in the turtle retina (Ammermüller and Kolb, 1996). To distinguish between feature sets of grayscale and collapsed RGB stimuli an additional scalar value of -1 or +1 was assigned to each stimulus.
Overviews over the abbreviations used for the extracted global stimulus features as well as a color-coded representation of the actual values are provided in Tab. 2.1 and Fig. 2.9 respectively.

2.4.1.2. Presentation of dynamic natural-video stimuli

Video stimulation consisted of two phases displayed in Fig. 2.7. In the first phase, the first frame of a video clip was flashed onto a uniform gray background for two seconds. After this flash-phase, the actual video playback started. This design allowed to dissociate the response components due to the sudden appearance of the stimulus from those due to the actual dynamic video stimulus.

The natural-video set| A video file containing footage from a natural pond environment was obtained from www.youtube.com (https://youtu.be/07rt2ao3Yrg) and preprocessed for usage as visual stimuli. The original footage was recorded with a camera mounted on a remote controlled submarine and contained episodes recorded above and under water. The video file was cut into shorter 10s clips with 2s overlap and ad-

Table 2.1.: Summary of the extracted global stimulus features which are later used as factors in the multilinear regression model. See text for more detailed descriptions of calculation.

Abbreviation	Stimulus feature
imLum	Estimated illuminance at turtle position
colorID	Identifier if stimulus was colored or grayscale
pxMean	Mean of pixel intensity distribution
pxVariance	Variance of pixel intensity distribution
pxSkewness	Skewness of pixel intensity distribution
pxKurtosis	Kurtosis of pixel intensity distribution
lcMean	Mean of local contrast distribution
lcMedian	Median of local contrast distribution
lcVariance	Variance of local contrast distribution
lcSkewness	Skewness of local contrast distribution
lcKurtosis	Kurtosis of local contrast distribution
woDistX-Y	Strength of local contrast binned from X to Y degrees
coNumber	Number of contour objects
coMean	Mean size of contour objects
coMedian	Median size of contour objects
coVariance	Variance of contour object size distribution
coSkewness	Skewness of contour object size distribution
coKurtosis	Kurtosis of contour object size distribution
coPercentile	99th percentile of contour object size distribution

justed in size (352x640 pixels). Clips were both stored in the original RGB color scheme and in a version that was converted to grayscale using rgb2gray.m for MATLAB (see previous section 2.4.1.1).

The set of control stimuli for the video stimulation paradigm contained colored and grayscale video clips in which either the spatial coherence, temporal contingency or both were artificially reduced.
The reduction of spatial consistency was achieved by subjecting the individual frames of the original video clips to the same phase-scrambling procedure that was used for static-scene stimuli (see above). Temporal consistency was reduced by randomly shuffling the order of the individual frames in the 10 second clips. In addition, both techniques were combined to generate video clips which neither contained spatially nor temporally coherent information. As a consequence, the control stimuli either lacked sharp contours (scrambled-sequential), temporally contingent motion (natural-shuffled) or both (scrambled-shuffled).

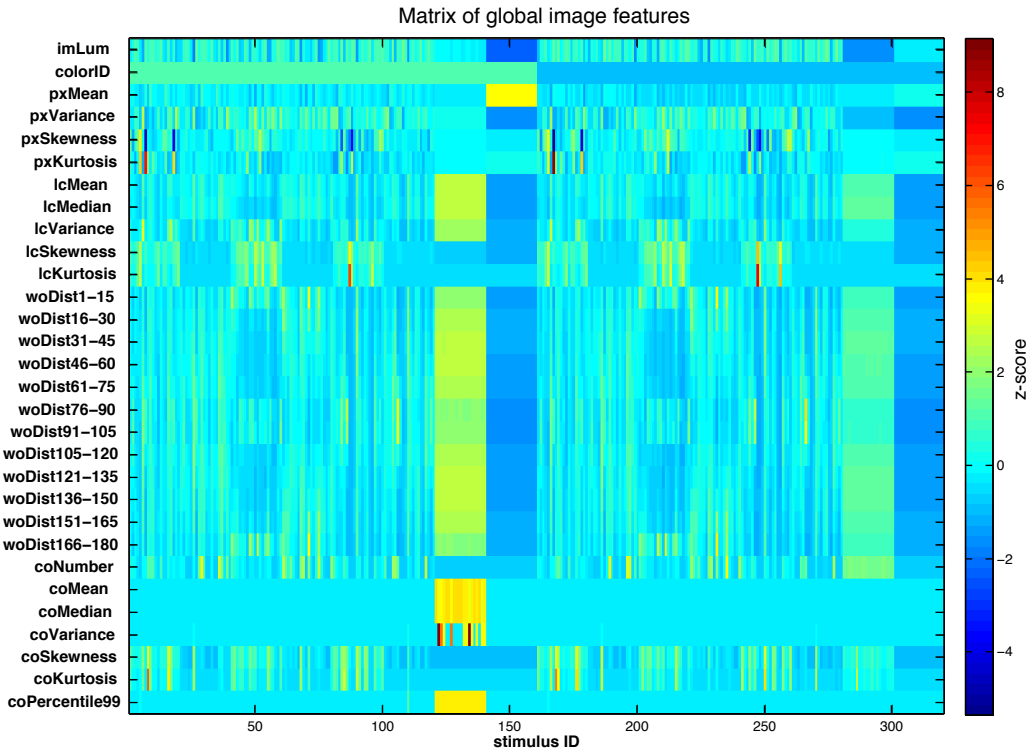

Figure 2.9.: Color-coded display of the normalized (z-scored) stimulus feature matrix showing individual features as rows and individual stimuli as columns. For a legend of the abbreviations used see Tab. 2.1.

2.5. Data analysis techniques

The following section gives an overview of the data analysis techniques applied to process the recorded ECoG data and obtain the results described later in the text. For all methods brief mathematical descriptions as well as motivations for their application are presented. For a more in depth review on signal processing techniques and their applications in the neurosciences the book 'Signal Processing for Neuroscientists' provides an accessible introduction (van Drongelen, 2006).

The applied analysis methods can be coarsely separated into two classes: (1) time-domain analyses and (2) frequency-domain analyses. The first class is localized in the time domain, because these methods are applied to signals which are described as functions of time. The second class describes analysis methods to transform time-domain data into the frequency-domain where signals are described to vary as functions of frequency. A special case are time-frequency analyses where the data are transformed into the frequency domain, but by doing this transformation in a windowed fashion, the time resolution is partially retained and signals can be described to change as functions of time and frequency.

2.5.1. Data import and preprocessing

Raw electrophysiology data were imported into MATLAB using a set of freely available MATLAB mex files (http://www.urut.ch/new/serendipity/index.php?/pages/nlxtomatlab.html) capable of reading the proprietary Neuralynx data format. Before cutting the continuous files into shorter segments they were filtered between 0.1Hz and 300Hz using a digital 5th order Butterworth bandpass filter. Phase shifts due to filtering were avoided by filtering the data both forward and backward using identical filter parameters.

In combination with the digital trigger stream recorded by the system, epochs of data corresponding to stimulation events were identified and extracted from the filtered continuous data stream. For each recording channel, short epochs of data (or trials) were cut out and sorted according to the stimulation condition under which they were recorded. In case of the natural-scene paradigm, six second long trials were cut consisting of a three second pre-trigger segment and a three second post-trigger segment. Data recorded in the natural-video paradigm were cut into 16 second epochs consisting of a three second pre-trigger segment and a 13 second post-trigger segment.
Each of the resulting trials was subsequently downsampled by a factor of 32, resulting in an effective sampling rate of 1kHz. All trials for each animal were subject to a contamination detection algorithm dedicated to identify trials containing head motion, eye-blinks, sensor jumps or spontaneous oscillatory activity unrelated to the visual stimulation. Data episodes containing any such contamination were labeled and excluded from data analysis.

2.5.2. Time-domain analysis techniques

Ensemble averaging| A recorded electrophysiological signal $x(k)$ can be considered as a mixture of the actual physiologically relevant stimulus-related signal $s(k)$ and unrelated noise $n(k)$ (cf. equation 2.4).

$$\overline{x(k)_N} = \frac{1}{N}\sum_{j=i}^{N} x_j(k) = \frac{1}{N}\sum_{j=i}^{N}\left[s_j(k) + n_j(k)\right] \tag{2.4}$$

$$Var(\bar{x}) = \frac{\sigma_s^2 + \sigma_n^2}{N} \tag{2.5}$$

Under the assumption that the noise is truly random with zero mean and not correlated to the physiological signal, while the stimulus-related signal occurs with a consistent time

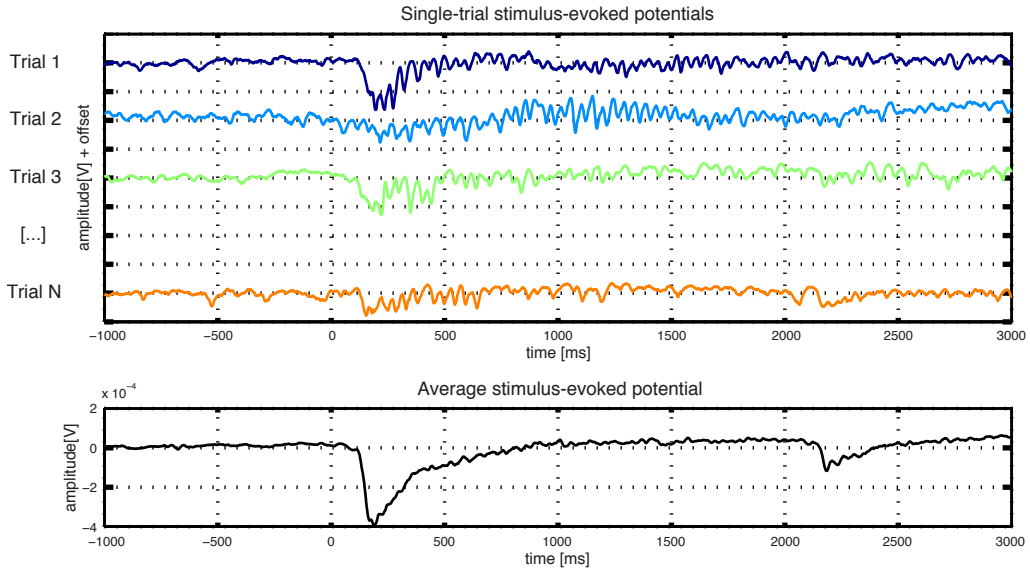

Figure 2.10.: Example computation of an ensemble average. Noisy single trial responses (1 . . . N) are averaged resulting in a cleaner average trace. Note that the average signal emphasizes the strong transients, but does not reflect the oscillations visible in the single-trial data.

delay, ensemble averaging is a valid standard approach to analyze event-related potentials (ERPs). The average signal ($\overline{x(k)}$) thus emphasizes stereotypical response components which are time-locked to the presented stimulus while noise and response components with variable time delays are removed or at least reduced by the averaging procedure. From equation 2.5 it can be appreciated that the signal estimate improves with the number of trials N or $\frac{1}{\sqrt{N}}$ and that the application of this technique allows to estimate even weak signals which are masked by noise.
Here, ensemble averaging was applied to the stimulus-evoked single trial data filtered between 0.1 and 300Hz to obtain average event-related potentials (see Fig. 2.10). Analyses and visualizations of event-related potentials were performed at the single-channel level as well as at the multi-channel level.

Hilbert transform and analytic signal| The Hilbert transformation is a special form of time-domain analysis aimed at the extraction and analysis of periodic signal components. Mathematically speaking, the term describes the convolution of a bandpass filtered time series signal $f(y)$ with $\frac{1}{\pi y}$.

$$g(t) = \mathcal{H}\{f(t)\} = \frac{1}{\pi} \int_{-\infty}^{\infty} \frac{f(x)}{y - x} dx = f(t) * \frac{1}{\pi t} \tag{2.6}$$

The term analytic signal (here x_a) is applied to the sum of a filtered signal $x(t)$ and the product of the Hilbert transform of the signal and the complex unit j (see Eq. 2.7). Its real component consequently contains information on the actual signal time course while its complex component captures information of the phase progression of the signal. The analytic signal thus contains information on both the strength of oscillatory activity (cf. eq. 2.8) as well as the instantaneous phase (cf. eq. 2.9) of oscillations within the specified frequency. The strength of oscillatory activity in the specified pass band is commonly quantified by taking the absolute values of the analytic signal called the Hilbert envelope.

$$x_a(t) = x(t) + jx(t) * \frac{1}{\pi t} \tag{2.7}$$

$$A(t) = \mid x_a(t) \mid \tag{2.8}$$

$$\phi(t) = arg\{x_a(t)\} \tag{2.9}$$

In this study, the Hilbert transformation was used to identify changes in oscillatory activity with variable time delays to the stimulation, which would cancel out during conventional averaging techniques. Single-trial data were filtered and Hilbert transformed to capture the strength of oscillatory activity while conserving the original time resolution of the signal (see Fig. 2.11).

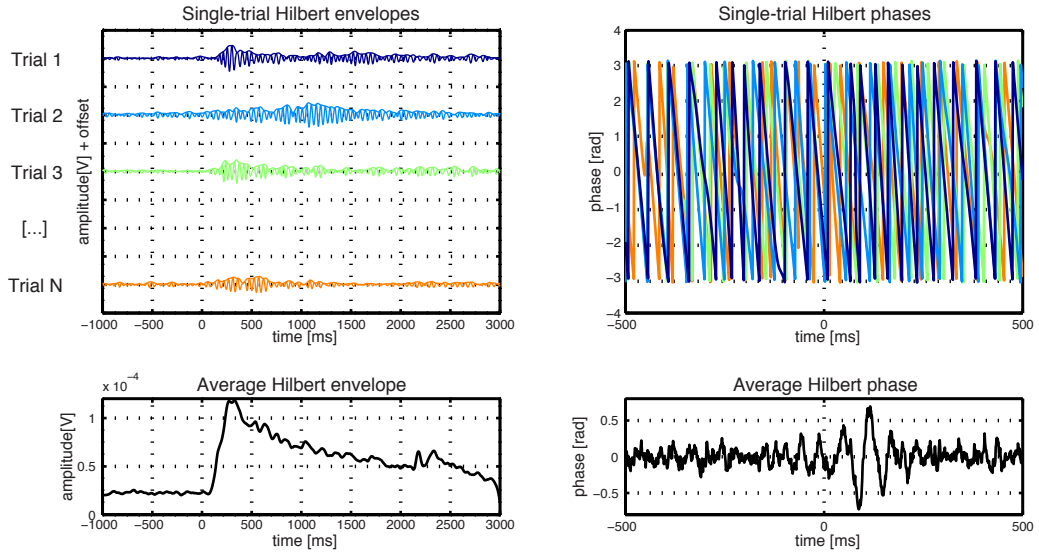

Figure 2.11.: Example computation of the Hilbert transformation on filtered (15-35Hz) versions of the data displayed in Fig. 2.10. **Left|** Computation of the Hilbert envelopes from filtered trials and their average. **Right|** Computation of the instantaneous phases of the trials displayed on the left and their average.

2.5.3. Frequency-domain analysis techniques

Similar to the Hilbert transformation, the following methods can be applied to quantify and describe periodic components in time series data which can only insufficiently be analyzed using trial averaging procedures. While the Hilbert envelope is usually estimated over a narrow frequency band, other frequency-domain analyses allow to estimate the signal power over a wide range of frequencies simultaneously.

Frequency analysis techniques are mainly based on the work of French mathematician Jean-Baptiste Joseph Fourier (1768-1830) who described that any periodic time series signal can be decomposed into a set of sine- and cosine basis functions. The discrete form of the mathematical principle and its inverse are given in equations 2.10 and 2.11 respectively.

After transforming the time-domain trials into spectra, they can be subject to ensemble averaging to obtain average spectral representations of the data (see Fig. 2.12).

$$X(k) = \sum_{n=0}^{N-1} x(n)\, e^{-j\frac{2\pi}{N}kn} = \sum_{n=0}^{N-1} x(n)\, W_N^{kn} \tag{2.10}$$

$$x(n) = \frac{1}{N} \sum_{k=0}^{N-1} X(k)\, e^{j\frac{2\pi}{N}kn} = \frac{1}{N} \sum_{k=0}^{N-1} X(k)\, W_N^{-kn} \tag{2.11}$$

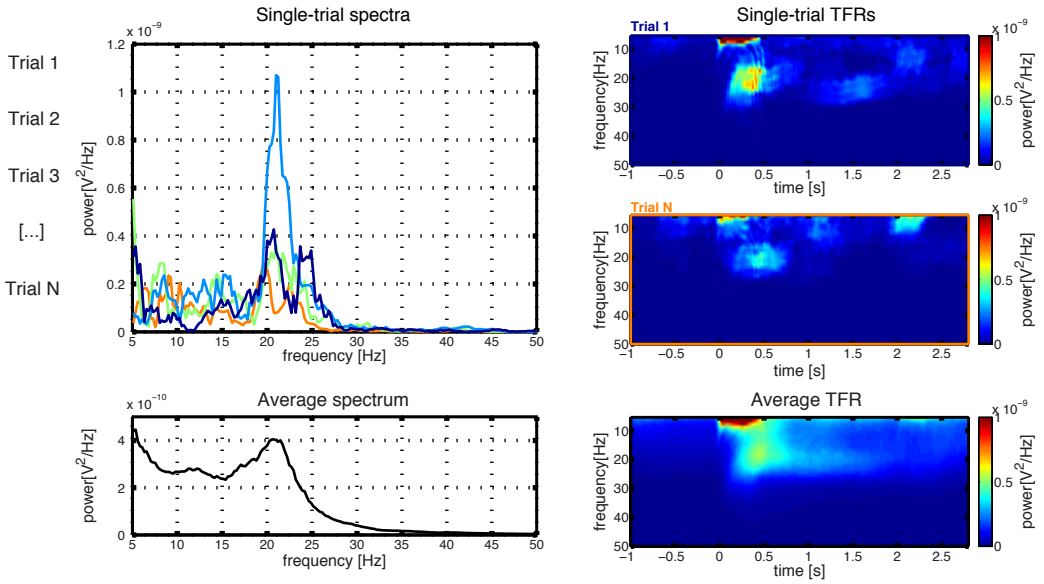

Figure 2.12.: Examples of common frequency-domain analysis techniques applied to the data displayed in Fig. 2.10. **Left|** Color-coded multi-taper frequency spectra of the single trials in Fig. 2.10 and the corresponding average spectrum. **Right|** Two exemplary single trial time-frequency representations (TFRs) as well as the average TFR over all trials.

Multi-taper spectral analysis| Multi-taper based spectral analysis methods represent a special case of spectral analysis techniques and have been devised to circumvent two major problems usually associated with the spectral analysis of finite time series data (Mitra and Pesaran, 1998): (1) Spectral estimation biases due to mixing of different frequency components of the analyzed signal; (2) A lack of convergence in the periodogram $|X(f)|^2$ when analyzing large datasets.

In the course of the multi-taper analysis, the original data are multiplied by a set of K orthogonal, slepian tapers $w_t(k)\,(k = 1, 2, \ldots, K)$ prior to subjecting them to the Fourier transformation. The final multi-taper spectral estimate $S_{MT}(f)$ is defined as the average of the K independent spectral estimates (cf. equations 2.12 and 2.13). However, special care needs to be taken when choosing the parameters of such analyses, because they directly influence the accuracy and resolution of the resulting spectral data.

$$S_{MT}(f) = \frac{1}{K}\sum_{k=1}^{K} |X_k(f)|^2 \tag{2.12}$$

where,

$$X_k(f) = \sum_{1}^{N} w_t(k)\, x_t e^{-2\pi i f t} \tag{2.13}$$

In this study, multi-taper spectral analysis was applied to individual trials to obtain both

power spectra and time-frequency representations reflecting the spectral composition of the stimulus-evoked ECoG responses.

Coherence analysis| Coherence between two signals (x and y in equations 2.14) is a frequency transformed variant of the cross-correlation analysis (see Eq. 2.15). Its computation requires the estimation of the so-called cross-spectrum S_{xy} which is the Fourier transform of the cross-correlation function and a subsequent normalization by the product of the power spectra of the individual signals (see Eq. 2.16).

$$C(\omega) = \frac{|S_{xy}(\omega)|^2}{S_{xx}(\omega) S_{yy}(\omega)} \tag{2.14}$$

$$R_{xy}(m) = E\{x(n) y(n+m)\} = \lim_{N\to\infty} \frac{1}{2N+1} \sum_{n=-N}^{n=N} x(n) y(n+m) \tag{2.15}$$

$$S_{xy}(\omega) = \mathcal{F}(R_{xy}) = \int_{-\infty}^{\infty} R_{xy}(m) e^{-j\omega m} \mathrm{d}m \tag{2.16}$$

From the complex-valued coherence data it is possible to determine the magnitude of coherence as well as the phase of coherence between two signals. Both properties were analyzed in this study to assess how coherent oscillations recorded from different recording sites on the ECoG array were and if they exhibited systematic phase differences as indicated by previous studies (Prechtl et al., 2000).
To assess the stability of oscillations evoked by stimulus super-categories (see below) the average coherence magnitude of the most active channel and its eight direct neighbors were computed.
To examine the temporal relations of responses across the ECoG grid, the coherence (magnitude and phase) between the maximally active channel and all other channels on the recording grid was computed.

2.5.4. Cluster-based statistical testing

Differences in activity patterns in response to different stimulation conditions can be quantified and statistically tested using a cluster-based non-parametric permutation test (Maris and Oostenveld, 2007). Because it is a non-parametric test, it does not require assumptions on the distributions of the tested samples. The variant of the tech-

nique used for the current study consists of several steps which will be briefly described here. For a more general and in depth description of motivations and advantages of the method refer to the original paper by Maris and Oostenveld, 2007.
In a first step, the differences between responses to different stimulation conditions were quantified in terms of independent samples t-values. However, this test-statistic was not directly used for the significance estimation. A threshold was applied to the test-statistics to remove samples which did not reach a particular effect size. The supra-threshold samples were subsequently clustered based on their spatial and temporal adjacency. For each cluster a cluster-test-statistic was computed by summing its constituent t-values. Now, a distribution of random cluster-test-statistics was estimated via Monte Carlo approximation (1000 permutations). For each real cluster a Monte Carlo p-value was calculated from the proportion of random test-statistics exceeding the real cluster-statistics. Finally, this p-value was used to estimate the significance of the cluster by comparing it to the critical alpha-level (i.e. 0.05).

Here, cluster-based statistical methods were applied to single-channel and multi-channel response data in the time as well as frequency domain. Depending on the data-type to be compared (voltage data, time-frequency data, coherence data), the data had to be pre-processed.
Single-channel data were directly used and test-statistics were clustered based on temporal (voltage data) or spectro-temporal (time-frequency data) adjacency.
Multi-channel potential data were directly used while multi-channel time-frequency data had to be reduced to a single frequency bin by selection or averaging. Afterwards the test-statistics in both metrics were clustered based on spatio-temporal adjacency.

Responses to both scene- and video-stimulation at the single- and multi-channel levels were sorted and pooled to compute statistical comparisons of responses to different stimulus super-categories (see lists below) across animals.

Stimulus subsets in the natural-scene paradigm

(A) Pre-stimulus **baseline** periods vs. post-stimulus **activation** periods

(B) Responses to **colored stimuli** vs. responses to **grayscale stimuli**

(C) Responses to **natural stimuli** vs. responses to **phase-scrambled stimuli**

Stimulus subsets in the natural-video paradigm

(A) Pre-stimulus **baseline** periods vs. post-stimulus **activation** periods

(B) Responses to **colored videos** vs. responses to **grayscale videos**

(C) Responses to **natural videos** vs. responses to **natural-shuffled videos**

(D) Responses to **natural videos** vs. responses to **scrambled-sequential videos**

(E) Responses to **natural videos** vs. responses to **scrambled-shuffled videos**

2.5.5. Analyses of average evoked oscillatory power

For an additional set of analyses the stimulus-evoked responses were collapsed to sets of single scalar values or short vectors for each trial. Because the analyses were focused on oscillatory activity, the methods described in the following paragraphs were restricted to the band of previously described oscillations (15-35Hz). The average evoked oscillatory power in this band was analyzed in three ways:

(A) The average oscillatory power evoked by different stimulus super-categories and categories was compared by means of regular analyses of variance.

(B) Response power values were pooled independent of the stimulus that had been used to evoke them and subsequently subdivided into equally sized quantiles to identify particularly effective stimuli.

(C) Relevant stimulus features and their influence on the observed variance in the response power were identified by means of multilinear regression analysis.

Pre-processing| Depending on the analysis to be applied, the dimensionality of the oscillatory response components was reduced in one of two ways.
(1) For the ANOVAs and quantile-splitting approaches, the oscillatory responses were reduced to a single scalar value by averaging the power values in the TFRs over a specific time and frequency window (dashed rectangle in Fig. 2.13 C). For both scene- and video-stimuli, the frequency window ranged from 15Hz to 35Hz. The time window for scene-stimuli extended from stimulus onset to 2.5s post onset and for video-stimuli from 2s to 12.5s post onset to account for the initial 2s flash.
(2) For the multilinear regression analysis, the Hilbert envelopes of the bandpass filtered (15-35Hz) trials were computed (see Fig. 2.13 B). The resulting time courses of oscillatory activity were binned (bin-width 50ms) and used as response vectors to estimate

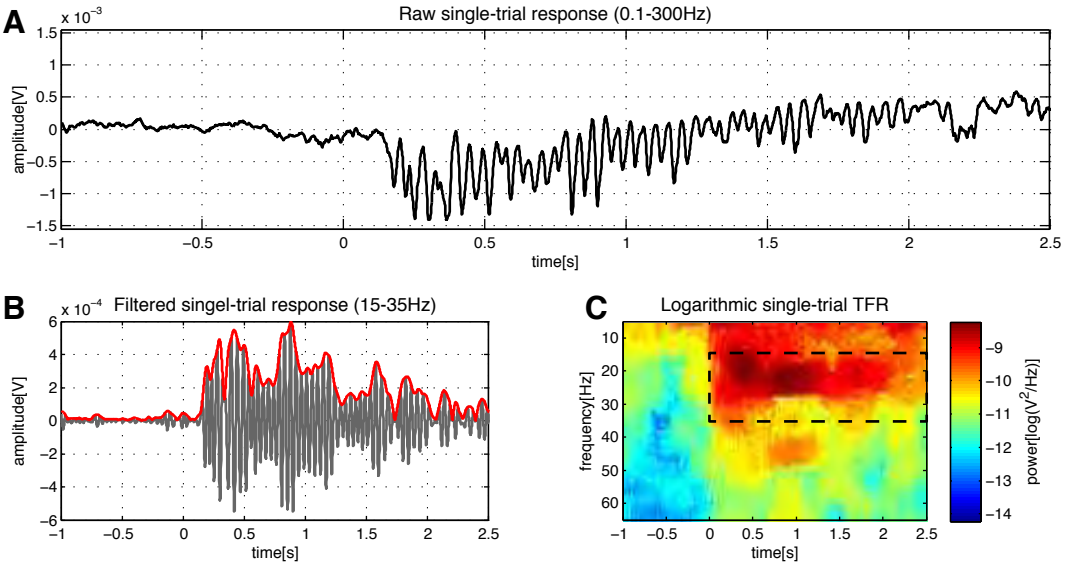

Figure 2.13.: A| Example of a single trial response evoked by a natural-scene stimulus filtered between 0.1-300Hz. **B|** Same trial as in A filtered from 15-35Hz (gray line) as well as its Hilbert envelope (red line). **C|** Logarithmic time-frequency power representation of the trial. The dashed rectangle indicates the time-frequency window used for averaging.

predictor weights in the multilinear regression analysis. Only responses from the animals H5, K12, K11, K8 were used for the multilinear regression. P44 had to be excluded, because it was the only animal stimulated with the novel VPixx projector.

Whenever average power values were compared across animals, z-scoring (Eq. 2.17) was applied to correct for potential inter-individual differences. For each animal the power values x_i were converted into z-scores z_i by subtracting the mean μ and dividing by the standard deviation σ of the dataset.

$$z_i = \frac{x_i - \mu}{\sigma} \tag{2.17}$$

Analysis of variance (ANOVA)| To compare responses evoked by stimulus super-categories and original stimulus categories (16 static-scene categories, 8 video-clip categories), the average response power values were mean normalized and subject to a n-factor ANOVA for unbalanced samples (anovan.m in MATLAB). The data design was chosen such that the first factor corresponded to the animal ID and the second factor to the stimulation conditions. After computing the ANOVA test statistics, the results were subject to a Tukey-Kramer multiple comparison correction (multcomp.m in MATLAB). This was necessary to extend the originally tested hypotheses (Data do or do not belong to the same population) to pairwise comparisons of all stimulus conditions with a

constant α-error level (of 5%).

Natural-scene-evoked responses were first partitioned according to whether they were evoked by colored or grayscale stimuli and within these partitions they were sorted into responses to natural scenes, scrambled scenes, white noise and uniform-color flashes. In a second ANOVA response power to all 16 original stimulus categories were grouped and compared.
Natural-video-evoked responses were partitioned according to the original eight video categories and compared. In addition to the comparison for average power between 15-35Hz a second ANOVA was computed for the average evoked power between 35-45Hz.

Quantile-splitting approach to identify effective stimuli| The grouping of the stimuli into the original categories was arbitrary and likely not meaningful to the animals or examined brain region. Thus stimuli evoking strong and weak cortical responses might have been lumped in one category. Therefore, the pooled, z-scored power values were split into three quantiles to identify effective and ineffective stimuli without prior grouping of the response data. This approach allowed to identify individual stimuli which consistently evoked strong cortical responses independent of their original stimulus category.

Multilinear regression analysis| Under the assumption that an observed response (i.e. oscillatory power) is linearly related to one or more stimulus features (i.e. luminance, mean pixel intensity) these relations can be quantified by multilinear regression. The method is based on solving sets of linear equations as displayed in equation 2.19. For each response observation y_n in Y a linear equation is constructed with the stimulus features represented as elements $x_{n,m}$ in X and unknown weights w_m. The weights are estimated by solving the linear equation system in equation 2.18. In addition to the stimulus-specific weights, a stimulus-independent offset component was estimated for each time bin.
To obtain a prior estimate for whether all extracted stimulus features contributed significantly to the fit, they were tested using a stepwise fitting algorithm (stepwisefit.m in MATLAB). The algorithm adds predictors in a step by step fashion and estimates whether they significantly improve the fit. Only if a coefficient improved the fit ($p<0.05$), it was kept in the final model. This stepwise fitting was done for each 50ms time bin in the response feature array. After identifying the significant stimulus features for one time bin, the weights in the regression model were estimated using a random subset of 95% of the response feature values in that time bin.

$$Y = w \cdot X \tag{2.18}$$

$$Y = \begin{bmatrix} y_1 \\ y_2 \\ \vdots \\ y_n \end{bmatrix}; w = \begin{bmatrix} w_1 & w_2 & \cdots & w_m \end{bmatrix}; X = \begin{bmatrix} x_{1,1} & x_{1,2} & \cdots & x_{1,m} \\ x_{2,1} & x_{2,2} & \cdots & x_{2,m} \\ \vdots & \vdots & \ddots & \vdots \\ x_{n,1} & x_{n,2} & \cdots & x_{n,m} \end{bmatrix} \tag{2.19}$$

The amount of variance in the responses (Y) that could be explained with the obtained weights (w) was quantified using the coefficient of determination (R^2; in Eq. 2.20). Similarly, the goodness of prediction was estimated by trying to predict the remaining 5% of the responses from the obtained weights. This procedure was repeated 100 times to estimate margins of error for the prediction and fitting.

$$R^2 = 1 - \frac{SS_{residual}}{SS_{total}} \tag{2.20}$$

$$SS_{total} = \sum_{i=1}^{n} (y_i - \bar{y})^2 \tag{2.21}$$

$$SS_{residual} = \sum_{i=1}^{n} (y_i - w \cdot X_{i,1:m})^2 \tag{2.22}$$

2.6. The experimental animals

In summary, five female red-eared slider turtles (*Trachemys scripta elegans*) were used as subjects for the chronic experiments. Because of the size of the chronic implant (see section 2.2.1) only animals above a weight of 950g could be used for these experiments. Only these animals had enough space on their skulls to allow a proper fixation of the implant. All animals were female; female red-eared sliders tend to be bigger than males and thus only female animals in the institute's husbandry reached the above mentioned size criterion.

Table 2.2 summarizes the main characteristics of the experimental animals used in the presented research project. The first three columns contain ID, sex and weight, and the last two columns display how many responses for each paradigm were recorded per category and how many of these trials had to be rejected due to signal contamination

Table 2.2.: Summary of the basic characteristics of the experimental animals used for chronic ECoG recording experiments. Displayed are sex, weight and amount of data collected per animal.

Animal ID	sex	weight[g]	trials per scene/video category	% clean
H5	f	957	140 / (160)	81 / (66.9)
K12	f	1230	200 / -	91.6 / -
K11	f	1325	240 / 256	80.3 / 70.5
K8	f	1276	220 / 416	81.9 / 60.6
P44	f	1464	180 / 64	83.1 / 61.5
Group Avg.	-	1042±186	196±38 / 245±176	-

with unrelated physiological signals or noise (cf. section 2.5).

Video-evoked responses from animal H5 could not be used for analysis, because the video paradigm used did not yet contain the initial 2 second static display of the first video frame. After pre-processing and artifact rejection a total set of 13099 clean responses to static natural-scene stimuli and 3270 responses to natural-video stimulation were available.

All experimental procedures were in accordance with legal requirements and approved by the local authorities at the Regierungspräsidium Darmstadt.

3. Results

The results chapter is divided into several individual sections with the intention to present the experimental data in a coherent way progressing from the most simple to more complex stimulus/response pairings. Initially, a brief description and example of resting-state ECoG dynamics is given (section 3.1.1). Subsequently, responses to simple uniform full-field flash stimuli are described (section 3.1.2). These were used as localizer and benchmark stimuli, applied to identify the cortical regions showing strong visually evoked responses, and to quantify the stability of these responses. After considering the responses to unstructured flash stimuli, the responses to static natural-scene stimuli (section 3.2) are presented, followed by responses to natural-video stimulation (section 3.3). Finally, the co-registration of physiological and anatomical data is presented (section 3.4).

Each major section is prefaced by a brief summary of its main results. Within each of the sections, the obtained results are subdivided into results at the single-channel level and results obtained at the multi-channel level.
The **single-channel** results illustrate general response characteristics in strongly active cortical sites and demonstrate basic stimulus/response relations. For each experimental animal, the μECoG channel exhibiting the strongest response to the localizer stimulus was selected out of the ensemble. The quantified response metrics comprised average event-related-potentials (ERPs) and oscillatory power in the 15-35Hz frequency range. Because these analyses were independent of the exact position of the strongest channel for each animal, the single-channel ECoG data were pooled over all experimental animals.
The **multi-channel** data on the other hand were used to analyze and describe large-scale spatiotemporal activity patterns and their relations to visual stimulation. It is described how the different response metrics were distributed across the entire ECoG array and how spatial patterns changed over the time-course of stimulation. Because the exact position of the ECoG array varied slightly between animals, it was not possible to pool data across animals. To avoid spatial smearing, the data presented in the multi-channel sections were taken from individual experimental animals without averaging across animals.

3.1. General characteristics of turtle ECoG recordings

Summary| *The ECoG signals recorded from awake turtles had a rich structure and showed both stimulus-evoked and spontaneous oscillatory activity patterns. Bouts of oscillatory activity were observed in bright and dark recording environments as well as in the presence and absence of head movement.*
Red-flash stimuli were reliable localizer stimuli which evoked strong ECoG responses in circumscribed regions (rostrocaudal extent: 2.7±0.3mm; lateromedial extent: 2.0±0.3mm) of dorsal cortex caudomedial to the cortical ridge. Location and magnitude of evoked responses remained stable over several weeks. For each animal, the ECoG channel showing the strongest flash-evoked responses was used for all subsequent single-channel analyses.

3.1.1. Characterization of resting-state ECoG dynamics

The spontaneous data were not systematically analyzed, but the following paragraphs will provide a brief anecdotal overview of spontaneous ECoG signals.
Figures 3.1 and 3.2 display episodes of spontaneous activity on a single ECoG channel recorded in an awake turtle in the presence (Fig. 3.1) and absence (Fig. 3.2) of ambient light. The ambient light condition corresponded to the background light levels which were also used during the stimulation session. For both lighting situations, a 100s stretch of raw voltage signal and a 600s long time-frequency representation are presented to illustrate the structure of spontaneous ECoG signals.

Spontaneous bouts of activity were frequently observed when analyzing long stretches of data without visual stimulation. In a large fraction of cases, these bouts of activity contained sustained (>1s) oscillatory components in the 15-35Hz frequency range. The oscillatory bouts were short events, but spread across several recording electrodes on the grid. Comparisons of the time of occurrence of the oscillations to head motion recorded by the head tracking system showed that spontaneous activity was observed both in the presence and absence of head motion.
In addition to the described intracranial physiological signal components, the ECoG signal contained both extracranial physiological low-frequency noise components (i.e. movement and breathing) and nonphysiological environmental noise components (i.e. 50Hz line noise).

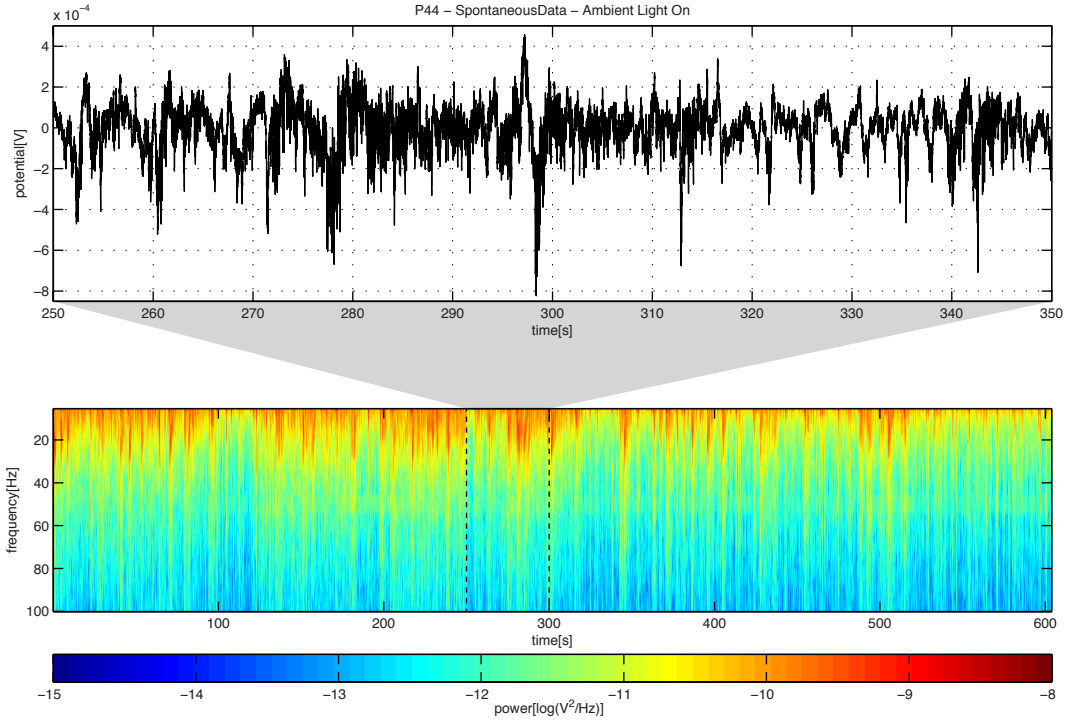

Figure 3.1.: Spontaneous activity recorded from a single ECoG electrode in the presence of ambient light. **Top|** 100 seconds of single-channel ECoG data showing spontaneous fluctuations and oscillations. **Bottom|** Time-frequency power representation of the 10 minute recording from which the 100 seconds were extracted.

3.1.2. Localization of visual responses and quantification of signal stability

Figure 3.3 shows average flash-evoked responses from all chronically implanted animals to uniform red flash stimuli. The center column displays the time-courses of the avg. potential and avg. Hilbert envelope (15-35Hz) of the strongest channel on the ECoG array. The panels on the left display the spatial distribution of potential values at the time point of the peak in the average ERPs. The rightmost panels display the peak potential and avg. power values for each individual flash response on the strongest channel.

Uniform red flash stimulation evoked average potentials (0.1-300Hz) which contained two clear peaks (Fig. 3.3, center, blue traces). The first corresponding to the stimulus onset occurred 144ms post stimulus onset with an average amplitude of -0.71±0.43mV. The second peak occurred 165ms post stimulus offset with an average amplitude of -0.35±0.24mV. The Hilbert envelopes between 15 and 35Hz showed three distinct peaks (Fig. 3.3, center, red traces). An onset peak with an average latency of 133ms and an average amplitude of 0.13±0.07mV, an intermediate peak with an average latency of 567ms and an average amplitude of 0.11±0.07mV, and an offset peak with an average

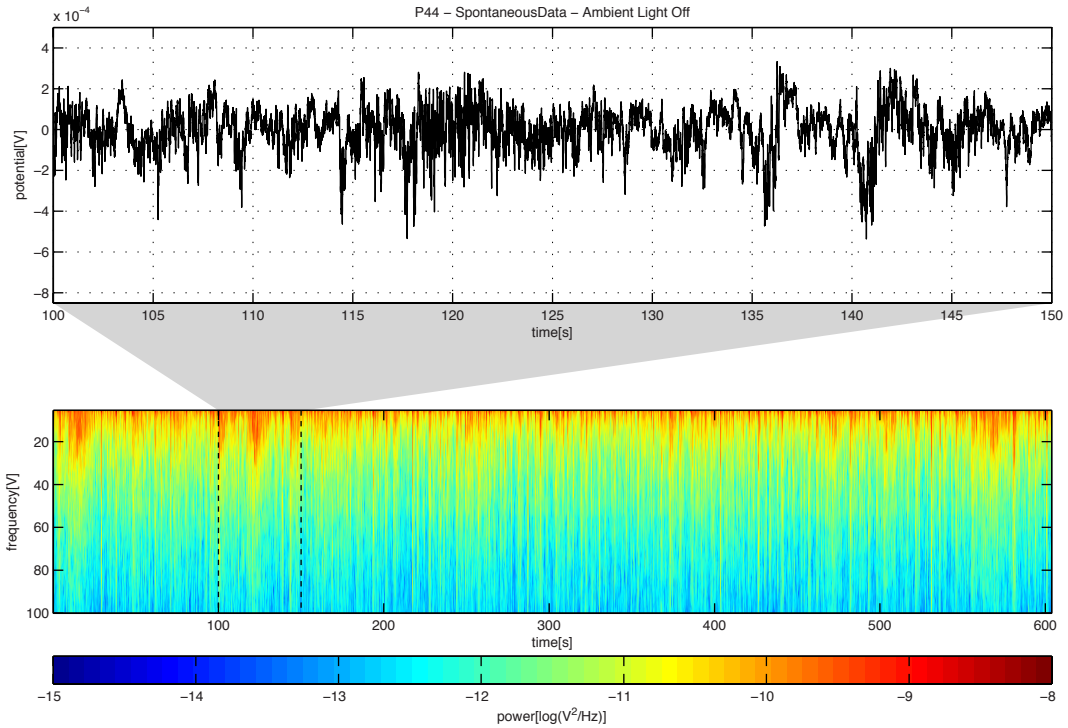

Figure 3.2.: Spontaneous activity recorded from a single ECoG electrode in the absence of ambient light. **Top|** 100 seconds of single-channel ECoG data showing spontaneous fluctuations and oscillations. **Bottom|** Time-frequency power representation of the 10 minute recording from which the 100 seconds were extracted.

latency of 2158ms and an average amplitude of 0.13±0.07mV.

The spatial representations of the observed onset peaks in the wide-band field potential showed that the peaks were located in single area of maximum responsiveness for each of the experimental animals, which did not change over the course of the recordings (Fig. 3.3, left). Based on the strongest quartile of evoked potential values, the average extent of the activated area was 2.7±0.3mm in the rostrocaudal axis and 2.0±0.3mm in the lateromedial axis.

The amplitude of the initial peak as well as the average oscillatory power (15-35Hz) after stimulus presentation were used to assess the response strength for each individual presentation (Fig. 3.3, right, blue: wide-band potential peak, red: oscillatory power). Both metrics showed considerable fluctuations over the time course of the individual experiments (∼4 weeks), but neither the potential peak, nor the oscillatory power decreased to zero.

In all subsequent single-channel analyses of stimulus evoked responses, the channel showing the strongest response to the localizer stimulus was selected for each of the experimental animals. This allowed to pool data across animals despite the fact that the exact location of the ECoG grid differed for the individual animals.

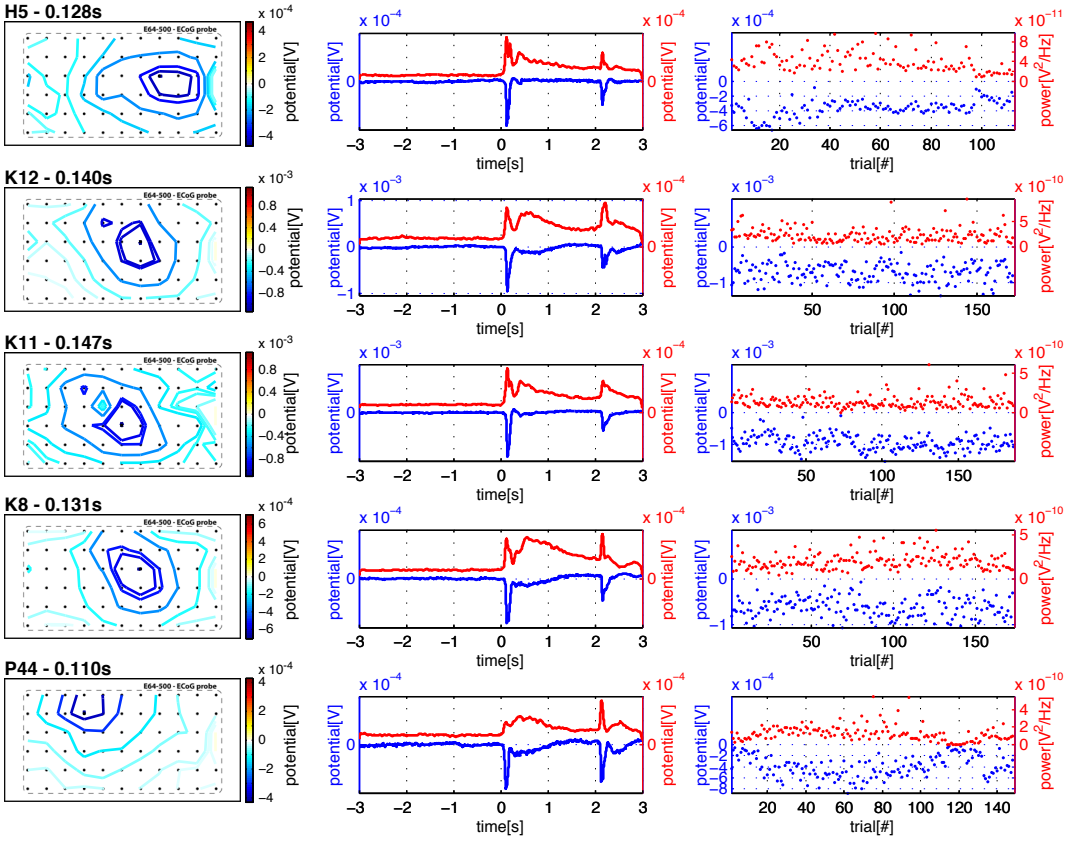

Figure 3.3.: Quantification of response stability for all experimental animals (rows). **Left column|** Spatial representation of the strongest negativity in the avg. flash-evoked potential (blue traces in middle column). Distance between to recording sites (black dots) is 500µm. **Middle column|** Average flash-evoked potentials (blue; left y-axis) and Hilbert envelopes from 15-35Hz (red; right y-axis) on the ECoG channel exhibiting the strongest response signal. **Right column|** Amplitude values of the strongest negativities in the average potential traces (blue; left y-axis) and average oscillatory power values (red; right y-axis) for individual stimulation trials.

3.2. Natural-scene-evoked responses

Summary| *Natural-scene stimuli reliably evoked ECoG responses in the dorsal cortex of awake turtles. Natural-scene-evoked responses were characterized by strong transients in the electrocorticogram signals as well as sustained and coherent oscillations in the 15-35Hz range. The transients were associated with the stimulus on- and offset while oscillations were sustained throughout the stimulation period. Evoked activity was consistently recorded in the same regions of dorsal cortex caudomedial to the cortical ridge and exhibited a rostrocaudal phase gradient across the area of strongest oscillatory activity (15-35Hz).*

Comparisons of responses to natural and control stimuli showed that colored natural stimuli evoked significantly stronger and more coherent oscillations in dorsal cortex than phase-scrambled or white noise stimuli.

Approximately 32% of the variance in the average evoked activity between 15 and 35Hz could be explained by a multilinear model using global stimulus features (i.e. moments of the intensity and local contrast distributions) as predictors.

3.2.1. Basic characteristics of natural-scene-evoked responses at the single-channel level

Visually evoked responses were clearly visible in the raw single-trial data (wide-band potential, 0.1-300Hz; power spectrum and TFR [time-frequency-power representation]) without prior ensemble-averaging (typical data in Fig. 3.4 A). The single trial plots indicate that stimulus-evoked responses to static natural-scene stimuli consisted of a low-frequency potential with superimposed oscillations in the 20Hz range.

Figure 3.4 B displays the average single-channel response characteristics for one experimental animal (K12) and provides a cleaner picture of the composition of the evoked responses.
The average event-related potential (ERP; 0.1-300Hz) exhibited emphasized on- and offset transients, but no trace of oscillatory activity. The transients were characterized by a sharp onset with relatively long time-constants. The onset peak was more pronounced than the offset peak with respect to its magnitude and occurred on approximately 180ms after the stimulus onset.
The average power spectra of the response period (see Fig. 3.4 B) showed that the low-frequency response components were accompanied by a wide-band, upward shift of ca. 0.5 order of magnitude compared to the baseline spectrum and a shoulder ranging from 15 to 35Hz. Both response and baseline spectra exhibited weak line-noise peaks at precisely 50Hz.
The average time-frequency power representation in Fig. 3.4 B reflects the initial onset transient and low-frequency potential as well as the sustained oscillatory activity in the 15-35Hz band and the offset transient. The oscillations were most pronounced in the first 500ms and peaked approximately 250ms post stimulus onset. After this period the power values decreased, but remained elevated throughout the entire stimulation period.

Figure 3.4 C shows the average stimulus-evoked potentials and average response spectra for all experimental animals individually (color-coded). It shows that the averages were similar in their general characteristics, but it should be noted that both metrics showed small inter-individual differences. Average evoked potentials consistently showed onset and offset associated transients and avg. spectra showed shoulders around 20Hz.

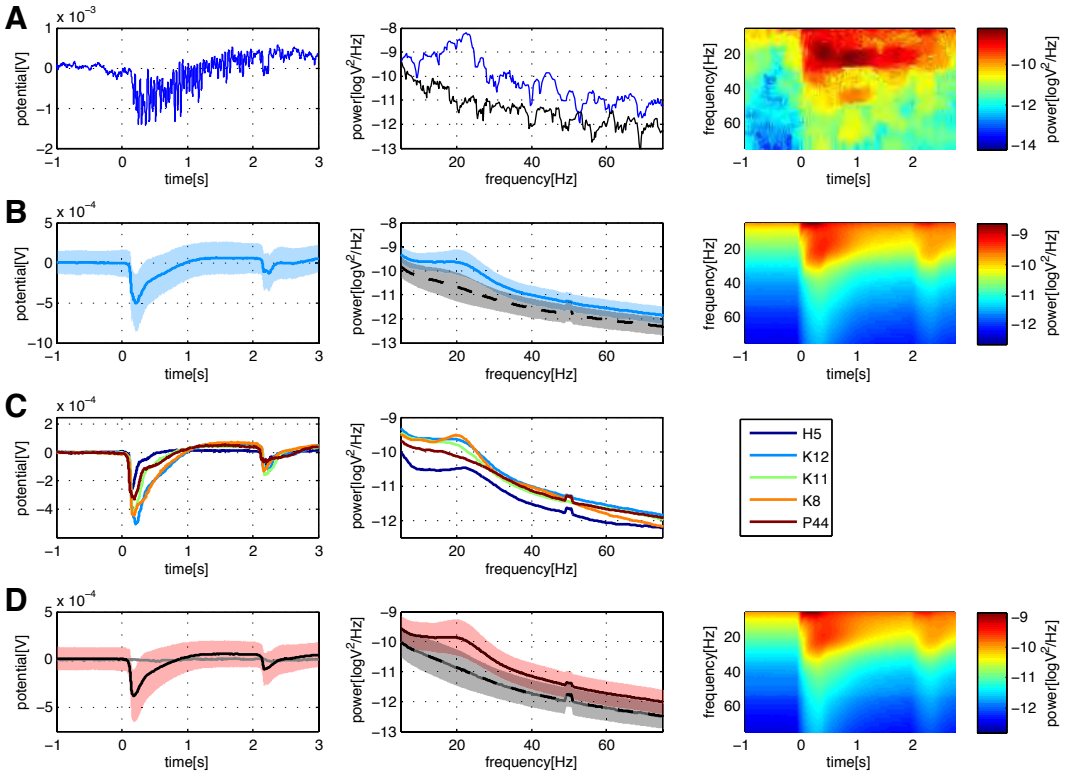

Figure 3.4.: Overview of visually evoked responses on the single channel level. Line plots display average and standard deviation as shaded area. **A|** Example evoked response, response spectrum(blue), baseline spectrum(black) and TFR. **B|** Average evoked response, spectra (as above) and TFR for one experimental animal.**C|** Color-coded overlay of average responses and average response spectra for all 5 animals. **D|** Grand-average evoked response, spectra and TFR over all 5 animals. Gray lines indicate the grand-average activity evoked by the mock stimulus.

The amplitude of the transients and the wave-shapes as well as the exact positions and magnitudes of the spectral peaks varied slightly across animals.

Because of the high degree of similarity, the single-channel data obtained for the experimental animals were pooled in most of the subsequent single channel analyses and figures. Panel D of Fig. 3.4 shows the grand-average response characteristics of all visually-evoked responses. All of the response characteristics visible on the single animal level (onset/offset transients, 15-35Hz oscillations) were clearly reflected in the grand-averages as well.

The onset transient in the grand-average potential (0.1-300Hz) occurred 184ms post stimulus onset and reached an average amplitude of -0.38$\pm$0.27mV. The offset transient peaked 177ms post stimulus offset and reached an amplitude of -0.10$\pm$0.17mV. Oscillatory activity as quantified via the Hilbert envelope from 15-35Hz (not shown) exhibited two similar, but temporally offset peaks. The onset peak occurred 272ms post stimulus with an average amplitude of 0.13$\pm$0.09mV while the offset peak occurred

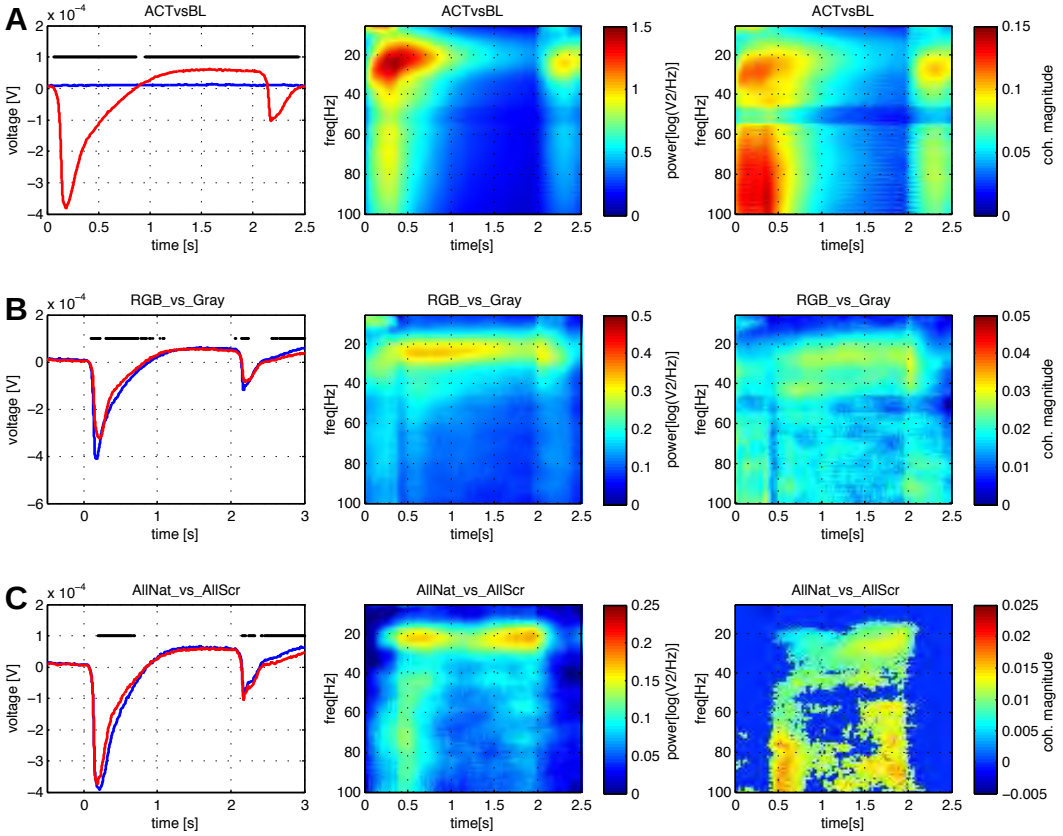

Figure 3.5.: Avg. evoked potentials for the compared stimulus conditions (left). Black marks over the curves indicate significant differences. Avg. difference-TFRs between stimulus conditions (middle). Avg. change in coherence magnitude on the channels surrounding the strongest channel (right). Only significant differences in power and coherence are displayed. **A:** Baseline (blue) vs. response (red); **B:** RGB stimuli (blue) vs. grayscale stimuli (red); **C:** Natural stimuli (blue) vs. scrambled stimuli (red).

2302ms post stimulus onset with an average amplitude of 0.07±0.05mV.
A peak oscillatory frequency of 20.02Hz was extracted from the grand-average response spectrum. The peak in the linearly scaled power spectrum reached an average power of $0.31 \pm 0.45 * 10^{-9} \frac{V^2}{Hz}$. In addition, panel D illustrates the absence of evoked activity in response to the uniform gray mock stimulus (gray lines) which was therefore excluded from most subsequent analyses.

3.2.2. Comparison of responses to stimulus super-categories at the single-channel level

Except for the evoked potentials (left column), Fig. 3.5 displays the results of the statistical comparisons of response super-categories in the form of grand-average difference patterns.

(a) Activation vs. baseline| Grand-average activation and baseline potentials (0.1-300Hz; in Fig. 3.5 A) differed almost over the entire analyzed time window. The activation period began to differ from the essentially flat baseline only a few milliseconds after stimulus onset and showed a sharp transient which reached a peak amplitude of -0.38mV within 184ms. Subsequently, the stimulus-evoked potential relaxed towards the baseline level and crossed it ∼950ms post stimulus onset. Baseline crossing was followed by a sustained positivity. 177ms post stimulus offset, a second negative transient which reached an amplitude of -0.10mV was observed. Again, this transient was followed by a slow relaxation towards the baseline which was reached 500ms post stimulus offset.
The grand-average difference-TFR in Fig. 3.5 A shows that all significant power differences (response - baseline) were positive, indicating that the response power was consistently stronger than the baseline. An initial surge in the low frequency range (∼175ms; <15Hz) was followed by a pronounced power increase (∼350ms) in the 15-35Hz oscillatory band accompanied by a wide-band increase in power. Both power and band-width of the 15-35Hz oscillations decreased over the duration of the stimulus presentation. Despite the marked decrease, the response power did not reach the baseline level and oscillatory power remained elevated until stimulus offset. Stimulus offset was associated with power surges similar to those following stimulus onset (∼2300ms), but the observed changes were weaker.
The pattern of coherence differences between activation and baseline periods was somewhat similar to the pattern of power differences. Whenever changes in oscillatory power were observed, the coherence changed as well. However, changes in coherence magnitude were not directly proportional to power changes, but showed stronger increases at higher frequencies.

(b) Colored vs. grayscale stimuli| Grand-average potentials (0.1-300Hz) in responses to colored and grayscale stimuli (Fig. 3.5 B) differed significantly during both the onset and the offset transient. Colored stimuli evoked significantly larger and earlier onset peaks (180ms;-0.41±0.29mV) than grayscale stimuli (221ms;-0.32±0.29mV), although the slopes of the transient were comparable. In addition, the relaxation back to baseline was less steep for the responses to colored stimuli. In both conditions, the onset transient was followed by a similar positive potential (∼0.05mV). The offset transient in responses to colored stimuli (2174ms;-0.12±0.19mV) was larger and earlier than for grayscale stimuli (2214ms;-0.08±0.16mV). After returning to the baseline level the traces showed a weak but significant divergence during which the responses to colored stimuli were more positive.

The difference-TFR in Fig. 3.5 B revealed consistently positive difference values, indicating that colored stimuli evoked significantly more oscillatory power than grayscale stimuli. Significant differences were observed directly after stimulus onset in the low frequency range (<15Hz), the 15-35Hz peak and in the wide-band surge. The initial difference in the 15-35Hz peak transitioned into a continuous difference-band which lasted for the entire stimulation period and later transitioned into a difference-peak after stimulus offset. The difference-band showed a period of high magnitude between 500ms and 1.25s post stimulus onset and was accompanied by weaker differences at frequencies up to 100Hz. Differences in the offset response included a low frequency component, a 15-35Hz peak and a wide-band component.
Significant differences in coherence magnitude were observed over a wide range of frequencies and almost throughout the entire stimulation period. The strongest changes in coherence were observed in the same frequency bands in which strong power differences were seen. Stimulus onset was followed by a brief difference in the low-frequency range <15Hz and during stimulus presentation a clear band of positive differences between 20 and 30Hz was observed. Throughout the entire period positive coherence differences were observed from 40-100Hz.

(c) Natural vs. phase-scrambled stimuli| Grand-average potentials (0.1-300Hz) evoked by natural scenes and phase-scrambled scenes (see figure 3.5 C) differed during both the onset and offset response phase.
Onset transients evoked by natural scenes (212ms;-0.39±0.29mV) were slightly stronger and later than those evoked by scrambled scenes (188ms;-0.37±0.26mV). During the relaxation phase, responses to natural-scene stimuli were consistently more negative than responses to phase-scrambled stimuli. The offset peak in responses to natural scenes (2176ms;-0.08±0.16mV) was weaker than in responses to scrambled scenes (2176ms;-0.1±0.16mV). After returning to the baseline level responses evoked by natural scenes were consistently more positive.
A comparison of the TFRs on the grand-average level (cf. Fig. 3.5 C) showed that all observed power differences were positive, indicating that natural-scene stimuli evoked significantly stronger oscillatory responses than scrambled scenes. Significant differences were restricted to the sustained oscillatory activity during stimulus presentation and excluded the onset and offset response phases. The most pronounced differences in the oscillatory activity were observed in the 15-35Hz band from ca. 500ms to 2.2s post stimulus onset. The difference-band showed a two peaked structure, with an early (720ms) and a later (1901ms) more pronounced peak. Both peaks were accompanied

by additional positive power differences up to 100Hz. These wide-band differences were strongest during the early peak.
The comparison of coherence magnitude for responses to natural and phase-scrambled stimuli revealed weak differences which were reminiscent of the power differences. Again coherence changes were only observed in frequency ranges in which power changes had been identified, and again coherence at higher frequencies changed more strongly than at lower frequencies. The increased power in the sustained oscillations as well as the two wide-band surges were associated with weakly increased coherence.

3.2.3. Topographic representations of scene-evoked responses

Figure 3.6 illustrates that both the wide-band potential (0.1-300Hz; blue trace in Fig. 3.6 A) and Hilbert envelope (15-35Hz; red trace in Fig. 3.6 A) showed extensive peak regions under the recording grid. The spatial distribution of wide-band potential (B) and Hilbert envelope (C) are shown for the peak time-points (dashed lines in A). The spatial location of both peaks was identical. The strongest difference to baseline occurred under the same recording electrode. However, both peaks were temporally offset, with the potential peak occurring 36ms earlier than the oscillatory peak.

The spatial representations of the peaks in the wide-band potential (left column) and Hilbert envelope (right column) for all animals individually are displayed in Fig. 3.7. For all animals, clear circumscribed peak regions were observed in both metrics. Because of differences in the exact peak locations under the recording grid (cf. Fig. 3.3), pooling data across animals was not possible and analysis results are thus shown for single individuals only. However, the general response characteristics and difference patterns were similar across animals.
Temporally, the peaks in both metrics were offset. The wide-band potential peak was observed on average 183.2±22.0ms post-stimulus onset and the oscillatory peak occurred on average 279.8±88.5ms post stimulus onset.
Based on the strongest quartile of response values, the average extent of the activated area was 2.8±0.2mm (osci. activity: 2.7±0.2mm) in the rostrocaudal axis and 2.0±0.3mm (osci. activity: 2.0±0.3mm) in the lateromedial axis.
Most of the multi-channel analyses will be focused on the oscillatory activity between 15 and 35Hz, because this metric showed strong and reliable difference-patterns at the single-channel level during stimulus presentation.

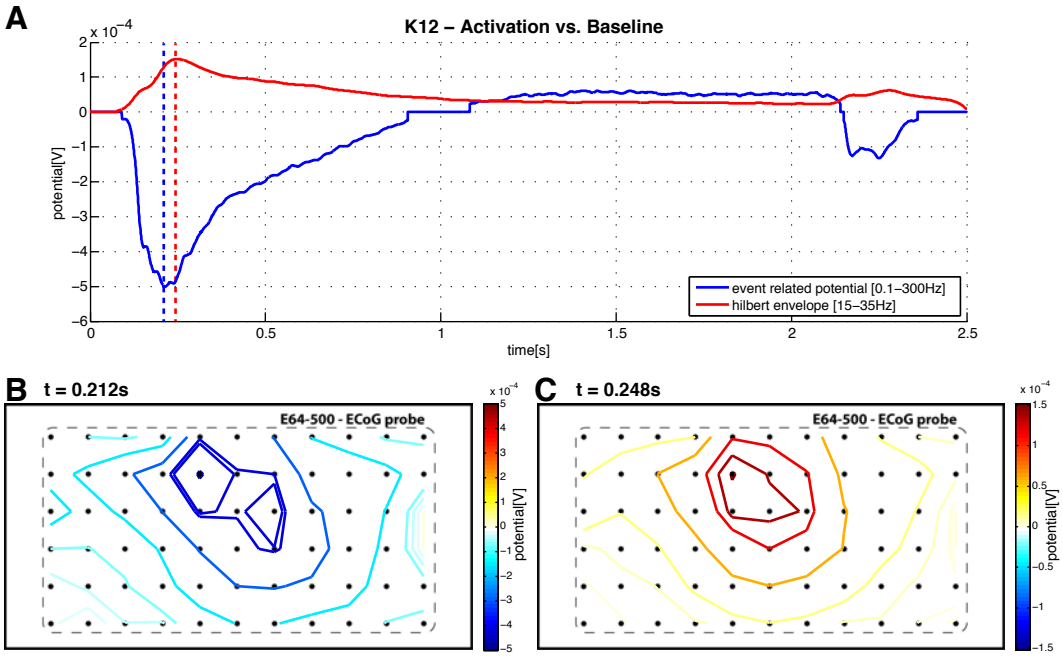

Figure 3.6.: Top: Overlay of the activation-baseline difference for wide-band (0.1-300Hz) evoked activity (blue) and the narrow-band (15-35Hz) Hilbert envelope (red). The time points of maximal difference for both metrics are displayed as dashed lines in the corresponding colors. **Bottom left:** Color-coded, interpolated, spatial representation of the avg. potential difference at the time point of the peak difference. **Bottom right:** Color-coded, interpolated, spatial representation of the avg. difference in the Hilbert envelope at the time point of the peak difference. Distance between two recording sites (black dots) is 500µm.

Topographies of responses to stimulus super-categories

Figures 3.8, 3.9 and 3.10, represent expanded versions of Fig. 3.6 and display more than a single spatially interpolated time-slice of activity. While the top traces show the average difference between the compared conditions on the strongest individual channel, the panels below show spatial representations of the corresponding metrics (wide-band field potential, 15-35Hz Hilbert envelope). Vertical dashed lines in the single-channel traces indicate the time points at which spatial representations are plotted. The time-points were selected so that the strongest difference periods were captured.

(a) Activation vs. baseline| The activation vs. baseline comparison at the multi-channel level revealed a set of three difference clusters in the wide-band potential (Fig. 3.8 A). The first and strongest cluster accompanied stimulus onset and reached a negative peak 212ms post stimulus onset. It slowly relaxed back to baseline and was followed by a brief period of no significant differences. Around 1.1s the second cluster, consisting of weak positive differences, set in and extended until 150ms post stimulus

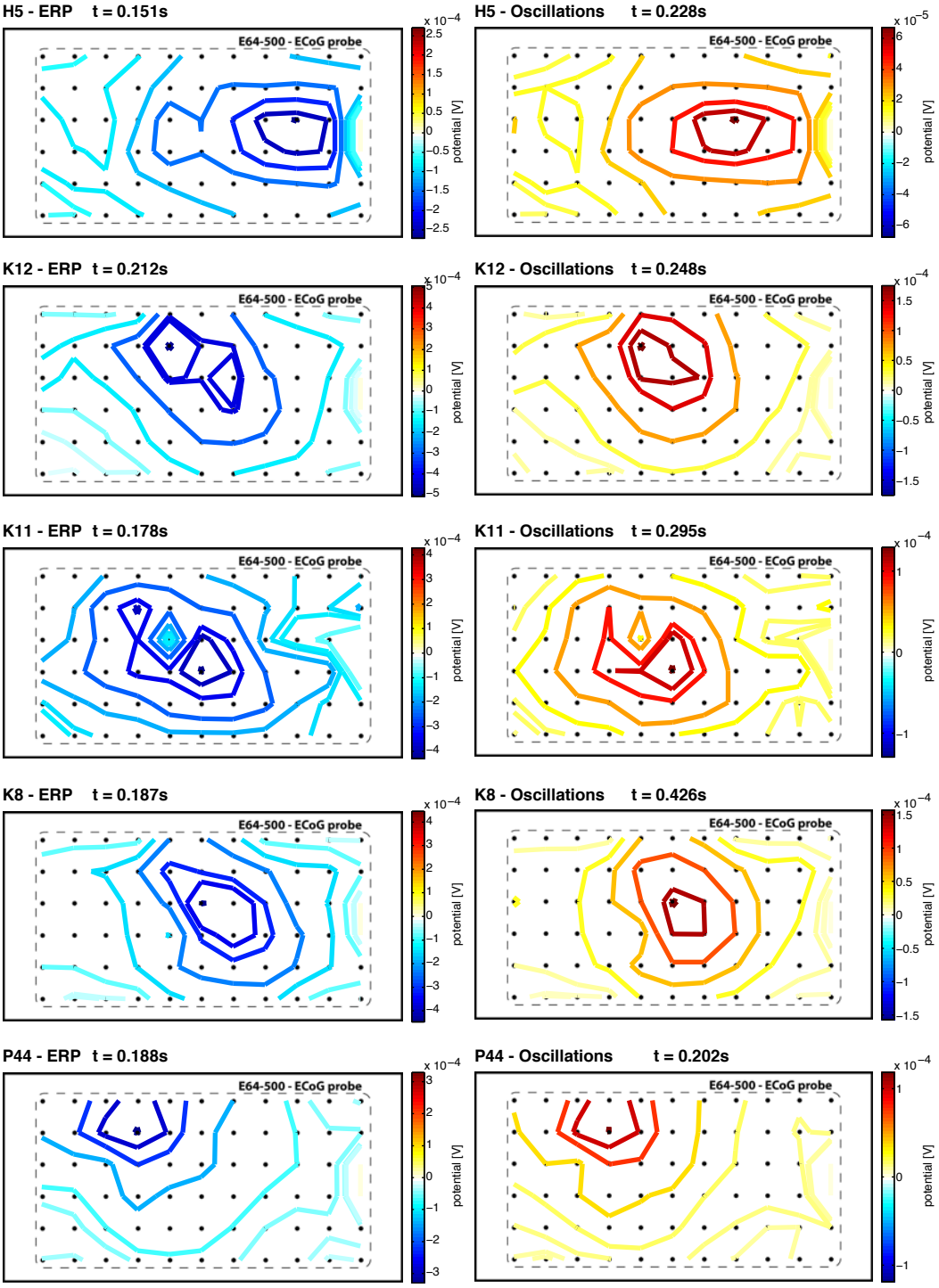

Figure 3.7.: Comparison of transient and oscillatory peaks across experimental animals (rows). **Left|** Topographies of the transient peaks in the avg. event-related potentials (0.1Hz-300Hz) for each experimental animal. **Right|** Topographies of the peaks in the avg. stimulus evoked oscillations (15Hz-35Hz) for each experimental animal. Distance between two recording sites (black dots) is 500µm.

offset. It was directly followed by the third difference cluster, which was 200ms wide and peaked 250ms post stimulus offset.
The comparison of the narrow-band Hilbert envelopes revealed an extensive cluster of positive difference-peaks that spanned almost the entire analysis window (Fig. 3.8 B). It exhibited two peaks associated with the stimulus onset (248ms post stimulus onset) and offset (282ms post stimulus offset) which were connected by sustained positive differences throughout stimulus presentation.
The spatial representations in Fig. 3.8 (A+B) show that the activity patterns of both metrics co-aligned and remained local within a radius of 500µm. This was clearer for the spatial pattern of oscillatory activity. The peaks in the average wide-band potential were more variable. In addition to the co-localization of peaks, the spatial patterns of both metrics showed considerable overlap.

(b) Colored vs. grayscale stimuli| The comparison of responses to colored and grayscale stimuli revealed two clusters of positive differences. The fact that the difference values are positive indicates that the oscillatory activity evoked by colored stimuli was significantly stronger than the activity evoked by grayscale stimuli. The top trace in Fig. 3.9 shows a significant positive peak 125ms after the stimulus trigger arrives. This peak is followed by a brief phase without significant differences in the evoked oscillatory activity and a subsequent extensive cluster of positive differences beginning 300ms post stimulus onset which did not fall to zero until the end of the analysis window. This second cluster exhibited two peaks (450ms and 2150ms post stimulus onset) of which the first was more pronounced than the second.
The spatial representations of the differences show that they were restricted to the same cortical location that was identified as visually responsive in the activation vs. baseline comparison (cf. Fig. 3.6). The active region corresponded to the main visually responsive area, although the position of the peak in each time-slice shifted slightly ($\sim$500µm). The early difference peak tended to be more anteriolateral than the sustained later cluster.

(c) Natural vs. phase-scrambled stimuli| The comparison of narrow-band activity evoked by natural and phase-scrambled scene stimuli revealed three positive clusters of significant differences. The positive polarity of the differences indicates that natural scenes consistently evoked stronger oscillatory activity than matched phase-scrambled scenes. The single-channel difference-trace in Fig. 3.9 showed a continuous stretch of significant positive differences, beginning 300ms post stimulus onset, that lasted until 250ms post stimulus offset (i.e. 2.25s post stimulus onset). It was followed by two brief

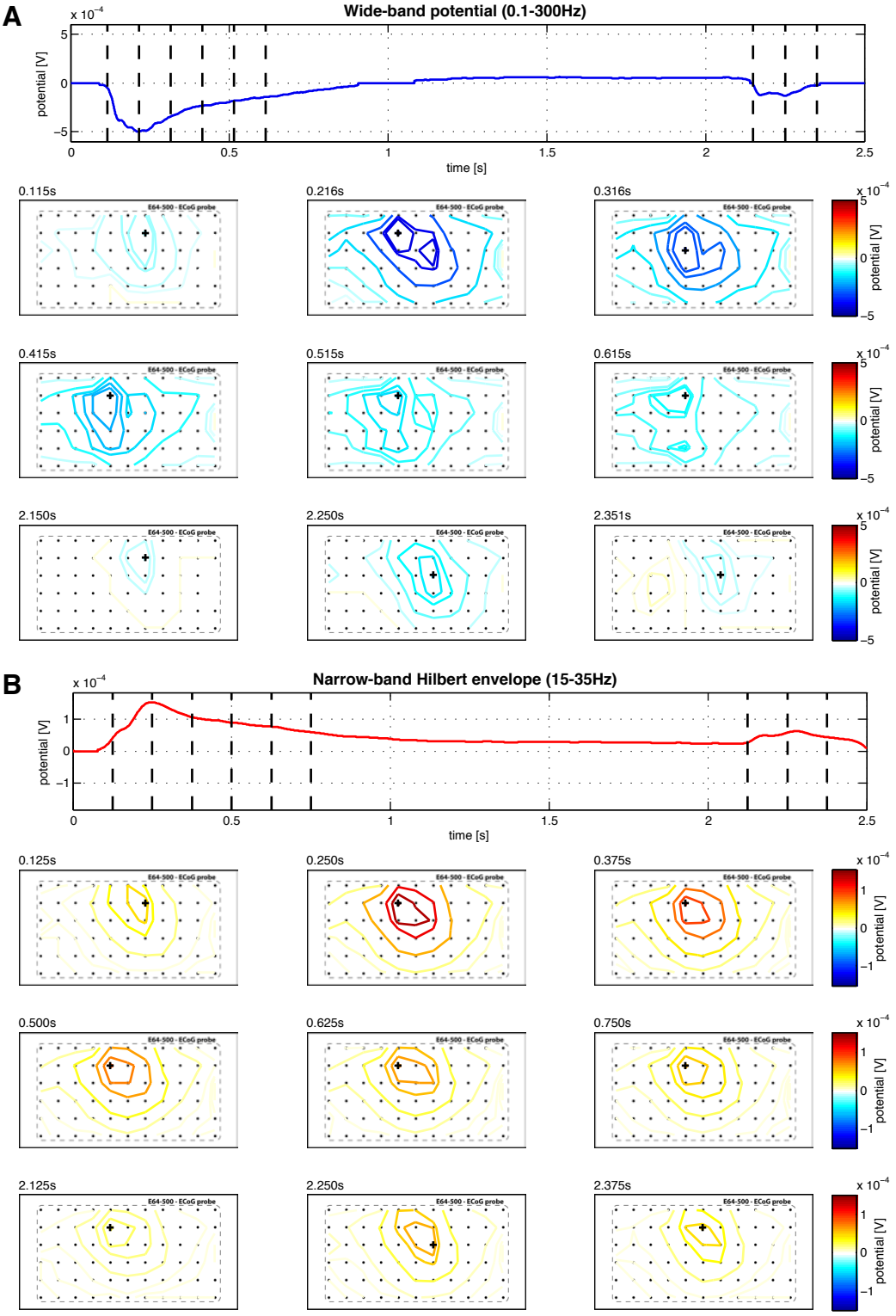

Figure 3.8.: A top| Single-channel representation of significant differences between wide-band (0.1-300Hz) baseline and stimulus-evoked activity. **B top|** Single-channel representation of significant differences between narrow-band (15-35Hz) baseline and stimulus-evoked activity. Vertical dashed lines indicate time-points for which spatial representations are given below. **A+B bottom|** Spatial representations of the differences indicated in the single-channel data. Black plus signs mark the most extreme value at each time-point. Distance between two recording sites (black dots) is 500µm.

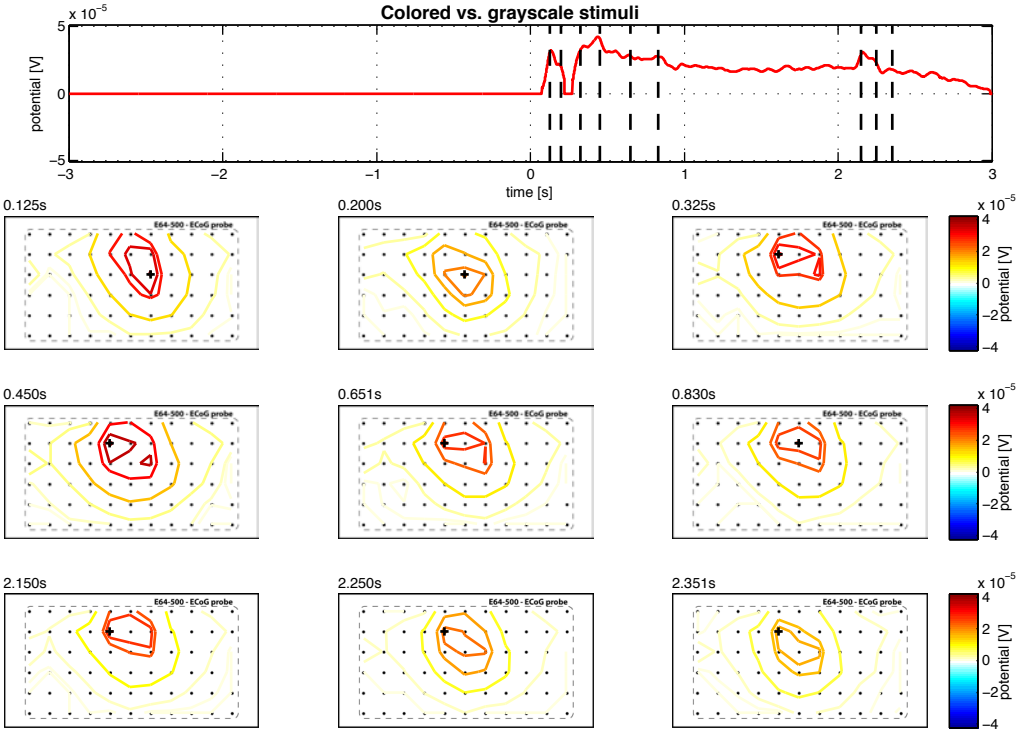

Figure 3.9.: Top| Single-channel representation of significant differences between narrow-band (15-35Hz) activity evoked by colored and grayscale stimuli. Vertical dashed lines indicate time-points for which spatial representations are given below. **Bottom|** Spatial representations of the differences indicated in the single-channel data. Black plus signs mark the most extreme value at each time-point. Distance between two recording sites (black dots) is 500µm.

weaker cluster after stimulus offset. The strongest difference in oscillatory activity was observed 385ms after stimulus onset.

Spatially, the differences were localized to the same cortical region that was shown to be significantly activated by visual stimulation (compare to Fig. 3.6). While the onset of the difference cluster was located more laterally, the differences remained stably in the same location and shifted only minimally (∼500µm) throughout the stimulation period.

3.2.4. Waves and propagation of activity

Figure 3.11 illustrates the results of a spatial coherence analysis over the entire 64-channel ECoG grid and all responses for a single experimental animal.

Panels A and B display the raw coherence magnitude and the activation vs. baseline contrast respectively. Panel A in Fig. 3.11 shows a marked increase in coherence during the stimulus presentation. The coherence plot shows an initial wide-band peak in coherence magnitude, followed by a sustained elevation of coherence between 15Hz and 35Hz. After stimulus offset, another weaker wide-band increase as well as a peak in the 15-35Hz coherence were observed. Onset and offset were associated with additional

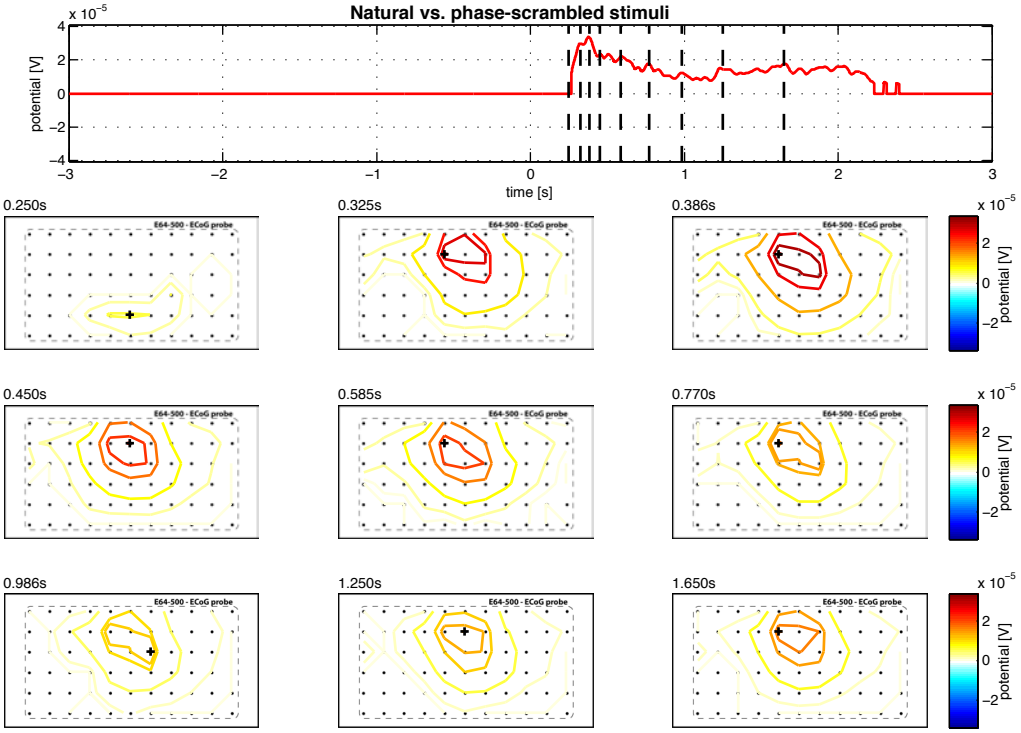

Figure 3.10.: Top| Single-channel representation of significant differences between narrow-band (15-35Hz) activity evoked by natural and scrambled scenes. Vertical dashed lines indicate time-points for which spatial representations are given below. **Bottom|** Spatial representations of the differences indicated in the single-channel data. Black plus signs mark the most extreme value at each time-point. Distance between two recording sites (black dots) is 500µm.

surges in low-frequency coherence (<15Hz). During both the baseline and response period, a clear line-noise related band of high coherence magnitude was observed at 50Hz.

The significance of these observations was confirmed by statistical comparison of the coherence magnitude in activation and baseline periods (see Fig. 3.11 B). Note that the pattern of changes in coherence magnitude largely correspond to the observed stimulus-evoked changes in oscillatory power. Also note that the coherence at 50Hz was slightly decreased during the activation period. The strongest increase in coherence magnitude was observed between 15 and 35Hz with a peak around 500ms after stimulus onset.

Figure 3.11 C shows a spatially interpolated representation of the average coherence magnitude from 0-2s post stimulus and 15-35Hz. It shows a peak region of high coherence magnitude with the reference channel (cf. Fig. 3.3; K8) in its center. The spatial representation of the coherence phase (Fig. 3.11 D) exhibited two extreme regions: A circumscribed caudal region of positive coherence phase values (0.41 radian) and a more rostromedial region of negative coherence phase values (-0.21 radian). Between both

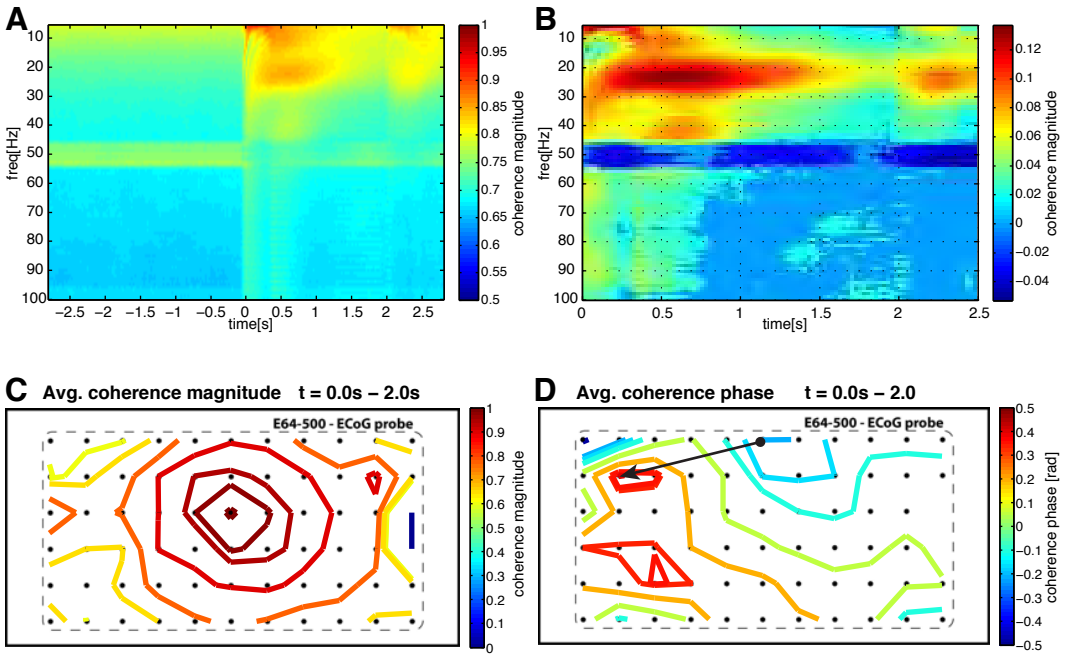

Figure 3.11.: Coherence analysis on the single animal level. Average coherence magnitude **A|** and significant stimulus evoked changes of coherence magnitude **B|** across all stimuli and the entire ECoG grid for animal K8. **C|** Spatial representation of the average coherence magnitude over the stimulation period (0-2s) **D|** Spatial representation of the average coherence phase over the stimulation period (0-2s). Distance between two recording sites (black dots) is 500µm.

extremes a phase gradient along the rostrocaudal axis was observed ($0.52\frac{mm}{ms}$; arrow in Fig. 3.11 D).

Spatial coherence maps for all animals are displayed in figure 3.12. The plots consistently show high coherence magnitude in the previously identified visually responsive areas of dorsal cortex as well as rostro-caudally oriented phase gradients across the area of largest coherence magnitude.

The strongest peak and trough in the phase maps were defined as poles of the phase gradients and the velocity of the corresponding propagating wave was estimated from their distance and difference in phase (black arrows in Fig. 3.12). The average propagation velocity across animals was $0.51\pm0.05\frac{mm}{ms}$. Due to inter-individual differences in the implantation a precise definition of propagation direction was not possible. The exact position of the phase poles differed across animals and the resulting orientation of the phase gradient differed accordingly.

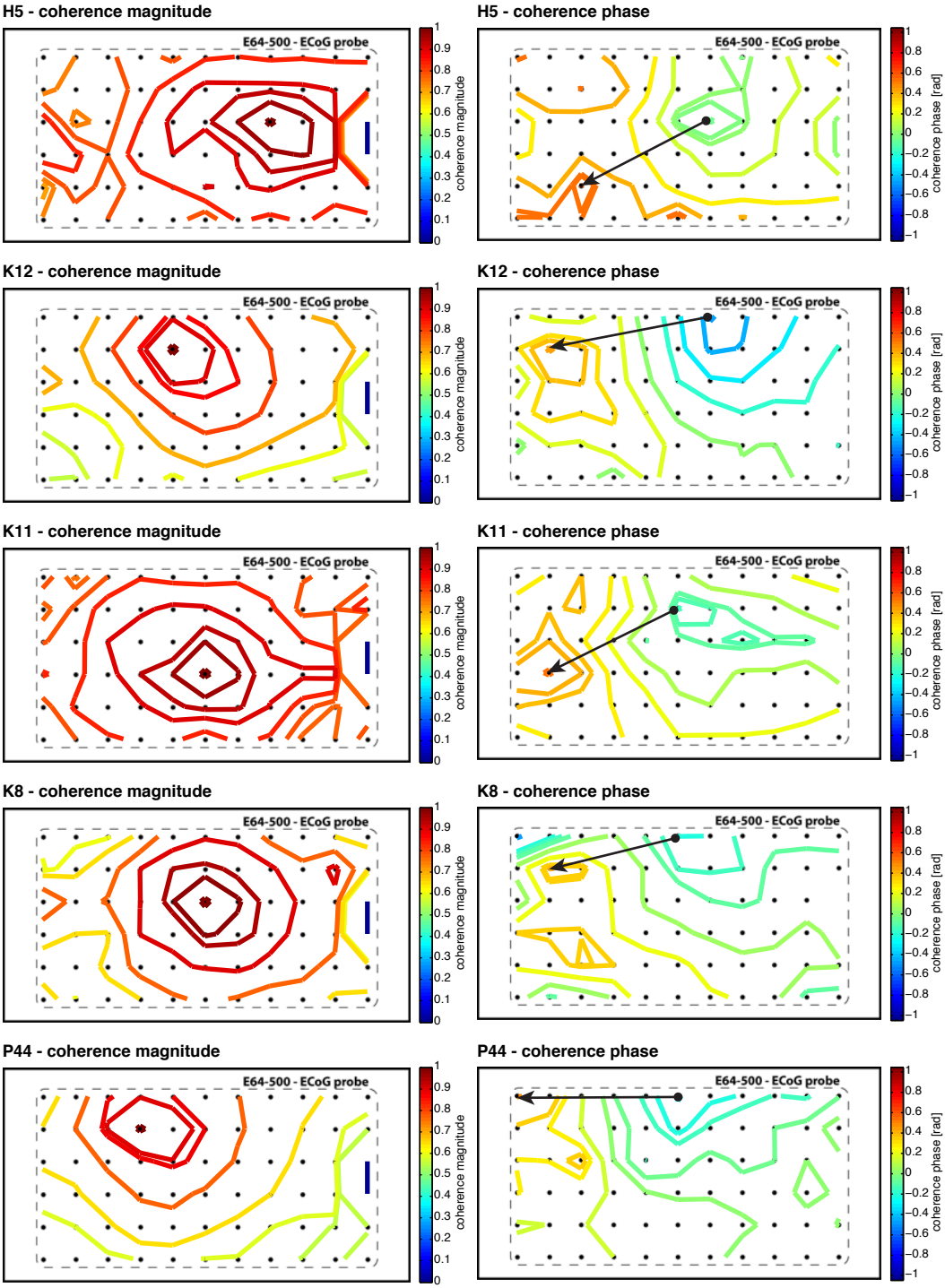

Figure 3.12.: Rows| Comparison of coherence topography for all experimental animals individually. **Left column|** Average coherence magnitude for 2s of activity post-stimulus onset. **Right column|** Average coherence phase for 2s of activity post stimulus onset. Distance between two recording sites (black dots) is 500µm.

3.2.5. Correlations of stimulus features with oscillatory activity

Comparison of average power evoked by stimulus super-categories

Figure 3.13 displays the results of a multiple comparison corrected two-factor ANOVA comparing the average evoked oscillatory response power to eight stimulus super-categories (natural-colored, scrambled-colored, white-noise-colored, red flash, natural-grayscale, scrambled-grayscale, white-noise-grayscale, gray flash).
The two-factor analysis showed that the first factor (animal ID) had no significant effect on the average response power ($F=0.06$; $p=0.994$). The second factor (stimulus super-category) had a significant effect on the response strength ($F=878.17$; $p<0.001$). In general, colored stimuli evoked stronger oscillations than grayscale stimuli. Tukey-Kramer multiple comparison correction showed that within both the color and grayscale partitions the natural scenes evoked significantly stronger oscillations than their matched phase-scrambled counterparts. These on the other hand evoked significantly stronger oscillations than simple white noise stimuli in color and grayscale. While uniform gray 'mock' stimuli consistently evoked no oscillations, the red flash stimuli evoked stronger oscillations than all other super-categories.

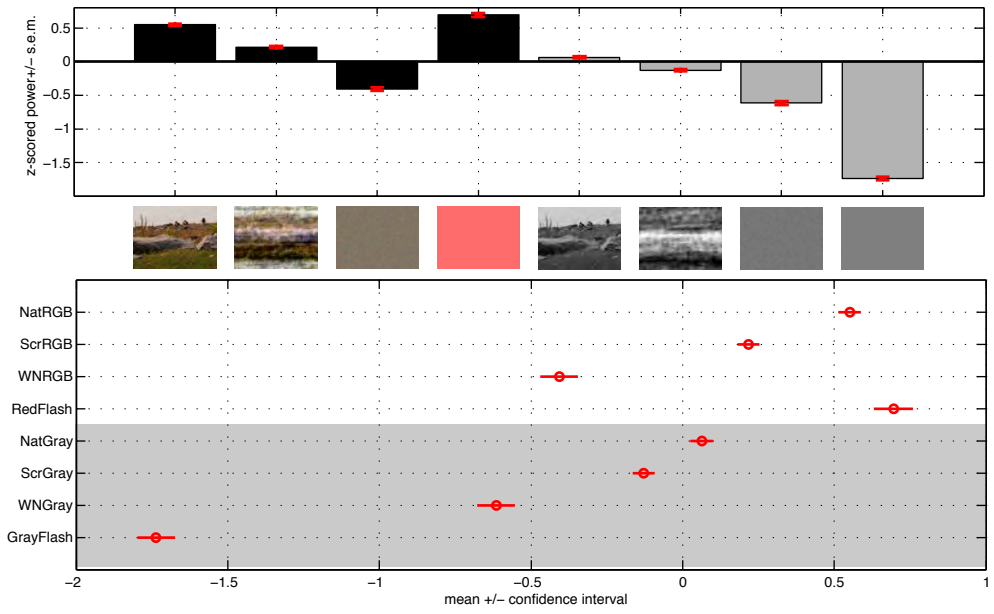

Figure 3.13.: Results of a multiple comparison corrected ANOVA. Comparison of avg. response power evoked by stimulus super-categories. Data were z-scored prior to analysis and bar plots represent means and standard errors of the mean. Non-overlapping whiskers in the multiple comparison plots indicate significant ($p<0.05$) differences between means.

Comparison of average power evoked by the original stimulus categories

Figure 3.14 displays the results of a second multiple comparison corrected ANOVA comparing the average response power to the 16 original stimulus categories (cf. Material & Methods 2.4). The ANOVA results confirmed that the animal ID had no significant influence on the mean response power (F=0.07; p=0.992), but that the stimulation condition did (F=420.96; p<0.001).
Overall, the colored scenes evoked stronger oscillatory response power than their grayscale counterparts. White noise stimuli in color and grayscale evoked similarly strong responses and were less effective in driving dorsal cortex than either natural or phase-scrambled scenes. Both natural and scrambled scenes in grayscale evoked less oscillations than colored scrambles. Only the responses to man-made scenes in grayscale reached power levels comparable to those of colored phase-scrambles. Except for the colored landscape images, all natural-image categories evoked significantly stronger oscillatory power than their phase-scrambled counterparts. The strongest average power was observed for colored animal scenes, manmade scenes, and the red localizer stimulus. The response power to these three categories did not differ significantly.

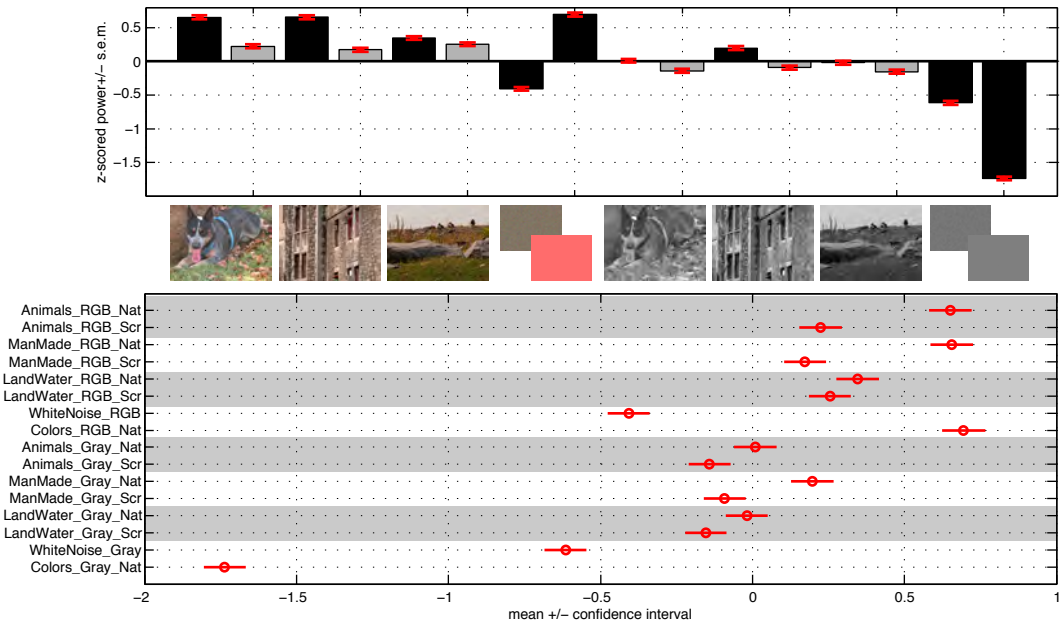

Figure 3.14.: Results of a multiple comparison corrected ANOVA. Comparison of avg. response power evoked by stimulus categories. Data were z-scored prior to analysis and bar plots represent means and standard errors of the mean. Non-overlapping whiskers in the multiple comparison plots indicate significant (p<0.05) differences between means.

Comparison of average power evoked by individual stimuli

Figure 3.15 displays the results of partitioning static-scene stimuli according to the average oscillatory power (15-35Hz) they evoked and reveals a set of consistently effective stimuli. Panel A displays the distribution of all 13099 recorded response power values after z-scoring to account for inter-individual differences. This distribution was split into three equally sized quantiles and responses were sorted according to the categories (panel B) and single stimuli (panel C) which had evoked them.

The histograms in panel B show that most of the stimuli evoking weak oscillatory responses (first quantile) belonged to grayscale stimulus categories (categories 9 to 16) and the colored white noise category (category 7). The second quantile contained similar proportions of stimuli from all categories. Only the mock stimuli in category 16 were underrepresented. The third quantile contained responses which were mainly evoked by colored stimulus categories (1 to 8) and only low numbers of responses evoked by colored and grayscale white noise or 'mock' stimuli.

A more detailed breakdown of the composition of the quantiles is presented in fig-

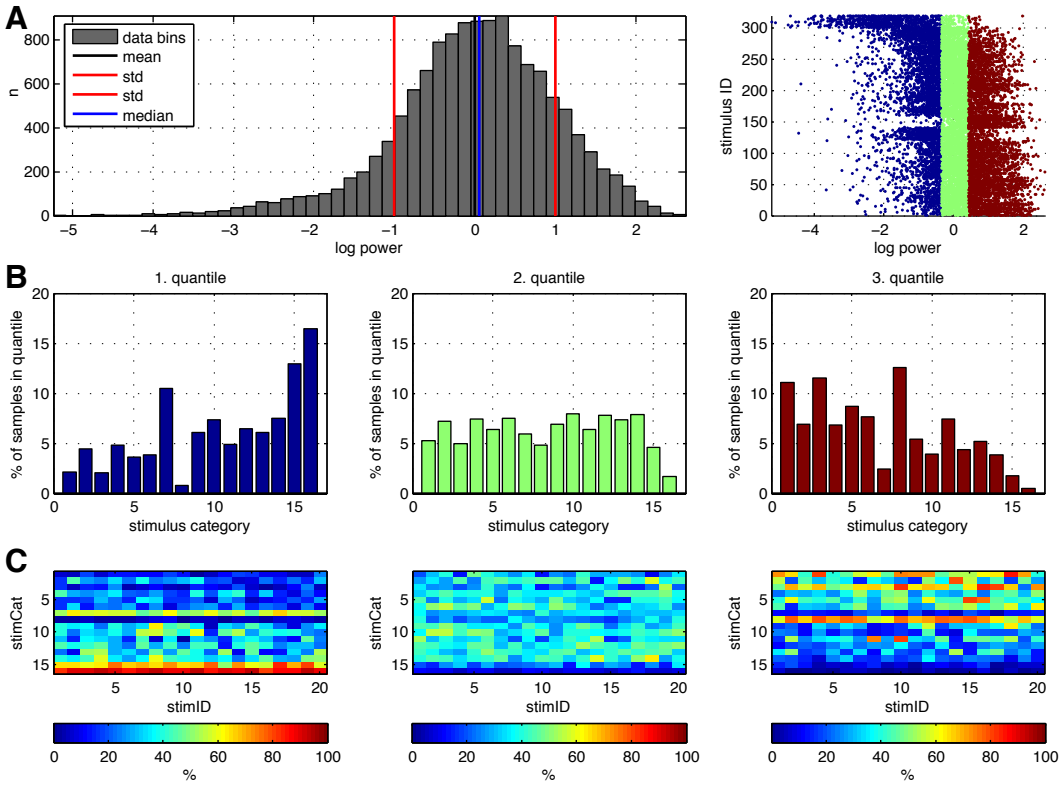

Figure 3.15.: A| Distribution of mean-normalized scene-evoked power values pooled over all experimental animals. Composition of the response data quantiles with respect to the original stimulus categories **B|** and with respect to individual stimuli **C|**.

ure 3.15 C. Each field in the presented color matrices corresponds to a particular stimulus in the stimulus set. Rows in the matrices correspond to stimulus categories and columns to individual stimuli within a given category. The color of each field represents the percentage of responses to this stimulus which were sorted into that particular quantile. The color patterns are obviously not random and support all previous observations providing additional information on particularly effective and ineffective stimuli.

Figure 3.16 displays a compilation of natural-scene stimuli which consistently evoked strong cortical oscillations. More than 66% of the responses evoked by the 20 displayed stimuli were sorted into the third quantile. Seven of the identified stimuli belonged to the colored animal-scenes, one to the colored scrambled animal-scenes, eight to the colored man-made-scenes, two to the colored landscape-scenes, and two to the grayscale man-made-scenes. Note that the uniform red flash stimuli are not displayed although they consistently evoked strong cortical activity. The identified effective stimuli do not share any obvious structural properties or show similarities of content which could be described or quantified in a straight-forward way.

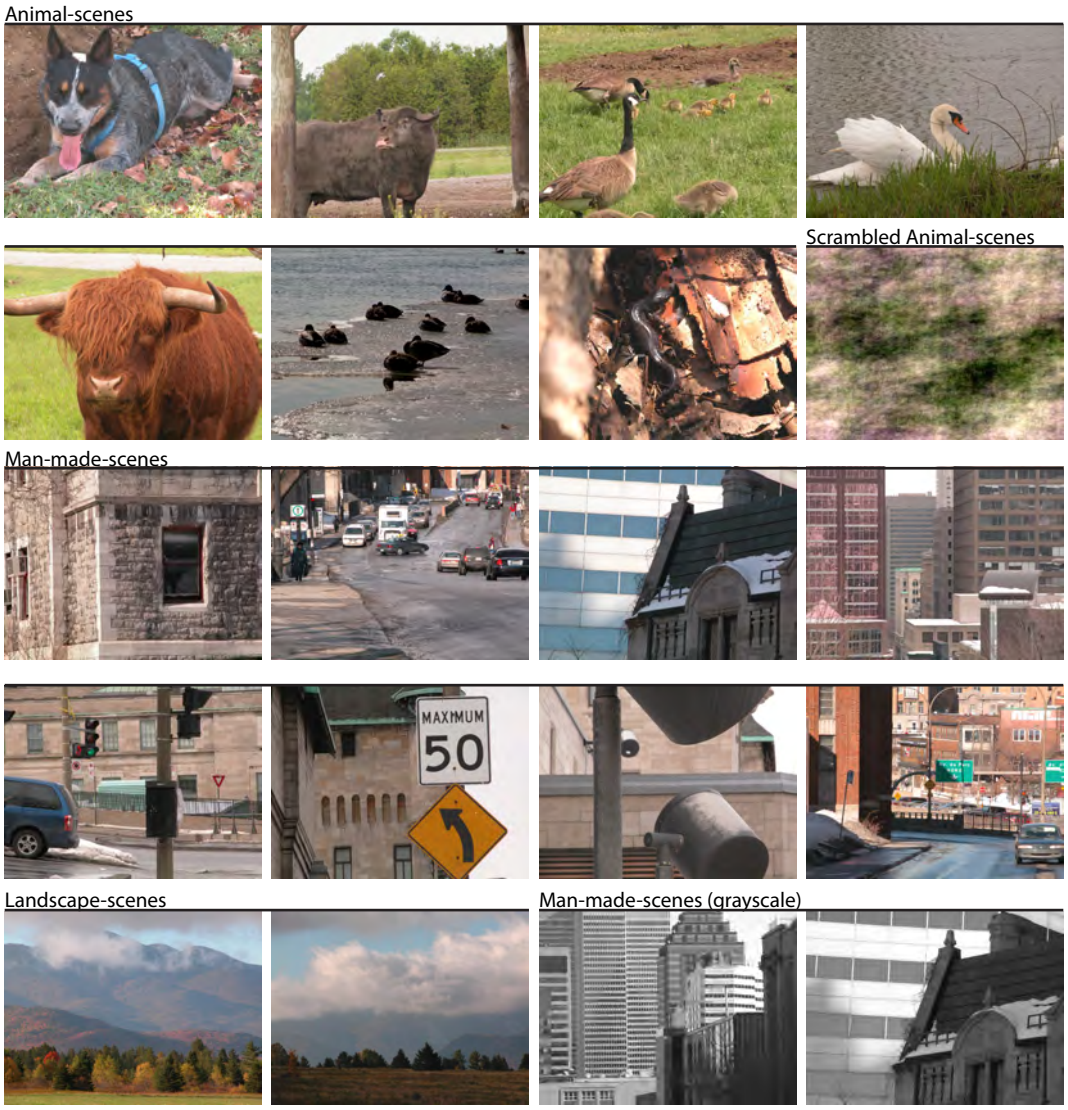

Figure 3.16.: A compilation of the natural-scene stimuli consistently evoking strong oscillations in turtle dorsal cortex. For each displayed stimulus more than 66% of the responses it evoked were sorted into the first quantile. The uniform red flash stimuli are not displayed.

A multilinear model to predict response power from stimulus features

Figure 3.17 displays the results of a multilinear regression analysis relating the response strength in the 15-35Hz range to a set of global stimulus features (see Tab. 2.1 and corresponding text). The intercept component for each time bin is displayed in Fig. 3.17 A and represents a stimulus-content independent component of the oscillatory response. A color-coded representation of the model's weight matrix is displayed in Fig. 3.17 B. It shows that for each time bin only a fraction of the stimulus features had a significant influence on the response. Prominent contributions were estimated for the color ID of

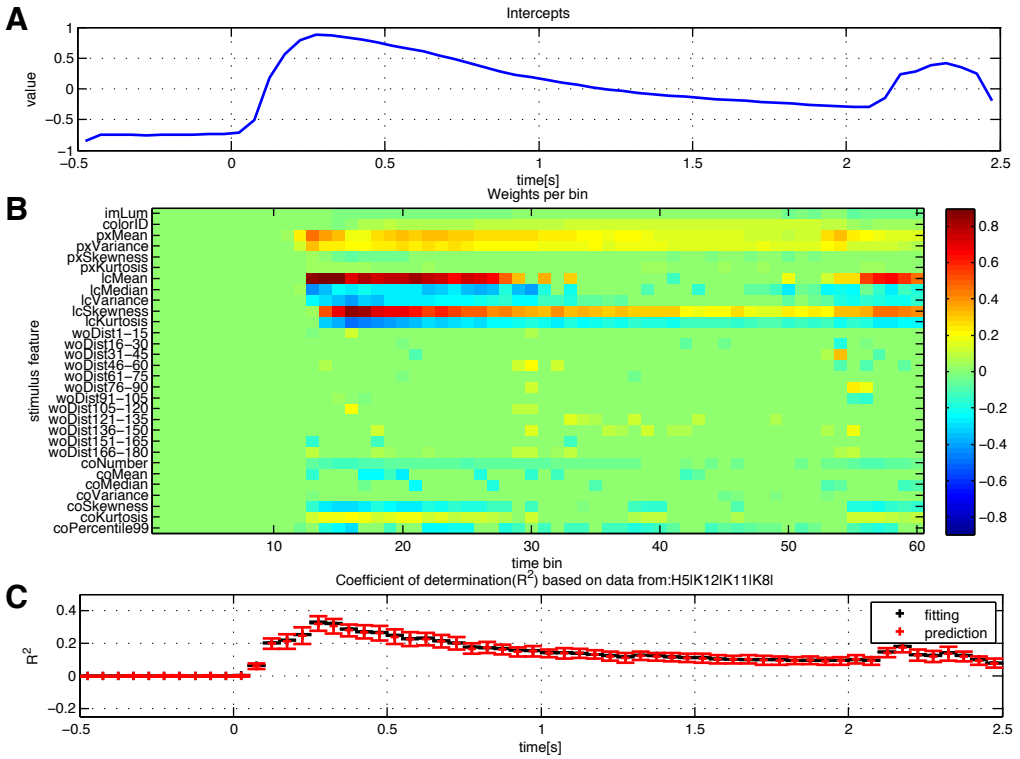

Figure 3.17.: Multilinear regression analysis of correlations between stimulus features and response strength. **A|** Stimulus-independent intercepts of the multilinear regression model. **B|** Color-coded weight matrix of the multilinear regression model. **C|** Fitting and prediction performance of the model.

a stimulus, the mean and variance of its intensity histogram, all four moments plus the median of the local contrast distribution and to a lesser extent the moments of the size distribution of contour objects.

After determining the significant stimulus features and their individual weights, the performance of fitting and prediction was assessed. Fig. 3.17 C shows the fractions of explained response variance for each time bin using the weights determined by the model. It was impossible to predict any of the recorded activity prior to stimulus onset. After the stimulus onset the R^2 values for both fitting and prediction increased and reached a peak of 32.72% and 32.0% respectively with a latency of 300ms. Subsequently, fitting and prediction performance decreased but remained larger than 10%. After the stimulus offset, both R^2 values show a second weaker peak (18.18% and 17.44% respectively). During the peak in prediction performance 17 stimulus features were determined to be significant. These were related to the feature complexes: (a) image luminance, (b) color, (c) intensity distribution, (d) local contrast distribution, (e) orientation of local contrast elements, and (f) size of coherent contour objects. Based on the most extreme quartile limits (1st and 3rd) of the weight distribution, the strongest weights were assigned to

the variance of pixel intensity histogram, the mean, variance, skewness and kurtosis of the local contrast distribution, local contrasts between 105 and 120 degrees, and the skewness and 99th percentile of the distribution of coherent contour elements.

3.3. Natural-video-evoked responses

Summary| *Natural-video stimulation evoked strong, reliable responses in the ECoG recordings from awake turtles. Video-evoked responses exhibited strong stimulus onset- and offset-related transients as well as sustained oscillations in the 15-35Hz band. Oscillatory power was significantly increased throughout the 10 second video presentation. Natural-video stimuli evoked significantly stronger oscillations (up to 45Hz) in dorsal cortex than spatially or temporally perturbed control stimuli.*
Video-associated activity co-localized with flash and natural-scene-evoked responses and showed similar coherence patterns with a rostrocaudally oriented phase gradient.

3.3.1. Basic characteristics of natural-video-evoked responses at the single-channel level

Video-stimulus-evoked responses were clearly visible at the single-trial level (wide-band potential, 0.1-300Hz; power spectrum and time-frequency-power representation) without prior ensemble-averaging (typical data in Fig. 3.18 A). The single trial data clearly show low frequency transient response components superimposed with sustained oscillatory activity in the 20Hz range during the initial flash phase and the subsequent video-playback phase.

Figure 3.18 B displays the average evoked potential (0.1-300Hz), spectra (activation and baseline) and time-frequency representation for experimental animal K8. The plots emphasize the stereotypical response components captured by the different metrics.
The average evoked potential showed a sequence of negative transients, which closely correlated with the temporal structure of the stimulation, but no oscillations. An initial strong transient with a long time-constant accompanied the static display of the first video frame and was followed by a second, less pronounced transient at the onset of the video playback (2s). After the video offset, a third weak negative transient is visible in the average evoked potential.
The average power spectrum calculated over the video playback period (2-12s) showed that the transients were accompanied by a wide-band, upward shift of approximately 0.5 order of magnitude compared to the baseline spectrum, as well as a pronounced shoulder

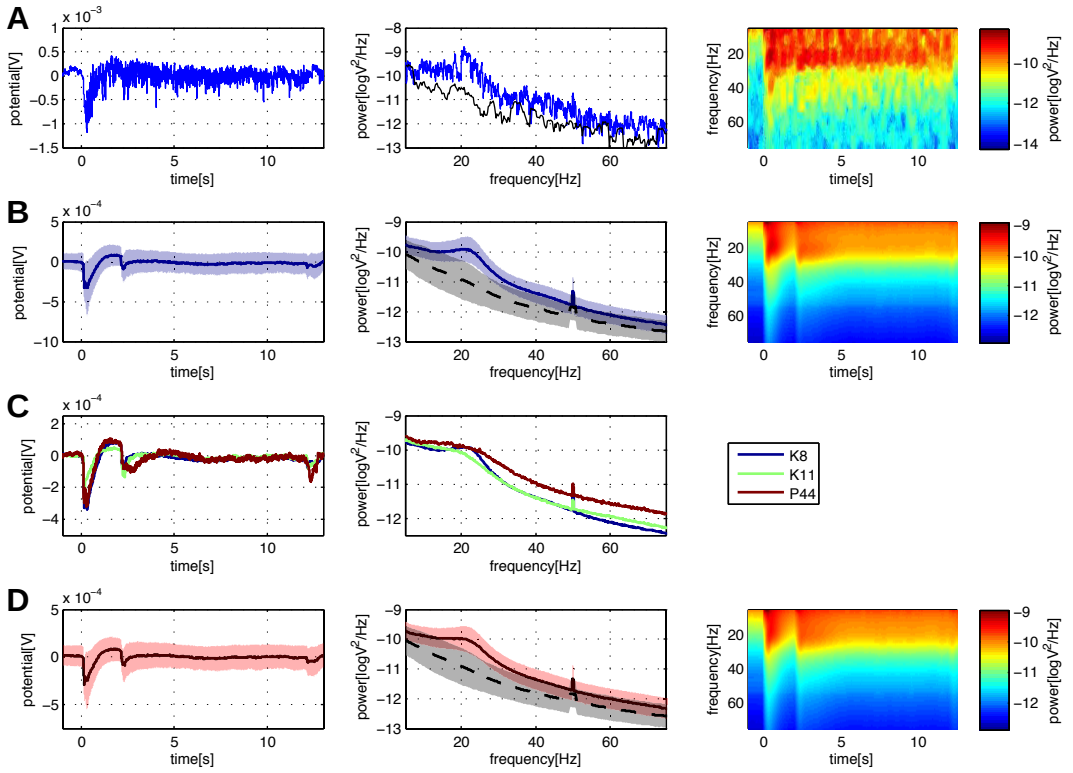

Figure 3.18.: Overview of visually evoked responses at the single channel level. Line plots display average and standard deviation as shaded area. **A|** Example evoked response, response spectrum (blue), baseline spectrum (black) and TFR. **B|** Average evoked response, spectra (as above) and TFR for one experimental animal.**C|** Color-coded overlay of average responses and average response spectra for all 3 animals. **D|** Grand-average evoked response, spectra and TFR over all 3 animals.

centered around 20Hz reflecting stimulus-evoked oscillatory activity. Both baseline and response spectra exhibited line-noise peaks at precisely 50Hz.
Transient as well as oscillatory response components are also reflected in the average TFR which shows clear wide-band surges corresponding to the former and a strong band of sustained oscillations in the 15-35Hz range corresponding to the latter. The band-width and power of oscillatory activity evoked by the static first frame and video playback decreased over the duration of the presentation. However, this decrease was less pronounced for the sustained video-evoked oscillations.

Figure 3.18 C displays average video-evoked potentials (0.1-300Hz) and spectra for all three animals (color coded). The average evoked potentials and spectra show a high degree of similarity with certain inter-individual variations. Amplitudes and timing of the three transients in the average evoked potentials showed minor differences across animals. All three power spectra contained wide shoulders around 20Hz with slight inter-individual variations in the exact position of the peaks in addition to sharp line noise peaks at

precisely 50Hz. The average response spectrum for animal P44 showed a shallower slope than the other two spectra.

Due to the high degree of similarity, the single-channel responses to video stimulation across all three animals were pooled in most of the subsequent single-channel analyses. The resulting grand-average plots are presented in Fig. 3.18 D and reflect the same response characteristics described on the individual level. The grand-average potential showed emphasized time-locked transients while the spectral averages consistently showed sustained oscillations during the video stimulation phase.
The grand-average onset transient peaked 166ms post stimulus onset and reached -0.29±0.22mV, the playback onset transient occurred 2.267s post stimulus onset and reached an amplitude of -0.09±0.17mV, and the offset transient occurred 12.187s post stimulus trigger and reached an amplitude of -0.06±0.15mV. The grand-average Hilbert envelope from 15-35Hz also exhibited three peaks. The onset peak occurred 330ms post stimulus onset and reached an amplitude of 0.13±0.09mV, the playback onset peak occurred 2.359s post stimulus onset with an amplitude of 0.09±0.06mV, and the offset peak reached an amplitude of 0.06±0.05mV 12.135s after the stimulus offset.
From the grand-average response spectrum a peak oscillatory frequency of 20.02Hz was determined. The peak in the linearly scaled power spectrum reached an average power of $0.37 \pm 0.48 * 10^{-9} \frac{V^2}{Hz}$.

3.3.2. Comparison of responses to stimulus super-categories at the single channel level

Responses to stimulus super-categories on the grand-average level

(a) Activation vs. baseline| The activation vs. baseline comparison of the grand-average evoked wide-band potentials (0.1-300Hz) showed extensive differences (Fig. 3.19 A) and confirmed the significance of the three described negative transients (flash onset: 166ms;-0.29±0.22mV / playback onset: 2.267s;-0.09±0.17mV / stimulus offset: 12.187s;-0.06±0.15mV). It also revealed that the potentials differed significantly between the flash onset and playback onset, from 3s to 8s after the playback onset, and several hundred milliseconds before the offset transient.
The difference-TFRs showed consistently positive power differences, indicating that the power in the analyzed frequency bands was consistently larger during the stimulation period than during the baseline. The onset of the static stimulus phase was accompanied by a surge in power below 15Hz (∼225ms), a strong peak in the 15-35Hz

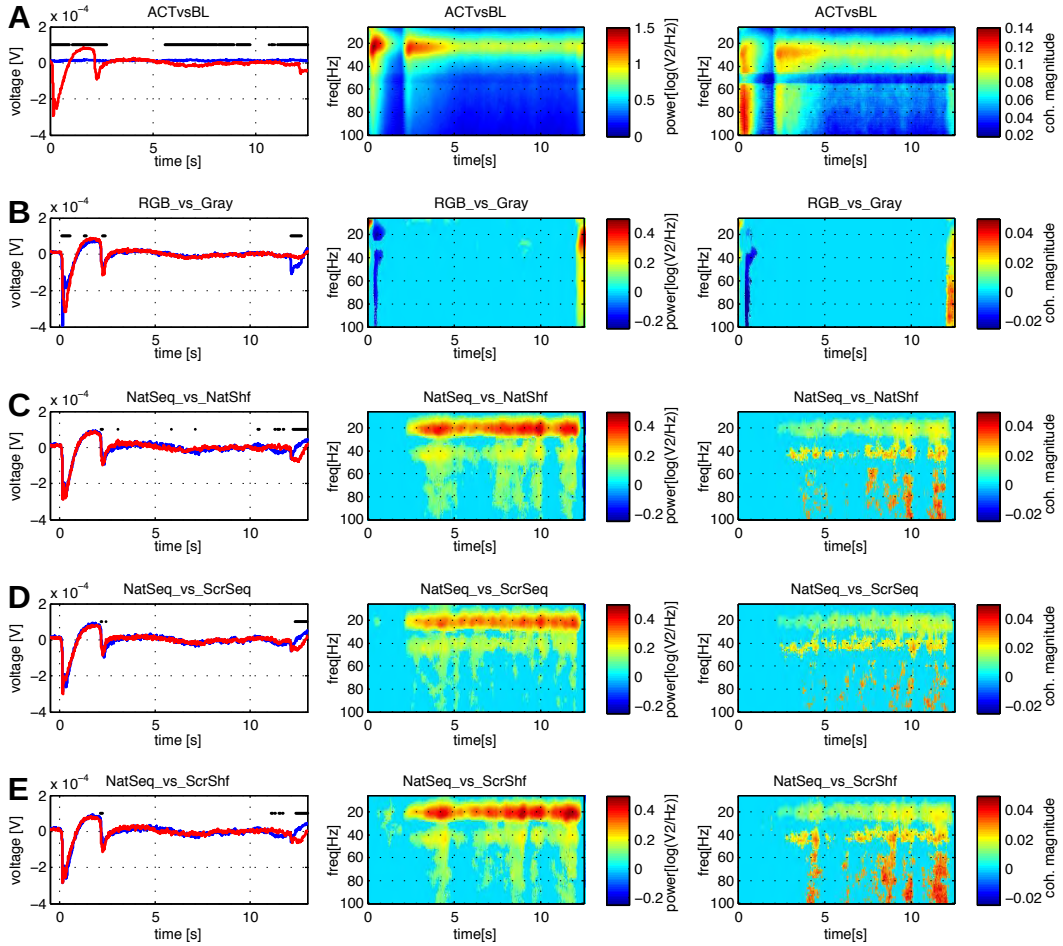

Figure 3.19.: Avg. evoked potentials for the compared stimulus conditions (left). Black marks over the curves indicate significant differences. Avg. difference-TFRs between stimulus conditions (middle). Avg. change in coherence magnitude on the channels surrounding the strongest channel (right). Only significant differences in power and coherence are displayed. **A:** Baseline (blue) vs. response (red); **B:** RGB stimuli (blue) vs. grayscale stimuli (red); **C:** Natural-sequential stimuli (blue) vs. natural-shuffled stimuli (red). **D:** Natural-sequential stimuli (blue) vs. scrambled-sequential stimuli (red). **E:** Natural-sequential stimuli (blue) vs. scrambled-shuffled stimuli (red).

range (∼400ms), and a strong wide-band response component. The onset of the video playback was associated with a second surge of oscillatory power in the 15-35Hz range (∼2.425s) accompanied by a wide-band power increase and followed by sustained 15-35Hz oscillations (see Fig. 3.19 A). During both the static and the playback phase the oscillatory power showed an initial wide-band surge and subsequent decreases in magnitude and band-width. However, the oscillatory power between 15 and 35Hz remained significantly elevated throughout the entire 10s video stimulation period and beyond. Following stimulus offset, another weak 15-35Hz peak (∼12.2s) accompanied by a wide-band surge was observed.

The difference-pattern of coherence magnitude between activation and baseline periods

somewhat resembled the difference-TFR. Changes in power were always associated with changes in the coherence magnitude. However, the changes in coherence for the wide-band transients were stronger than for the sustained oscillatory components and coherence changes were generally stronger at higher frequencies.

(b) Colored videos vs. grayscale videos| The comparison of wide-band potentials (0.1-300Hz) in response to colored and grayscale videos showed significant differences in the onset and offset transients. Both transients were stronger and earlier in response to colored video stimuli (onset: 164ms;-0.4±0.21mV / offset: 12.181s;-0.1±0.15mV) compared to the responses to grayscale videos (onset: 280ms;-0.32±0.28mV / offset: 12.522s;-0.27±0.14mV). The intermediate playback onset transient was stronger and later for the grayscale stimuli (color: 2.266ms;-0.07±0.17mV / grayscale: 2.344ms;-0.10±0.19mV). In addition, the positivity after the onset transient and the video-onset transient were weaker in response to colored videos.
The difference-TFR showed a quick succession of an early positive and a negative wide-band difference during the onset of the static first video frame as well as a positive wide-band difference after the stimulus offset. During the playback phase no significant differences were observed, indicating that colored and grayscale videos evoked 15-35Hz oscillations of equal power.
The differences in coherence magnitude resembled the difference-TFR. All power changes were associated with coherence changes of the same polarity. At high frequencies the observed coherence changes were stronger than at low frequencies.

(c_1 - c_3) Natural videos vs. control videos| The lower three panels Fig. 3.19 (C-E) display the results of the comparisons of responses to natural-sequential videos to natural-shuffled (C), scrambled-sequential (D) and scrambled-shuffled (E) videos.
Comparing the wide-band potentials (0.-300Hz) in response to natural-sequential and control video stimuli showed brief clusters of significant differences in the transients associated with the onset of video playback, the playback phase and the offset response. All transients in response to natural-sequential videos (flash onset: 167ms;-0.289±0.216mV / playback onset: 2.346s;-0.094±0.200mV / offset: 12.147s;-0.062±0.153mV) were minimally weaker than in responses averaged over all control videos (onset: 166ms;-0.295±0.218mV / playback onset: 2.266s;-0.097±0.168mV / offset: 12.473s;-0.066±0.157mV).
The difference-TFRs for the individual comparisons showed that responses between the natural and control categories differed in similar ways. During the initial flash phase

(0s-2s), the difference-TFRs show brief, weak positive differences. Flash responses to natural-shuffled videos did not differ from responses to natural-sequential videos. The difference-TFRs for the comparisons to scrambled-sequential and scrambled-shuffled videos revealed brief, weak positive difference clusters during the flash phase. All three difference-TFRs show a pronounced band of significant positive power differences between 15 and 35Hz during the entire video playback phase (2s to 12s). This band was accompanied by a weaker band of positive differences ranging from 35 to 45Hz as well as additional positive differences at higher frequencies >50Hz. The magnitude of the observed differences for the different comparisons was similar (cf. avg. power in Fig. 3.27).

In all cases, the positive differences indicate that natural-sequential video clips evoked significantly stronger oscillatory power in the described frequency ranges. In addition, all comparisons revealed negative differences after the stimulus offset at 12s.
Changes in oscillatory power at particular frequencies were associated with changes in coherence magnitude and both the 15-35Hz band and the 35-45Hz band are visible in the difference plots. Again, coherence changes at high frequencies were generally stronger than at low frequencies.

3.3.3. Topographic representations of video-evoked responses

Figure 3.20 displays spatial representations of the peaks in the wide-band evoked potential (0.1-300Hz) and in the oscillatory activity (15-35Hz) evoked by the onset of video playback for all animals individually. In all three animals, the transient and sustained components of the response were restricted to the same circumscribed regions of dorsal cortex. Note that the two-peaked structures for animal K11 were caused by a broken recording channel in the center of the ECoG array. While the location of the peaks for both metrics was consistent within one experimental animal, the peak locations differed across animals. Because of these inter-individual differences it was not possible to pool data across animals and analysis results are thus only shown for single individuals. However, the general response characteristics and difference patterns were similar across animals.
Based on the strongest quartile of response values, the average extent of the activated area was 2.6±0.3mm (Hilbert envelope: 2.6±0.2mm) in the rostrocaudal axis and 2.1±0.1mm (Hilbert envelope: 2.0±0.2mm) in the lateromedial axis.
Temporally, the peaks in both metrics were offset, but the latencies showed considerable variability. The wide-band potential peak was observed on average 2425.7±215.3ms post

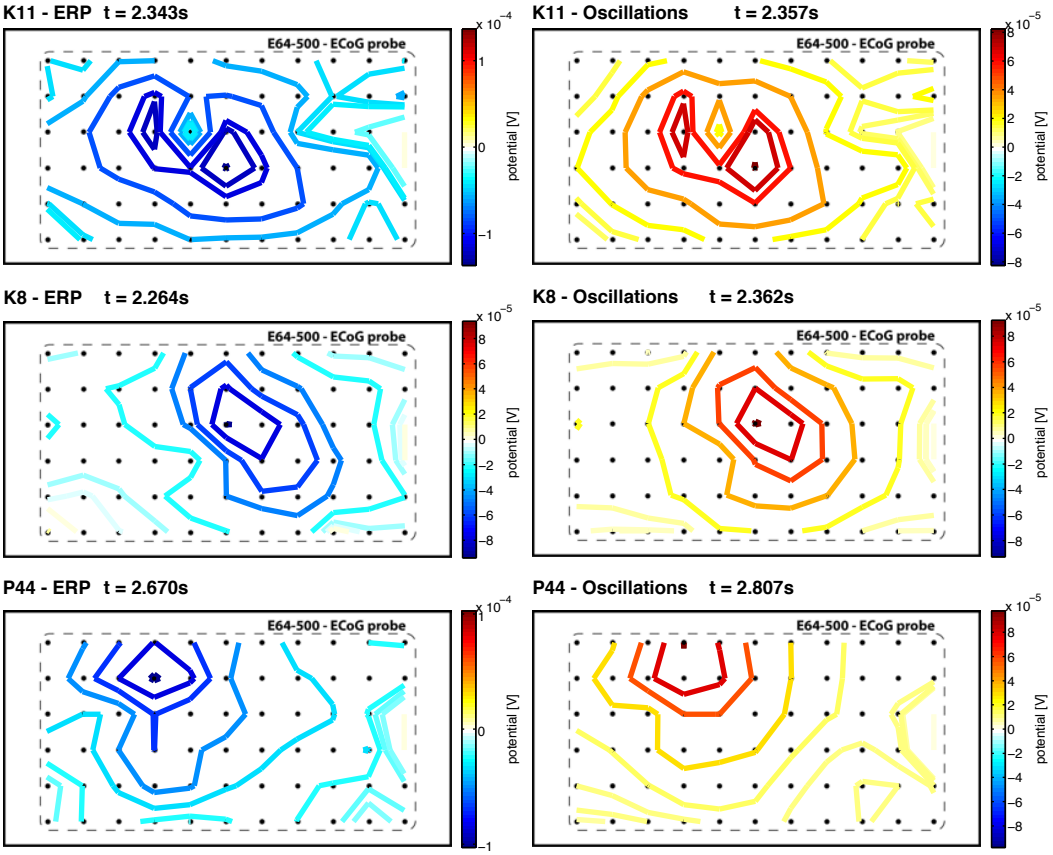

Figure 3.20.: Comparison of transient and oscillatory peaks across experimental animals (rows). **Left|** Topographies of the transient peaks in the avg. event-related potentials (0.1Hz-300Hz) for each experimental animal. **Right|** Topographies of the peaks in the avg. stimulus evoked oscillations (15Hz-35Hz) for each experimental animal.

playback onset and the oscillatory peak occurred on average 2508.7±258.4ms post playback onset.

Most of the multi-channel analyses will be focused on the oscillatory activity between 15 and 35Hz, because this metric showed strong and reliable difference patterns at the single-channel level during stimulus presentation.

Topographies of responses to stimulus super-categories

(a) Activation vs. baseline| The activation vs. baseline comparison on the multi-channel level revealed a set of three difference clusters in the wide-band potential (Fig. 3.21 A). The single-channel potential trace shows significant negative clusters associated with the flash onset (∼165ms), the onset of video playback (∼2.250s) as well as the stimulus offset (∼12.150s). In addition, a positive difference cluster was observed between the flash onset and the video onset and an extensive series of negative clusters that spanned between 3s and 8s post playback onset.

The comparison of the narrow-band Hilbert envelopes revealed an extensive cluster of positive difference-peaks that spanned almost the entire analysis window (Fig. 3.21 B). The difference-cluster exhibited a strong peak associated with the onset of the flash phase (∼350ms), a weaker peak following playback onset (∼2.350s) and significantly increased power during the playback phase as well as a weak offset peak (∼12.100s). The initial flash-evoked onset peaks for both the wide-band LFP (blue) and the narrow-band oscillations (15-35Hz) were considerably larger than the peaks associated with the onset of video playback.
The difference-clusters in both metrics were consistently located in the previously identified region showing strong flash-evoked responses. Furthermore, they remained stable (∼500µm) throughout the entire stimulation period. Also, the location of visually evoked activation did not differ between the initial flash phase and the subsequent video playback phase. The patterns remained stationary and appeared to be modulated in magnitude over time. The gradients surrounding the peak in the spatiotemporal representations of the wide-band potential differences were more variable than those for the oscillations.

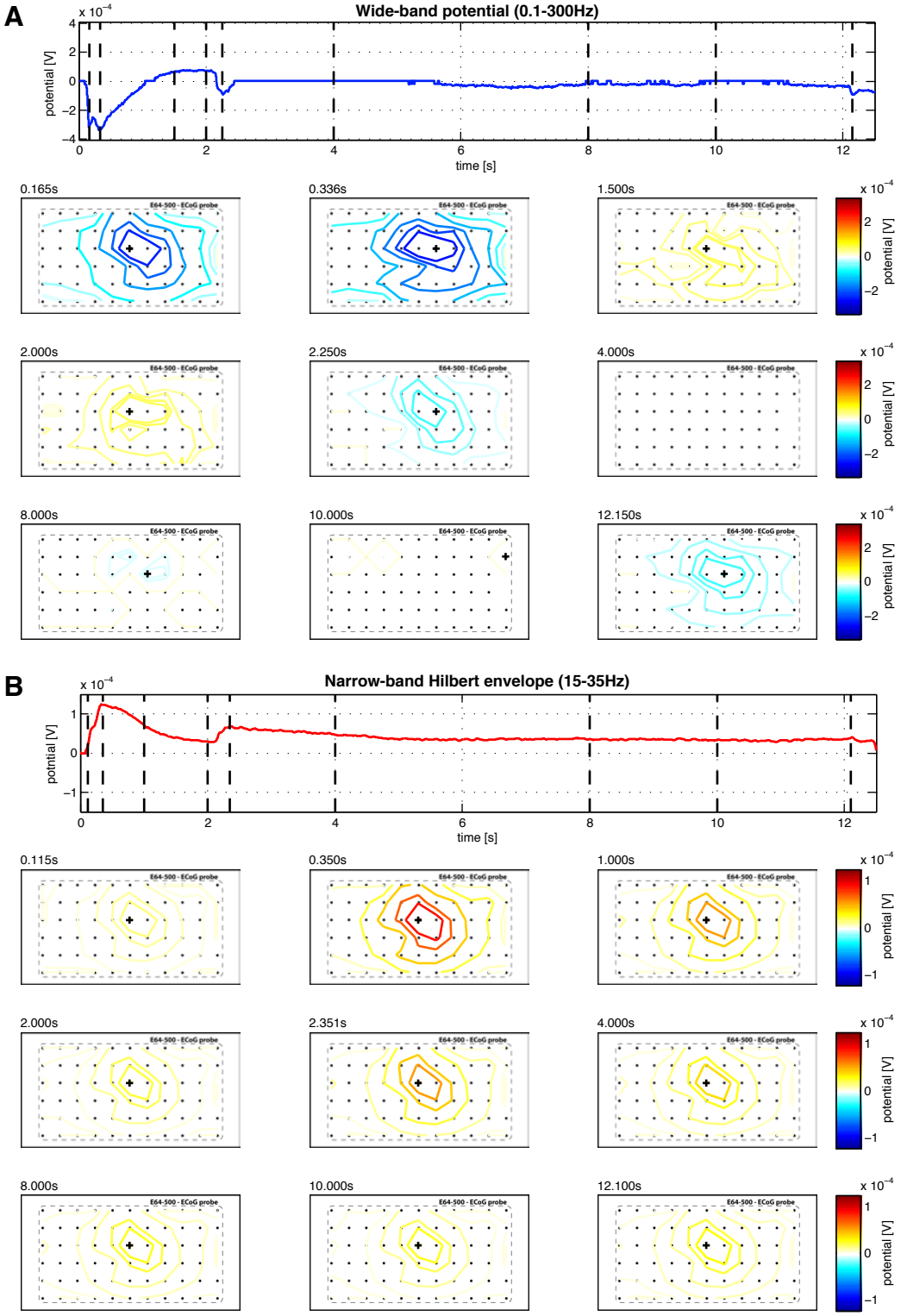

Figure 3.21.: A top| Single-channel representation of significant differences between wide-band (0.1-300Hz) baseline and stimulus-evoked activity. **B top|** Single-channel representation of significant differences between narrow-band (15-35Hz) baseline and stimulus-evoked activity. Vertical dashed lines indicate time-points for which spatial representations are given below. **A+B bottom|** Spatial representations of the differences indicated in the single-channel data. Black plus signs mark the most extreme value at each time-point. Distance between two recording sites (black dots) is 500µm.

(b) Colored vs. grayscale videos| Due to the lack of significant differences in the sustained oscillatory activity at the single-channel level, no spatial analysis of differences between the patterns evoked by colored and grayscale videos were calculated.

(c_1) Natural-sequential vs. natural-shuffled videos| The topographic analysis of differences in the oscillatory activity evoked by natural-sequential and natural-shuffled videos (see Fig. 3.22) showed no significant differences during the initial flash phase, a sustained cluster of positive differences during the video playback phase and a negative cluster after stimulus offset.
All observed differences in the Hilbert envelopes were located in the same cortical region identified as visually responsive in the initial activation vs. baseline comparison (compare Fig. 3.21) and remained stationary throughout the stimulus presentation. The polarity of the difference clusters indicates that natural-sequential videos evoke significantly stronger oscillatory responses than natural-shuffled videos during the stimulus playback, but weaker offset associated oscillations.

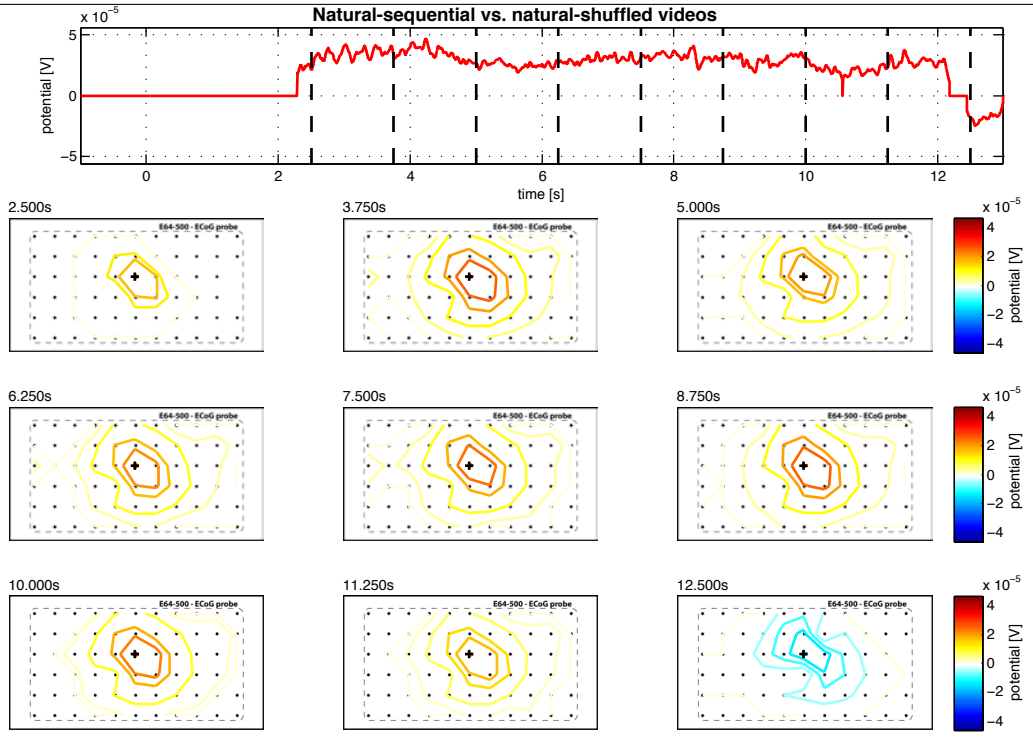

Figure 3.22.: Top| Single-channel representation of significant differences between narrow-band (15-35Hz) activity evoked by natural-sequential and natural-shuffled videos. Vertical dashed lines indicate time-points for which spatial representations are given below. **Bottom|** Spatial representations of the differences indicated in the single-channel data. Black plus signs mark the most extreme value at each time-point. Distance between two recording sites (black dots) is 500µm.

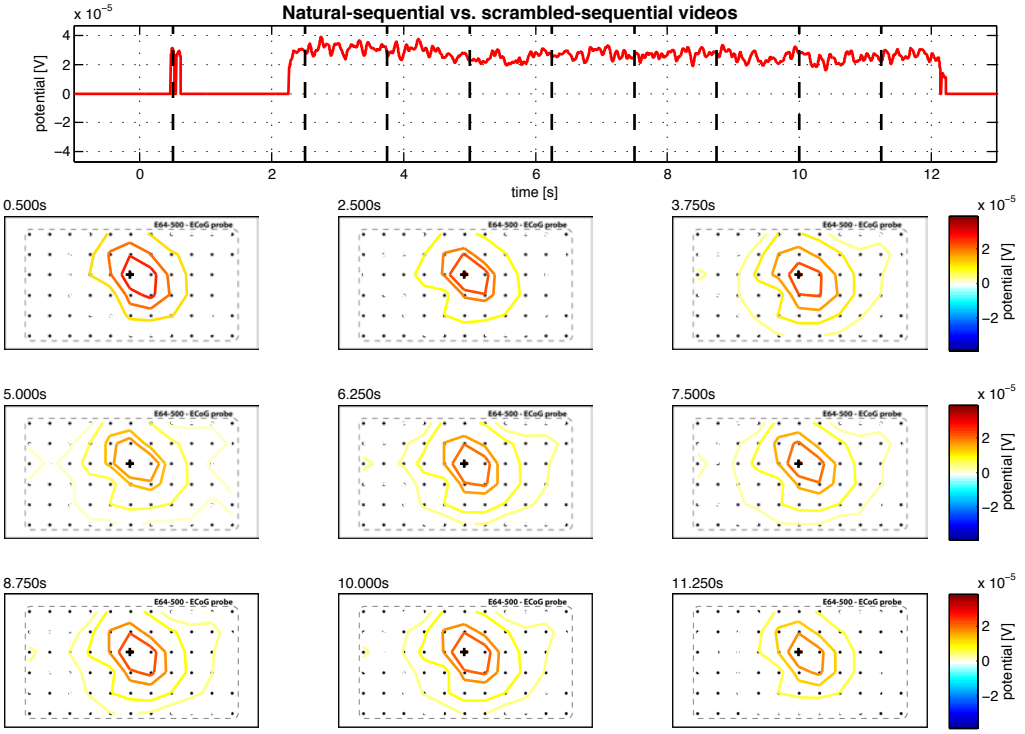

Figure 3.23.: Top| Single-channel representation of significant differences between narrow-band (15-35Hz) activity evoked by natural-sequential and scrambled-sequential videos. Vertical dashed lines indicate time-points for which spatial representations are given below. **Bottom|** Spatial representations of the differences indicated in the single-channel data. Black plus signs mark the most extreme value at each time-point. Distance between two recording sites (black dots) is 500µm.

(c_2) Natural-sequential vs. scrambled-sequential videos| Comparing the topographies of oscillations evoked by natural-sequential and scrambled-sequential videos (see Fig. 3.23) showed four clusters of positive differences. Positive differences indicate that the natural-sequential videos evoked significantly stronger oscillatory responses than the scrambled-sequential video stimuli. The first two clusters were short and occurred in short succession during the initial flash phase. The second positive cluster lasted approximately 10s, set in shortly after the onset of video playback and lasted until shortly after the playback offset. It was directly followed by a fourth brief positive cluster.
All significant differences were consistently observed in the same cortical location that was identified as showing the strongest flash- and video-evoked responses. The clusters during the flash-evoked response phase co-localized with the later clusters during the video-evoked response period and remained stationary throughout the entire stimulation period.

(c_3) Natural-sequential vs. scrambled-shuffled videos| The topographic representation of significant differences in the narrow-band Hilbert envelopes (15-35Hz) of

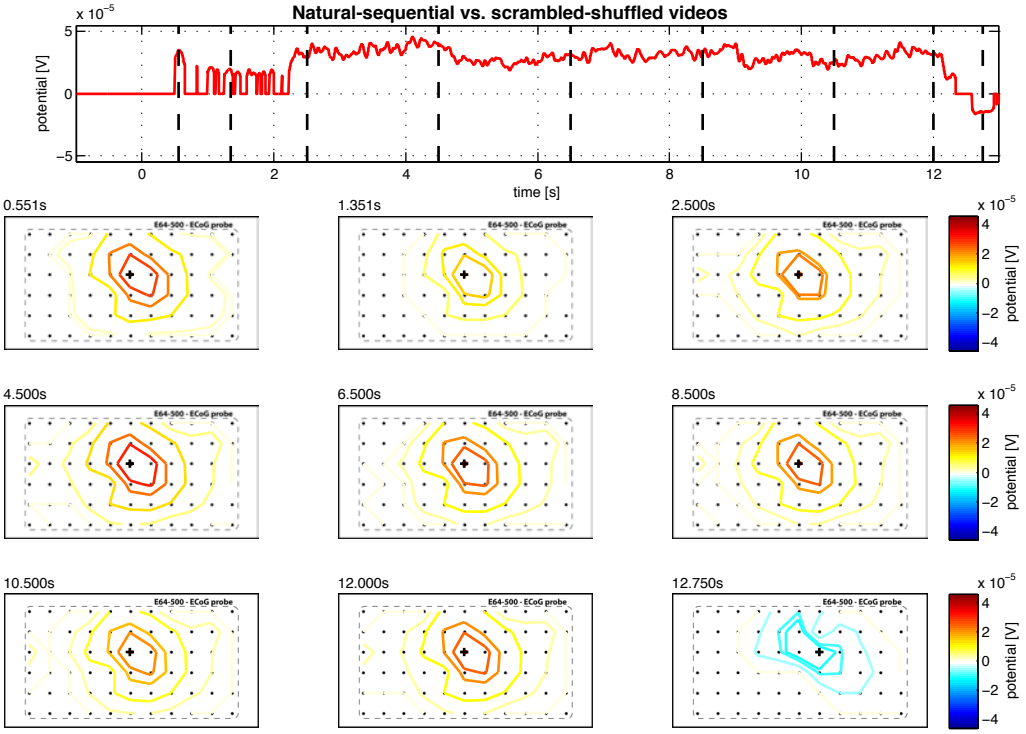

Figure 3.24.: Top| Single-channel representation of significant differences between narrow-band (15-35Hz) activity evoked by natural-sequential and scrambled-shuffled videos. Vertical dashed lines indicate time-points for which spatial representations are given below. **Bottom|** Spatial representations of the differences indicated in the single-channel data. Black plus signs mark the most extreme value at each time-point. Distance between two recording sites (black dots) is 500µm.

responses evoked by natural-sequential and scrambled-shuffled videos (see Fig. 3.24) revealed multiple clusters of positive differences as well as one cluster of negative differences. The initial flash-evoked phase contained a sequence of short positive clusters of decreasing magnitude. The playback phase exhibited an extensive (∼10s) cluster of positive differences followed by a short negative cluster after stimulus offset.
Again, the observed difference clusters were consistently located in the region that was identified as showing significant visually-evoked activation an remained stationary throughout the stimulation. Clusters during the flash-evoked phase were spatially co-aligned with the cluster during video playback. The cluster polarities indicate that natural-sequential videos evoked stronger cortical oscillations during the static phase as well as during the video playback phase, but that the oscillatory activity following stimulus offset was weaker than for scrambled-shuffled videos.

3.3.4. Waves and propagation of activity

Figure 3.25 illustrates the results of a spatial coherence analysis over the entire 64-channel ECoG grid and all responses for a single experimental animal.

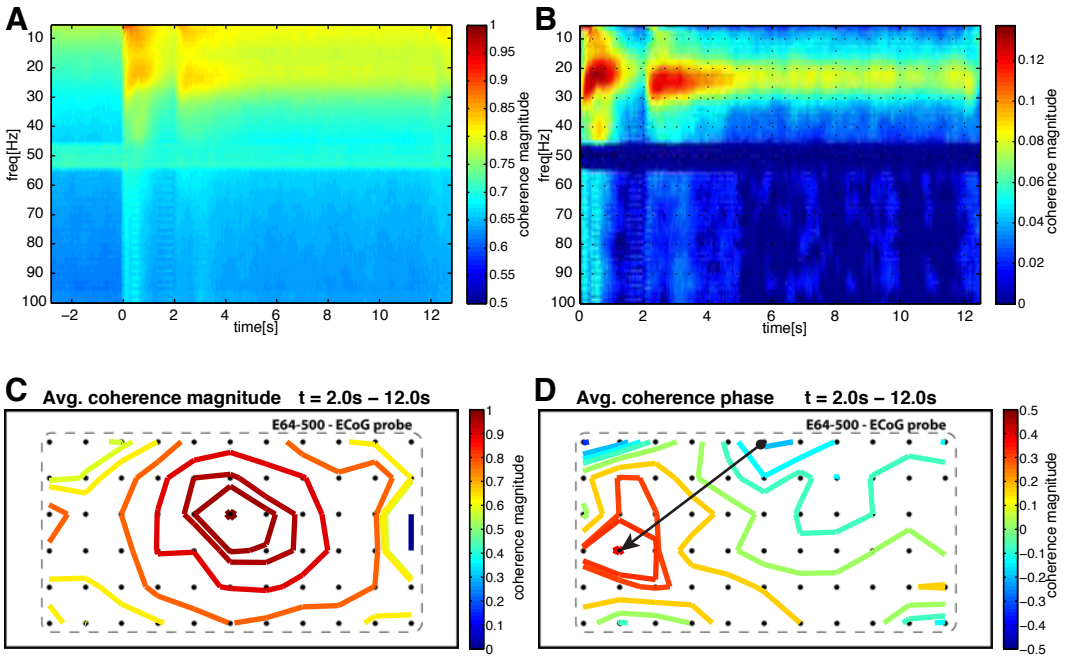

Figure 3.25.: Coherence analysis on the single animal level. Average coherence magnitude **A|** and significant stimulus evoked changes of coherence magnitude **B|** across all stimuli and the entire ECoG grid for animal K8. **C|** Spatial representation of the average coherence magnitude over the stimulation period (2-12s) **D|** Spatial representation of the average coherence phase over the stimulation period (2-12s). Distance between two recording sites (black dots) is 500µm.

Panels A and B display the raw coherence magnitude and the activation vs. baseline contrast respectively. The average coherence magnitude (Fig. 3.25 A) showed an increase in coherence during both the flash phase and the video-evoked phase. During the flash phase, a significant increase in the 15-35Hz band accompanied by a wide-band surge was observed. The video-playback phase was associated with a strong, sustained band of increased coherence in the 15-35Hz range which showed a clear peak associated with the onset of the video playback. During both the baseline and the stimulation period, a clear line-noise related band of high coherence magnitude was observed at 50Hz.

The significance of these observations was confirmed by statistical comparison of the coherence magnitude in activation and baseline periods (see Fig. 3.25 B). Changes in coherence magnitude largely reflected the previously described changes in evoked oscillatory activity. The strongest increases in coherence were observed between 15 and 35Hz during the onset of the flash phase and the onset of the playback phase. Coherence decreased, but remained significantly elevated throughout the video playback.

Figure 3.25 C shows a spatially interpolated map of the coherence magnitude in the 15-35Hz band during the video playback phase (2s-12s). It shows a region of high coherence magnitude covering the visually responsive area of cortex with the reference

channel in its center. A spatial representation of the coherence phase (Fig. 3.25 D) shows a rostrocaudally oriented phase gradient across the area exhibiting high coherence magnitude between two distinct phase poles (0.45 radian; -0.23 radian;$0.58\frac{mm}{ms}$; arrow in Fig. 3.25 D).

Figure 3.26 displays the spatial coherence maps for all animals used in the video stimulation experiments. In all three animals clear peak regions of high coherence magnitude corresponding to the previously identified visually responsive areas were observed.
In addition, for each animal a rostrocaudally oriented phase gradient was evident in the phase maps. The exact positions of the coherence peaks as well as the orientations of the phase gradients differed slightly across animals. The strongest peak and trough in the phase maps were defined as poles of the phase gradients and the velocity of the corresponding propagating wave was estimated from their distance and difference in phase (black arrows in Fig. 3.26). The average propagation velocity across animals was $0.76\pm0.18\frac{mm}{ms}$. Due to inter-individual differences in the implantation, the exact position of the phase poles on the ECoG grid differed across animals and the resulting orientation of the phase gradient differed accordingly. Thus, a precise definition of propagation direction was not possible.

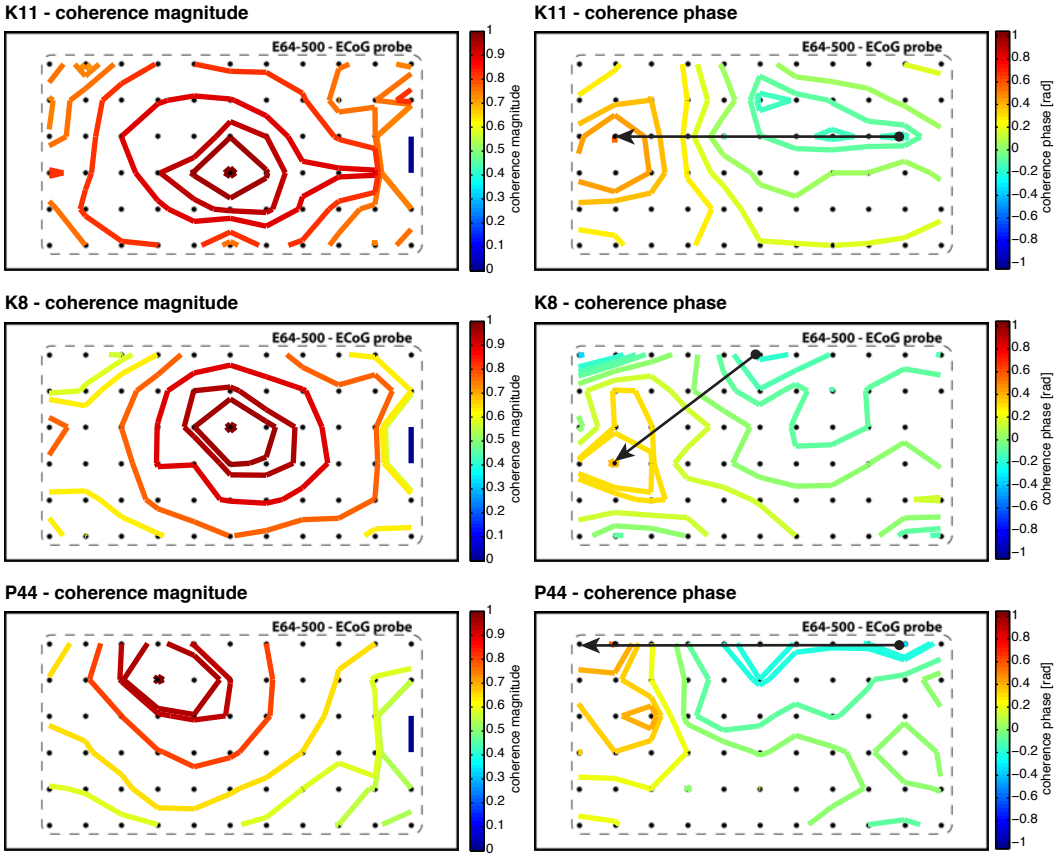

Figure 3.26.: Rows| Comparison of coherence topography for all experimental animals individually. **Left column|** Average coherence magnitude for 10s of activity post playback onset. **Right column|** Average coherence phase for 10s of activity post playback onset. Distance between two recording sites (black dots) is 500µm.

3.3.5. Correlation of stimulus features with evoked oscillations

Comparison of average power evoked by the original stimulus categories

Figure 3.27 displays the results of two multiple-comparison corrected, two-factor ANOVAs comparing the evoked oscillatory power (15-35Hz Fig. 3.27 A; 35-45Hz Fig. 3.27 B) across the eight original video categories. For oscillations between 15 and 35Hz, the ANOVA showed that the animal ID did not significantly influence the average response power ($F=0.15$; $p=0.860$), but that the stimulation condition did ($F=122.91$; $p<0.001$). A similar pattern was observed for oscillations between 35 and 45Hz. Again, the animal ID did not significantly influence the average response power ($F=0.03$; $p=0.970$) while the stimulus category did ($F=30.72$; $p=0.001$).

In both frequency ranges natural-sequential videos in color and grayscale evoked significantly stronger oscillations than any of the control categories. The average power evoked by colored and grayscale natural-sequential video clips were not significantly

different. Interestingly, the average power evoked by the control stimulus categories within the color classes showed no significant differences. In general, grayscale control videos tended to evoke weaker oscillatory responses than colored control videos.

Comparison of average power evoked by individual stimuli

Figure 3.28 displays the results of partitioning video stimuli according to the oscillatory power (15-35Hz) they evoked and reveals a set of videos which consistently evoked strong oscillations. Panel A displays a distribution of all 3270 recorded response power values after z-scoring to account for inter-individual differences. The distribution of single-trial response values was split into three quantiles and the values within each quantile were sorted according to the stimulus-categories (panel B) and single-stimuli (panel C) which had evoked them.
The histograms in panel B show that most of the stimuli evoking weak oscillatory responses (first quantile) belonged to the control videos (categories 2-4 and 6-8). Overall, more responses to grayscale control videos were sorted into the first quantile. The second quantile contained similar proportions of stimuli from all categories except for the natural videos (color and grayscale) which were slightly underrepresented. The third quantile contained responses which were mainly evoked by natural videos (categories 1 and 4). Control categories were represented in significantly smaller fractions.
A more detailed breakdown of the composition of the quantiles is presented in figure 3.15 C. Each field in the presented color matrices corresponds to a particular stimulus in the stimulus set. Rows in the matrices correspond to stimulus categories and columns to individual videos within a given category. The color of each field represents the percentage of responses to this stimulus which were sorted into that particular quantile. The color patterns are obviously not random and support the previous observations providing additional information on particularly effective and ineffective stimuli.

Unfortunately, the video-stimuli which most effectively evoked cortical oscillations can not be presented in form of a figure. A set of 44 video-stimuli were identified to evoke responses that where sorted into the first quantile in more than 66% of presentations. Of these stimuli, 18 belonged to the colored natural-sequential videos, three were colored scrambled-sequential videos, four were colored natural-shuffled videos, and 19 were grayscale natural-sequential videos. Averaging over color classes, 37 out of 44 videos consistently evoking strong cortical oscillations were natural videos. A subset of three natural-video stimuli in both grayscale and color evoked responses which were sorted

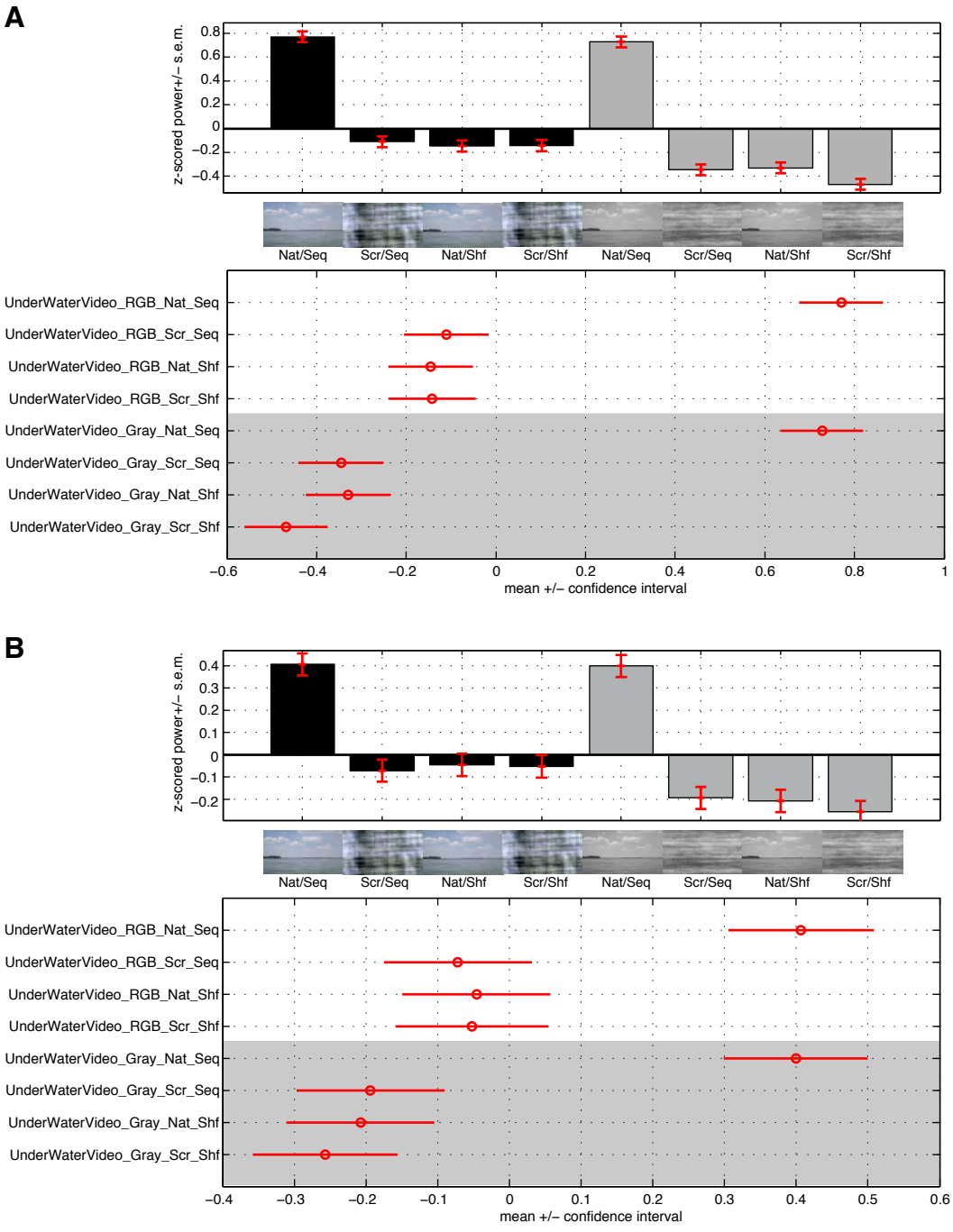

Figure 3.27.: Results of multiple comparison corrected ANOVA of evoked power **A|** from 15-35Hz and **B|** from 35-45Hz. Data were z-scored prior to analysis and bar plots represent means and standard errors of the mean. Non-overlapping whiskers in the multiple comparison plots indicate significant ($p<0.05$) differences between means. Comparison of avg. response power evoked by stimulus original stimulus categories.

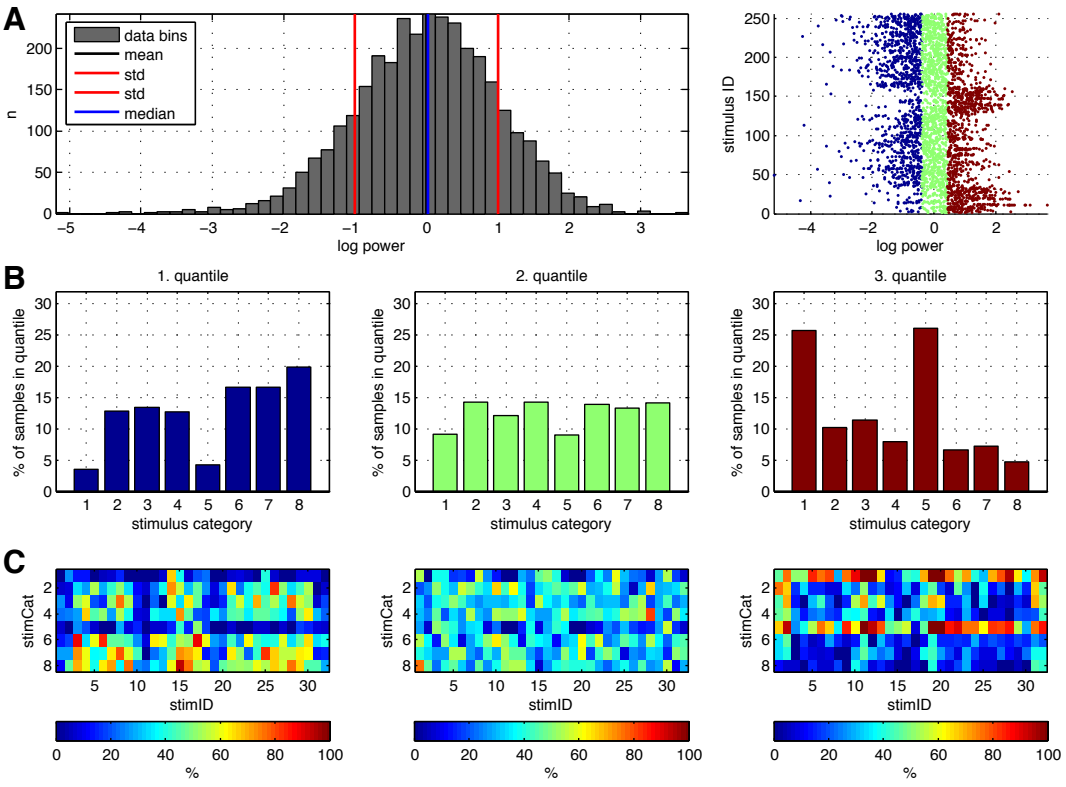

Figure 3.28.: A| Distribution of mean-normalized video-evoked power values pooled over all experimental animals. Composition of the response data quantiles with respect to the original stimulus categories **B|** and with respect to individual stimuli **C|**.

into the first quantile in more than 99% of the presentations. All three videos contained recordings above the water surface with a large proportion of reflective water surface, a cloudy sky, trees and/or shrubs.

3.4. Relating physiology and anatomy

3.4.1. Surface staining using a lipophilic fluorescent dye

Figure 3.29 shows an overview of the results of the DiI footprinting procedure for all animals used in chronic recordings. Photographies of the fixed brains in the visible spectrum (blue channel) are overlayed with the fluorescent signals of the DiI (red channel).

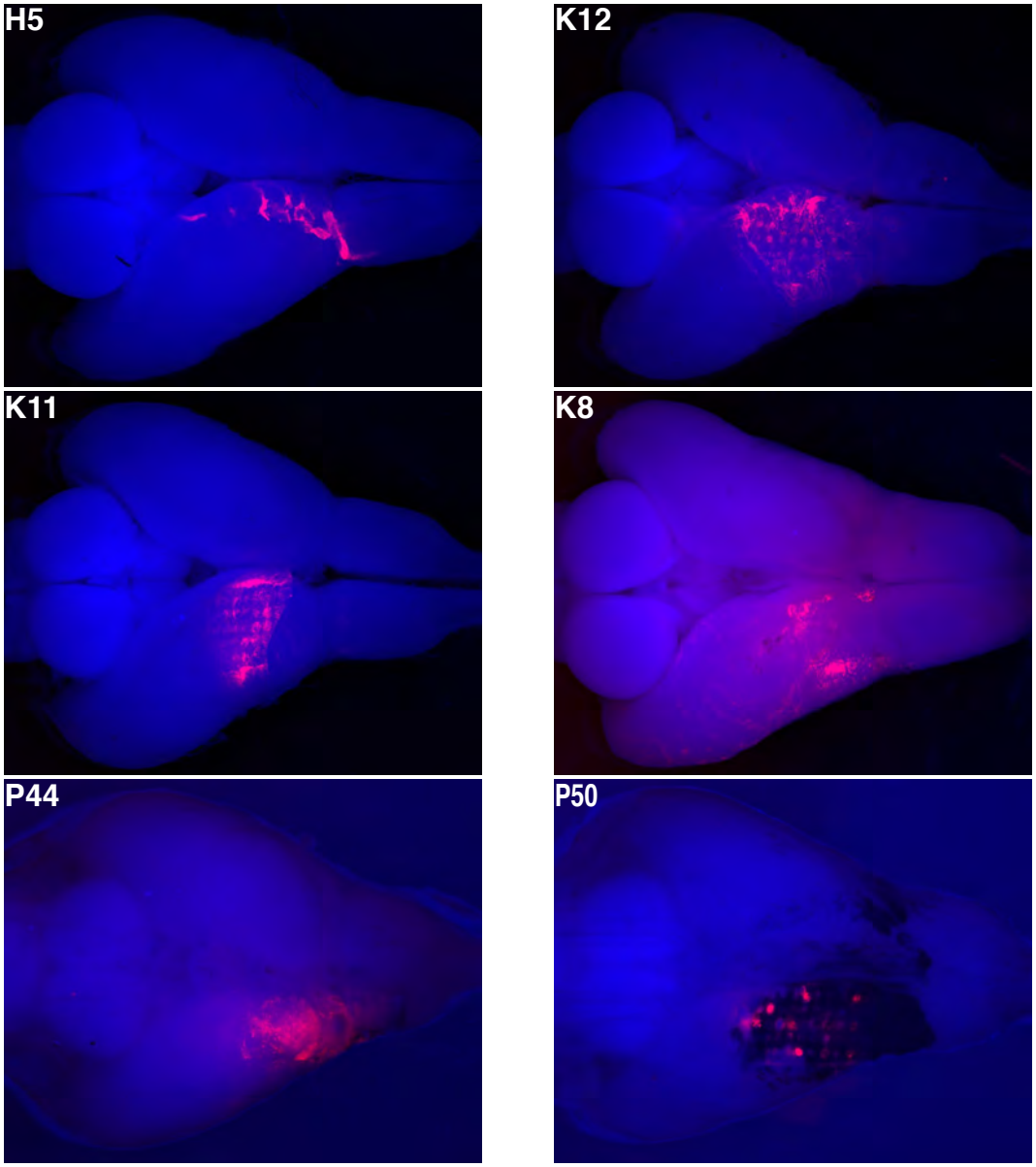

Figure 3.29.: Overview figures of six animals used for ECoG recordings. The blue channel represents an overview photograph of the brains taken in the visible range, while magenta represents the actual DiI fluorescent signal. H5, K12, K11, K8 and P44 had DiI coated surface probes implanted. P50 was used in an acute experiment and staining was locally applied.

The blue overview images of H5, K12, K11, and K8 are very crisp, while the brains of P50 and P44 were less clean and looked blurred. In the latter animals meninges, blood vessels and regenerating tissue were still in place and blurred the view of the underlying brains. DiI deposits were clearly visible and the dye had heavily stained the pia mater and embedded blood vessels. In none of the cases where the entire grid had been coated in DiI (H5, K12, K11, K8, P44) the entire contact area was stained. In animal P44, DiI deposits were visible, but the staining did not comprise the entire contact area. For

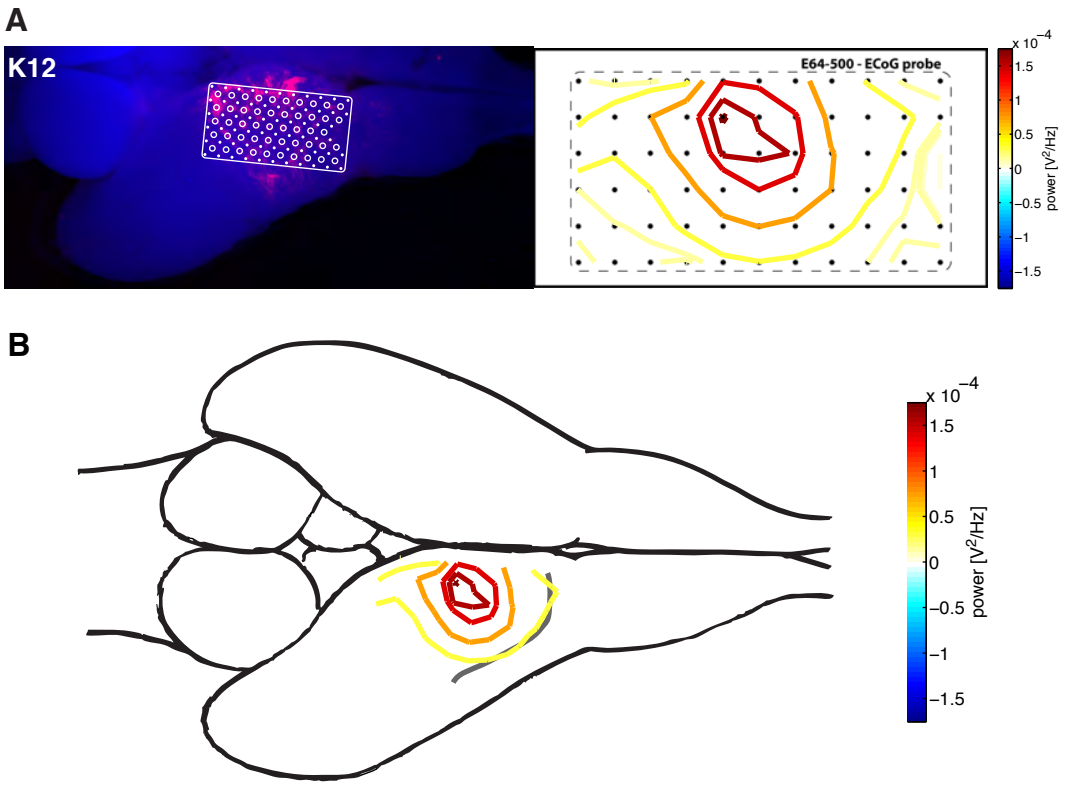

Figure 3.30.: Co-registration of physiological data and anatomical data. **A|** Left: Fluorescent photography of the brain of animal K12 superimposed with the reconstructed location of the ECoG grid. Right: Spatial representation of the peak in natural-scene-evoked oscillatory power (15-35Hz). Distance between two recording sites (black dots) is 500µm. **B|** Consensus location of visual stimulus-evoked oscillatory activity in the turtle brain.

animal P50, the electrode was not covered in DiI and therefore no surface staining was observed. These spotlike stains were clearly visible under the fluorescent microscope.

3.4.2. Mapping physiological data onto the brain

Panel A in Fig. 3.30 displays the co-registration of electrophysiological data (oscillatory power between 15-35Hz) onto a stained brain. The footprint of animal K12 was extensive and showed sufficient patterning to map the approximate location of the ECoG grid back onto the anatomy (cf. Fig. 3.29).
A combination of photographs taken during the implantation, the fluorescent footprint, and mechanical imprints on the brain surface allowed a coarse recovery of the recording locations in all animals. Fig. 3.30 B displays the identified consensus location of maximal visually evoked activity in the turtle brain. In all animals the identified area of maximal visual responsiveness was consistently located in the dorsal cortex caudomedial to the cortical ridge and covered an elliptic area with its long axis oriented rostrocaudally.

3.4.3. Relating the activity to the cortical subareas D2 and D1

Figure 3.31 illustrates the alternative approach to the focal DiI marking in animal P50. Panel A shows a schematic of the ECoG grid with a superimposed spatial map of evoked power (15-35Hz) in response to naturalistic visual stimulation. In addition, all perforations in the ECoG grid through which DiI had been deposited are displayed as filled green circles. Three exemplary brain slices in the adjacency of the cortical location showing strongest visually evoked responses were selected (dashed lines in Fig. 3.31 A) for further analysis. Panel B in Fig. 3.31 B shows these slices as composite, fluorescence images displaying NeuN in red, VGlut2 in blue and DiI in green. Panel C displays a magnified view of the dorsal cortex in slice 2 which was estimated to be closest to the location of the activity peak (cf. Fig. 3.31 A). The transition of the cell layer in dorsal cortex towards the ventricle occurs approximately halfway along the lateromedial extent of dorsal cortex (slices 1 and 2) while VGlut2 staining can be seen in the molecular layer along the entire lateromedial extent.

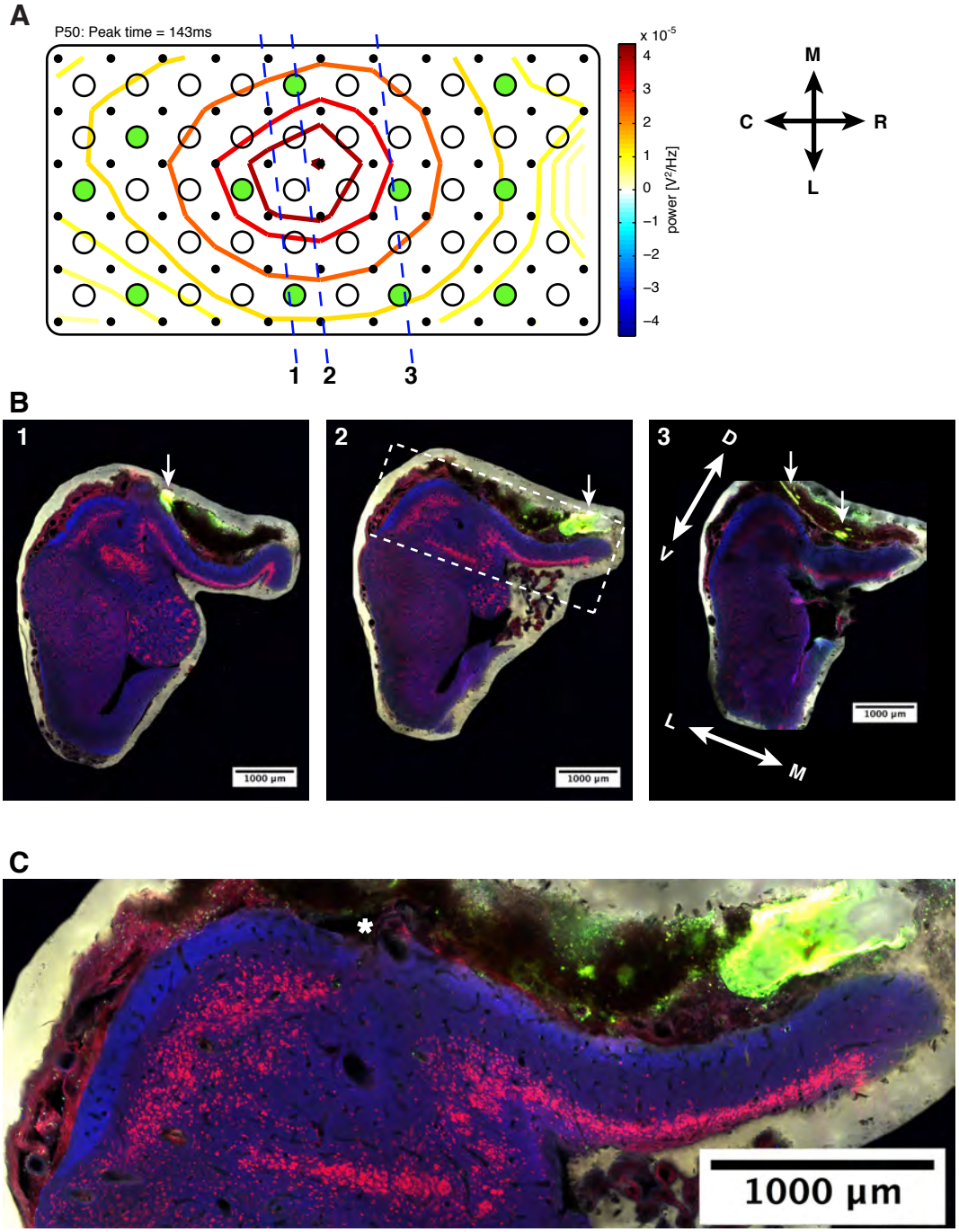

Figure 3.31.: Local application of DiI through perforation in the ECoG grid in an anesthetized animal. **A|** Schematic of the 64 channel ECoG probe. Filled circles represent locations of local DiI application during the implantation of the electrode. Oblique dashed lines indicate the approximate orientation of the three frontal sections displayed in B. Distance between two recording sites (black dots) is 500µm. **B|** Frontal sections of the brain of P50 at three different location (shown in A). Blue: VGlut2 / Red: NeuN / Green: DiI / White: residual embedding medium; Abbreviations: M=medial/L=lateral/R=rostral/C=caudal/D=dorsal/V=ventral. **C|** Magnified view of the cortex in **B2|**. Blue labeling indicates incoming thalamic afferents stained via VGlut2 and red labels neuronal cell bodies via NeuN. The asterisk denotes the cortical ridge that marks the lateral limit of dorsal cortex.

4. Discussion

Summary| *The presented research project aimed to address several open issues related to visually-evoked population dynamics in the dorsal cortex of turtles. The high-density, large-scale ECoG recordings were used to localize and circumscribe an extensive visually-responsive area in the dorsal cortex and to examine spatiotemporal response patterns evoked by a set of complex, natural stimuli (scenes and videos). Test and control stimuli used in the experiments were chosen to differ in global features like frequency content, spatial and temporal coherence.*

The basic response properties largely agreed with previous observations from unspecific visual stimulation paradigms in awake and anesthetized intact turtles as well as in isolated heads or eye-brain preparations (Prechtl, 1994, Prechtl, 1995, Prechtl et al., 2000). For all stimulation conditions, the evoked activity was consistently located in the same cortical area caudomedial to the cortical ridge. Natural stimuli (scenes and videos) evoked significantly stronger and more coherent oscillations than control stimuli with reduced spatial or temporal integrity. In responses to both scenes and videos, the 15-35Hz oscillations gave rise to a rostrocaudal phase gradient across the visually responsive cortical area. While oscillations in response to static stimulation were restricted to frequencies between 15 and 35Hz, responses to video stimuli evoked oscillations up to 45Hz.

The differences in cortical activation between responses evoked by natural stimulation and responses evoked by phase-scrambled stimuli suggest a similarity of turtle dorsal cortex to extrastriate cortex regions in the mammalian ventral object recognition pathway. In addition to the examined functional aspects, this study demonstrates the feasibility of chronically implanting large-scale μECoG grids in adult turtles without restricting their freedom of movement and to record stable signals over several weeks.

The discussion chapter is topically subdivided into several shorter sections. Initially, a brief overview of methodological considerations and limitations, as well as some considerations on the stability of recordings, are provided. Subsequently, the general turtle μECoG characteristics, the individual response components as well as the spatial and spatiotemporal activity patterns are discussed. Thereafter, considerations on the mechanistic underpinnings of oscillatory activity in the dorsal cortex and the potential functional role of turtle dorsal cortex are presented. Finally, short concluding remarks and outlooks for both stimulation paradigms (scenes and videos) are given.

4.1. Technical considerations and limitations

4.1.1. Turtles as model animals

Turtles unite characteristics which make them very interesting for the use as a neurophysiological animal model. The structural simplicity of their cortex makes them a promising model organism for the examination of cortical information processing and the resilience of their tissue against anoxic conditions enables a broad spectrum of experimental approaches ranging from *in-vitro* to *in-vivo* preparations.
However, they also exhibit several traits which make them problematic for particular experimental settings. The scarcity of recent literature and the sometimes questionable quality of older studies require a considerable effort to confirm previous results and to build a reliable data foundation. In addition, their very robustness poses several challenges for advanced neurophysiological methods. Head retraction into the shell prevents recording techniques requiring implants higher than a few millimeters. A particularly tough *pia mater* complicates the implantation of depth probes which represent a standard recording method in neurophysiology. Even after penetrating the *pia mater*, depth recordings are further complicated by a high degree of mobility of the brain within the liquid filled dura sack.
The Laurent department is currently undertaking parallel efforts to overcome the aforementioned problems and has already made considerable progress in establishing several widely used neuroanatomical and neurophysiological methods in different turtle preparations.

Selection of experimental animals| The turtles used for this study were bred in extensive farms and their individual history was not controlled or recorded. Therefore, their precise age was unknown and age estimates had to be based on the carapace length and

size of the animals. In addition to this uncertainty of age, a selection bias was inevitable. Due to size restrictions imposed by the implantation method only large (>950g) female red-eared sliders could be used in chronic recordings. Previous electrophysiological studies of turtle cortex did not report any size- or sex-specific differences in cortical activity patterns and parallel efforts in the lab have not shown such differences.

Turtle color vision| It should be noted that the observations made in this study allow no conclusion on the perception of color by turtles. The color spaces in most consumer cameras and display devices are optimized for the human trichromatic cone system and might be considerably different from the natural color space of the tetrachromatic turtle visual system. To reduce potential confounds introduced by the color composition of the natural scenes and videos, the stimuli were presented both in colored and grayscale versions. However, the mismatch in color spaces might also affect the perception of these grayscale stimuli.
In addition to this mismatch, the color calibration of the stimuli was only approximate and complicated by the non-linear color behavior of the Canon LCoS projector that was used for the majority of experiments.

4.1.2. The recording procedure

Because the animals were awake and free to move their heads and limbs, it was impossible to ascertain the absolute same posture and behavioral state in repetitive stimulation sessions. To exclude behavioral artifacts from analysis, the electrophysiological data were screened for unrelated physiological contaminations like eye-blink-related oscillations, head movement or spontaneous oscillatory activity. However, the head tracking procedure gave only an approximate measure for the animal's gaze direction. It was not possible to record eye tracking data while the animals were free to move their heads. This uncertainty posed a considerable difficulty for probing the dorsal cortex for retinotopic representations. It was not possible to repetitively stimulate precise retinal locations while the experimental animals could freely move their heads. Stimulation at specific locations of the screen did allow to assess allocentric representations (pilot experiments by Julien Fournier and Christian M. Müller) in cortex, but did not allow to test for retinotopy of visual inputs and processing. Thus, it was not possible to test whether the location of evoked activity changed with the position of the stimulus.

4.1.3. The visual stimulation paradigms

Sampling of the visual stimulus space| For the experiments presented in this study a relatively small set of naturalistic stimuli was arbitrarily selected and this selection could have been unconsciously biased. In addition, the limited number of stimuli was repeated over the course of the multiweek experiments. Although the order of stimuli was freshly randomized for each experimental run, learning effects can not be excluded and may contribute to the recorded signals. It is unlikely that the observed variability in response power was due to habituation, because it was prevented by randomizing the stimulus order and interstimulus intervals (Luo et al., 2010).
Furthermore, only objectively quantifiable characteristics of the stimuli were taken into account in the analysis of the stimulus features. Subjective (emotional, memory) characteristics have been neglected so far, but might well contribute to the responses. Because the individual histories of the tested animals are unknown, it is impossible to assess the subjective importance (danger, predator etc.) particular stimuli might have for individuals due to previous encounters.
An optimal stimulus set should contain an unbiased large set of natural stimuli (scenes and videos) sampled from natural habitats and responses should be recorded equally from male and female animals. Ideally, the stimuli should be recorded from the point of view of the studied species.

Processing of natural-scene stimuli| To minimize the influence of stimulus illuminance on the comparisons of responses to the different stimulus categories, all stimuli in the static-scene set were adjusted to create comparable ($\pm 5\%$) changes in illuminance at the location of the turtle head. Unfortunately, the initially applied procedure turned out to be insufficient so that the resulting estimated luminance changes for the white noise and uniform flash stimuli deviated significantly from those estimated for natural and scrambled scenes. However, the estimated illuminance changes for natural scenes and phase-scrambled scenes in color and grayscale did not differ. As a consequence, direct comparisons and conclusions on the effect of stimulus structure on the evoked activity should be restricted to the natural and scrambled scenes.

Processing of natural-video stimuli| Video stimuli were not luminance adjusted, to preserve natural differences in the lighting conditions of different locations in the video clips. This information was kept intact and thus represents a potential confound for the comparisons of responses evoked by different video stimuli.

Phase-scrambling strongly affects local (high spatial frequency) contrast elements. Low-frequency components like horizons and waterlines are less affected. Scrambled-sequential videos thus contain a residual temporal coherence in low-frequency elements and image luminance. Similar to the residual structure in scrambled videos, the shuffled videos might contain a residual temporal coherence, because shuffling was only performed over 10 seconds of the video clips.

Characterization of visual stimuli| Although a large set of objectively quantifiable stimulus features was selected for the analysis of correlations between stimuli and responses, it is possible that the applied stimulus analysis routines were insufficient and did not capture the most relevant features for the dorsal cortex. Global image analyses (i.e. the intensity distribution, local contrast distribution, spectral composition etc.) as they were used in this study allowed a coarse categorization of the stimulus set, but did not include the analysis of high-level features like particular types of visual objects (Thomson, 1999, Simoncelli and Olshausen, 2001, Torralba and Oliva, 2003). More recent stimulus classification frameworks like the application of deep convolutional neural networks (Krizhevsky et al., 2012, Donahue et al., 2013) might represent promising means to identify complex, high-level features in visual stimuli for the subsequent correlation with neurophysiological response data.

4.1.4. Stability of chronic μECoG recordings

Stability of signal strength| Responses to the red flash stimuli turned out to be useful to monitor the stability of the recordings within and across recording sessions.
The overall stability of the signal strength indicates that the electrodes did not loose contact to the brain and that no signal-attenuating tissue accumulated at the recording sites. In some cases regenerative tissue or blood clots were observed post-mortem, but the ECoG signals were never lost over the course of an experiment. The observed fluctuations in signal strength and oscillatory power are most likely explained by changes in the behavioral (gaze) and attentional (wakefulness) state of the experimental animals. These effects are not expected to significantly interfere with the comparisons of responses across stimulus categories, because they were counteracted by presenting the visual stimuli in a pseudo-randomized way over the course of the recording sessions.

Stability of location| The fact that little to no changes were observed in the peak locations over recording periods spanning more than four weeks indicates that the implanted electrodes remained in the same position once the craniotomy was sealed and

the animals had recovered. With respect to the high degree of mobility of the turtle brain within the liquid filled dura space, ECoG recordings have a distinct advantage over other recording techniques. The usage of a flexible, hydrophobic carrier material allows the electrode to follow the brain motion without losing contact. It should be noted that all observations of spatial and spatiotemporal activity patterns are limited by the spatial resolution of the custom ECoG grid. Shifts smaller than the electrode pitch of 500µm in x and y may have been missed by this recording approach.

Taken together, these results show that it is possible to reliably and stably record large-scale µECoG data from chronically implanted, freely behaving turtles over extensive periods of time.

4.2. General properties of ECoG recordings from turtle cortex

In the absence of visual stimulation, the µECoG signals from dorsal cortex exhibited bouts of spontaneous oscillations in the 15-35Hz range. Such oscillatory bouts occurred both in the presence and absence of ambient light. The signal amplitude as well as the complexity of waveforms was much higher when recording spontaneous activity from chronically implanted awake animals compared to recordings in deeply anesthetized turtles (data from pilot experiments not shown).
Similar spontaneous activity patterns had been previously reported to occur in the visually responsive areas of turtle dorsal cortex (Prechtl, 1994). Prechtl et al. mentioned a 100-150% increase of 15-20Hz power in the presence of light. The spontaneous oscillations observed in this study were not quantified, but from an inspection of the raw data the effects appeared weaker in the awake ECoG recordings. While Prechtl et al. further reported oscillations associated with gaze shifts, the oscillations reported here did also occur in the absence of head movement. However, these apparently spontaneous oscillations could still be related to optic flow induced by eye movements, because it was not possible to track the animal's eyes throughout the experiment. Although it was tried to exclude optic flow by recording spontaneous activity in darkness, the recording environment was not absolutely free of residual light. Therefore, shifts in the visual input could not be ruled out. However, spontaneous bouts of oscillations were also observed in lightly anesthetized and curarized turtles where all motion induced optic flow was excluded (personal communication from Julien Fournier and Christian M. Müller).

Visual stimulation of the chronically implanted turtles evoked responses in a circumscribed area of the dorsal cortex caudomedial to the cortical ridge. The evoked responses

contained transient response components superimposed with sustained oscillations between 15Hz and 35Hz (45Hz for video stimulation). Transients and oscillations differed in the extent to which they were time-locked to the visual stimulation. Transient, low-frequency response components were closely time-locked to changes on the stimulation screen, while oscillatory response components were less precisely time-locked and showed considerable variability in their time-course.

4.3. Decomposition of evoked responses into transients and sustained oscillations

4.3.1. Transient response components

Summary of experimental results| The onset transients of the evoked responses were closely time-locked to the stimulation. They were analyzed with respect to their amplitude, latency, and how these properties changed with stimulus parameters.
Red uniform flash stimuli evoked particularly strong and sharp onset transients with steep rising and falling flanks, an average amplitude of -0.71±0.43mV, and a latency of 144ms. Offset transients reached amplitudes of -0.35±0.24mV and occurred 165ms post stimulus offset. The transients in responses to natural-scene stimuli were usually less sharp, showed wider peaks, and were superimposed with oscillations. Onset transients had average amplitudes of -0.38±0.27mV and a latency of 184ms. Offset transients occurred 177ms post stimulus offset and reached an average amplitude of -0.10±0.17mV. Responses evoked by stimuli in grayscale and color showed brief phases of significant differences during the onset and offset transients. Colored stimuli (onset: 180ms;-0.41±0.29mV / offset: 2174ms;-0.12±0.19mV) evoked stronger and earlier transients than stimuli in grayscale (onset: 221ms;-0.32±0.29mV / offset: 2214ms;-0.08±0.16mV). The onset transients in responses to colored scene stimuli further exhibited a slightly longer time-constant until relaxation to baseline.
Natural-scene-evoked onset transients (onset: 212ms;-0.39±0.29mV) were slightly later and stronger than those evoked by scrambled scenes (onset: 188ms:-0.37±0.26mV). The offset transients occurred with similar latencies in both categories, but scrambled scenes evoked slightly stronger peaks (natural scenes: 2176ms;-0.08±0.16mV / scrambled scenes: 2176ms;-0.1±0.16mV).

Video-evoked potentials usually contained three distinct transients. The first transient was associated with the onset of the static display of the first video frame, occurred

166ms after the stimulus onset, and had an average amplitude of -0.29±0.22mV. It was followed by a second transient associated with the onset of video playback 2267ms after the stimulus onset and an average amplitude of -0.09±-0.17mV. The third and final transient followed the stimulus offset, occurred 12.187s after stimulus onset and reached an average amplitude of -0.06±0.15mV.
Video stimuli in color and grayscale evoked responses which significantly differed in their onset-, playback- and offset-transients. Colored video stimuli (164ms;-0.4±0.21mV / 12.181s;-0.1±0.15mV) evoked significantly stronger and earlier onset and offset peaks than grayscale videos (280ms;-0.32±0.28mV / 12.522s;-0.27±0.14mV). The playback-associated transient was later and stronger in responses to grayscale videos (color: 2266ms;-0.07±0.17mV / grayscale: 2344ms;-0.10±0.19mV).
All three transients in response to natural-video stimuli (167ms;-0.289±0.216mV / 2346ms;-0.094±0.200mV / 12.147s;-0.062±0.153mV) were weaker than those in response to all control videos pooled (166ms;-0.295±0.218mV / 2266ms;-0.097±0.168mV / 12.473s;-0.066±0.157mV).

Interpretation and relation to previous studies| Within a stimulus category, all animals except for one (P44) showed similar average latencies of the evoked onset transients. The observed difference in the response latency for animal P44 were likely due to the difference in the projection system. The PROPixx projector displayed stimuli much faster than the Canon LCoS device (cf. section 2.3.1.1) and thus responses appeared faster. Taking the projector-specific delays between 10 and 25ms into account, the observed latencies for flash-evoked responses lie in the same range of latencies as described by earlier studies (Mazurskaya et al., 1966, Prechtl et al., 2000). In both anesthetized and awake animals the onset amplitude and latency of the onset peak scaled with the contrast of the stimulus (data not shown). These findings are in line with previously described effects of the stimulus intensity on evoked potential amplitudes in turtle cortex (Zagorul'ko, 1968). The contrast-dependence could indicate that the initial onset transient reflects the strength of thalamic input signals arriving in dorsal cortex.
The exceptional effectivity of the red localizer/benchmark stimulus in evoking strong onset transients may also be partially explained by strong afferent inputs to the cortex. In a direct comparison with other pure color (red, green, blue) stimuli, responses to red flashes evoked the strongest cortical responses (data from pilot experiments not shown). This is compatible with a high proportion of 41-70% of red-sensitive photoreceptors in the retina of turtles (Ammermüller and Kolb, 1996) and previous field potential studies in turtle dorsal cortex (Zagorul'ko, 1968). Turtles have a well developed tetrachromatic

color vision with large amounts of photoreceptors in the red part of the visible spectrum (Ammermüller and Kolb, 1996). Thus, stimuli containing strong red components will also activate a large proportion of red photoreceptors in the retina and produce correspondingly large output signals.
However, a direct comparison of latencies and amplitudes across awake, anesthetized and reduced eye-brain preparations may not be reasonable, because various experimental parameters in reduced and anesthetized preparations like temperature and anesthetic dosage are known to interfere with the latency and magnitude of field potential responses. Furthermore, most older studies do not provide a detailed quantification of the observed transients in relation to their stimulation method.

Potential role of transient response components| All observed differences in the transient response components might be attributed to differences in the thalamic input drive. Stimulation with high-contrast stimuli or particular color compositions may be assumed to cause larger responses in the early parts of the visual system and could propagate into higher visual centers. Similarly, the differences in the onset transients when comparing responses to natural scenes in grayscale and color might be explained by this.
Therefore, it appears reasonable to interpret the time-locked, stimulus-evoked transients in the ECoG recordings of anesthetized and awake turtles as reflecting the strength of subcortical afferent signals arriving in the superficial layers of the dorsal cortex.

4.3.2. Sustained oscillatory components

Summary of experimental results| Stimulus-evoked oscillations were not time- or phase-locked to the stimulation. Spectral analyses (see Material & Methods 2.5.3) were focused on to their frequency, power, and coherence as well as the relation of these properties to the visual stimulation.
In this study, sustained stimulus-evoked oscillations in turtle dorsal cortex were typically observed in a frequency range from 15-35Hz. Response spectra showed wide shoulders and both magnitude and frequency of the spectral peaks differed slightly across animals. Compared to natural-scene-evoked responses, natural-video-evoked responses exhibited wider spectral peaks which contained increased oscillatory power up to 45Hz. The power of the oscillatory response components showed considerable variance and the stimulation was shown to have a significant influence on the oscillatory power. The observed differences across stimulus-categories were consistent across animals and significant on

the individual as well as on the grand-average level. The amount of oscillatory power in response to identical stimuli was similar, but showed fluctuations within and across stimulation sessions.
Colored scenes evoked significantly stronger cortical oscillations than grayscale scenes. The difference time-frequency representations (TFR; color vs. grayscale) showed an early ($\sim$300ms) low-frequency ($<$15Hz) positive cluster followed by significantly stronger and more coherent oscillations in the 15-35Hz range during stimulus presentation.
15-35Hz oscillations evoked by natural-scene stimuli were significantly stronger and more coherent than those evoked by matched scrambled scenes and white-noise patterns. The difference-TFRs (natural vs. scrambled) contained no early divergence as it was observed in the comparison of responses to colored and grayscale stimuli. Among the natural images, the images containing human-made scenes and images containing animals evoked the strongest oscillations while stimuli displaying landscapes evoked the weakest oscillations. The most efficient stimuli in driving dorsal cortex were identified by partitioning the individual response power values into quantiles ($>$66% of responses to a particular stimulus in the strongest quantile). They were visually inspected and compared (see Fig. 3.16), but no striking similarities were apparent. Further image feature analyses were required to identify the image features which are relevant for the turtle dorsal cortex (see multilinear regression analysis).

A comparison of responses to colored and grayscale videos revealed no differences in the sustained oscillatory activity (neither during the flash-phase nor during the playback phase) despite the differences observed in the onset-, playback- and offset-transients.
The responses to natural-video stimulation differed significantly from those evoked by control-videos. Power differences observed during the initial two second flash-phase (natural frames vs. scrambled frames) were similar, but weaker than those seen for natural- and scrambled-scene stimuli. The flashed display of a natural-video frame evoked stronger 15-35Hz oscillations than the display of a scrambled-video frame. During the video playback phase additional bands of significant, sustained power differences were observed between 35 and 45Hz in all difference-TFRs (natural-sequential vs. natural-shuffled; natural-sequential vs. scrambled-sequential; natural-sequential vs. scrambled-shuffled). Natural-sequential videos evoked the strongest cortical oscillations in both the 15-35Hz range and the 35-45Hz range. All control video categories evoked significantly less oscillatory power in both ranges. Control video categories within a color class evoked comparable average oscillatory power between 15 and 35Hz, but across color classes the colored control stimuli evoked significantly stronger oscillatory responses. Average oscillatory power between 35 and 45Hz exhibited a similar pattern, but the differences across

color classes were not significant. Splitting the average video-evoked oscillatory power between 15-35Hz into three quantiles revealed that a small subset of the natural-sequential videos was especially effective in driving cortical oscillations (>99% of responses to a particular stimulus in the strongest quantile). This subset contained footage from the water surface towards the horizon and displayed natural landscapes with a high proportion of reflective water surface.

Interpretation and relation to previous studies| Stimulus-evoked oscillations have already been described in several studies and in different turtle-derived preparations (Prechtl, 1994, Prechtl, 1995, Prechtl et al., 1997, Senseman and Robbins, 1999, Prechtl et al., 2000). In previous *in-vivo* and *in-vitro* studies oscillations are typically described as occurring at 20Hz, but it is usually acknowledged that power increased over a wider range of frequencies (Prechtl, 1994, Prechtl, 1995, Prechtl et al., 1997, Senseman and Robbins, 1999, Prechtl et al., 2000). Differences in the observed peak oscillatory frequency may be due to a combination of differences in the experimental methods and spectral analyses. Prechtl et al. (1997) applied a multi-taper frequency estimation method similar to the one used in this study and showed individual power spectra with wide-band power increases, but without displaying average power spectra or computing activation vs. baseline statistics.
Interindividual differences in oscillatory power and frequency under similar stimulation conditions are not trivial to explain. They might reflect an individual characteristic determined by the fine structure of the oscillating neuronal networks and the behavioral state. Mammalian visual cortex has been demonstrated to exhibit resonance phenomena when driven by rhythmic visual stimulation and these resonances were proposed to reflect an underlying non-linear system of coupled oscillators (Rager and Singer, 1998, Herrmann, 2001). However, they might also reflect problems with the implantation, like a weaker contact of the ECoG grid to the cortex, a piece of signal-attenuating tissue or a damaged connector. To minimize the influence of inter-individual power differences on the analysis results, the raw oscillatory power values were z-scored before computing comparisons across animals.
Interestingly, the evoked oscillatory power showed a contrast-dependent pattern similar to the onset transients. This indicates a correlation of the strength of thalamic input signals with the locally generated cortical oscillations. The further the stimulus deviated from the background, the stronger the evoked oscillations (preliminary contrast response curves not shown).

Predicting responses with a multilinear regression model| To test whether global stimulus characteristics have any predictive power on the evoked cortical oscillations, a multilinear regression model was constructed and used to fit the recorded responses using a set of such stimulus features (cf. Material & Methods section 2.5.5). At any given time point in the model, a subset of the 30 stimulus features was determined as being significant for the prediction of cortical oscillations. The subset was not static and at different time points during the response slightly different feature combinations were considered significant. Maximal prediction performance (32% of the total response variance) was achieved 300ms after the stimulus onset using a set of 17 stimulus features related to the: (a) image luminance, (b) color, (c) intensity distribution, (d) local contrast distribution, (e) orientation of local contrast elements, and (f) size of coherent contour objects. Within these feature complexes, the strongest weights were assigned to the variance of the pixel intensity distribution; the mean, variance, skewness and kurtosis of the local contrast distribution; local contrast orientations between 105 and 120 degrees; the skewness and 99th percentile of the distribution of coherent contour elements. The assignment of strong weights to features related to the distribution of contrast elements indicates that these features may be considered as relevant for the computations performed in turtle dorsal cortex. The detection and extraction of visual objects is an essential task for the brain and it is required in a variety of behavioral contexts like foraging for food, identification of predators and prey, and visual orientation. Considering that the recorded oscillatory power in the ECoG signal is a large-scale signal capturing the synchronous activity of extensive neuronal populations, the predictability of 32% of the response variance is surprising and not to be underestimated. While these results are encouraging, it is still possible that stimulus features with strong predictive power were missed or wrongly eliminated during the analysis. Several of the features described here are interrelated or interdependent and therefore complicate the applied multilinear regression analysis. In future analyses, special care should be taken when selecting the set of stimulus features in order to reduce interdependencies as well as to select analysis methods which are less susceptible to them. Furthermore, a promising alternative to using a battery of global stimulus features to identify correlations with neurophysiological response data is the extraction of complex, high-level stimulus features through the use of deep convolutional learning networks (Krizhevsky et al., 2012, Donahue et al., 2013).

Potential roles of oscillations in turtle dorsal cortex| Prechtl discussed the 20Hz oscillations in turtle dorsal cortex in the context of network oscillations observed

in the mammalian brain during sensory processing and attentive sensory-motor behaviors (Prechtl, 1994, Prechtl, 1995, Prechtl et al., 1997, Prechtl et al., 2000). However, the functional role of different oscillatory rhythms in mammals is also still unclear. As already indicated in the introduction of this study (cf. section 1.2), lumping oscillatory processes across taxa purely based on similarity of frequency should be avoided, because oscillations at identical frequencies may still serve different functions.

Without additional data on the microcircuit level it is difficult to comment on the functional role of the oscillatory rhythm in turtle dorsal cortex. In principle, all potential functions described in section 1.2 of the introduction are possible and could correlate with the observed evoked and spontaneous oscillations. It could be imagined that the cortical oscillatory rhythm in turtles (a) gates the processing of incoming afferent inputs from subcortical and/or cortical sources; (b) serves as short-term framework for information encoding that might be expanded by the rostrocaudal phase gradient; (c) synchronizes cell assemblies in distinct areas of the turtle brain [i.e. cortex and DVR; cf. (Prechtl, 1994)]; (d) serves to consolidate the memory of previous experiences through spontaneous oscillations in the absence of stimulation.

Because the naturalistic stimuli contained more structure and therefore potentially relevant information, the prolonged oscillatory responses might reflect sustained activity in the dorsal cortex associated with the processing of this information.

The comparison of responses to colored and grayscale stimuli revealed an early ($\sim$300ms), low-frequency ($<$15Hz) difference in power that might reflect differences in the thalamic drive due to the different color composition (see above).

The fact that natural-stimuli evoked stronger oscillations than control-stimuli in both color conditions indicates that the differences in response power are most likely due to differences in the spatial stimulus structure. While man-made scenes definitely contain the least information related to the natural habitats of slider turtles, they are very rich in strong, coherent, local contrast elements (i.e. sharp contours) and evoked particularly strong cortical oscillations.

The additional band of oscillatory activity between 35 and 45Hz observed in the difference TFRs and coherence plots might reflect a correlate of the processing of temporally coherent visual information. The fact that these oscillations are specifically elevated in natural sequential videos indicates that they are not artifacts of the video stimulation (i.e. frame rate) in general. Such artifacts would be observed in all video-evoked responses equally. Differences in power in this particular frequency range have not been observed in response to static-scene stimulation and were also not seen during the static presentation of the first video frame.

4.4. Spatial aspects of visually evoked activity in dorsal cortex

4.4.1. Localization of the visually responsive region and co-registration with anatomy

Summary of experimental results| Visually-evoked responses to uniform flash stimulation, natural-scene stimulation, and natural-video stimulation were consistently localized in the same cortical region caudomedial to the cortical ridge (cf. Fig. 3.30 for a consensus map). Both the transient response components as well as the sustained oscillations robustly co-localized and exhibited highly similar spatial maps.
The red localizer stimulus evoked onset transients which extended 2.7±0.3mm in the rostrocaudal axis and 2.0±0.3mm in the lateromedial axis. Natural-scene-evoked onset transients extended 2.8±0.2mm in the rostrocaudal axis (Hilbert envelope 15-35Hz: 2.8±0.2mm) and 2.0±0.3mm in the lateromedial direction (Hilbert envelope 15-35Hz: 2.0±0.3mm). Natural-video-evoked activation showed a similar average spread, but it should be noted that only three of the experimental animals were used in both paradigms. The onset transient extended 2.6±0.3mm rostrocaudally (Hilbert envelope 15-35Hz: 2.6±0.2mm) and 2.1±0.1mm lateromedially (Hilbert envelope 15-35Hz: 2.0±0.2mm). Both metrics (wide-band potential and narrow-band Hilbert envelope) did not show obvious patterns of peak propagation across the grid or multiple activated cortical (sub-)regions. The apparent two-peak structure in the topography of responses from animal K11 was caused by a defective channel on the probe or a broken wire in the adapter cable. This channel showed no valid physiological signal. The observed spatial patterns were very stable over time and both voltage and power metrics showed little to no changes of their peak locations over the course of the multiweek experiment.

A precise relation of physiological and anatomical data was difficult, because the labeling procedure (coating the ECoG array with a lipophilic fluorescent dye) worked less reliable than expected from pilot experiments. Portions of the staining were inadvertently removed with the meninges and residual blood vessels when cleaning the brains post-fixation. Due to this loss of staining it was not possible to precisely recover the location of the ECoG grid after the experiment.
Interestingly, brain slices with little residual surface staining showed strong fluorescent labeling of neuronal cell bodies in the cell layer. This labeling of the cell layer with DiI was due to active retrograde transport of the dye in the in-vivo situation. Instead of only labeling the surface, cells underneath the electrode were labeled. However, this also means that remote cells with dendritic processes which reach underneath the electrode

could have picked up the dye and could have been stained although their somata were not located directly underneath the electrode.
This labeling uncertainty added to the low spatial resolution of 500µm defined by the electrode pitch on the ECoG grid and the inherent spatial averaging of field potential recordings (Kajikawa and Schroeder, 2011).
Using an alternative approach based on placing a fluorescent dye pattern on the dorsal cortex through the perforations in the ECoG grid, allowed to partially circumvent the labeling problem and to obtain an approximate mapping of physiological signals to the underlying anatomy (cf. Fig. 3.31). It could be shown that the strongest physiological signal was recorded approximately halfway along the lateromedial extent of dorsal cortex (beginning at the cortical ridge). This position appeared to coincide with the location at which the cell layer in dorsal cortex shifts towards to ventricle. Furthermore, the thalamic afferents, as labeled by VGlut2 staining, occurred throughout the lateromedial extent of cortex and beyond the position at which the cell layer shifts its position. Rostrocaudally, the location of strongest evoked activity coincided with the anterior portions of the dorsoventricular ridge.

Interpretation and relation to previous studies| In earlier physiological and anatomical studies, the turtle dorsal cortex has been described to be divided into two cytoarchitectonically distinct subareas D2 and D1 (Desan, 1984). However, the classification of the proposed cortical subareas was not uniform and often unclear. Borders between the subareas were either based on the extent of thalamic projections arriving in dorsal cortex or on the density of the cell layer containing pyramidal-like neurons. The borders determined by both metrics were assumed to coincide (Heller and Ulinski, 1986).
James Prechtl had previously sampled the dorsal cortex of red-eared slider turtles with single extracellular electrodes and showed a co-localization of the strongest negative onset transient and the strongest 20Hz oscillations similar to what was observed in this study (Prechtl et al., 2000). The author reported that these peaks of cortical activity (wide-band and oscillatory) were located at the border between D2/D1 based on the density of the cell layer (Prechtl et al., 2000). A quantification for the localization of the border was not provided and the above mentioned spatial inaccuracies of the ECoG method made a direct comparison problematic.
Recent experiments on thalamocortical projection patterns conducted in this lab suggest a cleaner distinction of D2 and D1 based on afferent thalamic inputs (unpublished data). The results of these experiments indicate that thalamic projections to the dorsal

cortex extend beyond a presumed D2/D1 border based on the cell layer. Preliminary comparisons suggest that the extensive thalamorecipient area D2 overlaps with the visually responsive areas identified in this study. Thus, the visually activated region of dorsal cortex contained the previously used border based on the cell layer. This contradicts the original results from Heller and Ulinski that the border based on the cell layer coincides with the border based on thalamic projections.

4.4.2. Spatiotemporal activity patterns

Summary of experimental results| Spatiotemporal activity patterns (voltage and power) did not reveal any obvious low-frequency waves or shifts in the location of activity peaks over the course of the stimulus presentation. Throughout the stimulus presentation, the evoked activity remained in one location and no additional secondary active cortex regions could be identified.
Using coherence analysis of the responses across the ECoG electrode grid, a rostrocaudal phase gradient over a frequency band ranging from 15-35Hz, which extended over several millimeters, could be shown. Because the reference channel in each animal corresponded to the maximally active channel, the peak in coherence magnitude coincided with the cortical area showing strongest stimulus-evoked responses (see Fig. 3.11 bottom and Fig. 3.12) and the spatial coherence patterns reproduced the inter-individual differences observed before (cf. Fig. 3.7). Interestingly, the coherence patterns observed across the ECoG did not show a monotonous phase gradient, but in most cases two clear extremes (peak and trough) in the phase landscape were visible. The observed phase gradients corresponded to propagation speeds of $0.51 \pm 0.05 \frac{\text{mm}}{\text{ms}}$ for natural-scene stimulation and $0.76 \pm 0.18 \frac{\text{mm}}{\text{ms}}$ for natural-video stimulation. The data indicate faster wave propagation in the presence of video stimulation, but additional statistical testing is required to confirm this observation.

Interpretation and relation to previous studies| In earlier studies of turtle dorsal cortex, similar propagating wave patterns have been described as hallmark characteristic of visually evoked responses (Prechtl et al., 1997, Senseman, 1999, Senseman and Robbins, 1999, Prechtl et al., 2000, Senseman and Robbins, 2002). Previously, propagating waves have been observed primarily in VSD recordings conducted in intact and reduced preparations of the turtle visual system. As described in section 1.3.4 of the introduction, previous approaches to waves differed with respect to the applied data decomposition methods. The group of Senseman applied a variant of the well-established principal com-

ponent analysis called Karhunen-Loéve decomposition to high-speed and high-resolution VSD data and described two wave patterns in the evoked responses. Depolarization was shown to spread both intra- as well as intercortically over the course of several tens to hundreds of milliseconds. Prechtl et al. used an approach based on the transformation of response data into the frequency domain and described waves as complex patterns of phase gradients (plane and spiral waves). A systematic rostrocaudal phase gradient in populations of co-active neuronal oscillators was especially prominent. In addition to the rostrocaudal phase gradient, Prechtl described a perpendicular lateromedial phase gradient for activity below 5Hz. The authors concluded that the rostrocaudal waves are emergent phenomena of the dynamics and interconnectivity of weakly coupled intracortical oscillators while the low frequency waves are oriented along the thalamocortical afferents providing input to the visually responsive areas of cortex.

A direct comparison of the results obtained by both groups is difficult, because the two signal decomposition techniques used fundamentally different sets of basis functions. However, Senseman et al. were able to reproduce their set of wave patterns from VSD data obtained in the laboratory of James Prechtl. Therefore, both methods may be considered to produce compatible and complementary results.

Here, a coherence analysis similar to the one performed by Prechtl et al. was used and it reproduced their rostrocaudal phase gradient in the main oscillatory band (15-35Hz). However, because the analyzed frequency ranges were not equivalent to the ones used by Prechtl, the phase differences correspond to different temporal offsets. It was not possible to confirm or reproduce the lateromedial low-frequency wave, because the coherence analysis was cut off at 5Hz. It should also be noted that the spatial resolutions of the imaging systems used by both labs were significantly higher than the electrode pitch on the ECoG grid (500µm). Furthermore, the temporal characteristics of the applied voltage sensitive dyes as well as the filter settings of the data acquisition system might contribute to the shape of the observed wave patterns. An additional potential confound in the analysis of propagation patterns in µECoG data is that it is difficult to determine how well the electrodes across the recording grid make contact with the cortex and to ascertain this stability over the course of the chronic experiment. Differences in the contact strength across the grid could lead to deviations in the recorded signals and influence the recorded spatiotemporal patterns.

While no lateromedial waves were observed here, ongoing work in this lab on *in-vitro* eye-brain preparations indicates the existence of low-frequency waves traveling perpendicular to the direction of the 20Hz phase gradient (Mark Shein-Idelson personal communication). Similar non-periodic traveling waves in the visual cortex of mammals have been

demonstrated to be dependent on the stimulus context (see below). Thus, the absence of a non-periodic low-frequency wave in the ECoG data might be due to differences in the applied stimulus paradigm.

A functional discussion of the observed phase gradient is difficult considering the scarcity of knowledge on the function of turtle dorsal cortex. Prechtl et al. (2000) pointed out that phase-gradients smaller than 2π could serve to assign unambiguous oscillatory phases to cortex regions along the gradient. The authors suggested that this would represent a framework beneficial for the temporal segmentation and categorization of visual information as it was proposed within a theoretical temporal framework (von der Malsburg and Schneider, 1986, Sompolinsky and Tsodyks, 1994, Hopfield, 1995).
Alternatively, Nenadic et al. created a computational model of dorsal cortex which reproduced the wave patterns similar to those observed experimentally by Senseman et al. (Nenadic et al., 2000, Nenadic et al., 2002, Nenadic et al., 2003). Subsequently, the authors demonstrated that a Kahunen-Loéve decomposition-based approach to the modeled waves could be used to map out the theoretical visual space of the model. However, it is unclear to what extent the computational model is supported by experimental data. To my knowledge, none of the predictions have been tested experimentally.

Propagating waves of neuronal activity| Propagating waves of activity are well-known phenomena which have been observed in various brain structures [for reviews on the topic see (Ermentrout and Kleinfeld, 2001, Wu et al., 2008, Sato et al., 2012)]. Propagation can manifest itself in the form of plane-, target- or spiral waves and is usually subdivided based on whether the underlying activation is periodic or non-periodic. Wave motion can be apparent (or fictitious) if the active network consists of multiple elements which receive driving inputs from a single oscillating source, but with different temporal delays. Real wave motion may occur in neuronal networks with two different configurations: (1) Single oscillatory sources can generate activity that propagates along a chain of directly connected circuit elements or (2) systems of recurrently coupled intrinsically oscillating elements can generate phase gradients based on their connectivity. In addition, the interactions of active neuronal populations can give rise to complex spiral wave patterns. Functionally, waves in the neocortex have been suggested to (a) provide background depolarization to selectively activate cortical regions, (b) prime cortical regions by increasing their sensitivity to incoming inputs, and (c) spatially organize cortical regions by means of phase distributions (Wu et al., 2008).
Non-periodic waves have been described to occur in the visual cortex of anesthetized

and awake mammals (Sato et al., 2012). Relatively fast (0.1-0.4$\frac{m}{s}$), horizontally traveling waves were demonstrated in extra- and intracellular single-channel recordings (Cowey, 1964, Bringuier et al., 1999), VSD recordings (Grinvald et al., 1994, Benucci et al., 2007), as well as spiking activity (Busse et al., 2009). These traveling waves exhibit a strong context dependence and are strongest in responses to focal, low contrast stimuli while they are greatly reduced in responses to large, high contrast stimuli (Nauhaus et al., 2008, Nauhaus et al., 2012). Based on this context dependence they have been proposed to reflect a normalization process influencing the range of spatial integration in visual cortex (Carandini and Heeger, 2011, Sato et al., 2012). As was mentioned before, such non-periodic waves have been described to occur in turtle dorsal cortex, but was not observed in the chronic ECoG situation. This absence might be due to differences in the state of the preparation, the recording configuration, or the stimulus paradigm.

Propagating waves in oscillating neuronal circuits which manifest as systematic phase gradients have been described in many sensory and non-sensory systems across different species (Ermentrout and Kleinfeld, 2001, Rubino et al., 2006, Lubenov and Siapas, 2009). In 2001, Ermentrout and Kleinfeld reviewed the literature on phase waves observed in visual, olfactory and somatosensory cortices across a variety of species (Ermentrout and Kleinfeld, 2001). Based on theoretical considerations, the authors described systematic phase gradients in oscillating circuits as the consequence of weakly coupled, independent oscillatory units. Based on the characteristics of the oscillators and the nature of the coupling, different phase dynamics will emerge in such systems. Ermentrout and Kleinfeld suggest two potential computational roles for systematic phase gradients in cortical systems: (1) While synchronous oscillations rhythmically increase and decrease the excitability of a cortical circuit, propagating waves subdivide a network into more and less excitable subregions. (2) Because neurons are most sensitive to changes in their input during the oscillatory half period preceding the generation of an action potential, phase gradients cause a subset of neurons in the network to be maximally sensitive to input changes at any given time. In most networks exhibiting phase gradients, the observed maximal phase difference in smaller than 2π. Functionally, this means that subregions of the network are always uniquely labeled with an unambiguous phase, enabling the system to label simultaneously perceived stimulus features with unique phases and thereby segment sensory inputs based on the representation of the input in the oscillating network. Unfortunately, it is not known which stimulus features are represented in the dorsal cortex of the turtle and thus whether such a segmentation may or may not exist.

4.5. Mechanistic considerations

4.5.1. Local generation of oscillations in the turtle dorsal cortex

Unfortunately, the μECoG data presented in this study are unsuitable to directly address the mechanisms underlying the observed oscillations and waves. However, based on previous studies and observations made in this lab, an attempt will be made to work out a set of considerations on the potential mechanistic background of the described activity patterns.

Through depth recordings with multichannel silicone probes in combination with current source density analysis, Prechtl et al. obtained data indicating that the oscillations in turtle dorsal cortex (∼20Hz) are generated by local oscillatory current sources. Along the depth axis of cortex the authors found multiple (two to three) coherent pairs of current sources and sinks. This suggests that the oscillations are generated locally through intracortical connections between neuronal populations situated in different cortical layers. Neuronal networks have an inherent tendency to oscillate even in response to uncorrelated inputs (Reyes, 2003). Anatomical studies in turtle cortex have shown the presence of prominent feedfoward and feedback connections between interneurons and pyramidal-like neurons in the dorsal cortex (Kriegstein and Connors, 1986, Connors and Kriegstein, 1986, Colombe et al., 2004). Presumably, the recurrent circuit in turtle cortex comprises the excitatory pyramidal-like neurons in the cell layer as well as one or both of the interneuron types in the molecular (subpial cells; feedforward inhibition) and subcellular (stellate cells; feedback inhibition) layers. Unfortunately, the interplay of pyramidal-like neurons and interneurons in turtle cortex during oscillatory activity has not yet been established experimentally.

Acute experiments in lightly anesthetized turtles indicate a relation between the occurrence of oscillations in the cortical local field potential (LFP) and multi-unit spiking activity (MUA, Julien Fournier and Christian M. Müller personal communication). Increased oscillatory power could thus be interpreted as reflecting elevated spiking activity in the neuronal population underneath the ECoG electrodes. Oscillations without neuronal firing in the tissue may be considered unlikely if the oscillations are truly caused by the activity of local current sources (Prechtl et al., 2000). Unfortunately, it was not yet possible to quantitatively assess the relation of neuronal spiking and evoked oscillatory power in μECoG recordings under the very same experimental conditions. In addition to these correlations between oscillatory activity and MUA, studies in mammals have shown that wide-band shifts in LFP power spectra are associated with neuronal spiking activity in the tissue (Manning et al., 2009). The power spectra of stimulus-evoked activity in

turtle dorsal cortex exhibited such wide-band (5-100Hz) upward shifts of approximately 0.5 order of magnitude and may therefore also reflect elevated MUA in dorsal cortex.

Pharmacological observations and comparisons with previous studies suggest an involvement of GABAergic interneurons; specifically of the $GABA_A$ type. Initial experiments indicate that anesthesia depth has a substantial influence on the occurrence of oscillations in the dorsal cortex. In deeply anesthetized turtles ($\sim$3% Vol. Isoflurane) cortical oscillations were completely suppressed and flash-evoked responses were reduced to brief onset- and offset-transients (data not shown). The effects of volatile anesthetics (i.e. Isoflurane; used in pilot experiments) on spontaneous and stimulus evoked cortical activity in mammals have been examined in several studies. It was demonstrated that the administration of Isoflurane reduced the strength of sustained spontaneous and evoked oscillations in cortex (Peterson et al., 1986, Madler et al., 1991, Munglani et al., 1993). Subsequent *in-vitro* pharmacological studies support an effect of Isoflurane on GABAergic transmission. Especially $GABA_A$ transmission was shown to be up-regulated under the influence of Isoflurane (Antkowiak and Hentschke, 1997, Antkowiak and Helfrich-Förster, 1998, Antkowiak, 1999). The effects were demonstrated to be not exclusive to cortex, but responses of thalamic neurons appeared to be affected as well (Detsch et al., 1999). In a lightly anesthetized state, evoked as well as spontaneous oscillations can be routinely recorded in turtle cortex, indicating that previous findings of the dose-dependence of the Isoflurane effect observed in mammalian cortices might also apply in turtle cortex (personal communication from Julien Fournier and Christian M. Müller; 0.1% Vol. Isoflurane). The previously described fast, chloride-dependent, bicuculline-sensitive inhibitory pathway in turtle dorsal cortex (Connors and Kriegstein, 1986) represents a potential target for Isoflurane-mediated effects.
Taken together, these results suggest an involvement of GABAergic inhibitory connections in dorsal cortex networks in the generation and maintenance of network oscillations. If cortical inhibition is up-regulated by Isoflurane, the cortex might not be able to enter the resonant oscillating state, because feedforward and/or feedback inhibition are too strong and silence all residual excitation. Prechtl had already suggested that oscillations are generated locally in the dorsal cortex (Prechtl et al., 2000), indicating this as the potential location of the Isoflurane-mediated attenuation, but that does not exclude additional subcortical effects (Detsch et al., 1999).
The pharmacological observations are compatible with the general concept of "clocking" interneuron networks (section 1.2 of the introduction) in the synchronization of neuronal populations in insects and mammals (Laurent, 2002, Hu et al., 2014). Further work on

the neurochemical, morphological, and physiological subtyping of cortical cell types as well as more local recordings from cell assemblies will be required to describe the exact mechanistics of the generation of oscillatory activity in turtle cortex.
This reasoning apparently contradicts previous studies showing reliable stimulus-evoked oscillations in anesthetized turtles (Prechtl, 1994,Prechtl et al., 1997,Senseman and Robbins, 1999). It should be noted that several of the cited studies relied on the outdated ice-anesthesia method. This method was controversial and did not include the systemic administration of chemical anesthetics. Instead, the poikilothermic animals were placed in crushed ice (core temperature <4°C) prior to and/or during surgery. Subsequently, recordings were performed at room temperature (∼22°C) with only topical application of local anesthetics. Thus, it can be assumed that oscillations occurred in these animals, because there was no pharmacological effect on the structures involved in the generation of cortical oscillations. It can also be assumed that these animals were not really anesthetized.

4.6. Potential functional roles of turtle dorsal cortex

Natural visual stimuli in the visual neurosciences| Natural visual stimuli exhibit complex high-level statistics and are thus hard to control in neurophysiological and psychophysical experiments (Simoncelli and Olshausen, 2001). Categories of natural scenes (landscapes, human-made scenes, animals, etc) have been demonstrated to differ in their spatial frequency composition (Torralba and Oliva, 2003), but ultimately many of the high-level image statistics are determined by a regular phase-structure (Thomson, 1999, Wichmann et al., 2006). More recent attempts to achieve a robust classification of natural scenes with respect to their content have focused on the application of deep learning networks (Krizhevsky et al., 2012, Donahue et al., 2013). In these approaches deep convolutional neural networks are used to classify large sets of natural images based on complex criteria the networks develop during an intial training (or learning) phase.
The utility of natural visual stimuli in the visual neurosciences in comparison to well-controllable artificial stimuli has been the matter of longstanding debates. Proponents of artificial stimulation mainly emphasize that the precise control of stimuli is mandatory to examine well-defined properties of visual processing and that natural stimuli are too hard to control for the construction of reasonable models of the visual system (Rust and Movshon, 2005). However, they acknowledge the usefulness of natural stimuli when exploring the functions of higher extrastriate cortical areas which may exhibit highly complex stimulus preferences. Their opponents appreciate that artificial stimuli have been

used to gather most of our current understanding of visual processing, but stress that simple artificial stimuli are insufficient for the examination of real-life sensory tasks in natural environments (Felsen and Dan, 2005). This notion is supported by the finding that complex cells in cat primary visual cortex are more sensitive to their preferred feature if it is embedded into a natural context (Felsen et al., 2005). The authors could further demonstrate that the intact phase structure of natural scenes is required for this phenomenon to occur.

Naturalistic visual stimulation of turtles| In the presented study a variety of visual stimuli was used to explore their efficiency in driving oscillatory activity in turtle dorsal cortex. Natural-scene stimuli in the stimulus set evoked significantly stronger oscillatory power than matched phase-scrambled scenes. The initial choice to use natural stimuli was largely based on their efficiency in activating dorsal cortex in pilot experiments (data not shown). In addition, the scarcity of information on stimulus selectivity and response properties of dorsal cortex neurons complicated the sensible selection of any of the well-known parametric stimulus sets (i.e. sinusoidal gratings).

The observed strong and sustained cortical activation by natural visual stimulation could reflect that such stimuli contain relevant information that is processed in the dorsal cortex. From this point of view it might be concluded that the dorsal cortex exhibits a preference for coherent natural inputs. Here, the man-made images and animal-images evoked the strongest oscillations while landscape stimuli evoked the weakest oscillations. At this point, it should be repeated that several of the stimulus pictures in the set were taken at angles not corresponding to a turtles' natural point of view and of objects/scenery unrelated to the turtles' natural habitats. This discrepancy may have added to the variability of evoked responses within the arbitrary stimulus categories. Natural-video stimuli showed the strongest oscillations compared to all different control stimuli. They contain visual information which could be considered to be most natural to the animals, because the footage was filmed using a remote submarine close to the natural point of view of a turtle in its natural habitat.

Since the stimulus set in the presented study was intended for a general exploratory examination of the dorsal cortex that might help to shape future experimental approaches, it allows only speculations on what is represented by the recorded activity patterns. More suitable test and control stimuli would require more subtle changes in the temporal and spatial coherence of natural stimuli as well as a hypothesis of what aspect of visual information is actually processed in the dorsal cortex. Also, the degree of naturalness of a given stimulus depends on the animal model used. Kayser et al. analyzed natural visual

stimuli which had been recorded in the natural habitats of the examined animal models and from their viewpoints and showed that these scenes were characterized by particular spatial and temporal dynamics (Kayser et al., 2003). Alternatively, recent advances in the miniaturization of electrophysiological recording equipment makes it feasible to telemetrically record neural activity from animals behaving in their natural habitats (Lei et al., 2004).

Similarities of turtle dorsal cortex to mammalian extrastriate cortex| Despite the fact that the dorsal cortex is the first cortical processing station in the turtle forebrain, its constituent neurons exhibit striking dissimilarities to neurons in mammalian primary visual cortex. The receptive fields of neurons in turtle dorsal cortex have been described as very extensive (Mazurskaya, 1973b, Mazurskaya, 1973a), which stands in stark contrast to the small and specific receptive fields described in mammalian V1 (Hubel and Wiesel, 1959). The lack of a clear-cut retinotopy in turtle dorsal cortex forms an additional notable difference to mammalian striate as well as several extrastriate areas.
In 1992, Felleman and Van Essen described a distributed hierarchical network of 32 visual and visual-associative cortex areas in the macaque brain with an estimated 305 interconnections (Felleman and Van Essen, 1991, Van Essen and Felleman, 1992). With areas exceeding $10cm^2$, the primary (V1) and secondary (V2) visual cortices represent the largest visual areas while most other areas are significantly smaller (Van Essen and Felleman, 1992). Beginning in the retina, the mammalian visual system is typically subdivided into two parallel hierarchical information processing streams: (1) The ventral and (2) dorsal pathways. Cortical areas belonging to the former are mainly involved in the recognition of visual objects while areas belonging to the latter pathway are involved in processing attributes related to motion and visually guided action (Mishkin et al., 1983). Note that these streams represent a simplified view of the visual system and should not be considered as completely isolated units, but as interconnected subsystems [for a review of the human visual cortex please refer to (Grill-Spector and Malach, 2004)].
Since its initial description, the ventral object recognition system has received considerable attention and was extensively explored in human and non-human primates using both invasive and non-invasive experimental techniques as well as psychophysics. Early human fMRI studies aimed at identifying object-sensitive cortical areas in the ventral pathway using natural and scrambled visual stimuli (Malach et al., 1995, Grill-Spector et al., 1997). Malach et al. used photographs as well as matched phase-scrambled photographs and reported significant differences in the non-retinotopic lateral occipital complex (LO), but not in earlier retinotopic areas of human striate or extrastriate

cortex (Malach et al., 1995). Grill-Spector et al. examined the object selectivity of several striate and extrastriate areas along the human object-recognition pathway and reported increasingly differential activation along the pathway (Grill-Spector et al., 1997). The retinotopic areas V1 to V3 did not show a reduction of activity in response to scrambled images, while the retinotopic area V4v as well as the non-retinotopic LO were reported to exhibit significantly different activation in response to natural and scrambled images. However, the scrambling procedure applied by Grill-Spector et al. differed from that applied in this project. Grill-Spector et al. split the original photographs into subimages and shuffled them on the screen. In this study, random phase noise was added to the phase-spectra of natural images, destroying higher order correlations. Special care was taken to keep the statistics of natural and phase-scrambled stimuli as constant as possible and to manipulate only the phase spectra. By adding defined amounts of phase noise to the original phase spectra, the amount of strong local contrast elements in natural images can be systematically reduced (Wichmann et al., 2006). This decrease in sharp local contrast elements in phase-scrambled scenes is accompanied by a reduction of coherent contour objects which are formed by spatially arranged local contrast elements. Contours are essentially required to form recognizable visual objects which can be extracted from the surrounding background structures.

In a recent study, Freeman et al. used synthetic visual textures onto which higher-order natural-scene statistics had been imposed and filtered noise stimuli without these statistics to probe their efficiency in activating neurons in macaque V1 and V2 (Freeman et al., 2013). The authors could demonstrate that neurons in V2 responded significantly more strongly to the naturalistic textures than to the filtered noise and that this preference was absent in V1 neurons. In addition to single-cell electrophysiology the authors could reproduce their observations in BOLD fMRI responses (a large-scale population signal) in human observers. They concluded that neurons in V2 represent complex natural image structures which they extract from the inputs they receive from V1. Freeman et al. used photographs of real world textures to generate their artificial stimuli. The synthetic textures were created by successively imposing the high order statistics of the initial photographs onto initially random white noise patterns. The noise stimuli on the other hand were generated in a phase-randomization approach that removes statistical dependencies. Both stimulus categories may be comparable to the stimuli used in this study where truly natural images with natural higher order correlations and phase-scrambled natural scenes without these correlations were used.

In an earlier study, Willmore et al. already demonstrated that a subpopulation of neurons in macaque V2 shows a preference for complex visual features in natural scenes (Will-

more et al., 2010). Cortical areas and single neurons in later stages of the ventral visual pathway have been demonstrated to exhibit even higher feature selectivities regarding visual stimulation. Prominent examples are the fusiform face area (Tsao et al., 2003, Tsao et al., 2006) and the parahippocampal place area (Kornblith et al., 2013), which contain neurons selective for either stimuli displaying faces or places, respectively.

While the applied stimulation methods and recording techniques were not identical, an attempt will be made to relate the results obtained in the presented study to these previous observations in the mammalian visual system. Taken together, the comparison of response profiles in the large-scale ECoG metric to the large-scale fMRI signals reported in previous mammalian studies suggests a higher degree of similarity of turtle dorsal cortex to mammalian non-retinotopic extrastriate cortices rather than to the retinotopic striate and extrastriate areas where both stimulus categories evoked equal responses indifferent of the presence or absence of natural statistics.

Unfortunately, neurons in the dorsal cortex have not yet been tested with respect to a potential selectivity for complex visual stimuli. Therefore, it is difficult to select a specific mammalian visual cortex region for a direct comparison. Because of this uncertainty, a direct comparison of structures across taxa is complicated. The scarcity of reliable literature on the turtle anatomy and physiology make it necessary to re-assess several important issues before sound and detailed interpretations and comparisons on the functional role of dorsal cortex for visual processing are possible.

The presented project contributed to this effort by localizing a visually responsive area in the dorsal cortex of awake turtles and by demonstrating a selectivity for global features of natural visual stimuli.

4.7. Conclusions and outlook

The presented exploratory research project expands the general understanding of the turtle dorsal cortex in several important aspects. To my knowledge, it represents the first study to examine evoked ECoG dynamics in response to natural visual stimuli in fully awake turtles.

Methodologically, the obtained results demonstrate that it is possible to conduct μECoG recordings in chronically implanted, fully awake turtles over multiple weeks. The method was used to localize visually responsive areas in the dorsal cortex of awake turtles and to describe visually-evoked, spatio-temporal response patterns. Natural visual stimuli (scenes and videos) were demonstrated to evoke strong oscillatory activity, suggesting that the dorsal cortex of turtles might be involved in the processing of complex natural

stimulus features. Experiments in lightly anesthetized turtles and previous observations in mammalian studies suggest that the observed oscillatory activity is correlated with multi-unit spiking activity in the cortex and could be used as a proxy-metric for neuronal spiking activity.

While it is not possible to infer the precise role dorsal cortex plays in the processing of static visual scenes, it could be demonstrated that it is strongly activated by scenes with complex, natural statistics and that especially the distribution of local contrast elements influences the strength and coherence of evoked oscillations in the field potential. Multilinear regression showed that a small set of global stimulus features could be used to predict up to 32% of the observed variance in the recorded responses. The described differences in responses to natural and matched phase-scrambled scenes are reminiscent of observations in mammalian non-retinotopic extrastriate cortex.

Furthermore, μECoG responses to natural-video stimulation indicate that the dorsal cortex of turtles is not only strongly driven by static natural scenes with intact local contrast patterns, but also by videos composed of temporally coherent sequences of natural scenes. In addition to previously described oscillations in the 20Hz range, elevated oscillatory activity up to 45Hz was observed exclusively in response to natural-video stimulation. Control-videos with reduced spatial and/or temporal integrity evoked cortical responses with significantly weaker and less coherent oscillations. Remarkably, alterations of spatial and temporal coherence had similar effects on the evoked oscillatory responses in turtle cortex. These results indicate that both the spatial and the temporal structure contain relevant stimulus features which drive spatiotemporal activity patterns in turtle dorsal cortex.

In the future, more sophisticated high-density, single-unit recording techniques should be adapted for the chronic use in awake turtles in order to obtain a clearer picture of the selectivities of single neurons. Furthermore, these experiments should make use of extensive sets of naturalistic-stimuli sampled from the natural habitats of the examined species in order to eliminate the initial selection bias. Through the application of state-of-the-art spike sorting and analysis techniques the resulting response data could be used to examine how individual neurons and even specific neuronal cell types respond to the display of natural and non-natural stimuli and how complex features in visual stimuli influence these responses.

The experimental methods and protocols presented in this study represent a promising foundation and framework for the development and accomplishment of these experiments; ultimately leading to a deeper understanding of the functional role of turtle dorsal cortex.

Bibliography

[Aboitiz et al., 2002a] Aboitiz, F., Montiel, J., and Lopez, J. (2002a). Critical steps in the early evolution of the isocortex: insights from developmental biology. *Braz J Med Biol Res*, 35(12):1455–1472.

[Aboitiz et al., 2002b] Aboitiz, F., Montiel, J., Morales, D., and Concha, M. (2002b). Evolutionary divergence of the reptilian and the mammalian brains: considerations on connectivity and development. *Brain Res Brain Res Rev*, 39(2-3):141–153.

[Akam and Kullmann, 2010] Akam, T. and Kullmann, D. M. (2010). Oscillations and filtering networks support flexible routing of information. *Neuron*, 67(2):308–320.

[Akam and Kullmann, 2014] Akam, T. and Kullmann, D. M. (2014). Oscillatory multiplexing of population codes for selective communication in the mammalian brain. *Nat Rev Neurosci*, 15(2):111–122.

[Ammermüller and Kolb, 1996] Ammermüller, J. and Kolb, H. (1996). Functional architecture of the turtle retina. *Progress in Retinal and Eye Research*, 15(2):393–433.

[Antkowiak, 1999] Antkowiak, B. (1999). Different actions of general anesthetics on the firing patterns of neocortical neurons mediated by the GABA(A) receptor. *Anesthesiology*, 91(2):500–511.

[Antkowiak and Helfrich-Förster, 1998] Antkowiak, B. and Helfrich-Förster, C. (1998). Effects of small concentrations of volatile anesthetics on action potential firing of neocortical neurons in vitro. *Anesthesiology*, 88(6):1592–1605.

[Antkowiak and Hentschke, 1997] Antkowiak, B. and Hentschke, H. (1997). Cellular mechanisms of gamma rhythms in rat neocortical brain slices probed by the volatile anaesthetic isoflurane. *Neurosci Lett*, 231(2):87–90.

[Balaban, 1978] Balaban, C. D. (1978). Structure of anterior dorsal ventricular ridge in a turtle (Pseudemys scripta elegans). *Journal of Morphology*, 158(3):291–322.

[Balaban and Ulinski, 1981] Balaban, C. D. and Ulinski, P. S. (1981). Organization of thalamic afferents to anterior dorsal ventricular ridge in turtles. I. Projections of thalamic nuclei. *J Comp Neurol*, 200(1):95–129.

[Bass and Northcutt, 1981] Bass, A. H. and Northcutt, R. G. (1981). Retinal recipient nuclei in the painted turtle, Chrysemys picta: an autoradiographic and HRP study. *J Comp Neurol*, 199(1):97–112.

[Baylor and Hodgkin, 1974] Baylor, D. A. and Hodgkin, A. L. (1974). Changes in time scale and sensitivity in turtle photoreceptors. *J Physiol*, 242(3):729–758.

[Belkin, 1963] Belkin, D. A. (1963). Anoxia: tolerance in reptiles. *Science*, 139(3554):492–493.

[Benucci et al., 2007] Benucci, A., Frazor, R. A., and Carandini, M. (2007). Standing waves and traveling waves distinguish two circuits in visual cortex. *Neuron*, 55(1):103–117.

[Berger, 1929] Berger, P. D. H. (1929). Über das Elektrenkephalogramm des Menschen. *Archiv für Psychiatrie und Nervenkrankheiten*, 87(1):527–570.

[Bickler and Buck, 2007] Bickler, P. E. and Buck, L. T. (2007). Hypoxia Tolerance in Reptiles, Amphibians, and Fishes: Life with Variable Oxygen Availability. *Annual Review of Physiology*, 69(1):145–170.

[Boiko, 1980] Boiko, V. P. (1980). Responses to visual stimuli in thalamic neurons of the turtle Emys orbicularis. *Neurosci Behav Physiol*, 10(2):183–188.

[Bringuier et al., 1999] Bringuier, V., Chavane, F., Glaeser, L., and Frégnac, Y. (1999). Horizontal propagation of visual activity in the synaptic integration field of area 17 neurons. *Science*, 283(5402):695–699.

[Busse et al., 2009] Busse, L., Wade, A. R., and Carandini, M. (2009). Representation of concurrent stimuli by population activity in visual cortex. *Neuron*, 64(6):931–942.

[Buzsáki et al., 2012] Buzsáki, G., Anastassiou, C. A., and Koch, C. (2012). The origin of extracellular fields and currents — EEG, ECoG, LFP and spikes. pages 1–14.

[Buzsáki and Draguhn, 2004] Buzsáki, G. and Draguhn, A. (2004). Neuronal oscillations in cortical networks. *Science*, 304(5679):1926–1929.

[Buzsáki et al., 2004] Buzsáki, G., Geisler, C., Henze, D. A., and Wang, X.-J. (2004). Interneuron Diversity series: Circuit complexity and axon wiring economy of cortical interneurons. *Trends Neurosci*, 27(4):186–193.

[Buzsáki et al., 1992] Buzsáki, G., Horváth, Z., Urioste, R., Hetke, J., and Wise, K. (1992). High-frequency network oscillation in the hippocampus. *Science*, 256(5059):1025–1027.

[Carandini and Heeger, 2011] Carandini, M. and Heeger, D. J. (2011). Normalization as a canonical neural computation. *Nat Rev Neurosci*, 13(1):51–62.

[Cassenaer and Laurent, 2007] Cassenaer, S. and Laurent, G. (2007). Hebbian STDP in mushroom bodies facilitates the synchronous flow of olfactory information in locusts. *Nature*, 448(7154):709–713.

[Cassenaer and Laurent, 2012] Cassenaer, S. and Laurent, G. (2012). Conditional modulation of spike-timing-dependent plasticity for olfactory learning. *Nature*, 482(7383):47–52.

[Colombe et al., 2004] Colombe, J. B., Sylvester, J., Block, J., and Ulinski, P. S. (2004). Subpial and stellate cells: two populations of interneurons in turtle visual cortex. *J Comp Neurol*, 471(3):333–351.

[Connors and Kriegstein, 1986] Connors, B. W. and Kriegstein, A. R. (1986). Cellular Physiology of the Turtle Visual-Cortex - Distinctive Properties of Pyramidal and Stellate Neurons. *J Neurosci*, 6(1):164–177.

[Cowey, 1964] Cowey, A. (1964). PROJECTION OF THE RETINA ON TO STRIATE AND PRESTRIATE CORTEX IN THE SQUIRREL MONKEY, SAIMIRI SCIUREUS. *Journal of Neurophysiology*, 27:366–393.

[Crawford et al., 2012] Crawford, N. G., Faircloth, B. C., McCormack, J. E., Brumfield, R. T., Winker, K., and Glenn, T. C. (2012). More than 1000 ultraconserved elements provide evidence that turtles are the sister group of archosaurs. *Biology Letters*, 8(5):783–786.

[Crawford et al., 2014] Crawford, N. G., Parham, J. F., Sellas, A. B., Faircloth, B. C., Glenn, T. C., Papenfuss, T. J., Henderson, J. B., Hansen, M. H., and Simison, W. B. (2014). A phylogenomic analysis of turtles. *Molecular phylogenetics and evolution*.

[Desan, 1984] Desan, P. (1984). *The organization of the cerebral cortex of the pond turtle, pseudemys scripta elegans*. PhD thesis, Cambridge, Massachusetts.

[Detsch et al., 1999] Detsch, O., Vahle-Hinz, C., Kochs, E., Siemers, M., and Bromm, B. (1999). Isoflurane induces dose-dependent changes of thalamic somatosensory information transfer. *Brain Res*, 829(1-2):77–89.

[Donahue et al., 2013] Donahue, J., Jia, Y., Vinyals, O., Hoffman, J., Zhang, N., Tzeng, E., and Darrell, T. (2013). DeCAF: A Deep Convolutional Activation Feature for Generic Visual Recognition. *arXiv.org*.

[Dünser et al., 1981] Dünser, K. R., Maxwell, J. H., and Granda, A. M. (1981). Visual properties of cells in anterior dorsal ventricular ridge of turtle. *Neurosci Lett*, 25(3):281–285.

[Eckhorn et al., 1987] Eckhorn, R., Bauer, R., Jordan, W., Brosch, M., Kruse, W., Munk, M., and Reitboeck, H. J. (1987). Coherent oscillations: a mechanism of feature linking in the visual cortex? Multiple electrode and correlation analyses in the cat. *Biol Cybern*, 60(2):121–130.

[Ermentrout and Kleinfeld, 2001] Ermentrout, G. B. and Kleinfeld, D. (2001). Traveling electrical waves in cortex: insights from phase dynamics and speculation on a computational role. *Neuron*, 29(1):33–44.

[Felleman and Van Essen, 1991] Felleman, D. J. and Van Essen, D. C. (1991). Distributed Hierarchical Processing in the Primate Cerebral Cortex. *Cerebral Cortex*, 1(1):1–47.

[Felsen and Dan, 2005] Felsen, G. and Dan, Y. (2005). A natural approach to studying vision. *Nature Neuroscience*, 8(12):1643–1646.

[Felsen et al., 2005] Felsen, G., Touryan, J., Han, F., and Dan, Y. (2005). Cortical sensitivity to visual features in natural scenes. *PLoS biology*, 3(10):e342.

[Freeman et al., 2013] Freeman, J., Ziemba, C. M., Heeger, D. J., Simoncelli, E. P., and Movshon, J. A. (2013). A functional and perceptual signature of the second visual area in primates. *Nature Publishing Group*, 16(7):974–981.

[Freeman et al., 2000] Freeman, W. J., Rogers, L. J., Holmes, M. D., and Silbergeld, D. L. (2000). Spatial spectral analysis of human electrocorticograms including the alpha and gamma bands. *J Neurosci Methods*, 95(2):111–121.

[Fries, 2009] Fries, P. (2009). Neuronal gamma-band synchronization as a fundamental process in cortical computation. *Annu Rev Neurosci*, 32(1):209–224.

[Fries et al., 2007] Fries, P., Nikolić, D., and Singer, W. (2007). The gamma cycle. *Trends Neurosci*, 30(7):309–316.

[Gelperin and Tank, 1990] Gelperin, A. and Tank, D. W. (1990). Odour-modulated collective network oscillations of olfactory interneurons in a terrestrial mollusc. *Nature*, 345(6274):437–440.

[Granda and Dvorak, 1977] Granda, A. M. and Dvorak, C. A. (1977). Vision in Turtles. In *The Visual System in Vertebrates*, pages 451–495. Springer Berlin Heidelberg, Berlin, Heidelberg.

[Gray et al., 1989] Gray, C. M., König, P., Engel, A. K., and Singer, W. (1989). Oscillatory responses in cat visual cortex exhibit inter-columnar synchronization which reflects global stimulus properties. *Nature*, 338(6213):334–337.

[Gray and Singer, 1989] Gray, C. M. and Singer, W. (1989). Stimulus-specific neuronal oscillations in orientation columns of cat visual cortex. *Proc Natl Acad Sci U S A*, 86(5):1698–1702.

[Grill-Spector et al., 1997] Grill-Spector, K., Kushnir, T., Hendler, T., Edelman, S., Itzchak, Y., and Malach, R. (1997). A sequence of object-processing stages revealed by fMRI in the human occipital lobe. *Human Brain Mapping*, 6(4):316–328.

[Grill-Spector and Malach, 2004] Grill-Spector, K. and Malach, R. (2004). THE HUMAN VISUAL CORTEX. *Annu Rev Neurosci*, 27(1):649–677.

[Grinvald et al., 1994] Grinvald, A., Lieke, E. E., Frostig, R. D., and Hildesheim, R. (1994). Cortical point-spread function and long-range lateral interactions revealed by real-time optical imaging of macaque monkey primary visual cortex. *J Neurosci*, 14(5 Pt 1):2545–2568.

[Hedges, 1999] Hedges, S. B. (1999). A Molecular Phylogeny of Reptiles. *Science*, 283(5404):998–1001.

[Hedges, 2012] Hedges, S. B. (2012). Amniote phylogeny and the position of turtles. *BMC biology*, 10(1):64.

[Heller and Ulinski, 1986] Heller, S. B. and Ulinski, P. S. (1986). Morphology of geniculocortical axons in turtles of the genera Pseudemys and Chrysemys. *Anatomy and Embryology*, 175(4):505–515.

[Hergueta et al., 1994] Hergueta, S., Lemire, M., Ward, R., Reperant, J., Rio, J. P., and Weidner, C. (1994). Interspecific variation in the chelonian primary visual system. *Journal für Hirnforschung*, 36(2):171–193.

[Hergueta et al., 1991] Hergueta, S., Ward, R., Lemire, M., Rio, J. P., Reperant, J., and Weidner, C. (1991). Overlapping visual fields and ipsilateral retinal projections in turtles. *Brain Research Bulletin*, 29(3):427–433.

[Herrmann, 2001] Herrmann, C. S. (2001). Human EEG responses to 1-100Hz flicker: resonance phenomena in visual cortex and their potential correlation to cognitive phenomena. *Experimental Brain Research*, 137(3-4):346–353.

[Hopfield, 1995] Hopfield, J. J. (1995). Pattern recognition computation using action potential timing for stimulus representation. *Nature*.

[Hu et al., 2014] Hu, H., Gan, J., and Jonas, P. (2014). Interneurons. Fast-spiking, parvalbumin GABAergic interneurons: from cellular design to microcircuit function. *Science*, 345(6196):1255263–1255263.

[Hubel and Wiesel, 1959] Hubel, D. H. and Wiesel, T. N. (1959). Receptive fields of single neurones in the cat's striate cortex. *J Physiol*, 148:574–591.

[Huerta and Lisman, 1995] Huerta, P. T. and Lisman, J. E. (1995). Bidirectional synaptic plasticity induced by a single burst during cholinergic theta oscillation in CA1 in vitro. *Neuron*, 15(5):1053–1063.

[Joyce et al., 2013] Joyce, W. G., Parham, J. F., Lyson, T. R., Warnock, R. C. M., and Donoghue, P. C. J. (2013). A Divergence Dating Analysis of Turtles Using Fossil Calibrations: An Example of Best Practices. *dx.doi.org*, 87(4):612–634.

[Kaas, 2009] Kaas, J. H. (2009). *Evolutionary Neuroscience*. Academic Press.

[Kajikawa and Schroeder, 2011] Kajikawa, Y. and Schroeder, C. E. (2011). How Local Is the Local Field Potential? *Neuron*, 72(5):847–858.

[Karamian et al., 1966] Karamian, A. I., Vesselkin, N. P., Belekhova, M. G., and Zagorul'ko, T. M. (1966). Electrophysiological characteristics of tectal and thalamocortical divisions of the visual system in lower vertebrates. *J Comp Neurol*, 127(4):559–576.

[Kayser et al., 2003] Kayser, C., Einhauser, W., and König, P. (2003). Temporal correlations of orientations in natural scenes. *Neurocomputing*, 52-4:117–123.

[Klausberger and Somogyi, 2008] Klausberger, T. and Somogyi, P. (2008). Neuronal diversity and temporal dynamics: the unity of hippocampal circuit operations. *Science*, 321(5885):53–57.

[Kornblith et al., 2013] Kornblith, S., Cheng, X., Ohayon, S., and Tsao, D. Y. (2013). A network for scene processing in the macaque temporal lobe. *Neuron*, 79(4):766–781.

[Kosareva, 1967] Kosareva, A. A. (1967). Projection of optic fibers to visual centers in a turtle (Emys orbicularis). *J Comp Neurol*, 130(3):263–275.

[Kreiter and Singer, 1992] Kreiter, A. K. and Singer, W. (1992). Oscillatory Neuronal Responses in the Visual Cortex of the Awake Macaque Monkey. *Eur J Neurosci*, 4(4):369–375.

[Kriegstein, 1987] Kriegstein, A. R. (1987). Synaptic responses of cortical pyramidal neurons to light stimulation in the isolated turtle visual system. *J Neurosci*, 7(8):2488–2492.

[Kriegstein and Connors, 1986] Kriegstein, A. R. and Connors, B. W. (1986). Cellular physiology of the turtle visual cortex: synaptic properties and intrinsic circuitry. *J Neurosci*, 6(1):178–191.

[Krizhevsky et al., 2012] Krizhevsky, A., Sutskever, I., and HInton, G. E. (2012). ImageNet Classification with Deep Convolutional Neural Networks. pages 1–9.

[Larkum et al., 2008] Larkum, M. E., Watanabe, S., Lasser-Ross, N., Rhodes, P., and Ross, W. N. (2008). Dendritic properties of turtle pyramidal neurons. *Journal of Neurophysiology*, 99(2):683–694.

[Lasztóczi and Klausberger, 2014] Lasztóczi, B. and Klausberger, T. (2014). Layer-specific GABAergic control of distinct gamma oscillations in the CA1 hippocampus. *Neuron*, 81(5):1126–1139.

[Laurent, 2002] Laurent, G. (2002). Olfactory network dynamics and the coding of multidimensional signals. *Nat Rev Neurosci*, 3(11):884–895.

[Laurent and Naraghi, 1994] Laurent, G. G. and Naraghi, M. M. (1994). Odorant-induced oscillations in the mushroom bodies of the locust. *J Neurosci*, 14(5 Pt 2):2993–3004.

[Lee, 1997] Lee, M. S. Y. (1997). Reptile relationships turn turtle ... *Nature*, 389(6648):245–245.

[Lei et al., 2004] Lei, Y. L., Sun, N. L., Wilson, F., Wang, X. S., Chen, N. H., Yang, J. Z., Peng, Y. P., Wang, J. H., Tian, S. H., Wang, M. H., Miao, Y. D., Zhu, W. N., Qi, H., and Ma, Y. Y. (2004). Telemetric recordings of single neuron activity and visual scenes in monkeys walking in an open field. *Journal of Neuroscience Methods*, 135(1-2):35–41.

[Louie and Wilson, 2001] Louie, K. and Wilson, M. A. (2001). Temporally structured replay of awake hippocampal ensemble activity during rapid eye movement sleep. *Neuron*, 29(1):145–156.

[Lubenov and Siapas, 2009] Lubenov, E. V. and Siapas, A. G. (2009). Hippocampal theta oscillations are travelling waves. *Nature*, 459(7246):534–539.

[Luo et al., 2010] Luo, Q., Lu, H., Lu, H., Yang, Y., and Gao, J.-H. (2010). Comparison of visually evoked local field potentials in isolated turtle brain: patterned versus blank stimulation. *J Neurosci Methods*, 187(1):26–32.

[Luo et al., 2009] Luo, Q. F., Lu, H., Lu, H. B., Senseman, D., Worsley, K., Yang, Y. H., and Gao, J. H. (2009). Physiologically evoked neuronal current MRI in a bloodless turtle brain: Detectable or not? *Neuroimage*, 47(4):1268–1276.

[Lyson et al., 2012] Lyson, T. R., Sperling, E. A., Heimberg, A. M., Gauthier, J. A., King, B. L., and Peterson, K. J. (2012). MicroRNAs support a turtle + lizard clade. *Biology Letters*, 8(1):104–107.

[MacLeod and Laurent, 1996] MacLeod, K. and Laurent, G. (1996). Distinct mechanisms for synchronization and temporal patterning of odor-encoding neural assemblies. *Science*, 274(5289):976–979.

[Madler et al., 1991] Madler, C., Keller, I., Schwender, D., and Pöppel, E. (1991). Sensory information processing during general anaesthesia: effect of isoflurane on auditory evoked neuronal oscillations. *BJA: British Journal of Anaesthesia*, 66(1):81–87.

[Malach et al., 1995] Malach, R., Reppas, J. B., Benson, R. R., Kwong, K. K., Jiang, H., Kennedy, W. A., Ledden, P. J., Brady, T. J., Rosen, B. R., and Tootell, R. B. (1995). Object-related activity revealed by functional magnetic resonance imaging in human occipital cortex. *Proc Natl Acad Sci U S A*, 92(18):8135–8139.

[Manning et al., 2009] Manning, J. R., Jacobs, J., Fried, I., and Kahana, M. J. (2009). Broadband shifts in local field potential power spectra are correlated with single-neuron spiking in humans. *Journal of Neuroscience*, 29(43):13613–13620.

[Maris and Oostenveld, 2007] Maris, E. and Oostenveld, R. (2007). Nonparametric statistical testing of EEG- and MEG-data. *Journal of Neuroscience Methods*, 164(1):177–190.

[Markram et al., 1997] Markram, H., Lübke, J., Frotscher, M., and Sakmann, B. (1997). Regulation of synaptic efficacy by coincidence of postsynaptic APs and EPSPs. *Science*, 275(5297):213–215.

[Marshall et al., 2002] Marshall, L., Henze, D. A., Hirase, H., Leinekugel, X., Dragoi, G., and Buzsáki, G. (2002). Hippocampal pyramidal cell-interneuron spike transmission is frequency dependent and responsible for place modulation of interneuron discharge. *Journal of Neuroscience*, 22(2):RC197.

[Mazurskaya, 1973a] Mazurskaya, P. Z. (1973a). Organization of receptive fields in the forebrain of Emys orbicularis. *Neurosci Behav Physiol*, 6(4):311–318.

[Mazurskaya, 1973b] Mazurskaya, P. Z. (1973b). Retinal projection in the forebrain of Emys orbicularis. *Neurosci Behav Physiol*, 6(1):75–82.

[Mazurskaya et al., 1966] Mazurskaya, P. Z., Davydova, T. V., and Smirnov, G. D. (1966). Functional organization of exteroreceptive projections in the forebrain of the turtle. *Fiziol Zh SSSR Im I M Sechenova*, 52(9):1050–1057.

[Mazurskaya and Smirnov, 1966] Mazurskaya, P. Z. and Smirnov, G. D. (1966). Functional features of projections from exteroceptors to dorsal forebrain cortex in the turtle. *Comparative Biochemistry and Physiology*, 19(3):639.

[Medina and Abellan, 2009] Medina, L. and Abellan, A. (2009). Development and evolution of the pallium. *Semin Cell Dev Biol*, 20(6):698–711.

[Milner, 1974] Milner, P. M. (1974). A model for visual shape recognition. *Psychological review*, 81(6):521–535.

[Mishkin et al., 1983] Mishkin, M., Ungerleider, L. G., and Macko, K. A. (1983). Object Vision and Spatial Vision - 2 Cortical Pathways. *Trends Neurosci*, 6(10):414–417.

[Mitra and Pesaran, 1998] Mitra, P. P. and Pesaran, B. (1998). Analysis of Dynamic Brain Imaging Data. *arXiv.org*, (2):691–708.

[Mitzdorf, 1985] Mitzdorf, U. (1985). Current source-density method and application in cat cerebral cortex: investigation of evoked potentials and EEG phenomena. *Physiological reviews*, 65(1):37–100.

[Mulligan and Ulinski, 1990] Mulligan, K. A. and Ulinski, P. S. (1990). Organization of Geniculocortical Projections in Turtles - Isoazimuth Lamellae in the Visual-Cortex. *J Comp Neurol*, 296(4):531–547.

[Munglani et al., 1993] Munglani, R., Andrade, J., Sapsford, D. J., Baddeley, A., and Jones, J. G. (1993). A measure of consciousness and memory during isoflurane administration: the coherent frequency. *BJA: British Journal of Anaesthesia*, 71(5):633–641.

[Nase et al., 2003] Nase, G., Singer, W., Monyer, H., and Engel, A. K. (2003). Features of neuronal synchrony in mouse visual cortex. *Journal of Neurophysiology*, 90(2):1115–1123.

[Nauhaus et al., 2008] Nauhaus, I., Busse, L., Carandini, M., and Ringach, D. L. (2008). Stimulus contrast modulates functional connectivity in visual cortex. *Nature Neuroscience*, 12(1):70–76.

[Nauhaus et al., 2012] Nauhaus, I., Busse, L., Ringach, D. L., and Carandini, M. (2012). Robustness of traveling waves in ongoing activity of visual cortex. *J Neurosci*, 32(9):3088–3094.

[Nenadic et al., 2000] Nenadic, Z., Ghosh, B., and Ulinski, P. (2000). Spatiotemporal dynamics in a model of turtle visual cortex. *Neurocomputing*, 32:479–486.

[Nenadic et al., 2003] Nenadic, Z., Ghosh, B. K., and Ulinski, P. (2003). Propagating waves in visual cortex: a large-scale model of turtle visual cortex. *J Comput Neurosci*, 14(2):161–184.

[Nenadic et al., 2002] Nenadic, Z., Ghosh, B. K., and Ulinski, P. S. (2002). Modeling and estimation problems in the turtle visual cortex. *IEEE Trans Biomed Eng*, 49(8):753–762.

[Neuenschwander et al., 1992] Neuenschwander, S., Martinerie, J., Renault, B., and Varela, F. J. (1992). A dynamical analysis of oscillatory responses in the optic tectum. *Cognitive Brain Research*, 1(3):175–181.

[Northmore and Granda, 1991] Northmore, D. P. and Granda, A. M. (1991). Refractive state, contrast sensitivity, and resolution in the freshwater turtle, Pseudemys scripta elegans, determined by tectal visual-evoked potentials. *Vis Neurosci*, 7(6):619–625.

[O'Keefe and Recce, 1993] O'Keefe, J. and Recce, M. L. (1993). Phase relationship between hippocampal place units and the EEG theta rhythm. *Hippocampus*, 3(3):317–330.

[Perez-Orive et al., 2002] Perez-Orive, J., Mazor, O., Turner, G. C., Cassenaer, S., Wilson, R. I., and Laurent, G. (2002). Oscillations and sparsening of odor representations in the mushroom body. *Science*, 297(5580):359–365.

[Peterson et al., 1986] Peterson, D. O., Drummond, J. C., and Todd, M. M. (1986). Effects of Halothane, Enflurane, Isoflurane, and Nitrous Oxide on Somatosensory Evoked Potentials in Humans. *Anesthesiology*, 65(1):35.

[Peterson and Ulinski, 1979] Peterson, E. H. and Ulinski, P. S. (1979). Quantitative studies of retinal ganglion cells in a turtle, Pseudemys scripta elegans. I. Number and distribution of ganglion cells. *J Comp Neurol*, 186(1):17–42.

[Peterson and Ulinski, 1982] Peterson, E. H. and Ulinski, P. S. (1982). Quantitative studies of retinal ganglion cells in a turtle, Pseudemys scripta elegans: II. Size spectrum of ganglion cells and its regional variation. *J Comp Neurol*, 208(2):157–168.

[Powers and Reiner, 1980] Powers, A. S. and Reiner, A. (1980). A stereotaxic atlas of the forebrain and midbrain of the eastern painted turtle (Chrysemys picta picta). *Journal für Hirnforschung*, 21(2):125–159.

[Prechtl, 1994] Prechtl, J. C. (1994). Visual motion induces synchronous oscillations in turtle visual cortex. *Proc Natl Acad Sci U S A*, 91(26):12467–12471.

[Prechtl, 1995] Prechtl, J. C. (1995). Flutter-like response in visual cortex of the semi-isolated turtle brain. *Biol Bull*, 189(2):215–216.

[Prechtl et al., 2000] Prechtl, J. C., Bullock, T. H., and Kleinfeld, D. (2000). Direct evidence for local oscillatory current sources and intracortical phase gradients in turtle visual cortex. *Proc Natl Acad Sci U S A*, 97(2):877–882.

[Prechtl et al., 1997] Prechtl, J. C., Cohen, L. B., Pesaran, B., Mitra, P. P., and Kleinfeld, D. (1997). Visual stimuli induce waves of electrical activity in turtle cortex. *Proc Natl Acad Sci U S A*, 94(14):7621–7626.

[Rager and Singer, 1998] Rager, G. and Singer, W. (1998). The response of cat visual cortex to flicker stimuli of variable frequency. *Eur J Neurosci*, 10(5):1856–1877.

[Rainey, 1979] Rainey, W. T. (1979). Organization of nucleus rotundus, a tectofugal thalamic nucleus in turtles. I. Nissl and Golgi analyses. *Journal of Morphology*, 160(2):121–142.

[Rainey and Ulinski, 1982] Rainey, W. T. and Ulinski, P. S. (1982). Organization of nucleus rotundus, a tectofugal thalamic nucleus in turtles. III. The tectorotundal projection. *J Comp Neurol*, 209(2):208–223.

[Rainey and Ulinski, 1986] Rainey, W. T. and Ulinski, P. S. (1986). Morphology of neurons in the dorsal lateral geniculate complex in turtles of the genera Pseudemys and Chrysemys. *J Comp Neurol*, 253(4):440–465.

[Reyes, 2003] Reyes, A. D. (2003). Synchrony-dependent propagation of firing rate in iteratively constructed networks in vitro. *Nature Neuroscience*, 6(6):593–599.

[Rieppel, 1999] Rieppel, O. (1999). Turtle origins. *Science*, 283(5404):945–946.

[Rieppel and deBraga, 1996] Rieppel, O. and deBraga, M. (1996). Turtles as diapsid reptiles. *Nature*, 384(6608):453–455.

[Robbins et al., 2004] Robbins, K. A., Robinson, M., and Senseman, D. M. (2004). Visualizing cortical waves and timing from data. *Ieee Visualization 2004, Proceeedings*, pages 401–408 597.

[Rubino et al., 2006] Rubino, D., Robbins, K. A., and Hatsopoulos, N. G. (2006). Propagating waves mediate information transfer in the motor cortex. *Nature Neuroscience*, 9(12):1549–1557.

[Rust and Movshon, 2005] Rust, N. C. and Movshon, J. A. (2005). In praise of artifice. *Nature Neuroscience*, 8(12):1647–1650.

[Rutishauser et al., 2013] Rutishauser, U., Kotowicz, A., and Laurent, G. (2013). A method for closed-loop presentation of sensory stimuli conditional on the internal brain-state of awake animals. *J Neurosci Methods*, 215(1):139–155.

[Sato et al., 2012] Sato, T. K., Nauhaus, I., and Carandini, M. (2012). Traveling waves in visual cortex. *Neuron*, 75(2):218–229.

[Scharr, 2000] Scharr, H. (2000). Optimale Operatoren in der digitalen Bildverarbeitung.

[Senseman, 1996] Senseman, D. M. (1996). Correspondence between visually evoked voltage-sensitive dye signals and synaptic activity recorded in cortical pyramidal cells with intracellular microelectrodes. *Vis Neurosci*, 13(5):963–977.

[Senseman, 1999] Senseman, D. M. (1999). Spatiotemporal structure of depolarization spread in cortical pyramidal cell populations evoked by diffuse retinal light flashes. *Vis Neurosci*, 16(1):65–79.

[Senseman and Robbins, 1999] Senseman, D. M. and Robbins, K. A. (1999). Modal behavior of cortical neural networks during visual processing. *J Neurosci*, 19(10):RC3.

[Senseman and Robbins, 2002] Senseman, D. M. and Robbins, K. A. (2002). High-speed VSD Imaging of visually evoked cortical waves: Decomposition into intra- and intercortical wave motions. *Journal of Neurophysiology*, 87(3):1499–1514.

[Shadlen and Movshon, 1999] Shadlen, M. N. and Movshon, J. A. (1999). Synchrony unbound: a critical evaluation of the temporal binding hypothesis. *Neuron*, 24(1):67–77– 111–25.

[Shadlen and Newsome, 1994] Shadlen, M. N. and Newsome, W. T. (1994). Noise, neural codes and cortical organization. *Curr Opin Neurobiol*, 4(4):569–579.

[Siapas and Wilson, 1997] Siapas, A. G. and Wilson, M. A. (1997). Coordinated Interactions between Hippocampal Ripples and Cortical Spindles during Slow-Wave Sleep. *Neuron*, 21(5):1123–1128.

[Simoncelli and Olshausen, 2001] Simoncelli, E. P. and Olshausen, B. A. (2001). Natural image statistics and neural representation. *Annu Rev Neurosci*, 24:1193–1216.

[Singer, 1999] Singer, W. (1999). Neuronal synchrony: a versatile code for the definition of relations? *Neuron*, 24(1):49–65– 111–25.

[Singer, 2013] Singer, W. (2013). Cortical dynamics revisited. *Trends in Cognitive Sciences*, 17(12):616–626.

[Smeets et al., 1986] Smeets, W. J., Hoogland, P. V., and Lohman, A. H. (1986). A forebrain atlas of the lizard Gekko gecko. *J Comp Neurol*, 254(1):1–19.

[Smith et al., 1980] Smith, L. M., Ebner, F. F., and Colonnier, M. (1980). The thalamocortical projection in Pseudemys turtles: a quantitative electron microscopic study. *J Comp Neurol*, 190(3):445–461.

[Sompolinsky and Tsodyks, 1994] Sompolinsky, H. and Tsodyks, M. (1994). Segmentation by a Network of Oscillators with Stored Memories. *Neural Comput*, 6(4):642–657.

[Stein and Gaither, 1983] Stein, B. E. and Gaither, N. S. (1983). Receptive-field properties in reptilian optic tectum: some comparisons with mammals. *Journal of Neurophysiology*, 50(1):102–124.

[Steriade, 2001] Steriade, M. (2001). Impact of network activities on neuronal properties in corticothalamic systems. *Journal of Neurophysiology*, 86(1):1–39.

[Steriade et al., 1993] Steriade, M., McCormick, D., and Sejnowski, T. (1993). Thalamocortical oscillations in the sleeping and aroused brain. *Science*, 262(5134):679–685.

[Steriade et al., 2001] Steriade, M., Timofeev, I., and Grenier, F. (2001). Natural waking and sleep states: a view from inside neocortical neurons. *Journal of Neurophysiology*, 85(5):1969–1985.

[Stopfer et al., 1997] Stopfer, M., Bhagavan, S., Smith, B. H., and Laurent, G. (1997). Impaired odour discrimination on desynchronization of odour-encoding neural assemblies. *Nature*, 390(6655):70–74.

[Strogatz, 2001] Strogatz, S. H. (2001). Exploring complex networks. *Nature*, 410(6825):268–276.

[Thomson, 1999] Thomson, M. G. A. (1999). Visual coding and the phase structure of natural scenes. pages 1–10.

[Torralba and Oliva, 2003] Torralba, A. and Oliva, A. (2003). Statistics of natural image categories. *Network (Bristol, England)*, 14(3):391–412.

[Treisman, 1996] Treisman, A. (1996). The binding problem. *Curr Opin Neurobiol*, 6(2):171–178.

[Tsao et al., 2003] Tsao, D. Y., Freiwald, W. A., Knutsen, T. A., Mandeville, J. B., and Tootell, R. B. H. (2003). Faces and objects in macaque cerebral cortex. *Nature Neuroscience*, 6(9):989–995.

[Tsao et al., 2006] Tsao, D. Y., Freiwald, W. A., Tootell, R. B. H., and Livingstone, M. S. (2006). A cortical region consisting entirely of face-selective cells. *Science*, 311(5761):670–674.

[Ulinski and Nautiyal, 1988] Ulinski, P. S. and Nautiyal, J. (1988). Organization of retinogeniculate projections in turtles of the genera Pseudemys and Chrysemys. *J Comp Neurol*, 276(1):92–112.

[van Drongelen, 2006] van Drongelen, W. (2006). *Signal Processing for Neuroscientists*. An Introduction to the Analysis of Physiological Signals. Academic Press.

[Van Essen and Felleman, 1992] Van Essen, D. C. and Felleman, D. J. (1992). Information processing in the primate visual system: an integrated systems perspective. *Science*, 255(5043):419–423.

[Vanderwolf, 1969] Vanderwolf, C. H. (1969). Hippocampal electrical activity and voluntary movement in the rat. *Electroencephalography and clinical neurophysiology*, 26(4):407–418.

[von der Malsburg, 1981] von der Malsburg, C. (1981). The correlation theory of the brain. Technical report.

[von der Malsburg and Schneider, 1986] von der Malsburg, C. and Schneider, W. (1986). A neural cocktail-party processor. *Biol Cybern*, 54(1):29–40.

[Wang et al., 2011] Wang, W. Z., Oeschger, F. M., Montiel, J. F., Garcia-Moreno, F., Hoerder-Suabedissen, A., Krubitzer, L., Ek, C. J., Saunders, N. R., Reim, K., Villalon, A., and Molnar, Z. (2011). Comparative Aspects of Subplate Zone Studied with Gene Expression in Sauropsids and Mammals. *Cereb Cortex*.

[Watts and Strogatz, 1998] Watts, D. J. and Strogatz, S. H. (1998). Collective dynamics of 'small-world' networks. *Nature*, 393(6684):440–442.

[Wichmann et al., 2006] Wichmann, F. A., Braun, D. I., and Gegenfurtner, K. R. (2006). Phase noise and the classification of natural images. *Vision Res*, 46(8-9):1520–1529.

[Willmore et al., 2010] Willmore, B. D. B., Prenger, R. J., and Gallant, J. L. (2010). Neural representation of natural images in visual area V2. *Journal of Neuroscience*, 30(6):2102–2114.

[Wilson, 2002] Wilson, M. A. (2002). Hippocampal memory formation, plasticity, and the role of sleep. *Neurobiology of learning and memory*, 78(3):565–569.

[Wilson and McNaughton, 1994] Wilson, M. A. and McNaughton, B. L. (1994). Reactivation of hippocampal ensemble memories during sleep. *Science*, 265(5172):676–679.

[Womelsdorf et al., 2007] Womelsdorf, T., Schoffelen, J.-M., Oostenveld, R., Singer, W., Desimone, R., Engel, A. K., and Fries, P. (2007). Modulation of neuronal interactions through neuronal synchronization. *Science*, 316(5831):1609–1612.

[Wu et al., 2008] Wu, J. Y., Xiaoying, H., and Chuan, Z. (2008). Propagating waves of activity in the neocortex: what they are, what they do. *Neuroscientist*, 14(5):487–502.

[Zagorul'ko, 1968] Zagorul'ko, T. M. (1968). Effect of intensity and wavelength of photic stimulus on evoked responses of general cortex and optic tectum in turtles. *Neurosci Behav Physiol*, 2(2):659–668.

[Zardoya and Meyer, 1998] Zardoya, R. R. and Meyer, A. A. (1998). Complete mitochondrial genome suggests diapsid affinities of turtles. *Proc Natl Acad Sci U S A*, 95(24):14226–14231.

A. Abbreviations

avg.	average
cm	centimeter
dCtx	dorsal cortex
dLGC	dorsal lateral geniculate complex
DLP	digital light processing
DVR	dorsoventricular ridge
ECoG	electrocorticography
EEG	electroencephalography
EPSP	excitatory post-synaptic potential
ERP	event-related potential
Eq.	equation
Fig.	figure
GABA	gamma-aminobutyric acid
Hz	Hertz
ISI	interstimulus interval
LCoS	liquid crystal on silicone
LED	light emitting diode
LFP	local field potential
LTP	long term potentiation
MEG	magnetoencephalography
MUA	multi unit activity
PT	pallial thickening
RGC	retinal ganglion cell
s	second
std. dev.	standard deviation
Tab.	table
TFR	time-frequency representation
V	Volt
VSD	voltage sensitive dye

B. List of figures and tables

List of Figures

List of Tables

Danksagung

Abschließend möchte ich einigen Personen danken, ohne die diese Arbeit weder denk- noch durchführbar gewesen wäre.
First and foremost I would like to thank Prof. Dr. Gilles Laurent for giving me the great opportunity to join his (then) brand-new group at the MPI for Brain Research. Although it was challenging to start working on a rather exotic model animal, I learned a great deal during my time in this creative and inspiring environment.
Ebenso dankbar bin ich Prof. Dr. Lakes-Harlan, der mir nun schon zum zweiten Mal als lokaler Betreuer an der Justus-Liebig-Universität in Gießen zur Seite stand. Auch diesmal hatte er immer ein offenes Ohr bei organisatorischen Fragen und interessante fachliche Anmerkungen zu meinen Fortschrittsberichten in seiner Arbeitsgruppe.
Weiterhin möchte ich allen Kollegen am MPI für Hirnforschung in Frankfurt dafür danken, dass Sie zu einem grandiosen Arbeitsumfeld beitragen. Insbesondere sei hier natürlich die Abteilung Neuronale Systeme genannt, die in den letzten fünf Jahren eine Art zweite Heimat für mich war. Danke an das ganze Turtle-Team für kritische Diskussionen und den ein oder anderen Aha-Moment, aber auch für die unzähligen, absolut notwendigen Ablenkungen, ohne die einen die wissenschaftliche Arbeit in den Wahnsinn treiben kann. Vielen Dank für euer Feedback und die konstruktiven Diskussionen, die maßgeblich zur Qualität der Arbeit beigetragen haben.
Ein ganz besonderer Dank geht an Christian, der besonders zu Beginn meiner Arbeit mein Mentor war und mir mit Rat und Tat in Sachen experimenteller Neurophysiologie zur Seite stand. Ein weiteres besonderes Dankeschön geht an Michaela, die als nimmermüde TA immer hilfsbereit und für die Versorgung der Versuchstiere unersetzlich war.

Unendlicher Dank gilt meiner Familie, meinen Eltern und Schwiegereltern, die mich immer auf meinem Weg bestärkt und unterstützt haben. Jeder von euch hat mit seinen besonderen Stärken und auf seine besondere Weise zum Gelingen dieser Arbeit beigetragen. Ohne euch wäre all das garnicht möglich gewesen. Vielen Dank!
Zum Abschluß möchte ich mich bei meiner wunderbaren Frau Evi bedanken und ihr diese Arbeit widmen. Danke, dass Du mich in den vergangenen fünf Jahren ausgehalten und ertragen hast. Danke für Deine unendliche Geduld und Deinen Rückhalt.

Eidesstattliche Erklärung:

Ich erkläre: Ich habe die vorgelegte Dissertation selbständig und ohne unerlaubte fremde Hilfe und nur mit den Hilfen angefertigt, die ich in der Dissertation angegeben habe. Alle Textstellen, die wörtlich oder sinngemäß aus veröffentlichten Schriften entnommen sind, und alle Angaben, die auf mündlichen Auskünften beruhen, sind als solche kenntlich gemacht. Bei den von mir durchgeführten und in der Dissertation erwähnten Untersuchungen habe ich die Grundsätze guter wissenschaftlicher Praxis, wie sie in der Satzung der Justus-Liebig-Universität Gießen zur Sicherung guter wissenschaftlicher Praxis niedergelegt sind, eingehalten.

.....

Datum & Unterschrift